HOMOGENEOUS COMBUSTION AND ITS APPLICATION TO INDUSTRIAL FURNACES

by

Seung Jun Shin

A dissertation submitted in partial fulfillment
of the requirements for the degree of
Doctor of Philosophy
(Mechanical Engineering)
in The University of Michigan
2008

Doctoral Committee:

Professor Arvind Atreya, Chair
Professor James F. Driscoll
Professor Margaret S. Wooldridge
Associate Professor Hong G. Im

TABLE OF CONTENTS

LIST OF FIGURES

LIST OF TABLES

LIST OF ABBREVIATIONS

C_a, X_a	Mole fraction of species a
C_s	Smagorinsky constant
d, D	Nozzle diameter
D_r	Confinement ratio of the domain, W / d
E	Activation energy
F_B	Buoyant force
F_I	Inertial force
H	Height of the domain
I	Radiation intensity
I_b	Radiation blackbody intensity
J	Flow Momentum
K_u	Decay rate of velocity
K_c	Decay rate of concnetration
L_r	Length ratio of the domain, H / W
$\dot{m}_i'''$	Mass production rate of the i^{th} species per unit volume
MR	Momentum ratio between jets
$\dot{q}'''$	Heat release rate per unit volume
R	Half width of the domain, $W / 2$
Re	Reynolds number
R_i	Richardson number
S	Separation distance between jets
T	Temperature [$^\circ C$]
$T_{preheat}$	Preheat temperature [$^\circ C$]
T_w	Wall temperature [$^\circ C$]
$\mathbf{u} = (u, v, w)$	Velocity vector
U	Stream-wise velocity
$\dot{V}$	Volumetric flow rate
W	Width of the domain
$X_{O_2;ox}$	Inlet oxygen mole fraction in the oxidizer jet
X	Coordinate in the X direction
Y	Coordinate in the Y direction
Z	Coordinate in the Z direction
Z_o	Virtual origin Φ Equivalence ratio

ρ	Density of fluid
ε	Emissivity
κ	Absorption coefficient
σ	Stefan-Boltzmann constant

Subscripts

F	Fuel
OX	Oxidizer
C	Centerline of the jet
O	Properties at the jet exit

ABSTRACT

Improving furnace efficiency is a high priority need for steel, aluminum, glass and other metal casting industries. Consequently, there has been a great deal of research for developing efficient burners for furnaces motivated by pollutant prevention and global warming concerns. This work attempts to address these needs. It is different from the previous attempts because it considers the furnace as a system rather than furnace and burners separately. Fuel and air are injected separately as turbulent jets and mixed, heated and diluted inside the furnace. Thus, the flame pattern and emissions depend on the jet interaction and mixing in multiple turbulent jet flames. This study is divided into two parts: The first part presents an experimental and numerical investigation into mixing characteristics and the resulting concentration fields in unconfined, non-reacting multiple turbulent jets. An experimental study [1] is performed to investigate the effects of the separation distance and momentum ratio on jet interaction and mixing in multiple jets. The experimental results [1] are compared with predictions using a modified version of a LES code called the Fire Dynamics Simulator (FDS) developed by NIST.

In the second part, a laboratory-scale furnace is constructed to test the reacting turbulent jet concept and experiments are conducted to find parameters that increase combustion efficiency and reduce pollutant emissions. Intense flue gas recirculation with buoyancy stabilized mixing is employed to reduce the flame temperatures and thus thermal NO.

Local temperature, gas composition distributions and UV emission intensities are measured and analyzed for various oxidizer jet momentums, oxygen enrichments, and overall equivalence ratios. FDS is again used to simulate these buoyant confined reacting jets which are relevant for furnaces, and the computational results are compared with the experimental measurements to validate a code that can be used for designing furnaces.

The computational results were found to be in good agreement with the measurements. Numerical investigations show that the large scale recirculation is well established for higher momentum of the oxidizer jet. This is very helpful in obtaining the homogeneous combustion condition. The oxidizer jet momentum plays a very important role in mixing and achieving the homogeneous combustion condition. It was also found that the temporal UV emission is uniform with low intensity under homogeneous combustion conditions.

CHAPTER 1

Introduction

1.1. Background

Improving thermal efficiency is the highest priority need for furnaces used in industries such as aluminum, glass, steel and other metal casting. However, there is a conflict between high thermal efficiency and low pollutant emission. The resolution of these incompatible demands has been the goal of many research projects. Therefore, a great deal of activity has been conducted in developing efficient burners for furnaces motivated by pollutant prevention and global warming concerns.

It has been long recognized that significant energy savings in industrial furnaces can be accomplished by either recycling heat or reducing the flue gas volume (reducing the nitrogen concentration by oxygen enrichment) or combining both of them. In the heat recycling method, combustion air is preheated by recovering heat from the exhaust gases and transported back into the furnace using recuperators or regenerators [2]. However, the immediate drawback of these processes is an increase in the combustion temperature, leading to high NOx emission [3, 4]. In order to reduce NOx emission, innovative NOx reducing techniques have been developed and adopted in industrial applications. These are: exhaust gas recirculation, water and/or steam injection, air and fuel staging, and pure oxygen combustion.

Among these methods, Internal Exhaust Gas Recirculation (IEGR) has been found to be most effective technique in controlling NOx emissions [5]. Combining exhaust gas recirculation and above mentioned methods has led to the development of new combustion technologies. They are Flameless Oxidation (FLOX), High Temperature Air Combustion (HiTAC), and Moderate and Intense Low oxygen Dilution (MILD) which is being actively developed in Europe and Japan [6-8]. These technologies exhibit superior

combustion characteristics in terms of high energy efficiency, uniform heat flux distributions and low NOx emissions. Thus, these technologies enable overcoming the limitations of conventional combustion and achieve maximum energy savings and minimize pollutant emissions.

1.2. Literature Review

1.2.1. Principle

The different names of the above mentioned technologies originates from emphasizing the characteristic for each combustion phenomena, invisible flame, high preheating of air and low oxygen concentration. However, the concept of heat and exhaust gas recirculation is common to these technologies. Based on this work we find that the essential conditions for achieving the flameless oxidation are direct and separate injection of fuel and oxidizer with high momentum, producing intense recirculation of hot product gases, either internally or externally. These conditions strongly suppress early ignition and temperature hot spots of that are present in conventional burner flames. In addition, high preheating of combustion air, above the auto ignition temperature, along with excessive dilution by exhaust gases is able to make reaction possible even with very low oxygen concentration atmospheres and ensures a stable flame. The principal consequence of these conditions is that the temperature rise due to reactions is minimal everywhere resulting in a relatively uniform temperature field. The elimination of peak temperatures reduces thermal NOx production. The avoidance of temperature peaks also suppresses the emission in the visible spectrum if the flame is not sooty, hence the 'flameless' appellation [8].

Notable characteristics of the flameless oxidation are very wide flame stability limits, no flame color, and uniform thermal field. Many researchers have investigated the characteristics of flameless oxidation using experimental and numerical techniques. These aspects of the flameless oxidation will be briefly discussed below.

1.2.2. Flame Stability and Characteristics

Wünning and Wünning [8] reported that flame stabilization was enhanced through the high recirculation of the combustion products (>1000°C), and the flame can then no

longer be seen [9, 10], and combustion is distributed throughout the volume of the combustion chamber. Hasegawa and Gupta [11] investigated on the thermal and chemical characteristics of high temperature air combustion (HiTAC) using liquefied petroleum gas (LPG) as the fuel. The authors concluded that the flame stability limits and thermal field uniformity in the combustion zone were much wider under high-temperature air combustion conditions than conventional combustion. The uniformity of temperature in the furnace was found to be far greater with extremely low oxygen concentration combustion air preheated to 1000 ℃ as compared to that obtained with room temperature air or that found in conventional fames. Gupta [12] noted the flame stability limits increase significantly at high air preheats and even with low oxygen concentration air. Under high temperature air combustion conditions the flame stability are infinite. The results also suggested that it is possible to use exhaust gases from a furnace as oxidant since these gases often contain several percent of oxygen. Lille et al. [13] observed the addition of nitrogen to methane and the increase of fuel jet inlet velocity gives a less visible flame, decreases flame luminosity, and increases lift-off distance. The author also noted that reduced oxygen concentration in the flue gases increases the flame size, lift-off distance and decreases luminosity and visibility. The author reported the flame becomes bluish first and then non-visible at oxygen concentration in the oxidizer below 15%. The flame volume was found to increase with increase in air preheat temperature and decrease in O2 concentration in the combustion air.

The majority of researchers believe that higher momentum of the fuel jet ensures higher scalar of dissipation closer to the jet exit [6, 8, 10], which suppresses the flame ignition in this region and ensures mixing of the fuel with vitiated air before it reacts. This is an essential criterion for flameless oxidation combustion to occur.

Many researchers have also investigated the ignition delay in the lift-off flame with preheated combustion air. Kishimoto et al. [14] reported a large ignition delay of natural gas flames as well as lift-off flame due to combustion air dilution with nitrogen. The authors also measured the reduction of the flame lift-off height with higher temperature of preheated air. Bolz and Gupta [15] also noted a decrease of the flame standoff distance (ignition delay) from the nozzle exit with an increase in the air preheat temperature and observed that the ignition delay was smaller for methane than for propane flames.

Fujimori et al. [16] observed in methane flames that the lift-off height changed with the air temperature and the fuel mass fraction of the jet. In their work, two types of lifted flames (near-lifted and far-lifted flames) were observed. As the fuel was diluted by nitrogen, a rapid decrease of the NOx emission level by the far-lifted flame occurred in the high temperature oxidizer flow. Plessing et al. [7] found that the momentum of the fuel jet has a large effect on the distance of the reaction location above the jet exit.

1.2.3. NOx emission

The methods to reduce NOx emission are based on schemes to reduce either peak flame temperature or the residence time and oxygen concentration in high temperature zones [17, 18]. The flameless oxidation mode allows a large reduction of NOx emissions by avoiding peaks of operating temperature and by reducing the concentration of oxygen through high internal recirculation. This high internal recirculation leads to a significant dilution of the air by the combustion products before the reaction. The local volumetric concentration of O2 can achieve values of between 3 and 15%.

In conventional burner and furnace systems, such pre-heating of the air leads to very high local temperatures in the flame, and therefore high NOx emissions. The temperature profile induced by a flameless combustion is relatively flat. The emissions of nitrogen oxides strongly influenced by the local temperature in the flame are thus greatly reduced and the homogeneity of the temperature in the enclosure is improved. As a result of the reduction of temperature peaks in the flame, the mean temperature level of the furnace zone can be increased, without leading to local hot spots in the vicinity of the burners. The heat transfer to the product can thus be considerably increased. In addition, the noise level induced by the combustion is greatly reduced [6, 8].

Gupta [12] observed very low NOx emission under high temperature and low oxygen concentration combustion conditions. The experimental results showed NOx emission at air preheat temperature of 1150°C decreased from 2800 ppm at 21% O2 to 40 ppm at 2% O2. The emission of CO and UHC was negligible (below the detection limits). Hasegawa and Gupta [11] reported emission of NOx and CO was much lower with combustion air preheated to high temperatures with low oxygen through lowered operating flame temperatures.

The main reason for this excellent result stems from the well known circumstance, that thermal NO formation is extremely sensitive to flame temperature peaks or spikes and these are now cut away in flameless firing. But also the other known NO formation mechanisms are positively modified, as prompt NO depends on radicals (that are abundant in a flame front, but much reduced in flameless mode [7] and also fuel NO may undergo reburning effects capable of reconverting NO into N2 species [19, 20]. Plessing et al. [7] observed instantaneous measurements of temperature and OH concentration along with NOx emission from recuperative furnace. They found a threefold drop in the total NOx emission under the flameless oxidation mode in comparison with standard flames and homogeneous distribution of OH in the burnt side of the flame. Dally et al. [21] noted that dilution of the fuel stream with inert gases can help achieve moderate and intense low oxygen combustion and reduced NOx emission.

1.2.4. Heat Flux Distribution

A large volume reaction zone recognized by a moderate temperature rise with low luminosity is a typical feature of highly preheated air combustion that is definitely different from ordinary combustion burning with luminous flames. Nevertheless, heating furnaces run by highly preheated air show efficient heating ability.

Gupta [12] concluded that high heat flux in HiTAC flames is due to high velocity of the air in the test section, which increases the convective heat flux. In addition the radiative heat flux is higher due to enhanced radiation heat flux from the furnace walls resulting from uniform heating. It can, therefore, be concluded that the heat flux from HiTAC flames is much higher and uniform. This can be translated to uniform heating of the material to be heated and reduced energy requirement. Lallemant et al. [22] showed that the percentage of the total heat release radiated by the flame exceeds the range of 10-15% quoted for radiative heat transfer in non-luminous conventional flames of natural gas. Awosope and Lockwood [23] noted that radiative losses from the reaction zone are larger than for conventional flames due to the large recirculation ratio of high emissivity product gases. The authors also reported that enhance thermal radiation is essential to reduce the NOx emission in flameless oxidation application.

The uniformity in temperature distribution allows raising the mean furnace chamber temperature, and this leads to an improvement of heat transfer and high energy savings [2].

1.2.5. Homogeneous Combustion

Atreya et al. (2004) proposed a novel solution for efficient energy saving in industrial furnaces. The authors combined both concepts of recapturing wasted flue gas enthalpy to preheat the combustion air and reducing the total amount of exhaust by using oxygen-enriched air. Clearly, reducing or eliminating the exhaust of hot N2 by using oxygen-enriched air will significantly increase the energy utilization efficiency. However, it will also create significant temperature non-uniformities (or hot spots) and increase NO production if nitrogen is present without uniform burning in reaction zones and energy transfer via radiation.

This concept is diametrically opposite to the flameless oxidation concept. In the flameless oxidation concept, high regenerative preheating (above the auto ignition temperature) of combustion air along with excessive dilution by exhaust gas recirculation is utilized to enable burning in a very low oxygen concentration atmosphere. However, both these concepts can be profitably combined to yield additional advantages under the conditions that uniform burning is accomplished in distributed reaction zones and flame temperatures are reduced by intense flame radiation, thus energy is transferred at a very high rate from these reaction zones via radiation. Since radiation is the primary mode of heat transfer in the furnace, intense and spatially uniformly radiating reaction zones are desirable. Thus, oxygen enriched conditions can be beneficial as long as they are accompanied by significant flue gas dilution and high flame radiation.

1.3. Turbulent jet mixing

Multiple turbulent jet configurations are widely employed in many industrial applications such as a furnace, diesel engine and aircraft propulsion system. In most industrial furnaces, fuel and oxidant are injected with high momentum through a nozzle, orifice and diffuser. As a result, the flame pattern and emissions strongly depend on the jet interaction and mixing under this configuration. Therefore, it is very important to

understand the mutual interaction of multiple jets from the practical point of view. The essential conditions for achieving homogeneous combustion mode are direct and separate injection of fuel and oxidant with high momentum, and the high recirculation of hot exhaust products. Another important condition is that the fuel and oxidant should be sufficiently diluted by the surrounding fluid before they react. Thus, the analysis of the interaction, mixing and dilution patterns between the separate jet flows is essential for understanding the homogeneous combustion process.

Although numerous works on a single turbulent jet are available in literature, very little investigations have been conducted on the flow structure and passive scalar transport of multiple jets due to the complicated characteristics of the multiple turbulent jets. Krothapalli et al. [24] investigated the detailed structure of the flow field with an array of rectangular lobes. Raghunathan and Reid [25] showed that a multiple jet configuration with five nozzles have an advantage in terms of noise reduction without significant momentum reduction of the jet. Mostafa et al. [26] performed the experimental and numerical studies on three rectangular turbulent jets. In this work, the authors confirmed that there is a strong mutual entrainment and turbulent transport between jets. Theoretical approaches to parallel rectangular multiple jets were conducted by Chuang et al. with a kinetic theory of turbulence [27] and Wang et al. with the thin layer theory [28]. Experimental studies on twin round interacting jets were performed by Becker and Booth [29], Moustofa [30], and Okamoto et al. [31].

The co-flowing plane jets with different velocity and momentum ratio have been studied by Grandmaison et al. [32]. The effect of the nozzle spacing on jet interaction was studied by Wlezien et al. [33]. Manohar et al. [34] presented the experimental and numerical results of the interaction between multiple incompressible air jets. The authors found that the merge distance between jets increase for larger jet spacing and the entrainment is more enhanced under multiple jet configurations than a single jet. Yimer and Becker [35] investigated the strong-weak jet coupling for developing a new concept for low-NOx burners. They found that the point of jet confluence strongly depends on the jet separation distance and momentum ratio between jets. However, the majority of these works were mainly focused on the behavior of the velocity flow field. Research on the

fundamental aspects of passive scalar mixing such as the concentration and temperature fields in multiple turbulent jets is very limited.

This study presents an experimental and numerical investigation of the mixing characteristics and the resulting concentration fields in unconfined, non-reacting multiple turbulent jets in Chapters 2 and 3. Experimentally, Planar Laser Induced Fluorescence (PLIF) was employed to study the effects of the Reynolds number, separation distance, and momentum ratio on jet interaction and mixing in three round collinear jets. The experimental results are compared with numerical predictions presenting extensive investigations in a representative five turbulent jet configuration with a center fuel jet surrounded by four oxidizer jets.

The situation of real industrial furnaces is quite different from the unconfined conditions. The confinement due to the existence of wall alters considerably the flow fields, entrainment and resulting mixing characteristics. Thus, the effects of the confinement should be considered to investigate the characteristics of flow and mixing in industrial furnaces. However, there are relatively less studies on the confined multiple turbulent jets while considerable experimental and numerical efforts have been performed on the study of turbulent jets issuing into a free environment. The numerical study on the effects of the confinement for non-reacting turbulent jets is presented in Chap. 4.

Finally, confined and reacting jets are studied for real furnace applications. The experimental methods and procedure for the reacting flow study are presented in Chapter 5, and the numerical methods are presented in Chapter 7. The experimental results of reacting flow are discussed in Chapter 6, and compared with the numerical calculations in Chapter 8.

1.4. Objectives

This work is motivated by the need to develop the innovative combustion technology to reduce energy usage and pollutant emissions while improving productivity. To investigate the structure of homogeneous combustion operating in a combustion furnace, a laboratory scale furnace has been constructed with the objective of increasing the efficiency within the strict constraints on NOx, CO, total unburned hydrocarbons (THC) and particulate emissions.

The objectives of this work are:

- Increase combustion efficiency and reduce pollutant formation by intense exhaust gas recirculation and oxygen enrichment.
- Conduct experiments on the resulting homogeneous combustion to identify the viable operative range.
- Conduct numerical simulations for developing a simulation and design tool and validate it by comparing with the experimental results. This code will enable determining the optimal value of control parameters.
- Based on the experimental and numerical investigation, this work will provide the optimized operating parameters such as fuel type, jet arrangement, jet concentration, jet momentum, and overall equivalence ratio for industrial application and control.

CHAPTER 2

Experimental and Numerical methods for unconfined non-reacting turbulent jets

2.1. Experimental apparatus and method

These experiments were done by Dr. Hyoseok Lee. They are briefly described here because the results were used by the author to validate the numerical model that was used to design the furnace. While the author did not write the Fire Dynamics Simulator computer code, it had to be adapted for the present simulations. Thus, comparison with experiments was necessary to determine appropriate sub-grid models and the required grid resolution. A more complete description may be found in [1].

2.1.1. Experimental Setup

Figure 2.1 (a) shows the schematic of water reservoir and water jet supply unit. The large rectangular water reservoir 1.5×1.5 m wide and 1.0 m high contains quiescent fresh water 0.75 m deep. Three circular nozzles of 10.4 mm exit diameter are installed vertically below the water surface. They are aligned in series at distance S separated from each other, measured from the centers of the circular nozzles. The separation distance between the jets can be adjusted to 38.1, 57.2 and 76.2 mm, which equals 3.66, 5.50 and 7.33 times the jet diameter. The jet flows are injected downward from the nozzles into the water in reservoir.

The flow velocity from the nozzles is maintained nearly constant during the experiment by two water supply units with two tanks and pumps which are designed to keep water level constant in tanks 2. The head from the water surface of the reservoir to the water surface in the tanks 2 is about 2 m. The center jet (containing the dye to simulate the fuel) is driven by one unit and the two other jets are driven by the other unit. To identify fluids

from each jet, either one of the water supply units may contain the fluorescent dye (Rhodamine WT). The dye is well dissolved in one of the water supply units to obtain a concentration of about 1.5 mg per 1 L of water.

To obtain the concentration profile, planar Laser Induced Fluorescence (PLIF) is used as the flow visualization technique. Schematic of the PLIF system is illustrated in Figure 2.1 (b). Nd-YAG laser (Surelite I PIV 10 Hz, Continuum) having a wavelength of 532 nm and power of about 2 W is used as a light source and the laser is synchronized with the CCD camera (PIVCAM 10-30, TSI Inc.) having 1000×1016 resolution and 8 bit dynamic range. The pulsed laser beam passes through a pinhole to adjust the size and then passes through the cylindrical plano-concave lens which expends it vertically to a laser sheet. Finally by a slit the laser sheet is trimmed into a thin layer sheet about 1 mm wide.

The vertical laser sheet is adjusted to pass through the centerline of the aligned center of the three jet nozzles. When the jet containing the fluorescent dye is injected from the nozzle, the dye is excited by the laser light sheet to create the fluorescent image. The image is taken by the CCD camera. Laser pulse duration time is 6 ns, camera shutter exposure time is $255 \mu s$, and laser pulse repetition rate is 10 Hz. The resolution based on the camera setup is 0.64×0.64 mm per pixel.

2.1.2. Experimental Method

In this study, all the jet image data are averaged during 25s, i.e. 250 laser shots, after the flows turn to be steady and fully developed. Even though the data is averaged over time, there is still the possibility of instrumental noise. Specially, in case of the pulsed laser used in this experiment, the laser light intensity of shots varies randomly within in a range. While there is other instrumental noise involved together, the prediction of the proper noise level for each event and each pixel is indistinct. After series of calibration applications by Dr. Hyoseok Lee [1], it was determined that the noise can be optimally removed by the convolution of 5×5 matrix.

The range of Reynolds' numbers in the experimental work were $0.96 \times 10^4 < Re < 2.4 \times 10^4$. The Reynolds number was calculated based on the nozzle diameter and the mean jet velocity of the exit flow. Water is used as the working fluid for

the experiments. It has a Schmidt number, $Sc > 600$ implying little diffusion-enhanced mixing. The turbulent jet is injected into the quiescent water with the same temperature. Since the density of the jet flow and the ambient fluid is the same, no buoyant effect is involved in these experiments.

While the pulsed laser light sheet passes vertically through the center of the aligned jets, the fluorescent dye is injected through the middle jet into the water reservoir. The fluorescent images are taken by the CCD camera synchronized with the laser pulse. In the beginning, the experimental setup and procedure is validated by measuring the concentration characteristics of turbulent single jet. The single jet was tested for four different jet exit velocities: 1.0, 1.5, 2.0 and 2.5 m/s. Corresponding Reynolds numbers were 1.16×10^4, 1.75×10^4, 2.33×10^4, and 2.91×10^4.

In order to investigate the effect of the separation distance and in particular to evaluate the effect of the side jets on the middle jet, three different separation distances, *S/D* = 3.66 , 5.50 and 7.33, were tested. The effect of the momentum ratio between jets is investigated by changing the velocity of the jets while the diameter and flow rate of the jets are kept the same.

After performing the calibration procedure, mean concentration is obtained. In experimental studies, the measurements are made up to *Z/D*=50 because of the spatial limitations. The coordinate system used in this experimental study is given in Figure 2.1 (c).

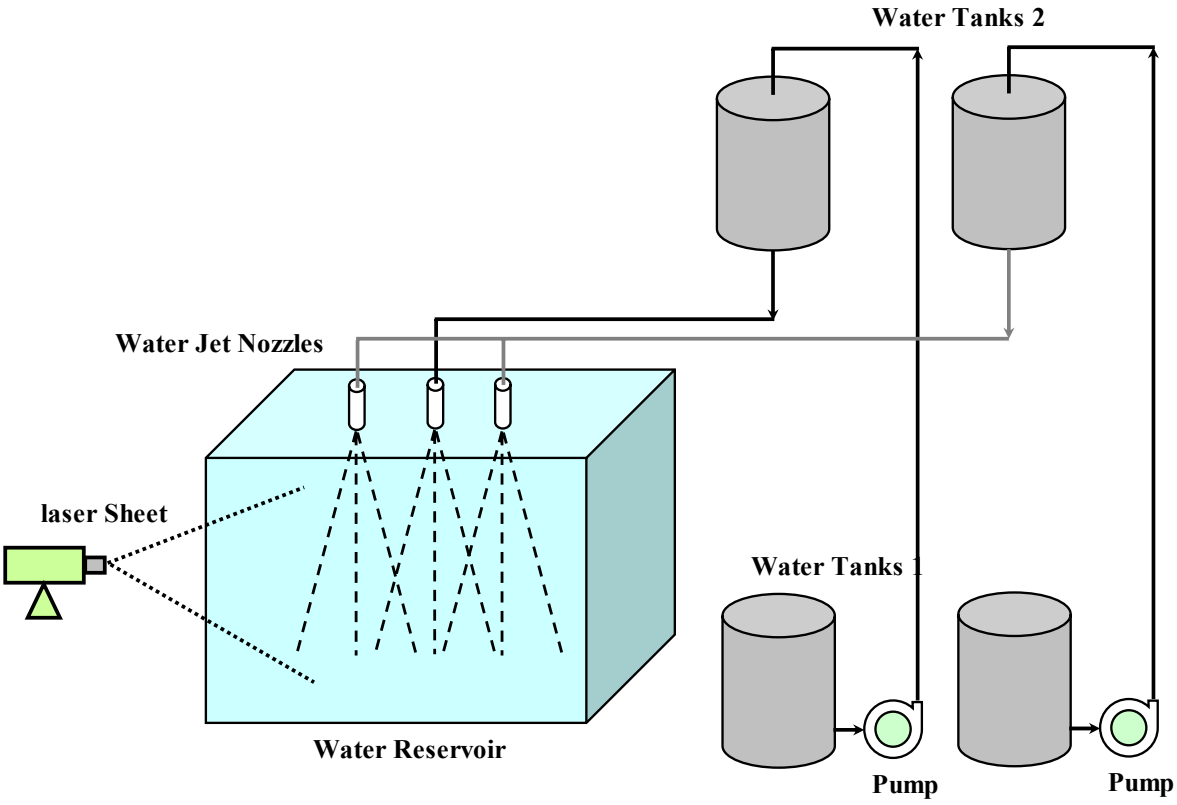
Water Tanks 2
Water Jet Nozzles
laser Sheet
Water Tanks 1
Water Reservoir
Pump
Pump

(a)

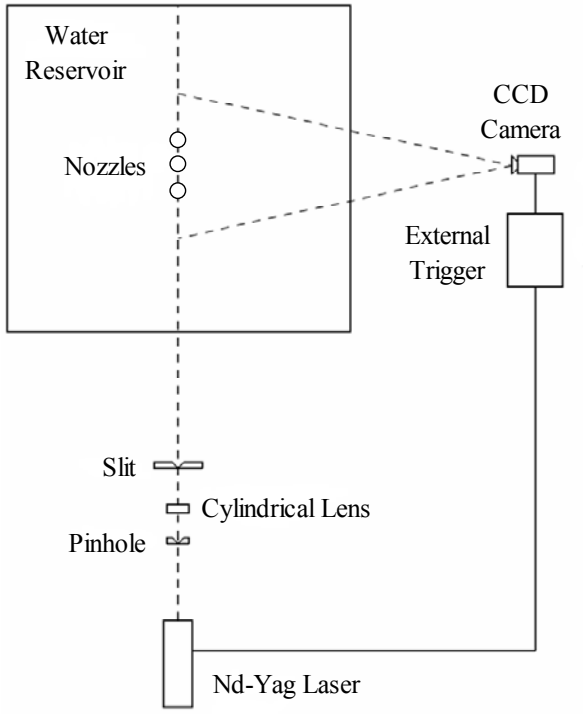

(b)

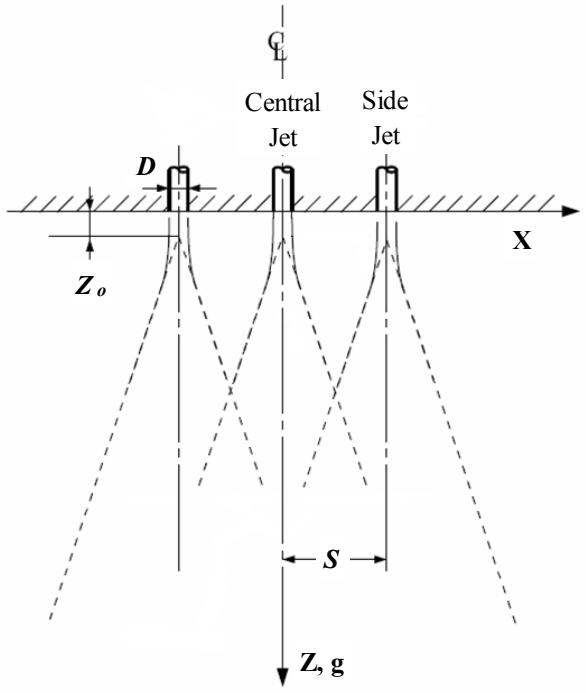

(c)

Figure 2.1: Schematics of: (a) The water reservoir and water jet supply system (b) The PLIF system (c) The coordinate system nomenclature [1]

2.2. Numerical Simulation Method

In this study, the numerical simulations are performed by using the Fire Dynamics Simulator (FDS) developed at the National Institute of Standards and Technology (NIST) [36]. This model has so far been used for compartment fires and had to be adapted for this study. NIST itself is looking for calibration of FDS. One such calibration is provided by this work & reference [37] has been provided to NIST.

2.2.1. Governing equation

In the FDS code, the flow field is modeled by solving the conservation equations for mass, species, momentum and equation of state for the gas with low Mach number assumption. Under this assumption, the basic governing equations are simplified to,

$$\frac{\partial \rho}{\partial t} + \nabla \cdot \rho \mathbf{u} = 0 \tag{2-1}$$

$$\frac{\partial}{\partial t}(\rho Y_l) + \nabla \cdot \rho Y_l \mathbf{u} = \nabla \cdot \rho D_l \nabla Y_l + \dot{m}_l''' \tag{2-2}$$

$$\rho\left(\frac{\partial \mathbf{u}}{\partial t} + (\mathbf{u} \cdot \nabla)\mathbf{u}\right) + \nabla p = \rho \mathbf{g} + \mathbf{f} + \nabla \cdot \tau \tag{2-3}$$

$$p_o(t) = \rho TR \sum_i \frac{Y_i}{M_i} \tag{2-4}$$

Where, $\mathbf{u} = (u, v, w)$ is the velocity field, $\mathbf{f}$ is the external force on the fluid, τ is the viscous stress tensor, and $\dot{m}_l'''$ is the mass production rate of the i^{th} species per unit volume.

2.2.2. The turbulence model

The effect of the flow field turbulence is modeled using LES, in which the large scale eddies are computed directly and the sub-grid scale dissipative processes are modeled. To approximate the turbulent stress, the Smagorinsky model with a constant coefficient C_s is used everywhere in the flow field. In this model, the dynamic viscosity is defined at cell centers as,

$$\mu_{LES} = \rho (C_s \Delta)^2 \left(2(def\mathbf{u}) \cdot (def\mathbf{u}) - \frac{2}{3}(\nabla \cdot \mathbf{u})^2 \right)^{\frac{1}{2}} \tag{2-5}$$

Where, C_s is the Smagorinsky constant, Grid size $\Delta = (\delta x \delta y \delta z)^{\frac{1}{3}}$, and the deformation term is related to the dissipation

$$\Phi \equiv \tau \cdot \nabla \mathbf{u} \equiv \mu \left(2(def\mathbf{u}) \cdot (def\mathbf{u}) - \frac{2}{3}(\nabla \cdot \mathbf{u})^2 \right)$$
$$= \mu \left[\begin{array}{l} 2\left(\frac{\partial u}{\partial x}\right)^2 + 2\left(\frac{\partial v}{\partial y}\right)^2 + 2\left(\frac{\partial w}{\partial z}\right)^2 + \left(\frac{\partial u}{\partial y} + \frac{\partial v}{\partial x}\right)^2 \\ + \left(\frac{\partial u}{\partial z} + \frac{\partial w}{\partial x}\right)^2 + \left(\frac{\partial v}{\partial z} + \frac{\partial w}{\partial y}\right)^2 - \frac{2}{3}\left(\frac{\partial u}{\partial x} + \frac{\partial v}{\partial y} + \frac{\partial w}{\partial z}\right)^2 \end{array} \right] \quad (2\text{-}6)$$

The key coefficient in this model is the Smagorinky constant C_s which is the sub-grid scale model coefficient that is flow dependent and has been optimized over a range from 0.1 to 0.25 for various flow configurations. As reported in literatures, the Smagorinsky coefficient is not a universal constant. It should be noted that the optimization of C_s in numerical simulation is generally ad hoc [38]. It was found that good results with the Smagorinsky model can be obtained when C_s=0.1 for channel flow [39, 40], C_s=0.12 for the flow around a bluff body [41], C_s=0.16 for a mixing layer [38] and an indoor airflow with force convection [42], and for homogeneous isotropic turbulence [40, 43] C_s ranges from 0.17 to 0.20 [38]. Geurts et al. [44] concluded that C_s=0.1 roughly corresponds to the averaged dynamic coefficient in the developed flow condition. Even though there are some suggested values of the Smagorinsky constant for various flow configurations, theoretical guidelines have never been provided [38]. It is therefore necessary to find the optimum value of C_s for each flow configuration.

2.2.3. Numerical method

Figure 2.2 shows the Smagorinsky constant effects on the decay rates of the centerline velocity and concentration for a free single turbulent jet. It is observed that the case of C_s=0.14 overestimates the length of potential core region, and low decay rates of the centerline velocity and concentration for the case of C_s=0.10. On the other hand, the

cases of C_s =0.11 and 0.12 are in good agreement with the results in literature as shown in Figure 2.3 and 2.4. However, it is observed from Figure 2.4 that the value of scaled centerline concentration with C_s =0.11 is near the upper limit of previous works. Therefore, it is found that C_s =0.12 is the best value for the current configuration in this study. This value of the Smagorinsky constant is used for further numerical calculations without change. Even though the Smagorinsky model has some shortcomings, it is still widely used for a number of applications.

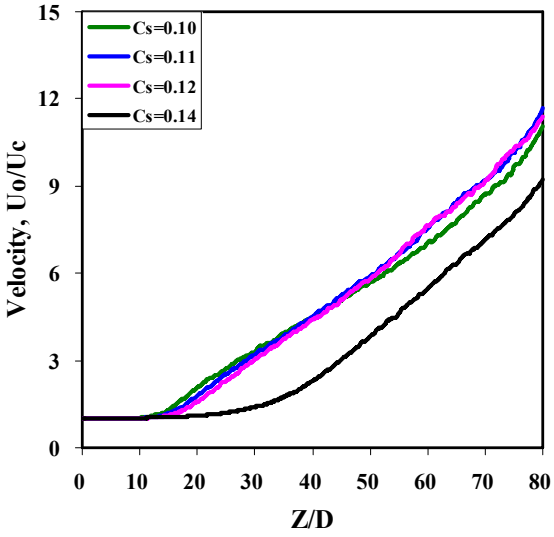

(a)

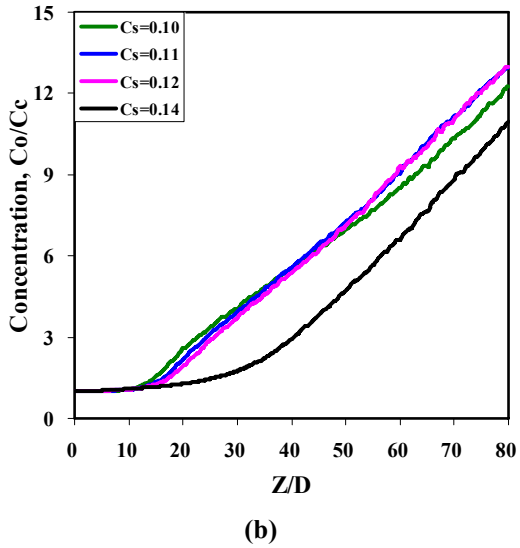

(b)

Figure 2.2: The effect of the Smagorinsky constant on mean centerline (a) velocity and (b) concentration decay profile for a free single turbulent jet.

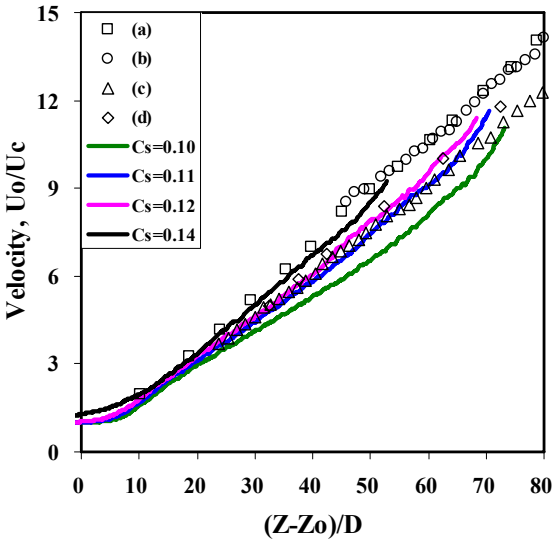

Figure 2.3: The effect of the Smagorinsky constant on mean centerline velocity for a free single turbulent jet, and comparison of current results with the previous works for the mean centerline velocity, □ (a) Hussein et al. [45], ○ (b) Webster et al. [46], △ (c) Fukushima et al. [47], ◇ (d) Panchapakesan and Lumley [48].

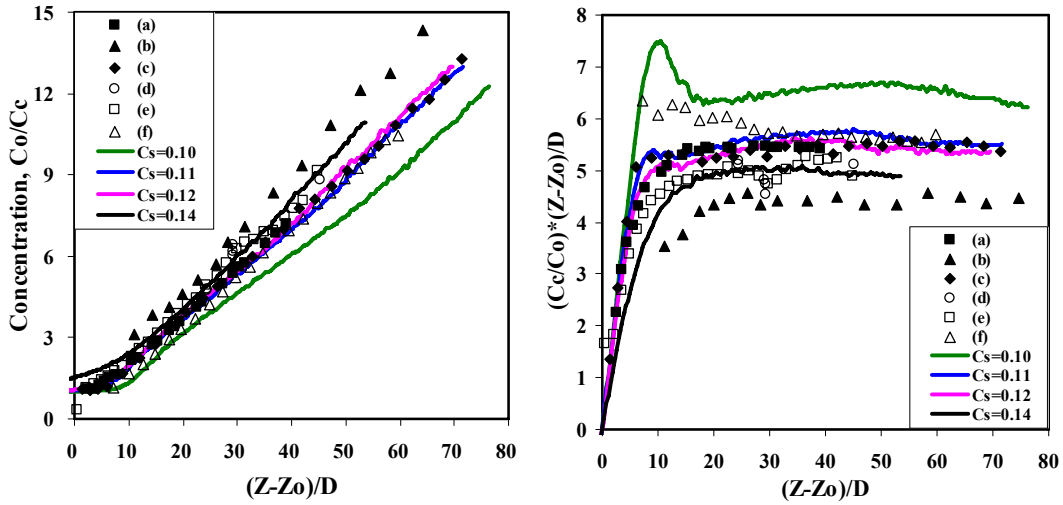

(a) **(b)**

Figure 2.4: The effect of the Smagorinsky constant on mean centerline (a) concentration decay profile and (c) scaled centerline concentration for a free single turbulent jet, and comparison of current results with the previous works for the mean centerline velocity, ■ (a) Becker et al. [49], ▲ (b) Birch et al. [50], ◆ (c) Dahm [51], ○ (d) Dowling and Dimotakis [52], □ (e) Lockwood and Moneib [53], △(f) Wilson and Danckwerts [54].

The effects of the grid numbers on the mean centerline velocity and concentration for a free single turbulent jet are shown in Figure 2.5 and 2.6. The numerical predictions are carried out for three different grid numbers, 0.26, 1.64 and 2.05 million with the same Smagorinsky constant C_s =0.12. It can be seen that the length of the potential core region is over-predicted with 0.26 million grids. The case of 1.64 and 2.05 million grids are found to be in very good agreement with previous works in the literature. Considering the prediction ability and computing times, 1.64 million grids are used in this study.

Figure 2.7 shows the schematic diagram of the computational domain used in the current study. The computational domain is $20D \times 20D \times 80D$ for single and three jets and $40D \times 40D \times 160D$ for the five jet configuration based on the center jet diameter. The domain consists of 1,638,400 grid points for all cases. It has been proven that this resolution is sufficient to describe the flow and concentration fields considering the accuracy and computation time. Thus, all numerical calculations in this study have been performed within a domain that is made up of rectangular mesh, each with its own rectilinear grid.

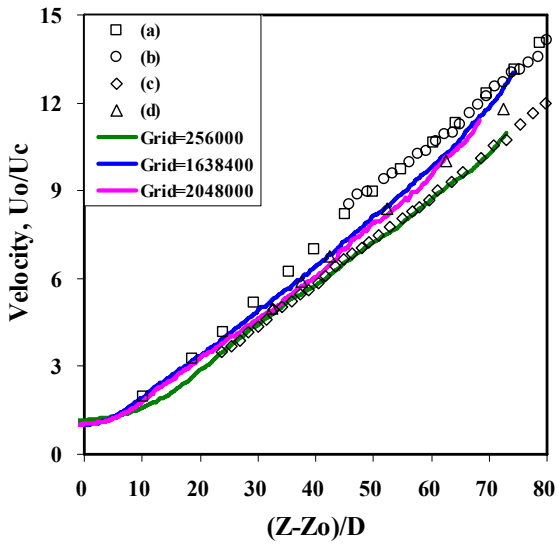

Figure 2.5: The effect of the grid numbers on mean centerline velocity for a free single turbulent jet, and comparison of current results with the previous works same as plotted in Figure. 2.4.

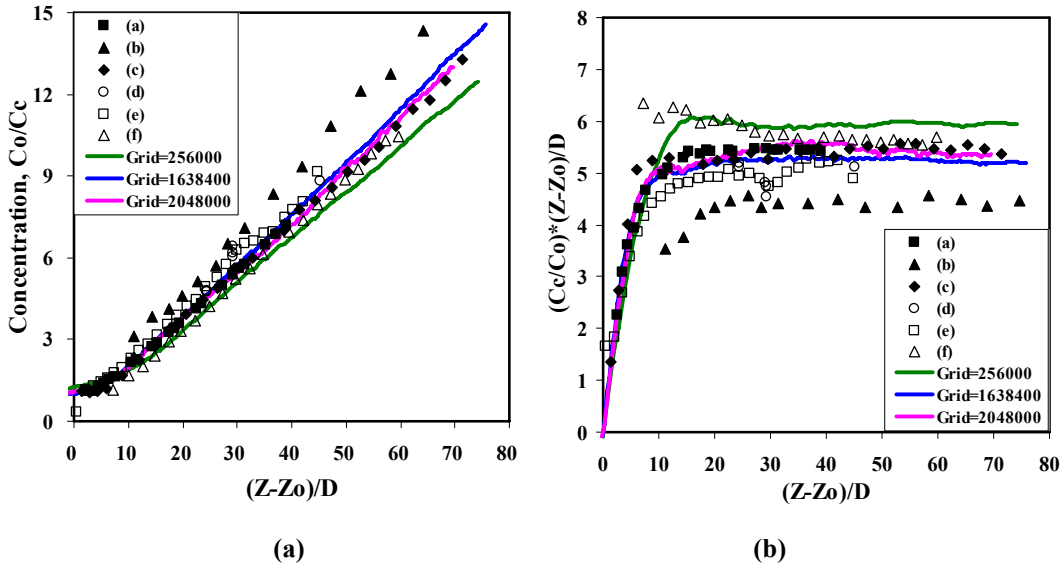

Figure 2.6: The effect of the grid numbers on mean centerline (a) concentration decay profile and (c) scaled centerline concentration for a free single turbulent jet, and comparison of current results with the previous works same as plotted in Figure 2.5.

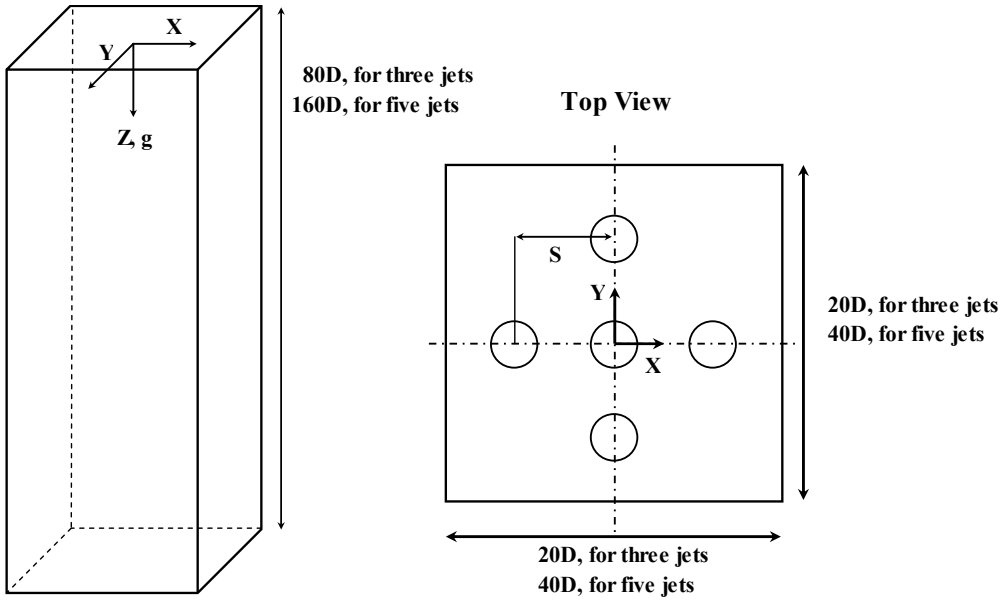

Figure 2.7: Schematic diagram of the computational domain and coordinates.

CHAPTER 3

Experimental and numerical results of unconfined non-reacting turbulent jets

In this section, the experimental and numerical results of velocity and passive scalar concentration field for single and three collinear water jets are presented. The experimental results were obtained by Dr. Hyoseok Lee [1] and the numerical results were obtained by the present author [37]. Results of an extensive numerical study conducted on five gas phase multiple turbulent jets, used in the experimental furnace, are also presented. In this study, the Reynolds number of the jets is kept above 10^4 for sustaining the fully developed turbulence condition according to Dimotakis [55]. The parameters and properties of the turbulent jets in this study are listed in Table 3.1.

3.1. Free single turbulent jet

For validation, experiments and numerical simulations are performed on an unconfined single water jet. In addition, numerical simulations are conducted on a single gas jet as the basis of investigation of multiple turbulent gas jets. For a single jet, the working and the ambient fluid are the same, thus no density effect is involved.

The mean centerline stream-wise velocity and mean concentration along with the centerline of the longitudinal axis are plotted in Figure 3.1 and 2 (a), and scaled mean centerline concentrations are shown in Figure 3.2 (b) along with the results of current [1] and previous experimental works [49-54]. As shown in Figure 3.1 and 3.2(a), the value of the mean centerline stream-wise velocity U_c and concentration C_c are constant in the potential core region, and decays linearly with the stream-wise distance after becoming fully developed as expressed in equation (3-1) and (3-2).

$$\frac{U_o}{U_c} = \frac{1}{K_u}\left(\frac{Z - Z_{ou}}{d}\right) \tag{3-1}$$

$$\frac{C_o}{C_c} = \frac{1}{K_c}\left(\frac{Z - Z_{oc}}{d}\right) \tag{3-2}$$

In above equations, U_o and C_o are the injection velocity and concentration, respectively, and d is the jet diameter. The mean decay rate for the velocity K_u and concentration K_c, and the virtual origin of the centerline velocity Z_{ou}, concentration Z_{oc} for each condition are obtained according to equation (1) and (2). The decay rates and virtual origins obtained from the current experiments and numerical simulations are listed in Table 3.2. In Figure 3.2 (b), the mean centerline concentration is scaled by $(C_c / C_o)(Z - Z_o)/d$, same as that used in Ref. [52], and plotted as a function of the distance from the jet virtual origin.

It is seen from Figure 3.1 and 3.2 that both of the experimental and numerical results show good agreement with the previous works in literature. The numerical simulation predicts a little longer potential core region up to *Z/d*=10. However, the numerical predictions of the value of the decay constant K_u and K_c for all calculations are almost the same, and $(C_c / C_o)(Z - Z_o)/d$ is nearly constant irrespective of the Reynolds number and the working fluids. Experimental measurements, on the other hand, show considerable scatter. The scatter in the experiments is attributed to the uncertainty in the initial conditions of the jet. Since the simulations have much less uncertainty, the curves are closer together. Nevertheless, the general similarity for a single turbulent jet is well established both experimentally and numerically [56].

The mean radial concentration profiles at different axial positions are plotted in Figure 3.3. Literature data are also plotted for comparison [49-52]. As shown in the literature, the profiles appear self-similar and Gaussian-like for (*Z-Zo)/d*>20. Clearly, the experimental results and numerical calculations agree well with the results in literature.

Configurations	Working/ Surrounding Fluids	Jet Diameter (m)		Velocity (m/s)		Reynolds No.		Momentum Ratio	Separation Distance	Confinement Ratio	
		Center	Side	Center	Side	Center	Side	MR	S/D	Diameter Ratio, Dr[a]	Length Ratio, Lr[b]
	Air	0.1		20.0		1.29×10^5			5.0	16.0	
		0.1		20.0		1.29×10^5			10.0	8.0	
		0.1		20.0		1.29×10^5			20.0	4.0	
S/D effect	Methane & Air/ Nitrogen	0.05	0.1	40.4	24.0	6.54×10^4	1.55×10^5	0.39	4.0		
		0.05	0.1	40.4	24.0	6.54×10^4	1.55×10^5	0.39	8.0		
		0.05	0.1	40.4	24.0	6.54×10^4	1.55×10^5	0.39	12.0		
MR effect	Methane & Air/ Nitrogen	0.05	0.1	40.4	24.0	6.54×10^4	1.55×10^5	0.39	10.0		
		0.05	0.1625	40.4	9.1	6.54×10^4	9.54×10^4	1.03	10.0		
		0.05	0.2	40.4	6.0	6.54×10^4	7.75×10^4	1.57	10.0		

Table 3.1: The parameters and properties of turbulent jets in experiments [1] and numerical simulations.

Jet phase	Exit velocity		Decay rate K_u	Virtual origin Z_{ou}	Decay rate K_c	Virtual origin Z_{oc}
Water Jet	Vel=1.0	Experiment	4.69	5.30d	4.69	5.30d
		FDS	6.33	6.42d	5.30	4.71d
	Vel=2.0	Experiment	5.59	4.70d	5.59	4.70d
		FDS	6.13	7.05d	5.12	5.65d
Air Jet	Vel=10	FDS	6.06	5.90d	5.23	4.21d
	Vel=20	FDS	6.31	4.91d	5.23	4.30d

Table 3.2: Decay rate K_u , K_c and virtual origin Z_o of a single turbulent jet obtained from experiment [1] and numerical simulation.

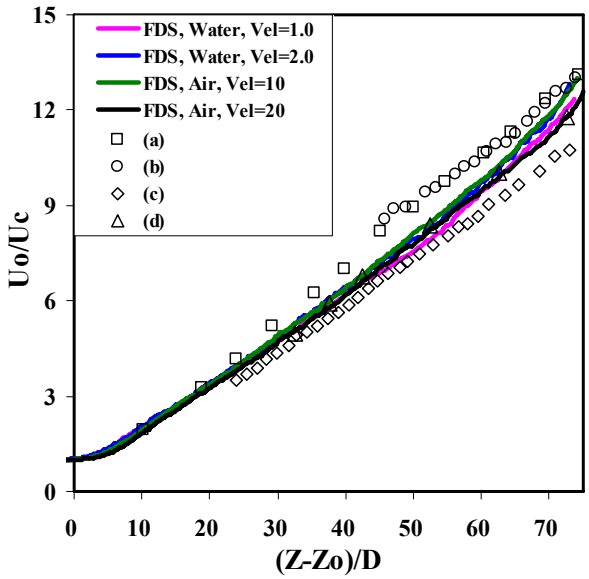

Figure 3.1: The mean centerline stream-wise velocities obtained from numerical simulation for a single jet, and (b) comparison of current results with the previous works for the mean centerline velocity, □ (a) Hussein et al. [45], ○ (b) Webster et al. [46], △ (c) Fukushima et al. [47], ◇ (d) Panchapakesan and Lumley [48].

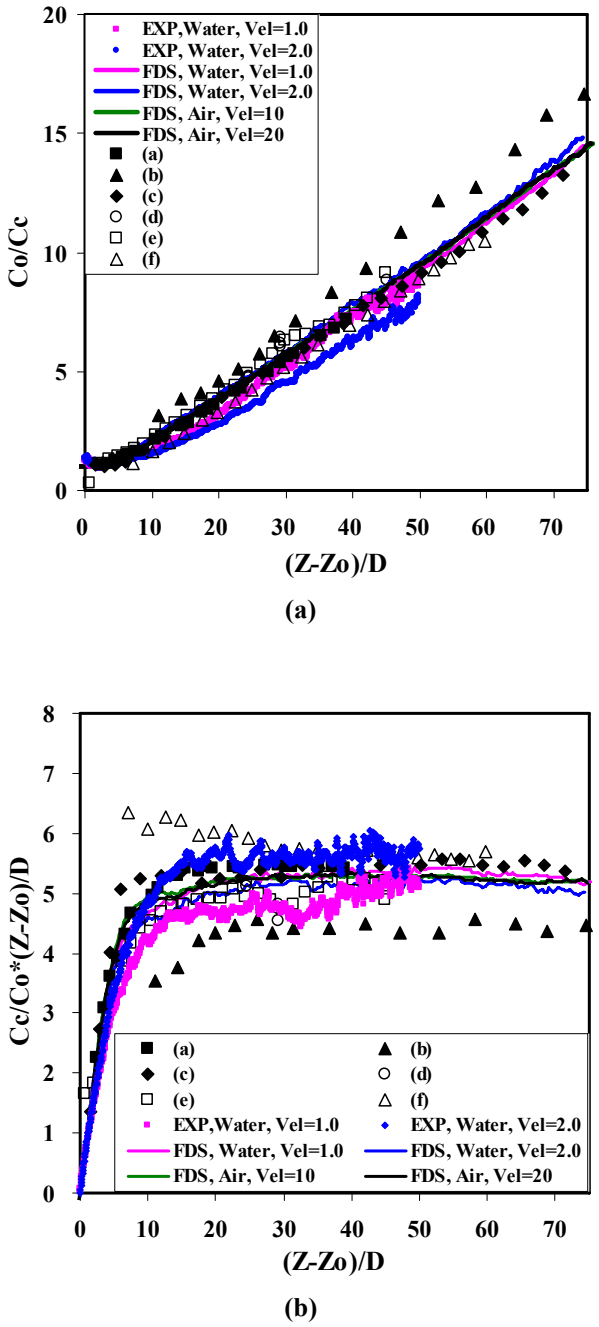

Figure 3.2: (a) The mean centerline concentration obtained from experiment [1] and numerical simulation for a single jet, and (b) comparison of current results with the previous works for the scaled mean centerline concentration, (a) Becker et al. [49], (b) Birch et al. [50], (c) Dahm [51], (d) Dowling and Dimotakis [52], (e) Lockwood and Moneib [53], (f) Wilson and Danckwerts [54].

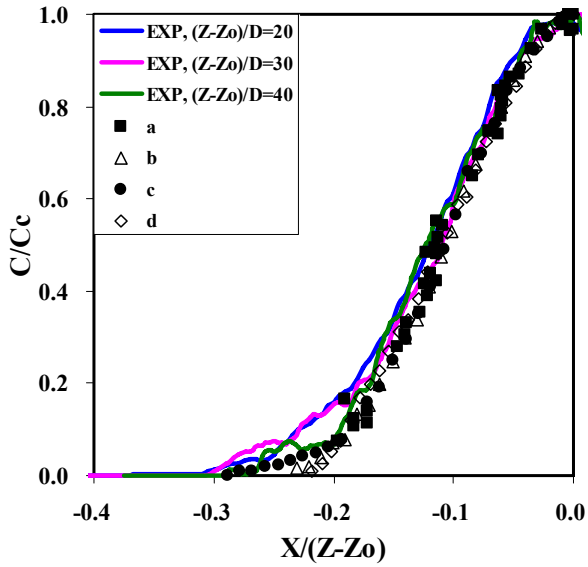

(a)

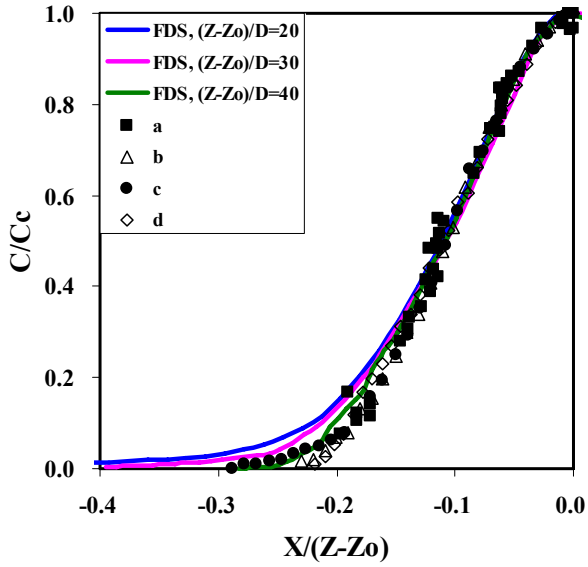

(b)

Figure 3.3: The mean radial concentration profiles obtained from experiment [1] and numerical simulation at exit velocity 1.0 m/s for a water single jet, and results of (a) Dowling and Dimotakis [52] (b) Becker et al. [49], (c) Birch et al. [50] and (d) Dahm [51].

3.2. Unconfined multiple turbulent jets

3.2.1. Water 3 Jets

To investigate the characteristics of mixing and concentration for the unconfined multiple turbulent jets, experimental [1] and numerical studies are performed on three collinear water jets. In this section, the effects of the separation distance and momentum ratio between jets as the control parameters in jet mixing are examined. The separation distance *S/d* and momentum ratio *MR* investigated in this study are listed in Table 3.1. For identification of the concentration of the center jet, salt water having the same properties as the side water jets is used as the center jet fluid in the numerical study.

Separation Distance Effects

Figure 3.4 shows the numerical predictions of the decay rate of the mean centerline stream-wise velocities of the center jet for three different separation distances *S/d*=3.66, 5.50 and 7.33 with fixed jet velocity, 1.0-1.0-1.0 m/s. The radial velocity profiles at different axial positions for the above cases are shown in Figure 3.5. In this study, the velocity is normalized by the injection velocity of the center jet.

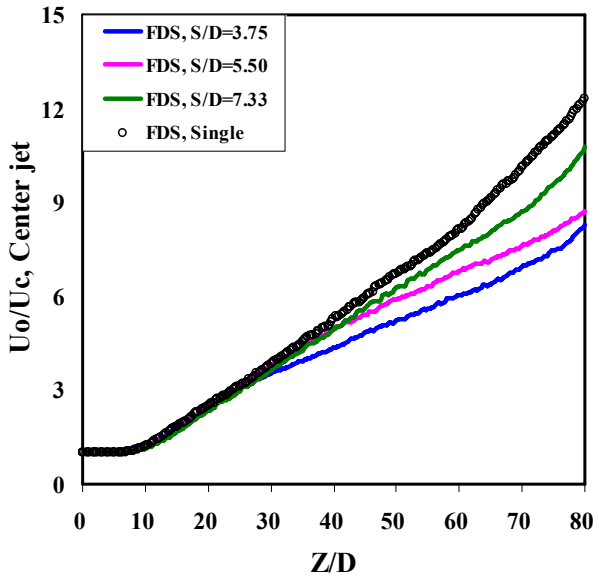

Figure 3.4: The results of numerical simulations for the mean centerline stream-wise velocity of the center jet for *S/d*=3.66, 5.50 and 7.33 with jet velocity, 1.0-1.0-1.0 m/s for three water jets.

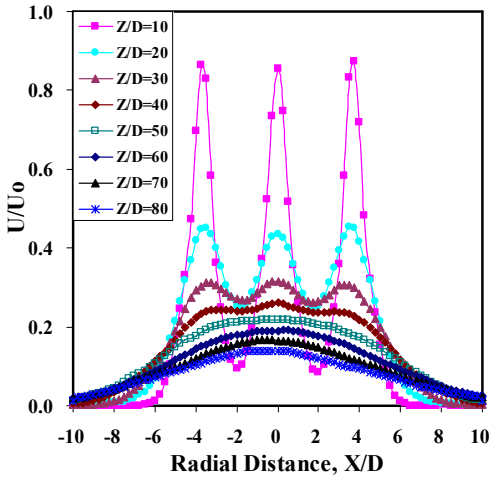

(a)

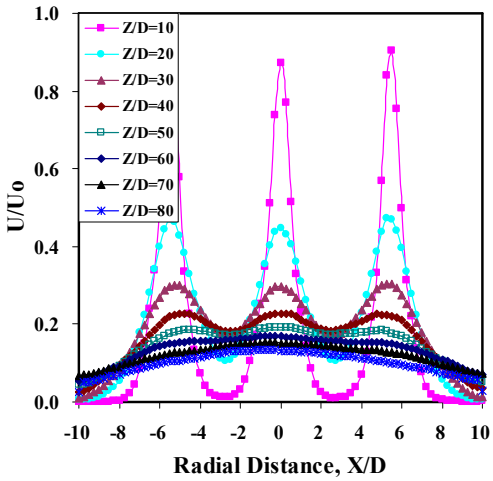

(b)

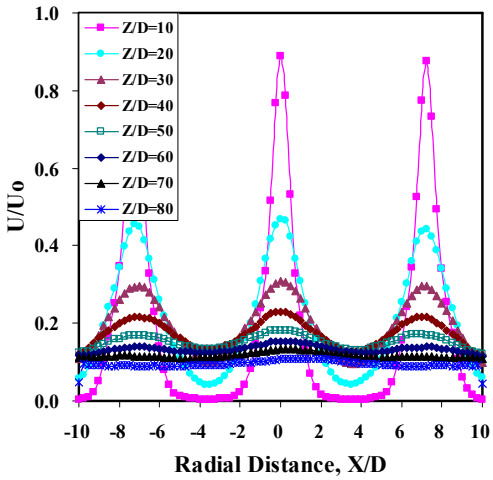

(c)

Figure 3.5: The radial velocity profiles at different axial positions for (a) *S/d*=3.66, (b) *S/d*=5.5 and (c) *S/d*=7.33 with jet velocity, 1.0-1.0-1.0 m/s for three water jets.

It is clearly observed from Figure 3.4 that the values of the reciprocal normalized centerline velocity U_o / U_c in multiple jets are lower than that of a single jet, which indicates that the mean centerline velocity of the center jet in the multiple jets decays slower than a single jet. This can be attributed to the observation from Figure 3.5 that jets finally merge into one jet after some distance from the jet exit, thus the momentum of the center jet in multiple jets can be enhanced by momentum addition from the side jets. Another observation from Figure 3.4 is that the decay rate of the mean centerline velocity of the center jet is higher with increase of the separation distance. It might be thought that the jets merge into one jet early with small separation distance, and the center jet begins to be affected by the side jets early as shown in Figure 3.5. On the other hand, jet merging is delayed to further downstream with large separation distance, thus each jet acts like a single jet for a longer downstream distance. As a result, the behavior of the centerline velocity becomes closer to that of a single jet with large separation distance.

The mean centerline concentration and scaled concentration of the center jet for three different separation distances *S/d* =3.66, 5.50 and 7.33 with fixed jet velocity, 1.0-1.0-1.0 m/s, are plotted in Figure 3.6 (a) and (b). It is clearly observed that the linearity of the mean centerline concentration is broken and the value of $\left(C_c / C_o\right)\left(Z - Z_o\right) / d$ is no longer constant in multiple turbulent jets, which means that the general similarity is no longer valid in multiple jets. Even though using the concept of the virtual origin and scale factor $(Z - Z_o) / d$ for the mean centerline concentration is not proper for the multiple jets, it is still useful to investigate that how the behavior of the multiple jets is different from a single jet. For this purpose, the virtual origin of the single jet is used for describing the value of $\left(C_c / C_o\right)\left(Z - Z_o\right) / d$ in multiple jets.

As observed in Ref. [24, 27], Figure 3.6 (a) and (b) clearly show that the center jet initially follows the single jet path, and then deviates from the path after some distance. This deviation distance is the merge distance where the center jet begins to be affected by the side jets. From the merge distance onward, the concentration of the center jet shows a completely different trend from that of a single jet. It is seen from Figure 3.6 (a) that the values of the reciprocal normalized centerline concentration C_o / C_c of the center jet in multiple jets are higher than that of a single jet, which indicates that the centerline

concentration in the multiple jets decays faster than that of a single jet because of enhanced mixing and interaction between jets by exchange of momentum with side jets. It is also reported that multiple jets relatively entrain more surrounding fluid than a single jet, thus the mean centerline concentration decays faster in the multiple jet configuration [34, 57]. The mean centerline concentration of the center jet decays rapidly with decreasing the separation distance, which can be thought that strong mutual entrainment and turbulent transport between jets starts earlier at shorter distance from the jet exits for the case of small separation distance. Thus, the centerline concentration of the center jet drops rapidly.

The radial concentration profiles do not fall on a single curve for multiple jets and show a narrower width than a single jet as shown in Figure 3.7. This can be attributed to the fact that the mutual interaction between jets creates a sub-atmospheric pressure region and in this region, the jets attract each other toward the centerline and thus the transverse transport rate decreases more than that of a single jet [26].

The discrepancy in the scaled mean concentration is observed between experiments and numerical prediction, because of the sensitivity of the scale factor $(Z - Z_o)/d$ to the virtual origin. As stated before, the virtual origin of a single jet was used for multiple turbulent jets. While there is some discrepancy between the experimental results and numerical predictions, the trend shows good agreement.

Momentum Ratio Effects

The effects of the momentum ratio between jets are investigated by changing the velocity of the jets while the diameter and flow rate of the jets are kept constant (see Table 3.1). The results of numerical calculations for the mean centerline stream-wise velocities of the center jet for three different momentum ratios *MR*=0.25, 1.0 and 4.0 with same separation distance *S/d*=3.66 are shown in Figure 3.8. The radial velocity profiles at different axial positions for above cases are shown in Figure 3.9. In this study, the momentum ratio *MR* is defined as the ratio of center jet momentum to side jet momentum.

As described in previous section, the decay rate of the mean centerline stream-wise velocity of the center jet in multiple jets is higher than that of a single jet due to momentum addition from the side jets by strong interaction between jets. It is observed

that the behavior of the centerline velocity of the center jet approaches that of the single jet at high momentum ratio *MR*=4.0. This can be attributed to the fact that the center jet having higher momentum is better able to penetrate into the side jets having lower momentum. Thus, the side jets are merged more rapidly into the center jet with increase of the momentum ratio between jets as shown in Figure 3.9.

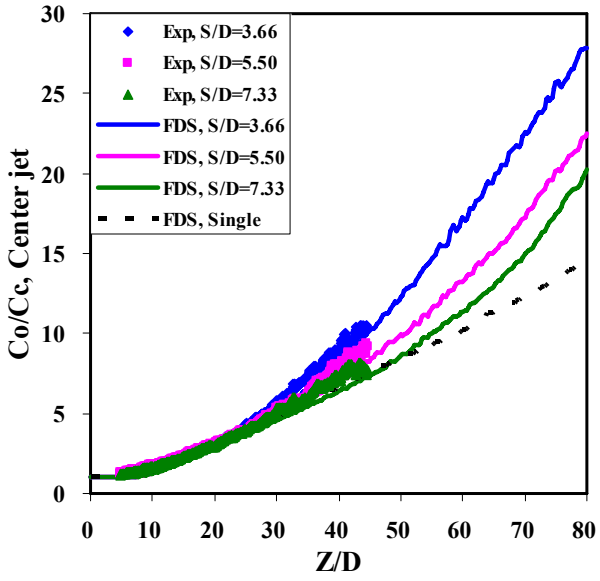

(a)

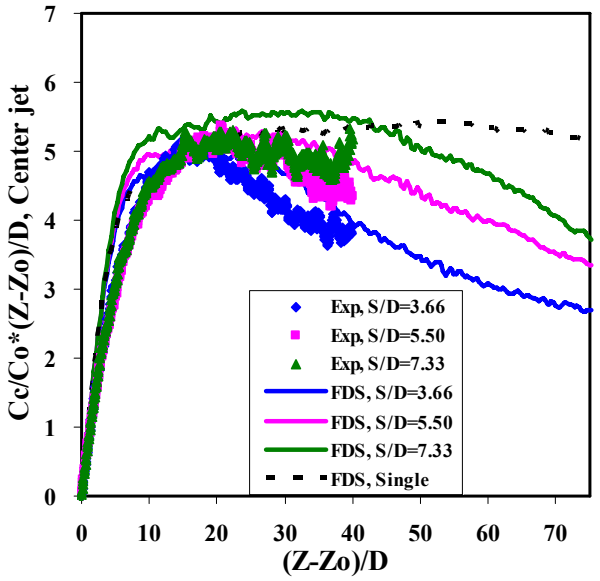

(b)

Figure 3.6: Comparison of current experimental results [1] with the numerical simulations for (a) mean centerline concentration and (b) scaled mean centerline concentration of the center jet for *S/d*=3.66, 5.50 and 7.33 with jet velocity, 1.0-1.0-1.0 m/s for three water jets.

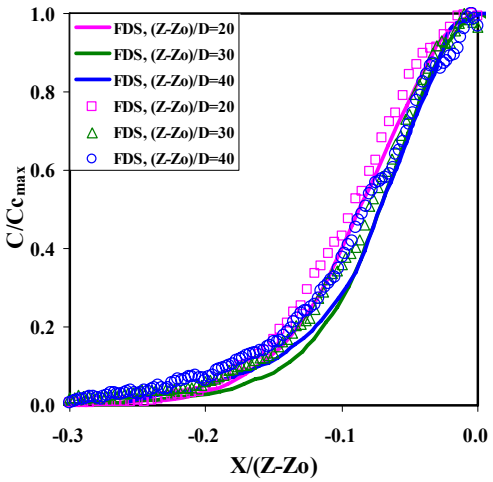

(a)

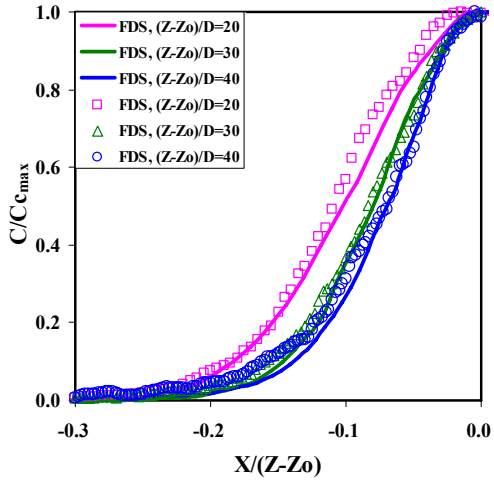

(b)

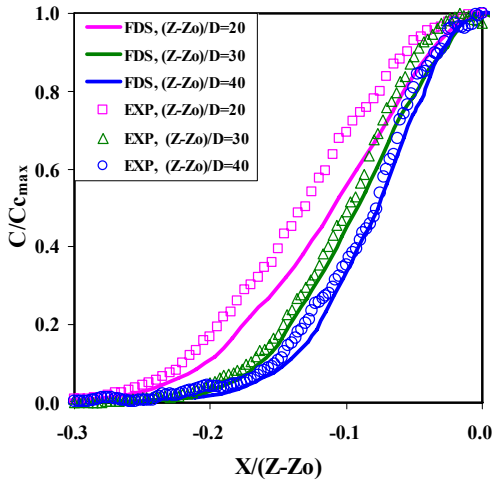

(c)

Figure 3.7: Comparison of current experimental results [1] with the numerical simulations for radial concentration profiles at different axial positions for (a) *S/d*=3.66, (b) *S/d*=5.50 and (c) *S/d*=7.33 with jet velocity, 1.0-1.0-1.0 m/s for three water jets.

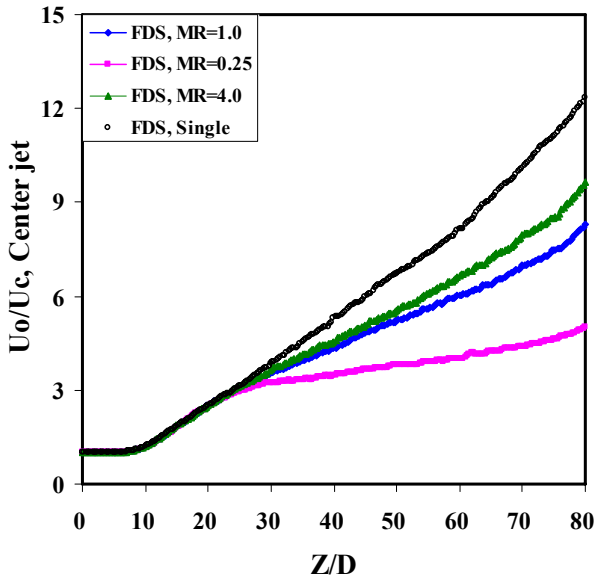

Figure 3.8: The results of numerical simulations for the reciprocal mean centerline stream-wise velocity for *MR*=0.25, 1.0 and 4.0 with separation distance *S/d*=3.66 in three water jets.

Figure 3.10 shows the mean centerline concentration and the scaled mean concentration of the center jet for three different momentum ratios *MR* of 0.25, 1.0 and 4.0 with fixed separation distance *S/d*=3.66.

As shown in Figure 3.10, numerical predictions are in very good agreement with the experimental results. It is clearly observed that the centerline concentration of the center jet decays rapidly with decrease of the momentum ratio (increase the momentum of the side jet). The centerline concentration deviates quite rapidly from a single jet for small momentum ratio *MR*=0.25. An explanation could be that the entrainment of the ambient fluid into the side jets is enhanced due to their high momentum, and the side jets are also able to penetrate into the region of the center jet because of their higher momentum than the center jet. Thus, the center jet decays rapidly due to mixing with the side jets having enhanced entrainment of the ambient fluid. This is important from the combustion point-of view. Assume that the side jets are air, the center jet is fuel, and the ambient fluid is combustion products. Then, the entrainment of the side jet into the center jet will start combustion early before appropriate dilution, which is an undesirable consequence. On the other hand, if both the side and the center jets are appropriately diluted by the ambient fluid due to the high momentum of the side jets, then it is a desirable consequence.

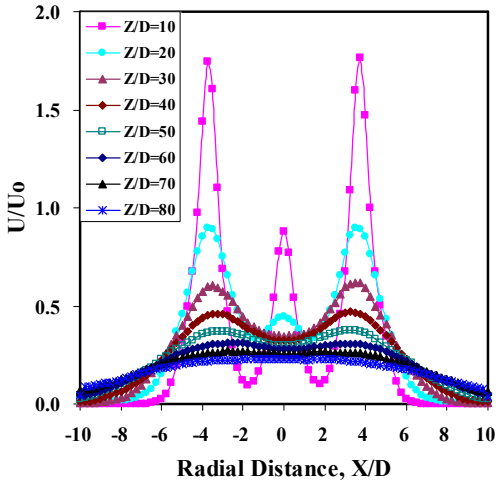

(a)

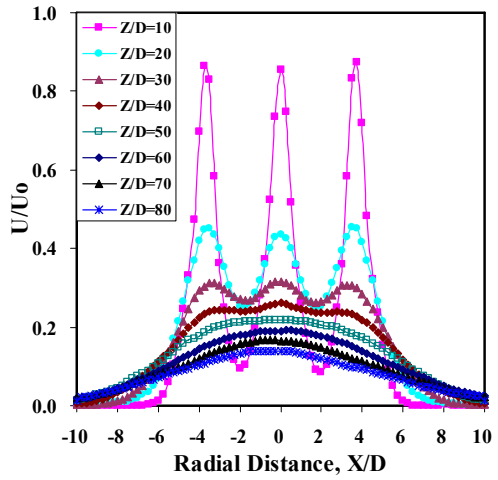

(b)

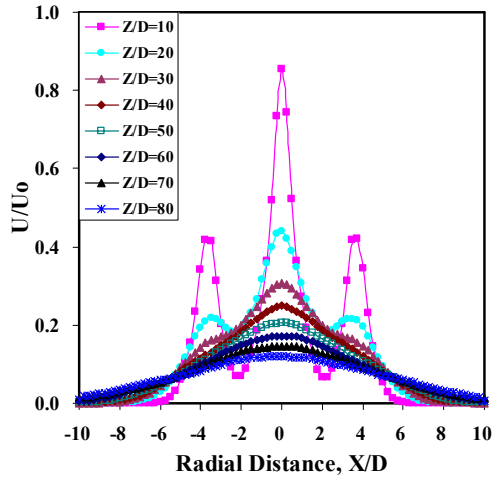

(c)

Figure 3.9: The radial velocity profiles at different axial positions for (a) *MR*=0.25, (b) *MR*=1.0 and (c) *MR*=4.0 with separation distance *S/d*=3.66 in three water jets.

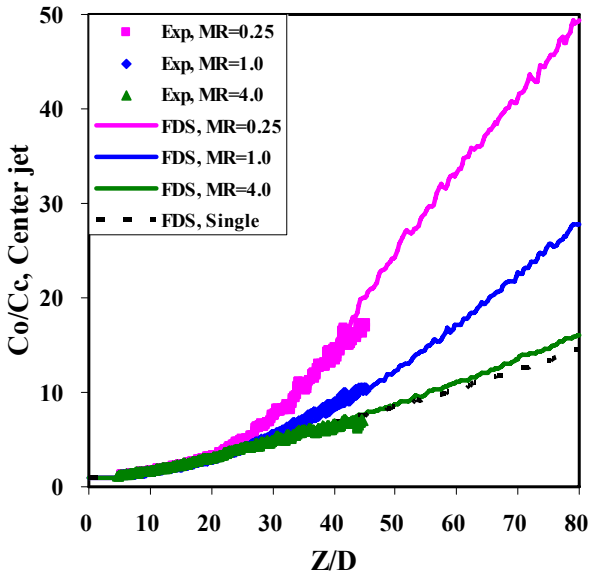

(a)

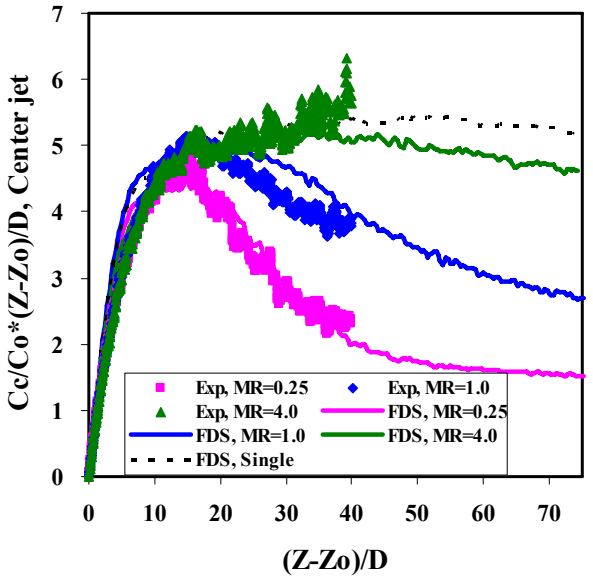

(b)

Figure 3.10: Comparison of current experimental results [1] with the numerical simulations for (a) mean centerline concentration and (b) scaled mean centerline concentration for *MR*=0.25, 1.0 and 4.0 with separation distance *S/d*=3.66 in three water jets.

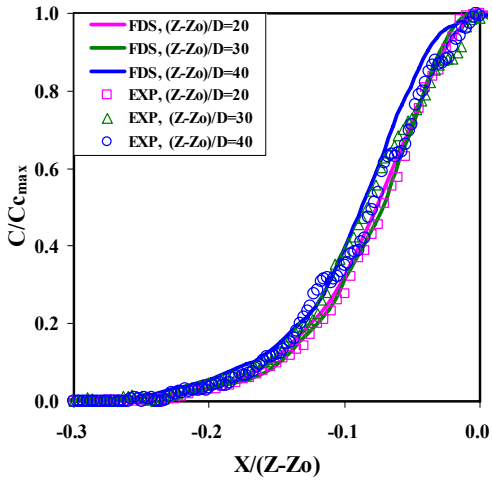

(a)

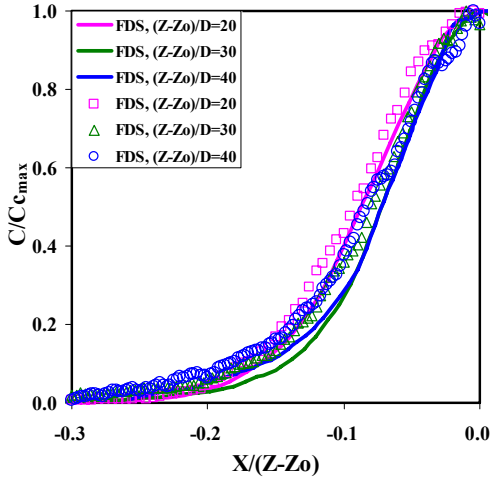

(b)

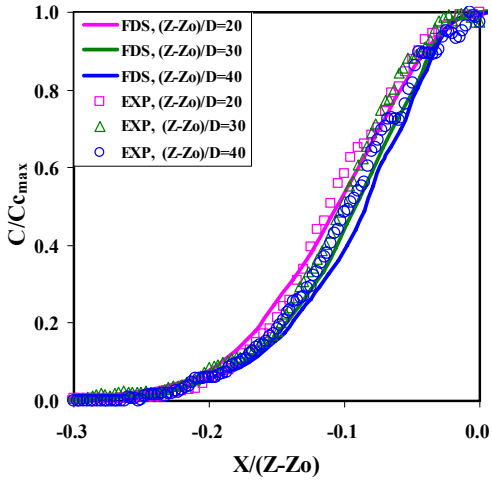

(c)

Figure 3.11: Comparison of current experimental results [1] with the numerical simulations for radial concentration profiles at different axial positions for (a) *MR*=0.25, (b) *MR*=1.0 and (c) *MR*=4.0 with separation distance *S/d*=3.66 in three water jets.

It is also observed that the behavior of the centerline concentration of the center jet becomes closer to the single jet path as with higher momentum ratio, which results from the quite same reason explained in trend of the centerline velocity.

The radial concentration profiles at different axial positions are shown in Figure 3.11. As same trend in previous section, the radial concentration profiles do not fall on a single curve for multiple jets and the general similarity is no longer valid in multiple jets.

3.2.2. Unconfined gas-phase five Jets (Fuel & Oxidizer jets)

In this section, methane and normal air are used as a fuel and oxidizer, respectively. The center fuel jet is of 0.05 m diameter and the diameter of the four side oxidizer jets is varied to maintain the same flow rate and the overall equivalence ratio of 1.0 for all cases. There are two available sources of jet dilution – one is the ambient fluid (combustion products) and the other is the jet fluids. For the current configuration, it is desirable that the jets are diluted by the entrainment of the ambient fluid and not by the other jets for achieving the homogeneous combustions. Therefore, it is important to identify the dilution source of the jets. For this purpose, methane and normal air are used as fuel and oxidizer, respectively, and water vapor is used as the ambient fluid. Thus, it is easy to investigate the dilution sources and mixing pattern between jets. It is noted that the background species cannot participate in the reaction except as a diluent in the FDS [36].

Numerical simulation for the configuration of a center jet (fuel) surrounded by four equidistant oxidizer jets are carried out for Reynolds number 6.5×10^4 of the center jet. The separation distance is varied as S/d=4.0, 8.0, 12 and the momentum ratio MR=0.39, 1.03 and 1.57.

Separation Distance Effects

The mean centerline concentration of the center (fuel) jet, and scaled mean centerline concentration of the center jet for three different separation distances with jet momentum ratio MR=0.39 in the five multiple jet configuration are shown in Figure 3.12. For more detailed analysis, the mean concentrations of oxygen in the center (fuel) jet and methane in the side (oxidizer) jet are plotted in Figure 3.13. The mean centerline velocity of the

center jet and radial velocity profiles at different axial positions for *S/d*=4.0, 8.0 and 12.0 are plotted in Figure 3.14 and 15, respectively.

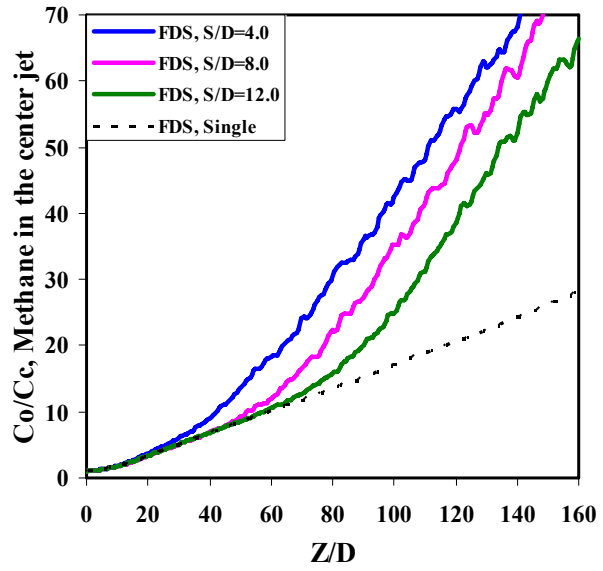

(a)

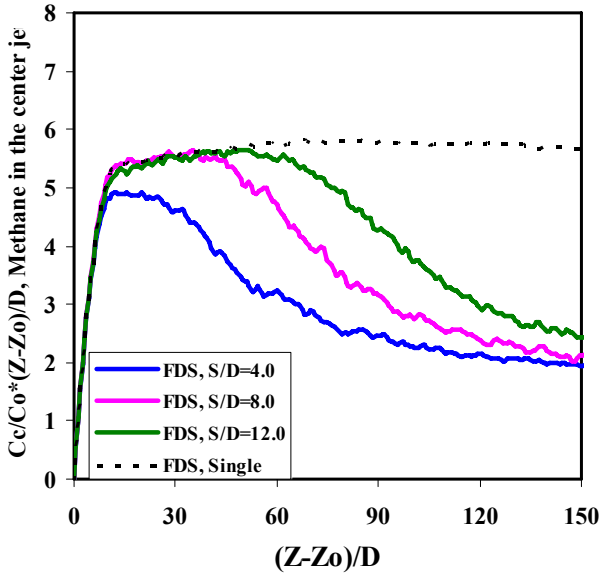

(b)

Figure 3.12: The mean centerline concentration of the (a) center (fuel) jet and (b) scaled mean centerline concentration of the center jet for *S/d*=4.0, 8.0 and 12.0 with jet momentum ratio *MR*=0.39 in five multiple jet configuration.

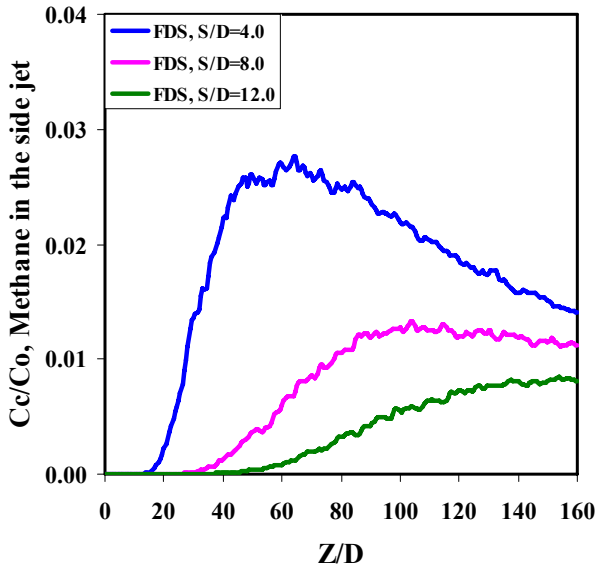

(a)

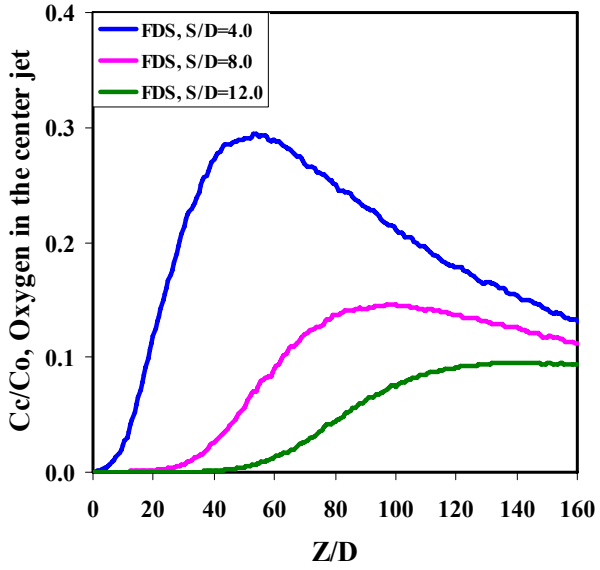

(b)

Figure 3.13: The mean concentration of the (a) methane in the side (oxidizer) jet and (b) oxygen in the center (fuel) jet for *S/d*=4.0, 8.0 and 12.0 with jet momentum ratio *MR*=0.39 in five multiple jets.

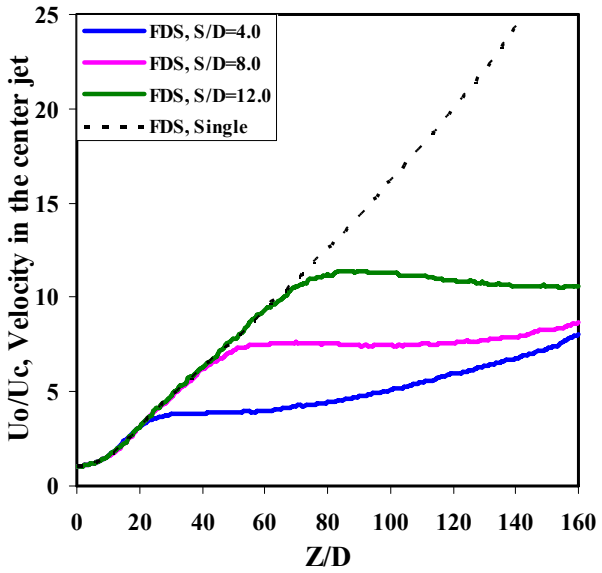

Figure 3.14: The mean centerline stream-wise velocities of the center (fuel) jet for *S/d*=4.0, 8.0 and 12.0 with jet momentum ratio *MR*=0.39 in five multiple jet configuration.

As shown in Figure 3.12 and 14, the behaviors of the mean centerline concentration and velocity of the center jet are similar to those of the three water jets. The center jet deviates from the single jet path after interacting with the side jets. It is also observed that the mean centerline concentration of the center jet decays rapidly with decreasing the separation distance, whereas the decay rate of the centerline velocity increases with larger jet spacing. Both of the behavior of the mean centerline concentration and velocity are close to that of a single jet at large separation distance. In addition, the merge distance increases for larger jet spacing, which means that the separation distance between jets governs the distance after which the jets begin to interact [28, 30].

Figure 3.13 shows lots of oxygen in the center (fuel) jet and some methane in the side (oxidizer) jets at a separation distance *S/d*=4.0. These concentrations begin to increase sharply near the jet exit and keep increasing up to *Z/d*=50, where the jet merging is completed, they then decrease far downstream. It is also observed from Figure 3.15 that the velocity profiles rapidly merge into the center jet after *Z/d*=40 and the peak of velocity exists only at the centerline of the center jet for *S/d*=4.0 case. This can be attributed the fact that there exists a strong interaction between jets due to rapid merging into one jet, thus, strong mixing of fuel and oxidizer occurs earlier. Therefore, for *S/d*=4.0,

the center jet concentration decays faster by mixing with side jets in the upstream region. After merging with the side jets, the jets act like a single jet. Consequently, the jets are diluted by the entrainment of the ambient after merging.

On the other hand, for large separation distance, the S/d=12.0 case shows that much small amount of oxygen and methane exist in the center (fuel) and side (oxidizer) jets, respectively. It is observed that the concentration of methane and oxygen start to increase after Z/d=40, and then show quite flat profiles. Clearly, the mixing between jets is delayed by increasing the separation distance and meanwhile the jets are being diluted by the ambient fluid. This is a mechanism to control homogeneous combustion. Comparing the velocity profiles with the small separation distance, the S/d=4.0 case, the peaks in the velocity profiles still exist near the centerline of the side jets up to Z/d=100 and the velocity profiles become quite flat after merging. This indicates that there exits a lot of entrainment of the ambient fluid for large separation distance. In other words, each jet follows the behavior of a single jet before merging and the concentration decays by the entrainment of the ambient fluid. After merging, all jets decay by mixing between jets and the entrainment of the ambient fluid. Similar trends were reported in Ref. [34] where multiple jets were shown to entrain more ambient fluid than a single jet, especially for larger separation distances.

Thus, it can be concluded that the entrainment of the ambient fluid is promoted before mixing between jets at large separation distances, while the mutual interaction between jets in the upstream region is enhanced for small separation distances. To get homogeneous combustion, the separation distance should be sufficiently large so that the jets are sufficiently diluted by the ambient fluid before they meet.

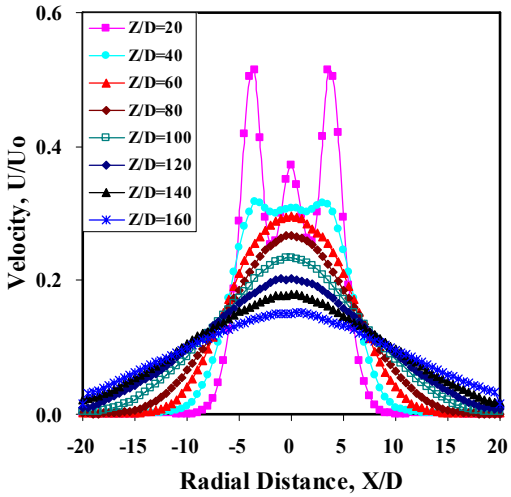

(a)

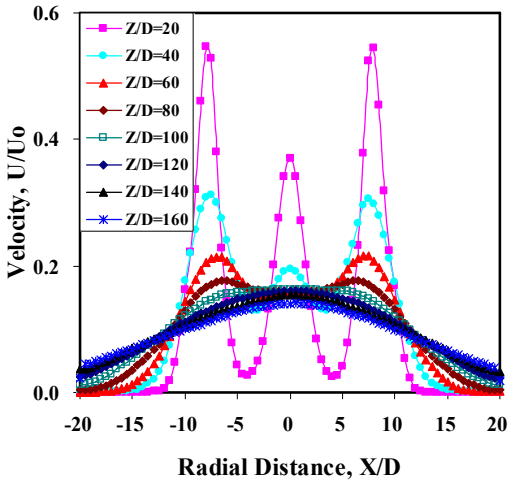

(b)

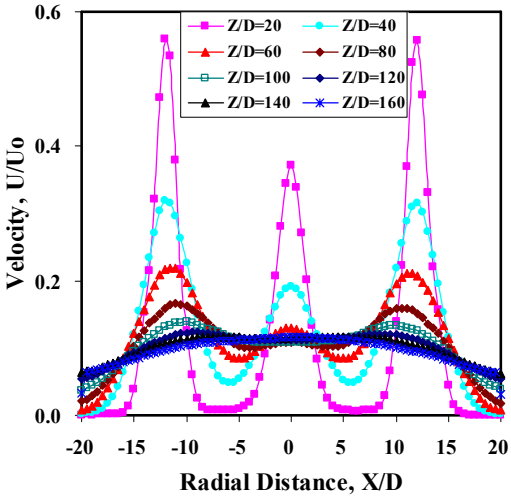

(c)

Figure 3.15: The radial velocity profiles at different axial positions for (a) *S/d*=4.0, (b) *S/d*=8.0 and (c) *S/d*=12.0 with jet momentum ratio *MR*=0.39 in five multiple jet configuration.

Momentum Ratio Effects

Figure 3.16 shows that the mean centerline concentration of the center and scaled mean centerline concentration of the center jet for three different momentum ratios with separation distance *S/d*=10.0 in the five multiple jet configuration, and the mean concentrations of oxygen in the center jet and methane in the side are plotted in Figure 3.17. The mean centerline velocities of the center jet and radial velocity profiles at different axial positions for *MR*=0.39 and 1.57 are shown in Figure 3.18 and 19, respectively.

It is seen from the Figure 3.16 that the center jet shows the larger decay rate of the mean centerline concentration at low momentum ratio *MR*=0.39, while relatively small amount of methane and oxygen exist in the side and center jet, respectively for *MR*=0.39, as shown in Figure 3.17. This indicates that both jets are more diluted by the entrainment of the ambient fluid than the high momentum ratio cases. It is clearly shown in Figure 3.19 (a) that the peaks in the velocity profiles of the side jets still exist up to *Z/d*=80 and overall level of the velocity profiles is larger than the large momentum ratio case *MR*=1.57 because the side jets have higher momentum. Therefore, the side jets continue to entrain the ambient fluid, and as a result of mixing with side jets, the centerline concentration of the center jet also decays faster than the large momentum ratio case *MR*=1.57.

On the other hand, the mean centerline concentration of the center jet decays slowly at high momentum ratio *MR*=1.57, and lots of oxygen in the center jet and methane in the side jet are found, as shown in Figure 3.17. This can be attributed the fact that the interaction between jets is promoted with high momentum ratio due to rapid merging into the center jet, thus advection of scalar is enhanced. As a result, mixing between jets is enhanced at high momentum ratios [58]. However, as shown in Figure 3.19 (b) that the peaks of the velocity profiles of the side jets decrease rapidly and merge into one jet with relatively lower level of the velocity than small momentum ratio *MR*=0.39 case and at relatively shorter distance, about *Z/d*=60. The entrainment of the ambient fluid is less for the high momentum ratio case, as a result, less decay rate of the jet fluid concentrations.

Moderate momentum ratio *MR*=1.03 shows similar trends in the mean centerline concentration of the center jet and methane concentration in the side jets as the *MR*=1.57

case. The difference is the behavior of the side jets, which have intermediate momentum when compared with the momentum ratio *MR*=0.39 and 1.57 cases.

Thus it may be concluded that the entrainment of the ambient fluid is promoted at low momentum ratio, while the mutual interaction between jets is enhanced at high momentum ratio. However, the overall behavior of the three momentum ratio cases is very similar; the difference between cases is not big due to the narrow range of the ratios. It should also be noted that the mixing between jets starts at the same distance and at the same rate. However, it is observed that the entrainment of the ambient fluid is enhanced by decreasing the momentum ratio.

Considering the small separation distance case, it is possible that the reaction occurs early and near the jet exit region with high momentum ratio because of enhanced mixing between jets. Therefore, lower momentum ratio between jets is preferable for small and moderate separation distance to promote the dilution by the ambient fluid before mixing between jets occurs, whereas higher momentum ratio is preferable for larger separation distance to enhance fuel dilution with ambient fluid before mixing between jets to achieve homogeneous combustion.

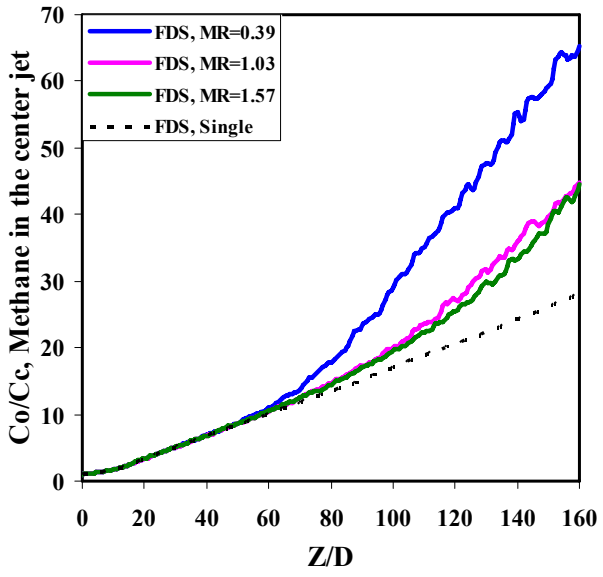

(a)

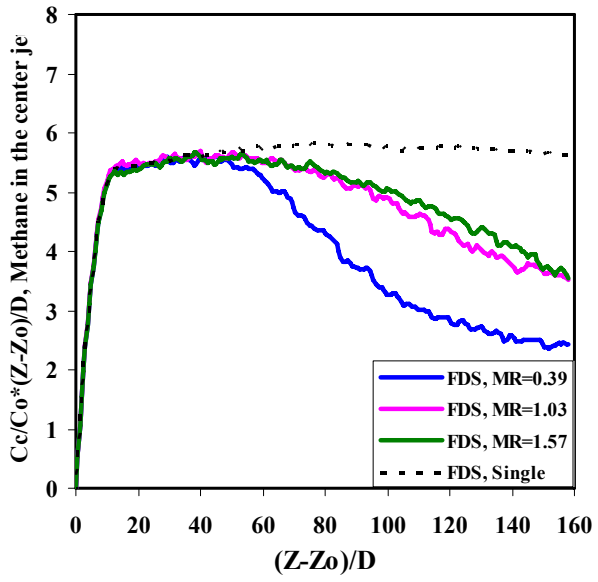

(b)

Figure 3.16: Mean centerline concentration of the (a) center (fuel) jet and (b) scaled mean centerline concentration of the center jet for *MR*=0.39, 1.03 and 1.57 with jet separation distance *S/d*=10.0 in five multiple jets.

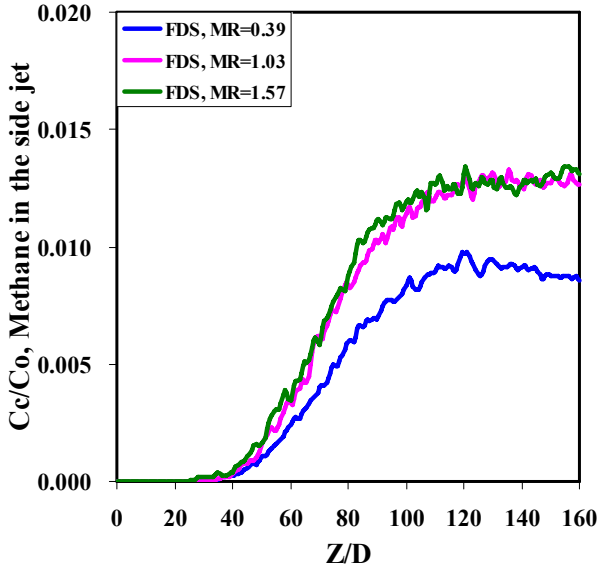

(a)

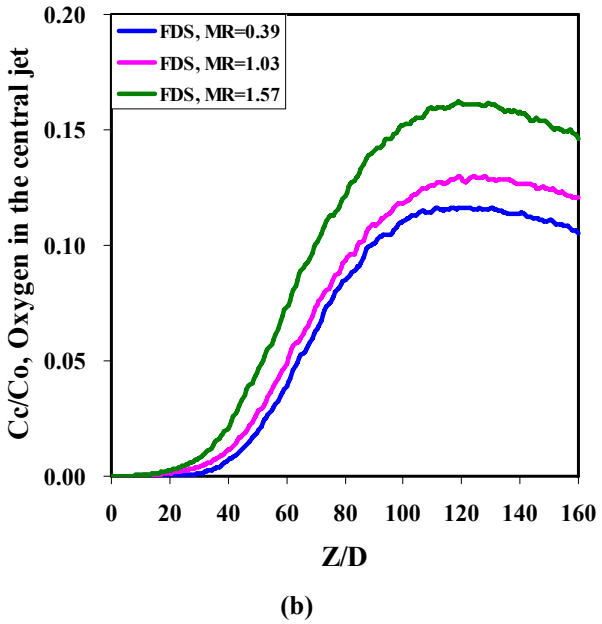

(b)

Figure 3.17: Mean concentration of the (a) methane in the side (oxidizer) jet and (b) oxygen in the center (fuel) jet for *MR*=0.39, 1.03 and 1.57 with jet separation distance *S/d*=10.0 in five multiple jets.

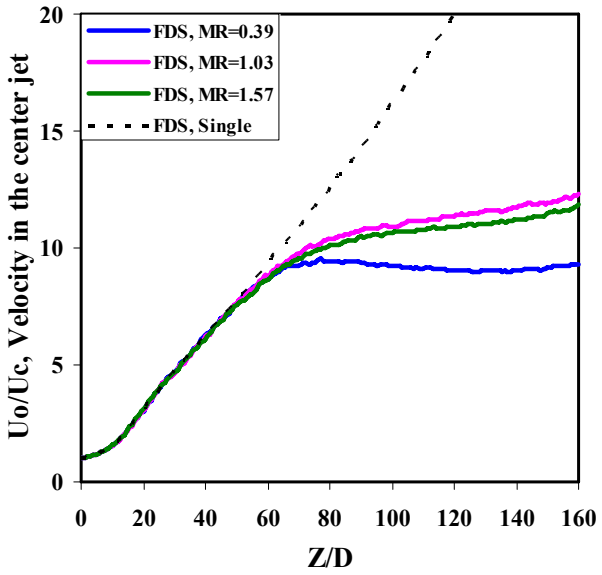

Figure 3.18: The mean centerline stream-wise velocities of the center (fuel) jet for *MR*=0.39, 1.03 and 1.57 with jet separation distance *S/d*=10.0 in five multiple jets.

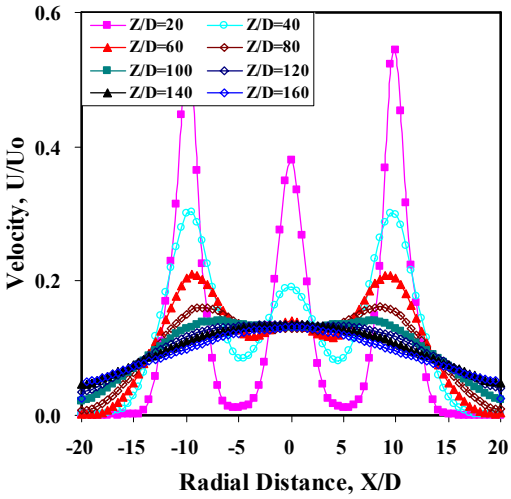

(a)

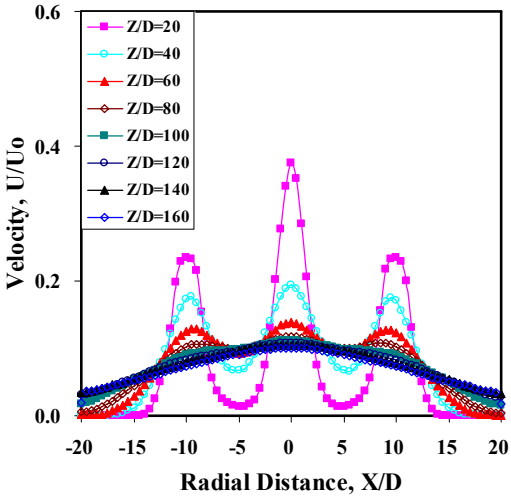

(b)

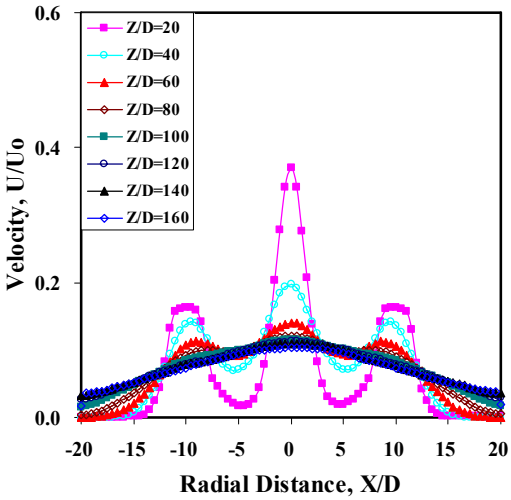

(c)

Figure 3.19: Mean radial velocity profiles at different axial positions for (a) *MR*=0.39, (b) *MR*=1.03 and (c) *MR*=1.57 with jet separation distance *S/d*=10.0 in five multiple jets.

CHAPTER 4

Numerical investigations on the effects of confinement for non-reacting multiple turbulent jet flows

The patterns of flow and mixing in confined turbulent jets are quite different from those of unconfined jets because of the existence of the walls. The confinement alters considerably the flow fields, entrainment and resulting mixing characteristics. Thus, the confined multiple turbulent jets are complex flows involving turbulent shear layer, boundary layer and pressure gradients. In addition, the situation of real industrial furnaces is quite different from the unconfined conditions in previous study. The effects of the confinement and chemical reaction must be considered to investigate the characteristics of flow and mixing in industrial furnaces. However, there are relatively few studies on confined jets while considerable experimental and numerical efforts have been spent on the study of turbulent jets issuing into a free environment.

In this study, the numerical investigations of the mixing characteristics and the resulting concentration fields in confined, non-reacting multiple turbulent jets are performed by using FDS. In addition, extensive numerical studies in a representative five turbulent jet configuration with a center fuel jet surrounded by four oxidizer jets are presented to provide fundamental guidelines for optimization of the control parameters, jet spacing, momentum ratio of fuel to oxidizer jet, for industrial furnaces with multiple turbulent jets.

4.1. Numerical method

Figure 4.1 shows the schematic diagram of the computational domain used in the current study. The computational domain is composed of $40d \times 40d \times 160d$ for the five jet configuration based on the center jet diameter. The domain consists of 1,638,400 grid points for all cases. It was proved earlier that this resolution is sufficient to describe the

flow and concentration fields considering the accuracy and computation time based on the experimental results in author's previous work [37]. All numerical calculations in this study have been performed within a domain of this size that is made up of rectangular mesh, each with its own rectilinear grid. It is noted that the steady state is decided by monitoring the mass production in the domain, and all data is averaged after reaching the steady state.

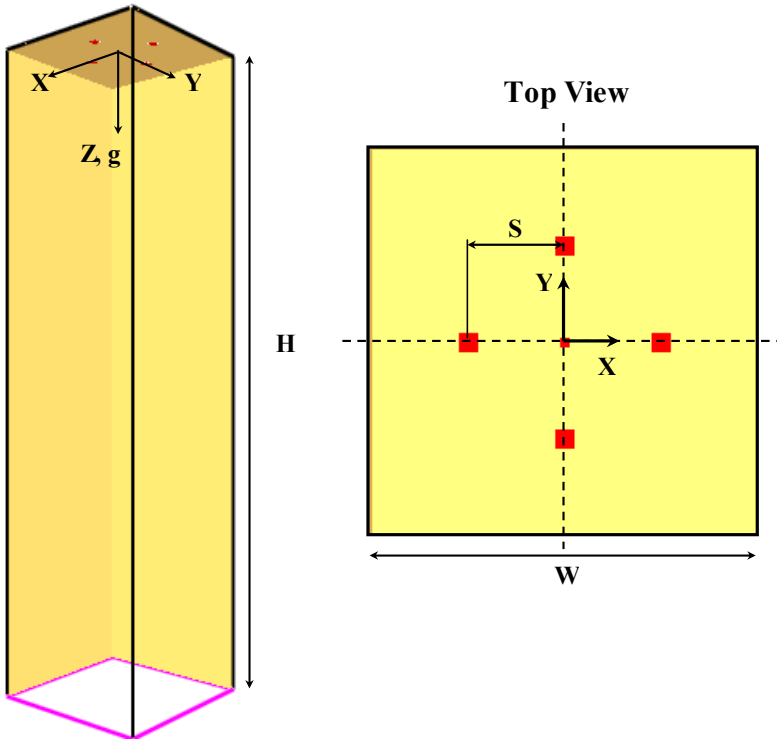

Figure 4.1: Schematic diagram of the computational domain and coordinates

Configurations		Working/ Surrounding Fluids	Jet Diameter (m)		Velocity (m/s)		Reynolds No.		Momentum Ratio	Separation Distance	Confinement Ratio	
			Center	Side	Center	Side	Center	Side	MR	*S/d*	Diameter Ratio, Dr^a	Length Ratio, Lr^b
Single		Air	0.1		20.0		1.29×10^5				5.0	16.0
			0.1		20.0		1.29×10^5				10.0	8.0
			0.1		20.0		1.29×10^5				20.0	4.0
5 Jets	S/D effect	Methane & Air/ Nitrogen	0.05	0.1	40.4	24.0	6.54×10^4	1.55×10^5	0.39	4.0		
			0.05	0.1	40.4	24.0	6.54×10^4	1.55×10^5	0.39	8.0		
			0.05	0.1	40.4	24.0	6.54×10^4	1.55×10^5	0.39	12.0		
	MR effect	Methane & Air/ Nitrogen	0.05	0.1	40.4	24.0	6.54×10^4	1.55×10^5	0.39	10.0		
			0.05	0.1625	40.4	9.1	6.54×10^4	9.54×10^4	1.03	10.0		
			0.05	0.2	40.4	6.0	6.54×10^4	7.75×10^4	1.57	10.0		

Table 4.1: The parameters and properties of confined turbulent jets in numerical simulations
a: $D_r = W / d$ **, b :** $L_r = H / W$

4.2. Results and Discussion

In this section, first the numerical results of a confined single turbulent jet are presented to investigate the basic characteristics of confined turbulent jets. Later, an extensive numerical study of five gas phase confined multiple turbulent jets is presented. The Reynolds number of the jets is kept above 10^4 for sustaining the fully developed turbulence condition as recommended by Dimotakis [55]. The parameters and properties of the confined turbulent jets are listed in Table 4.1.

4.2.1. Confined Single Jet

Figure 4.2 shows the centerline stream-wise velocities for various confinement ratios. In this study, the confinement ratio is defined as $D_r = W / d$, where W is the width of the domain and d is the diameter of the jet. In addition, the centerline stream-wise velocity is scaled in the same manner used in the concentration for comparison.

It can be seen from Figure 4.2 that the centerline stream-wise velocities of the confined jets decays much faster compared to the unconfined single jet. The main difference between unconfined and confined jets is the availability of surrounding fluid. In unconfined configuration, the entrainment from surrounding fluid which is unlimited in amount occurs, whereas the quantity of surrounding fluid is limited in confined configuration. Hence, the recirculation flow is established as a stable part of the flow. As a result, the turbulent dissipation should increase, and the jet velocity decays fast and has enhanced radial spreading that promotes the mixing of the jet in the confined configuration [59-61].

It is also clearly observed that the decay rate of the centerline velocity increases with decrease of the confinement ratio. This means that the effect of the wall becomes more significant with decrease of the confinement ratio. The case of Dr=5, the smallest confinement ratio, shows that the centerline stream-wise velocity is nearly constant after Z/d=50, which is similar to the fully developed pipe flow. On the other hand, the behavior of the centerline velocity approaches the unconfined single jet for large confinement ratio because the effect of the wall becomes weak. According to the Kandakure et al [62], the confinement effect diminishes for Dr>50.

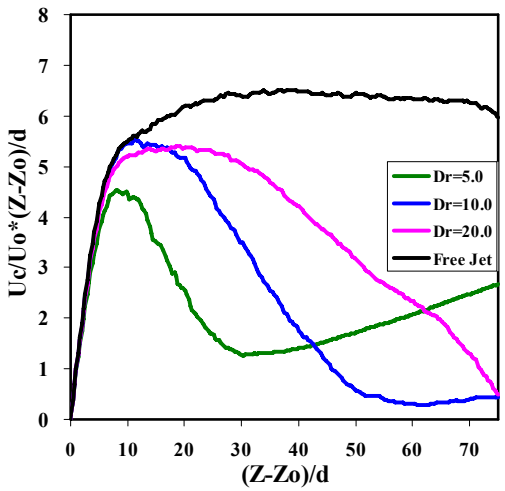

Figure 4.2: The scaled centerline stream-wise velocity of confined single turbulent jets for various diametric confinement ratios, *Dr*=5, 10 and 20.

Figure 4.3 shows the radial stream-wise velocity profiles at *Z/d*=20 for unconfined and confined single jet (*Dr*=10), respectively. It is clearly seen that there are re-circulating flow regions near the walls in confined jet even far upstream region, *Z/d*=20, which it is not found in unconfined jet. It is generally known that re-circulating flow exists as a stable part of the flow under certain circumstances [60]. In addition, the confined jet loses momentum faster than unconfined jet because of the re-circulating flow entrained by the jet. In confined jet, the quantity of entrainment is limited, thus re-circulating flow is established and entrained by the jet if the jet fluid fails to fill up the domain completely.

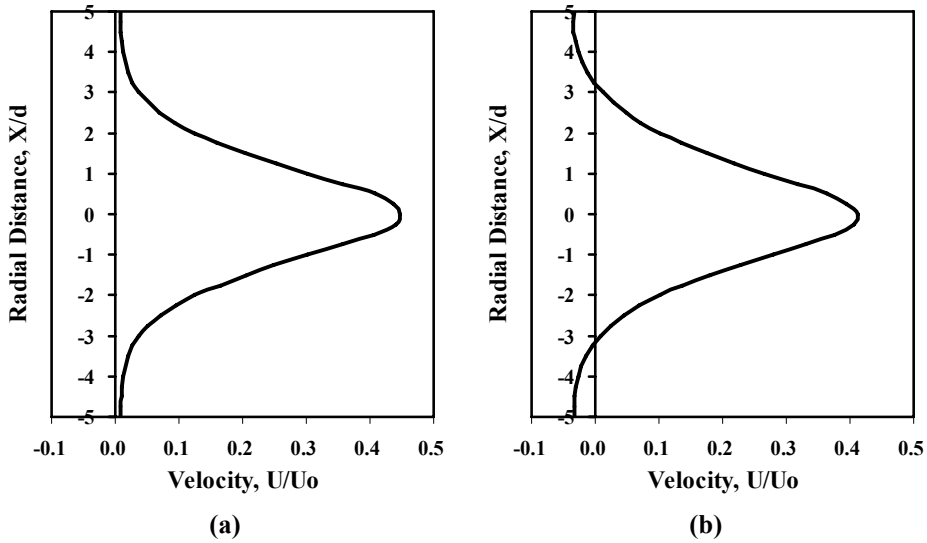

Figure 4.3: The radial velocity profiles of (a) unconfined and (b) confined single turbulent jet with *Dr*=10 at *Z/d*=20

Another main difference between the unconfined and confined jets is that the pressure is the same everywhere in the unconfined jet, whereas the pressure varies axially in the confined jet [61]. It is clearly observed from Figure 4.4 that the flow induced perturbation pressure shows the negative peak in confined jets. The pressure decreases sharply and hence pressure gradient increases with decrease of the confinement ratio, which means that the effect of wall become significant as decrease of the confinement ratio. As seen in Figure 4.4, the pressure recovers sufficiently before the exit of the domain for *Dr*=5 and 10, thus the jet can push the flow out of the domain. However, the pressure still remains below the atmospheric pressure and recovery of the pressure is small for large confinement ratio *Dr*=20. This adverse pressure gradient caused by the confinement considerably alters the entrainment and mixing [62].

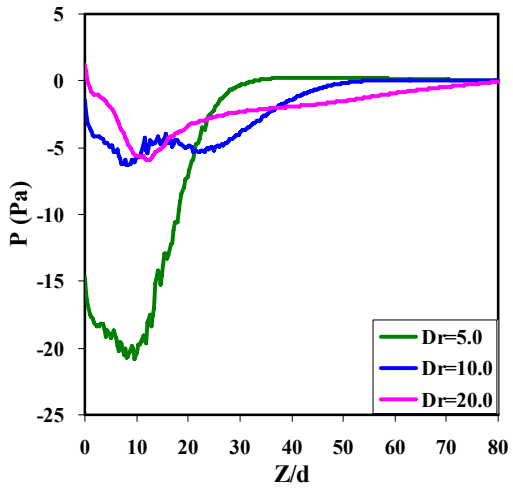

Figure 4.4: The centerline perturbation pressure profiles of confined single turbulent jets for various diametric confinement ratios, *Dr*=5, 10 and 20.

Figure 4.5 shows the centerline concentration for various confinement ratios. It is clearly seen that the concentration is constant and is equal to that of a jet all over the domain for small confinement ratio, *Dr*=5 and 10. This can be attributed the fact that the jet flow becomes like a fully developed pipe flow when the jet can expand to the width of the domain, thus the jet fluid fills up the domain. However, as the confinement ratio increases, the concentration is not constant because infiltration from outside of the domain occurs at the exit of the domain due to short length ratio, *H/W*. In other words,

the length ratio *H/W* decreases with increase of the confinement ratio *W/D*, and thus the effect of the confinement becomes weaker.

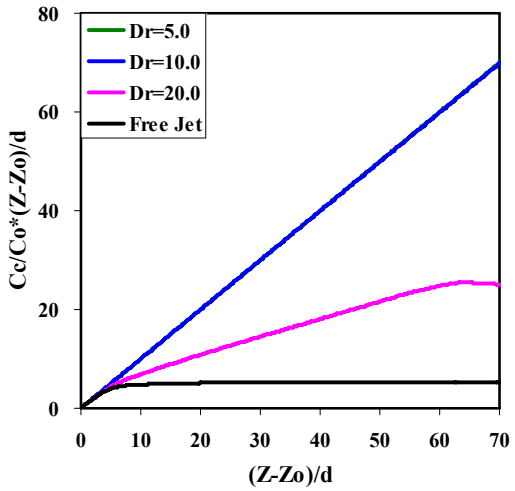

Figure 4.5: The scaled centerline concentration of confined single turbulent jets for various diametric confinement ratios *Dr*=5, 10 and 20

Consequently, the jet fluid fails to fill up the whole domain and infiltration from outside of the domain should occur to make up for the deficient flow amount. However, the value of the centerline concentration of the confined jets shows still higher than that of the unconfined jet because the sufficient amount of surrounding fluid is not present for the entrainment in the confined jet. The quantity of surrounding fluid is unlimited in the unconfined jet, thus the jet can be diluted continuously by the surrounding fluid in the unconfined jet. On the other hand, in the confined jet, the main source of entrainment by the jet is the jet fluid itself because of the re-circulating flow and lack of the amount of surrounding fluid. Consequently, the jet is diluted mainly by its fluid which is the re-circulating flow entrained by the jet, thus the centerline velocity decays faster and concentration remains relatively constant compared to the unconfined jet.

4.2.2. Gas-phase Five Jets (Fuel & Oxidizer jets)

In this section, methane and normal air are used as the fuel and oxidizer, respectively. The diameter of central fuel jet is 0.05 m while the diameter of the four side oxidizer jets

is varied to maintain the same flow rate and the overall equivalence ratio, $\Phi_{overall}$=1.0 for all cases.

Numerical simulation for the configuration of a central jet (fuel) surrounded by four equidistant oxidizer jets are carried out for Reynolds number 6.5×10^4 of the central jet. The separation distance is varied as *S/d*=4, 8, 12, which are corresponding to *S/W*=0.1, 0.2 and 0.3, respectively. The momentum ratio varied as *MR*=0.39, 1.03 and 1.57. It is noted that all properties presented in this section are normalized by those of center jet.

4.2.2.1. Confinement Effects on multiple turbulent jets

Figure 4.6 shows the scaled centerline stream-wise velocity and concentration in the center jet of unconfined and confined turbulent multiple jets, respectively, with same momentum ratio, *MR*=0.39, and separation distance, *S/d*=10 (*S/W*=0.25). It is clearly seen from Figure 4.6 (a) that the confinement considerably alters patterns of the centerline stream-wise velocity. The value of scaled centerline velocity increases along the axial direction because of adding momentum from side oxidizer jets for unconfined multiple jets. On the other hand, the turbulent dissipation increases by re-circulating flow for confined multiple jets, as a result, the jet decays faster and has enhanced radial spreading that promotes the mixing of the jet. Therefore, the value of scaled centerline stream-wise velocity of the confined jet decays faster than that of the unconfined jet. It is also observed from Figure 4.6 (a) that there are negative velocity zones in confined multiple jets, which indicates that re-circulating flow occurs.

It is observed from Figure 4.6 (b) that the scaled centerline concentration of the confined multiple jets initially shows flat shape that is the similar trend of the unconfined single jet at upstream region of the computational domain, which means that the centerline concentration *Cc/Co* keeps decreasing by entraining ambient fluid like a single free jet. After some distance from the jet exit, the value of the scaled centerline concentration increase is nearly linear, this means that the centerline concentration remains almost constant at middle region of the computational domain. Finally, the scaled centerline concentration of the confined multiple jets again becomes flat that is the similar trend of the unconfined single jet at further downstream region. It may be attributed the fact that the center jet entrains the surrounding fluid before merging with side jets, thus initially

follows the path of the free single jet in unconfined multiple jets. After merging with side jets, the center jet can still entrain surrounding fluid and mix with the side jets, thus the centerline concentration falls lower than that of the free single jet. On the other hand, the source of jet dilution is not surrounding fluid, but mainly the mixture of the fuel and oxidizer jets in confined multiple jets as explained before. Therefore, the mixing between jets and re-circulating flow of the mixture of the jets are simultaneously occurred in confined multiple jets. In other words, the jet mixed with other jets by the interaction between jets as same way in unconfined jets, and also diluted by the re-circulating flow of the mixture of the jets in confined multiple jets. Therefore, the confined multiple jets initially has lower concentration due to re-circulating flow entrained by the jets, and remains nearly constant over the middle region of the computational domain.

The radial stream-wise velocity profiles for unconfined and confined jets at Z/d=40, 80 and 160 which correspond to upstream, middle and downstream region of the computational domain are shown in Figure 4.7. It can be seen that the confined multiple jets lose momentum faster than the unconfined multiple jets from upstream region. In unconfined multiple jets, the jets are finally merged into center jet and the peak of the velocity is located at the center jet region, whereas the confined multiple jets lose momentum quite fast and re-circulation flow region appears near the walls at even quite upstream region Z/d=40, and center jet flow region at Z/d=80 in confined multiple jets. It might be thought that the turbulent dissipation increases in confined multiple jets due to confinement, thus radial spreading is enhanced and the jets keep entraining their mixture. As a result, the confined multiple jets lose momentum faster than unconfined multiple jets and re-circulating flow exists.

It should be noted that the flow patterns may vary with control parameters such as the separation distance and momentum ratio between jets. Thus, the effects of these parameters on flow and concentration fields are investigated in the next sections.

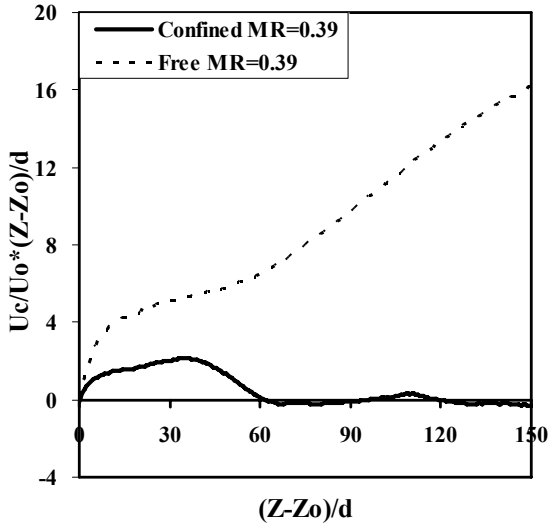

(a)

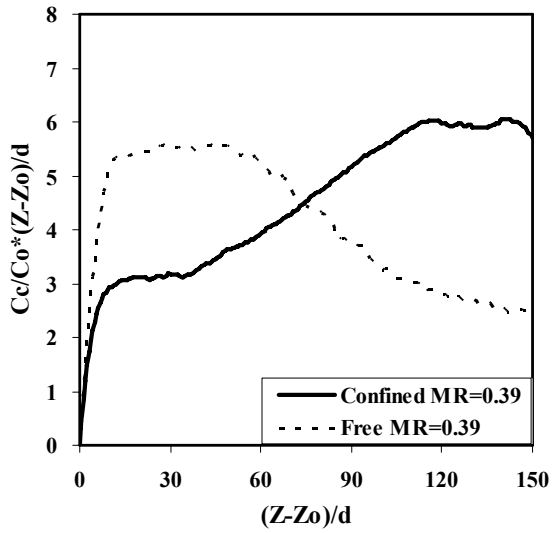

(b)

Figure 4.6: The scaled centerline (a) stream-wise velocity and (b) concentrations of unconfined and confined multiple turbulent jets with momentum ratio *MR*=0.39 and separation distance *S/d*=10.

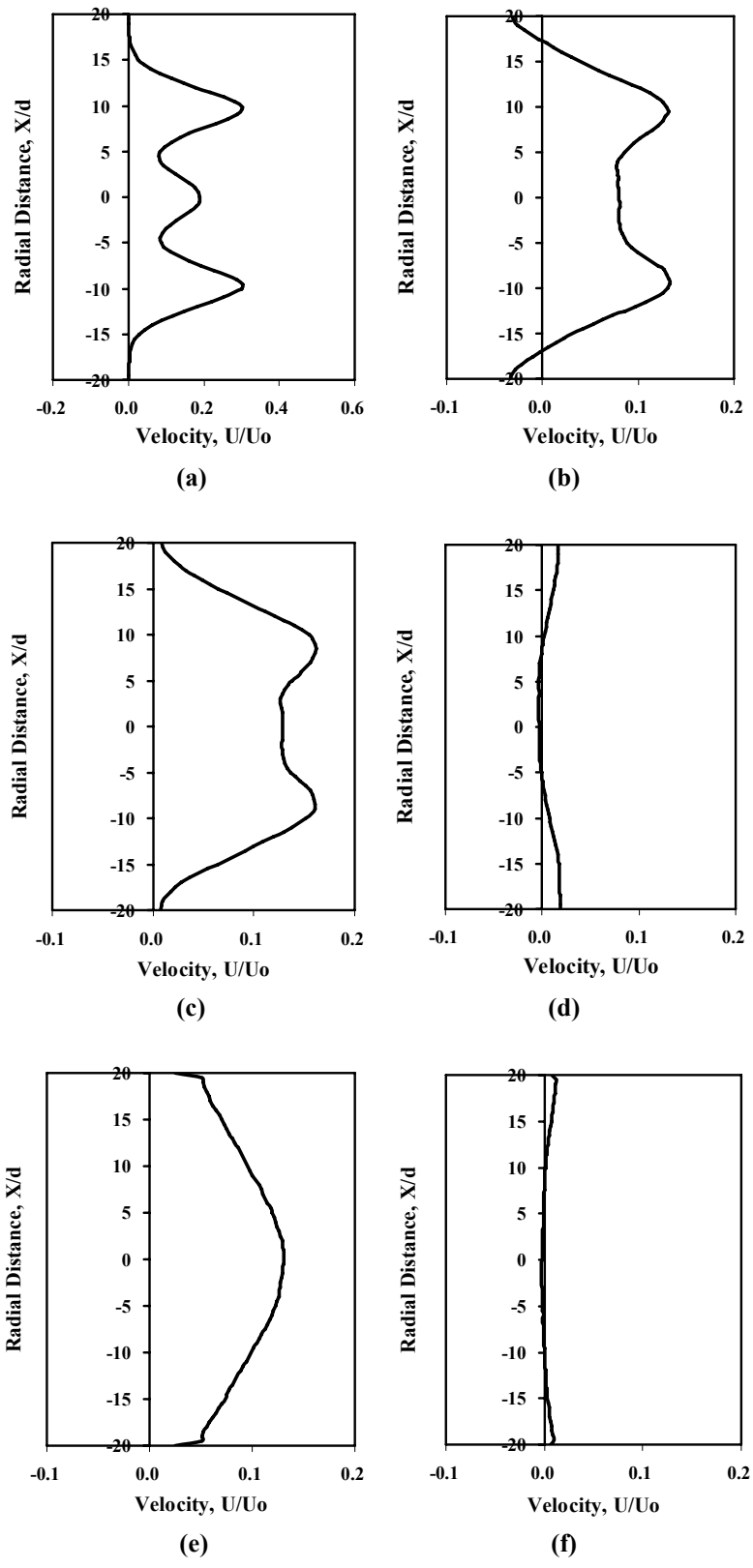

Figure 4.7: The radial velocity profiles of (a) (c) (e) of unconfined and (b) (d) (f) confined multiple turbulent jets at *Z/d*=40, 80 and 160 with momentum ratio *MR*=0.39, and separation distance *S/d*=10.

4.2.2.2. Separation Distance Effects on multiple turbulent jets

The scaled centerline stream-wise velocity and concentration in the center jet of confined multiple turbulent jets for various separation distances *S/d*=4, 8 and 12 (*S/W*=0.1, 0.2 and 0.3) with same momentum ratio *MR*=0.39 are shown in Figure 4.8 and 4.9. It is observed that there are two kinds of trend in the scaled centerline stream-wise velocities. The first is one parabolic shape with positive peak for *S/d*=4 and 8. In these cases, the separation distance between jets is relatively small, thus the jets are merged earlier than large separation distance cases. As mentioned in previous work [37], the behavior of multiple jets with small separation distance is close to that of the single jet. Therefore, the jets are merged into one jet quickly and act like a single jet, consequently have positive peak of velocity at some distance from the jet exit and finally centerline velocity decreases by momentum change. The second is two parabolic shapes with positive and negative peak for *S/d*=12. For large separation distance, each jet acts like a single jet before merging, thus the behavior of the centerline velocity of the center jet is similar to that of a single jet even though the magnitude of the peak is lower than that of the unconfined single jet. After merging, the center jet loses momentum quickly due to high momentum of side jets which promotes the re-circulating flow. As a result, re-circulating flow occurs at the region of center jet, and the center jet has negative velocity peak. As close to the exit of the domain, the velocity recovers as flow goes out.

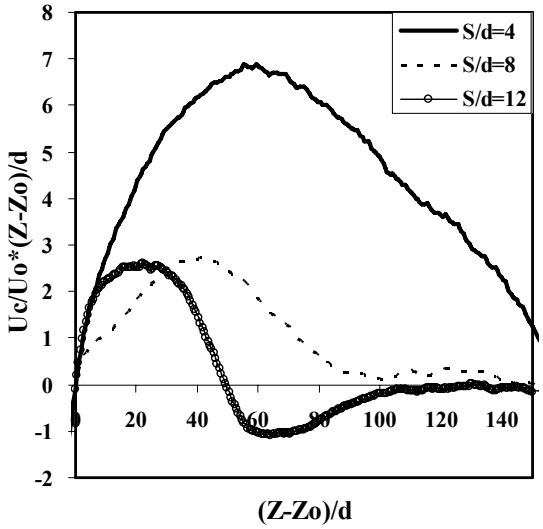

Figure 4.8: The scaled centerline stream-wise velocity in the center jet of confined multiple turbulent jets for *S/d*=4, 8 and 12 with momentum ratio *MR*=0.39.

It is observed from Figure 4.9 that there are also two kinds of behavior in centerline concentration of the center jet in confined multiple jets with various separation distances *S/d*=4, 8 and 12. The one is that the slope of the scaled centerline concentration is nearly linear from *(Z-Zo)/d*=40 for *S/d*=4 and 8, which means that the centerline concentration *Cc/Co* is almost constant. This behavior is very similar to that of the confined single jet. The other is that the concentration initially increases linearly and then decreases sharply, finally follows the same path of other cases from *(Z-Zo)/d*=60 for *S/d*=12. For large separation distance case, the center jet is more prone to act like a single jet before merging with side jets [37]. Therefore, the centerline concentration approaches the path of a single jet at upstream region, and then shows the trend of the confined jet which is similar to small separation distance cases after merging with side jets.

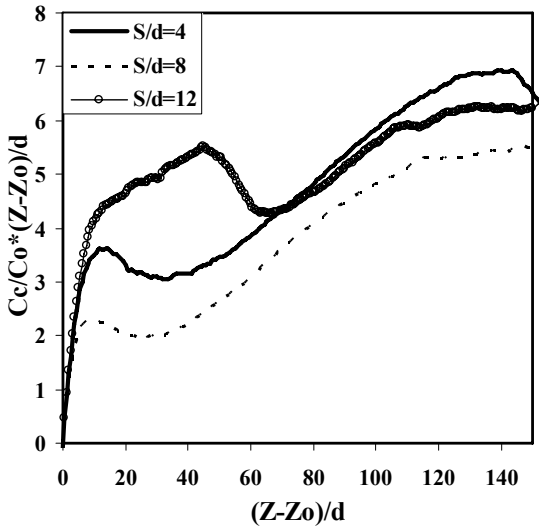

Figure 4.9: The scaled centerline concentration in the center jet of confined multiple turbulent jets for *S/d*=4, 8 and 12 with momentum ratio *MR*=0.39.

The radial stream-wise velocity profiles at *Z/d*=20, 40 and 80 for various separation distances with same momentum ratio *MR*=0.39 are shown in Figure 4.10. It is clearly observed that the jets merge into one jet faster with decrease of the separation distance between jets, and the peak of stream-wise velocity is located at the center jet region and becomes lower with decrease of the separation distance for *S/d*=4 and 8. However, the peak of velocity appears at the side jet region, and the re-circulating flow exists at the

center jet region for *S/d*=12. This might be thought that the jets merge very quickly and act like a confined single jet with small separation distance because of strong interaction between jets, thus recirculation pattern is formed from the center jet to side jet region, as a result, re-circulating flow appear near the walls. On other hand, the case of large separation distance shows that the recirculation of flow occurs from the side jets toward the center jet with given momentum ratio *MR*=0.39 that the side jets have higher momentum than the center jet. Thus, the re-circulating flow appears at the center jet region.

Figure 4.11 shows the radial equivalence ratio profiles at *Z/d* =20, 40 and 80 for various separation distances with same momentum ratio *MR*=0.39. It is observed that the radial equivalence ratio reaches quite combustible range quickly for all cases even at *Z/d*=40. This might be attributed the fact that the mixture of the jets fills the domain up in the confined multiple jets, thus the main source of jet dilution is the mixture of the jets, not the surrounding fluid that is different from the jet fluids. Therefore, the jet mixes with other jet by the interaction between jets as same way in unconfined multiple jets and simultaneously entrains the mixture of the jets by re-circulating flow, which is the same effect of mixing with other jet again in confined multiple turbulent jets. Consequently, the mixing is enhanced by both of interaction between jets and entraining re-circulating flow of the mixture of the jets. As a result, the concentration can remain similar level, and reach the local equilibrium state very quickly over the domain in confined multiple jets. It is observed that the case of moderate separation distance *S/d*=8 shows nearly flat shape of radial equivalence ratio profiles even at *Z/d*=40, which indicates the well mixing in the domain in views of combustion. On the other hand, the highest separation distance *S/d*=12 shows the highest equivalence ratio near the region of center jet flow at *Z/d*=20 and 40 because mixing between jets at upstream region is less with large separation distance as explained in unconfined multiple jets, and the case of *S/d*=4 is in between two cases. This result is quite interesting because interaction between jets is strongly promoted as the separation distance decreases, whereas dilution of the jet is enhanced for large separation distance in the unconfined multiple turbulent jets according to the previous work on unconfined multiple turbulent jets [37]. Thus, it is expected that the

case of small separation distance *S/d*=4 shows well mixing and flat radial equivalence ratio profiles.

However, it should be noted that the interaction between jets occurs intensively with small separation distance while the entrainment of re-circulating flow of the jet mixture is less because the area of re-circulating flow region is formed narrowly as shown in Figure 4.10. On the other hand, wide re-circulating flow region exists in the center jet region for the case of large separation distance while the interaction between jets is weak at upstream region. Therefore, it is believed that the entrainment of jet mixture is stronger than the case of small separation distance before merging distance, and the intensity of interaction is between the cases of small and large separation distance with moderate separation distance. As a result, the entrainment of jet mixture and interaction between jets occur very ideally with moderate separation distance.

In terms of the homogeneous combustion, the reaction should be delayed to further downstream region of the domain, not near the region of the jet exit. For this purpose, the jets are sufficiently diluted by the surrounding fluid before they react in real furnace. Therefore, the separation distance should be sufficiently large to avoid early reaction between jets. In addition, the large separation distance is preferable to form large scale of re-circulating flow region over the domain for concentration fields to reach the local equilibrium state quickly over the domain in confined multiple jets.

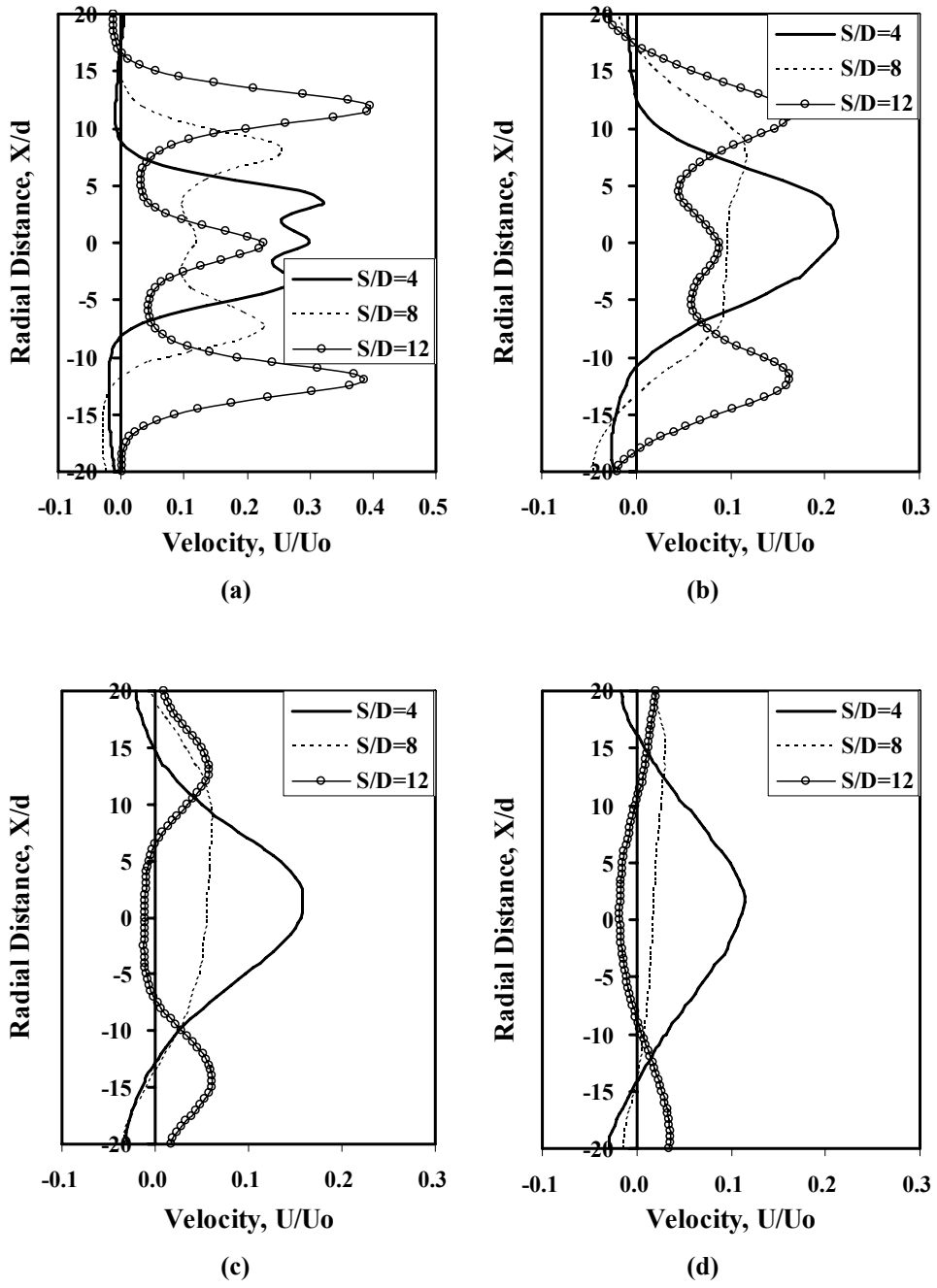

Figure 4.10: The radial stream-wise velocity profiles of confined multiple turbulent jets (a) *Z/d*=20 (b) *Z/d*=40 (c) *Z/d*=60 and (d) *Z/d*=80 for *S/d*=4, 8 and 12 with momentum ratio *MR*=0.39.

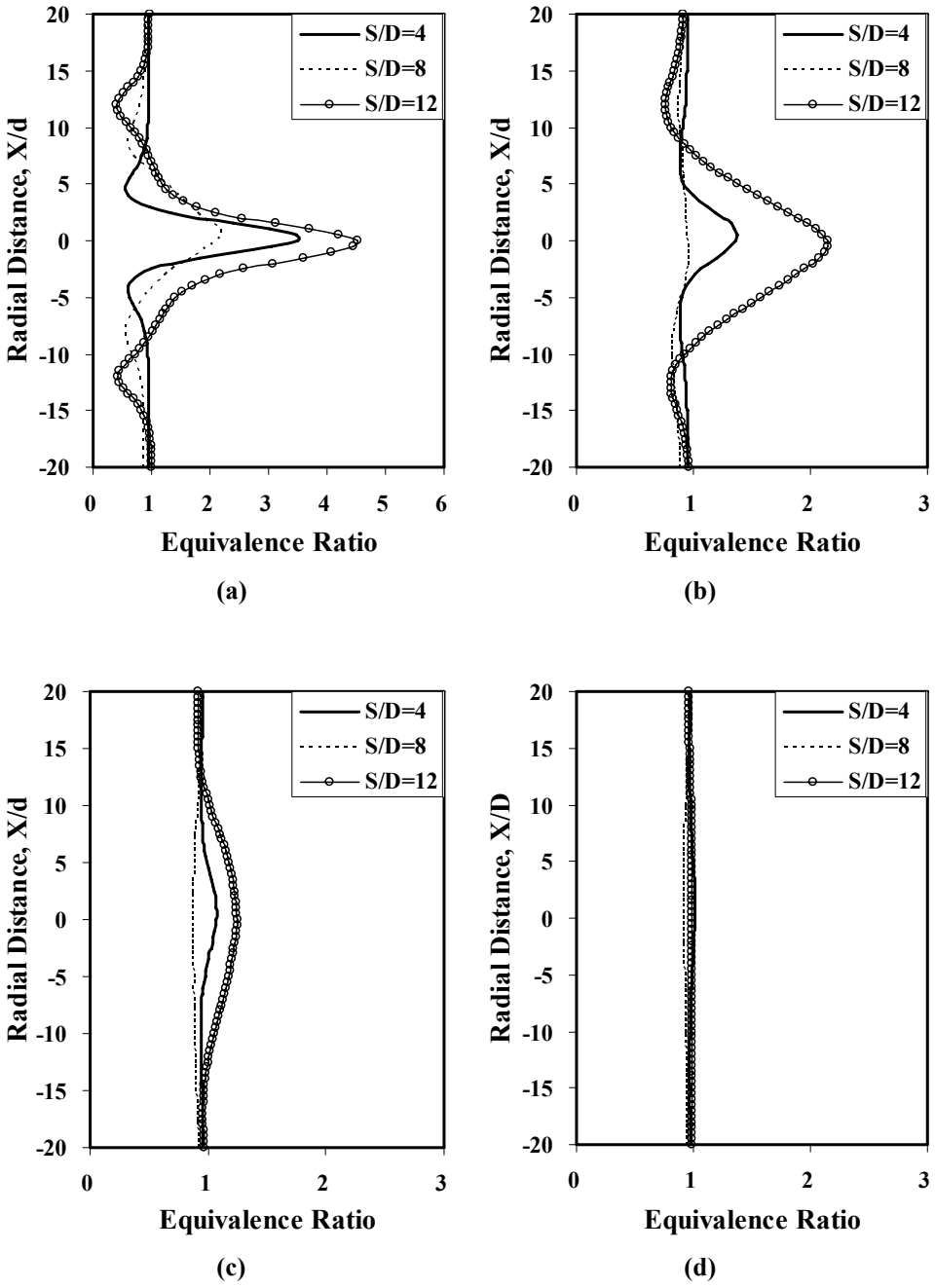

Figure 4.11: The radial equivalence ratio profiles of confined multiple turbulent jets at a) *Z/d*=20 (b) *Z/d*=40 (c) *Z/d*=60 and (d) *Z/d*=80 for *S/d*=4, 8 and 12 with momentum ratio *MR*=0.39.

4.2.2.3. Momentum Ratio Effects on multiple turbulent jets

The scaled centerline stream-wise velocity and concentration in the center jet for various momentum ratio *MR*=0.39, 1.03 and 1.57 with same separation distance *S/d*=10 are shown in Figure 4.12 and 4.13. It is observed from Figure 4.12 that the scaled centerline velocities show similar patterns for various momentum ratios, the value of scaled centerline velocity initially shows the trend of the free single jet and then decreases along with the axial distance after merging point where the center jet begins to be affected by the side jets. This might be thought that the jets act like a single jet before merging other jets, and then the turbulent dissipation occurs actively due to confinement, thus the jets lose momentum quickly. Another observation is that the value of scaled centerline velocity decreases with decrease of momentum ratio *MR* in order, and the re-circulating flow regions are found with *MR*=0.39, which indicates that the effect of the side jets on the center jet becomes more significant with decrease of momentum ratio.

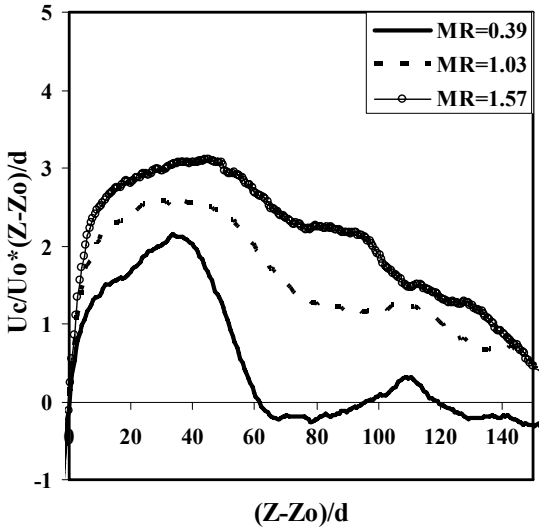

Figure 4.12: The scaled centerline stream-wise velocity in the center jet of confined multiple turbulent jets for *MR*=0.39, 1.03 and 1.57with separation distances *S/d*=10.

It is seen from Figure 4.13 that all cases show similar trend of the scaled centerline concentration in the center jet. The scaled centerline concentration initially follows the path of the unconfined single jet, and deviate from the path after about *Z/d*=40 where the side jets begins to affect the center jet. After the deviation point, the value of scaled

centerline concentration is nearly proportional to the scale factor *(Z-Zo)/d*, which means that the centerline concentration remains nearly constant after *Z/d*=40 for all cases. This can be attributed the fact that the mixture of the center and side jets fills the domain, thus the concentration is nearly constant in the middle of the domain.

Both of the scaled centerline stream-wise velocity and concentration show the larger decay rate with decrease of momentum ratio as shown in Figure 4.11. It might be thought that radial spreading of the jets is more enhanced with low momentum ratio because the momentum of the side jets increases with lower momentum ratio, thus the side jets with high momentum promote the entrainment of mixture of the jets. As a result, the center jet loses momentum quickly, and shows lower concentration with lower momentum ratio.

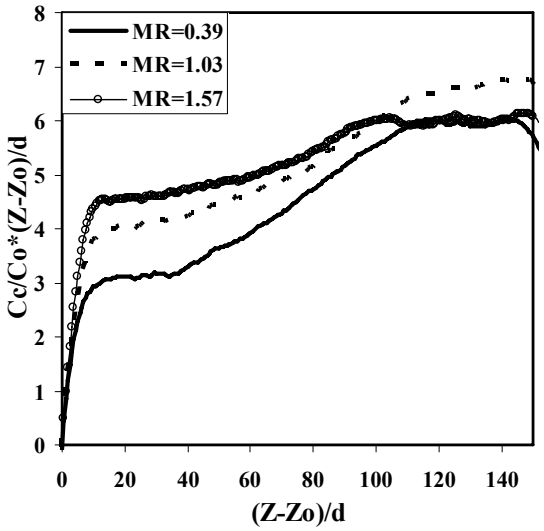

Figure 4.13: The scaled centerline concentration in the center jet of confined multiple turbulent jets for *MR*=0.39, 1.03 and 1.57 with separation distances *S/d*=10.

The radial stream-wise velocity profiles at *Z/d*=20, 40, 60 and 80 for various momentum ratios *MR*=0.39, 1.03 and 1.57 with same separation distance *S/d*=10 are shown in Figure 4.14. It is observed that the jets merge into the center jet and the peak of velocity is located at the center jet, and becomes flat at further downstream region for *MR*=1.03 and 1.57. On the other hand, the peak of velocity appears at the center of side jets, and the center jet lose momentum quickly and then negative velocity region is shown at *Z/d*=80 for *MR*=0.39. For large momentum ratio, the jets merge into one jet so early that the jets act like the confined single jet, hence the region of re-circulating flow is distributed

narrowly near the walls as seen in Figure 4.14. On the other hand, the flow pattern from the side jets to the center jet is established because of high momentum of the side jets for small momentum ratio, thus the region of re-circulating flow is distributed widely at the center region.

Figure 4.15 shows the radial equivalence ratio profiles of confined turbulent jets at Z/d=20, 40, 60 and 80 for various momentum ratios with separation distance S/d=10. It is observed that low *MR* case shows quite flat radial equivalence ratio profiles and reaches the local equilibrium state very quickly, whereas other two cases show similar trend.

In general, the entrainment of surrounding fluid is enhanced for low *MR* while the mixing between jets is promoted for high *MR* In unconfined multiple jets [37], which is also true in the confined multiple jets. However, the mixing between jets in the confined multiple jets is achieved by both interaction between jets and entrainment of the mixture of the jets. Considering the mixing characteristics of confined multiple jets, the interaction between jets is enhanced because the jets merge into one jet so early that the jets act like the confined single jet while the region of re-circulating flow is distributed narrowly near the walls for large momentum ratio. On the other hand, the entrainment of the jets is promoted for small momentum ratio due to high momentum of the side jets; consequently the jets can entrain more mixture of the jets. In addition, the mixing in the domain is more enhanced with the aids of the widely distributed re-circulating flow region of mixture for small momentum ratio. Therefore, the radial equivalence ratio profiles can converge to equilibrium state quickly and show well mixing patterns in the domain. It is noted that the radial velocity and equivalence ratio profiles become identical for all cases, and converge equilibrium state after Z/d=80.

Based on above results, it can be concluded that high momentum ratio between jets is preferable for large separation distance to enhance interaction between jets, whereas lower momentum ratio is preferable for small separation distance to promote the re-circulating flow for better mixing in multiple turbulent jets with the configuration used in this study. In addition, the combination of higher momentum ratio and small separation distance should be avoid to obtain the homogeneous combustion because of strong interaction between jets, hence early reaction at upstream region.

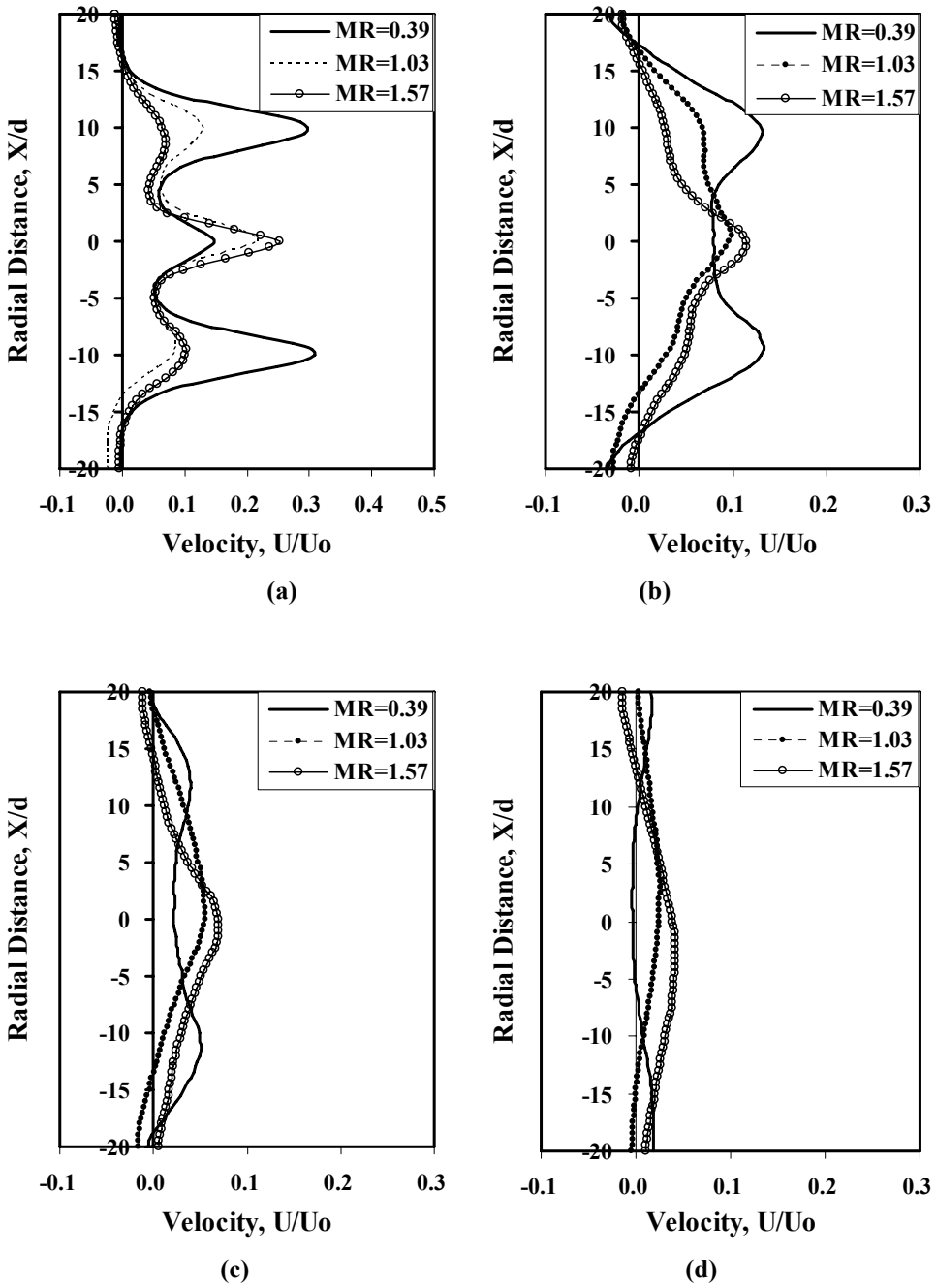

Figure 4.14: The radial stream-wise velocity profiles of confined multiple turbulent jets at (a) *Z/d*=20 (b) *Z/d*=40 (c) *Z/d*=60 and (d) *Z/d*=80 for *MR*=0.39, 1.03 and 1.57 with separation distance *S/d*=10.

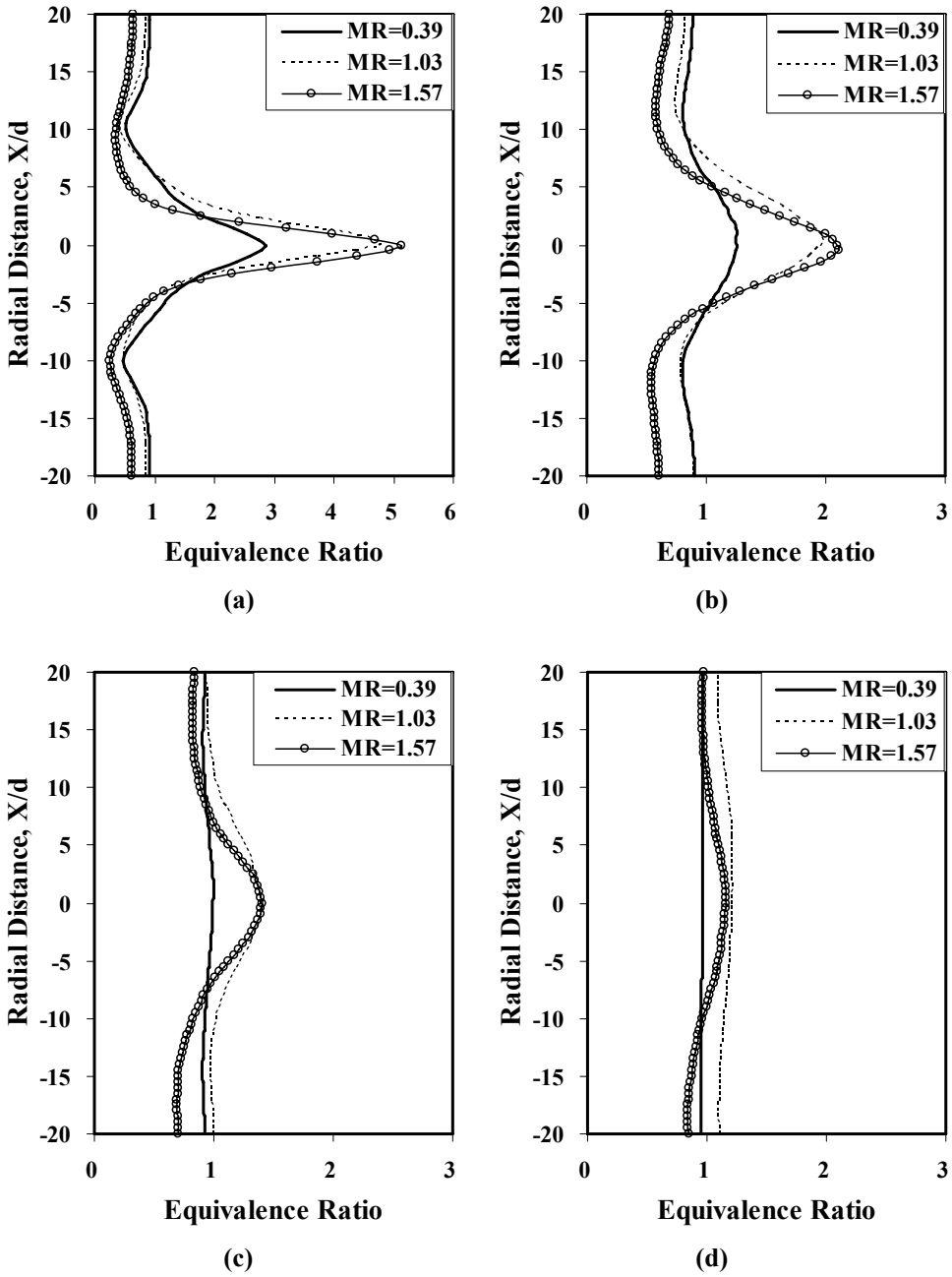

Figure 4.15: The radial equivalence ratio profiles of confined multiple turbulent jets at (a) *Z/d*=20 (b) *Z/d*=40 (c) *Z/d*=60 and (d) *Z/d*=80 for *MR*=0.39, 1.03 and 1.57 with separation distance *S/d*=10.

CHAPTER 5

Experimental methods for reacting flows

5.1. Experimental Setup

5.1.1. Experimental Setup

Based on previous guiding principles, a furnace has been designed to increase the efficiency within the strict constraints on NOx, CO, total unburned hydrocarbons (THC) and particulate emissions. A newly constructed mid-sized laboratory furnace is illustrated in Figure 5.1. It is noted that these experimental study were done with Dr. Hyoseok Lee [1]. The furnace is divided into upper and lower chambers in order to access the inside of the furnace. The combustion takes place inside a cylindrical chamber (840 mm diameter and 1170 mm height). The nozzle of the fuel jet is located in the center of the reaction chamber ceiling, and four air nozzles are located in a square pattern around the fuel jet and are 280 mm apart from the fuel jet. The separation distance between the fuel and oxidizer jet is fixed in this study. This separation distance is intended for enhancing entrainment of product gases to achieve the homogeneous combustion condition. According to previous work, entrainment can be promoted at large separation distance [37]. In addition, the jets are issued vertically down from the ceiling for promoting recirculation of hot product gases with aids of buoyancy effect. Therefore, it can be expected that strong internal recirculation of product gases is achieved by buoyancy effect and large separation distance between the fuel and oxidizer jets. Six exhaust vents are located in the bottom of the reaction chamber. After passing through the exhaust vents, the exhaust gas travels through the co-annular channel between the inner and the outer shells and is extracted into a hood installed on the top of the furnace.

The heat sink with 810 mm diameter is located at the bottom surface of the furnace and cooling water flows inside the heat sink. This acts as the furnace load. The flow rate of

the cooling water (250 cm^3/s) was controlled by flow-meter and the flow-in and out temperature was recorded. Therefore, the amount of heat absorption from the combustion furnace can be calculated using flow rate and temperatures. The effective surface area of the heat sink is about 0.5 m^2.

Along the circumference of the furnace, three sets of five sampling ports are made of ceramic tubes. Sampling probes are inserted to measure the temperature and the reacting gases. The behavior of flame in the reaction chamber is visually monitored through the window opening in the center of the lower chamber of the furnace. Because the window is made of 3.175 mm quartz plate, the radiation emission in the spectral range from UV to IR passed through the window and can be captured by a photo detector. The shop laboratory air and pure oxygen are mixed to obtain the desired enrichment of oxygen in the oxidizer. The flow meters are calibrated and the four oxidizer flow streams are equally distributed by adjusting valves.

5.1.2. Measurement Setup

The spatial distribution of temperature and gas compositions (total unburned hydrocarbon, oxygen, carbon monoxide, carbon dioxide and nitric oxide) in the reaction zone and additionally total ultraviolet (UV) emission from the reaction zone are measured under various conditions. There are twelve K-type thermocouples on the wall and the ceiling of the reaction chamber to measure the surface temperature of the reaction zone. Temperature and gas composition in the reaction zone are sampled by using sampling probe made of quartz tube. The sampling probes are designed based on aerodynamic quenching techniques [63]. The nozzle on the tip of the probe is tapered to 1.5 mm ID. While K-type thermocouple is installed, the probe can be applied for both temperature measurement and gas sampling. A metal bellows pump is used to extract gas through the sampling nozzle. The sampled gas in the suction line passes through a particulate filter and is distributed into two lines. The first line is connected to the total hydrocarbon analyzer and heated to avoid condensation of water vapor. These measurements are on a wet basis. The second line is connected to the other analyzers and passed through a cold bath and a water trap to remove water vapor. These gases are measured on a dry basis.

A modified flame ionization detector (Shimadzu Gas Chromatograph GC-3BF) is used to measure the total hydrocarbons (THC) contained in the sampling gas [64]. To measure the concentration of oxygen, carbon monoxide, and carbon dioxide, SIEMENS Ultra/Oxymat 6E is used. It consists of two parts: a non-dispersive infrared analyzer for measuring carbon monoxide and carbon dioxide, and a paramagnetic oxygen analyzer for the oxygen measurement. The nitric oxide concentration is measured by a chemiluminescence analyzer (Thermo 42C High Level NO-NO_2-Nox analyzer). A calibration gas (10.03 % CO_2, 4.04 % CO, 22.98 % CH_4, 1.99 % H_2, 1.01 % N_2 and He as balance) is used to calibrate CO, CO_2 and CH_4. A calibration gas of 0.21 % CO, 1.01 % CH_4 and N_2 as balance is used to calibrate low span of CO and CH_4. A calibration gas of 57.6 ppm NO and N_2 as balance is used for NO analyzer and air is used for O_2 analyzer, while N_2 is used as a zero gas. All gas compositions are reported on volume basis in this study.

5.1.3. Experimental Procedure

Since the furnace configuration used in this work has no preheating, the inlet temperature of the fuel and oxidizer flows into the reaction chamber is about room temperature. The oxidizer is heated and diluted by internal exhaust gas recirculation since the nozzles are located on the ceiling, and the jets are injected downward.

Natural gas supplied by DTE Energy in Ann Arbor, Michigan is used as the fuel. Typical natural gas component supplied by DTE Energy is 89.5 ~ 92:5 % methane, 5.1 ~ 2:0 % ethane, 2.1 ~ 0.7 % propane, 1.6 ~ 0.5 % butane, 0.6 ~ 1.9 % nitrogen and 1.1 ~ 2.4 % carbon dioxide. The heat of combustion is about 32~ 35 MJ/m^3 and the flammability range is 5~15 %.

In these experiments, the flow rate of fuel is fixed to 1900 cm^3/s and the flow rate of oxidizer is adjusted for various equivalence ratios and oxygen fractions. The diameter of the circular fuel nozzle is 15.2 mm, the velocity is 10.4 m/s and the flow momentum is 0.0142 N. Three circular air nozzles of varying diameters are used (7.94, 15.9 and 31.8 mm). By changing the air nozzle diameter or the oxygen enrichment in the air streams, the experiments can be performed at various conditions of the oxidizer velocity (or flow momentum) and/or equivalence ratio. In this study, the condition of overall equivalence

ratio is in the range of $\Phi_{overall}$ = 0.8, 0.9, 1.0 and 1.1. By mixing oxygen with air, the oxygen fraction in the oxidizer jet is adjusted to $X_{O2;ox}$ =0.21, 0.30 and 0.40 for the oxidizer. The parametric conditions for measuring the temperature or the gas composition are listed in Table 5.1, where $\Phi_{overall}$ is overall equivalence ratio, $X_{O2;ox}$ oxygen fraction in the oxidizer, D_{ox} the diameter of the oxidizer nozzle, V_{ox} the exit velocity from each oxidizer nozzle, and J_{ox} the flow momentum of each oxidizer nozzle. In the measurement column, 'T' is for the temperature measurement, 'U' is for the UV emission intensity measurement, 'P' is the visual image taken, and 'G' is the gas sampling for gas composition analysis, respectively.

To ignite the furnace, the fuel stream is heated with a ceramic igniter. In the beginning stage, the color of flame is yellow and then shifts to blue, which indicates that the flame is unstable and has the potential to be extinguished. After the furnace wall is fully heated to the auto-ignition temperature of the fuel, the reaction transitions to the homogeneous combustion mode and becomes stable. After the stable conditions are achieved, the temperature and gas composition are measured. The coordinate used to locate the measurement point is defined in Figure 5.2. The Y-direction passes through the center of the oxidizer nozzle with the center of the fuel nozzle as the origin. The X-direction is rotated 45 degrees from the Y-direction. The measurement positions for temperature and gas sampling are the matrix made by X = 0, 75, 150, 230, 305 mm and Z = 220, 430, 640, 850, 1060 mm; and by Y = 0, 75, 150, 230, 280 mm and Z = 220, 430, 640, 850, 1060 mm, where X = 0 mm (or Y = 0 mm) is the location of the fuel nozzle and Y = 280 mm is the location of the oxidizer nozzle. The thermocouples are installed on the wall at Z = 220, 430, 640, 850, 1060 mm of X and Y direction (i.e. X = 420 mm, and Y = 420 mm).

In the homogeneous combustion mode, the fluctuation of temperature is minimal, so the temperature data is averaged over the test duration. The response of the gas analysis system is slow because of the length of the suction line connecting the sampling probe to the gas analyzers. The gas composition data is averaged after all the measurements converge to a stable value. In order to verify the stability of the reaction, UV emission from the reaction zone is measured and the visual appearance of the flame is also recorded. In the homogeneous combustion regime, it has been reported that conventional flame detectors can not work normally [8, 65]. OH radical (radiation bands of 281.1 nm

and 306.4 nm) associated with chemical reaction is the main source of UV emission in a normal flame. However, the concentration of the OH radical is significantly lower in homogenous combustion mode than in conventional flame [7, 65]. From this idea, the intensity of the UV emitted from the flame zone is considered as a standard measurement to evaluate the activation of homogenous combustion.

In order to measure the UV emission, Si photodiode (Hamamatsu S1226-5BQ) and UV filter (HOYA U-340) are used. Radiation emission from the reaction zone passes through the fused quartz plate (GE Type 124, 1/8 in thickness) of the window beneath the furnace to the UV filter. The transmittance of the quartz plate and the UV filter, and the sensitivity of the photodiode are summarized in Figure 5.3. Signals from all the thermocouples, gas analyzers and UV photodiode are collected by a data acquisition device about every 0.5 to 1 sec.

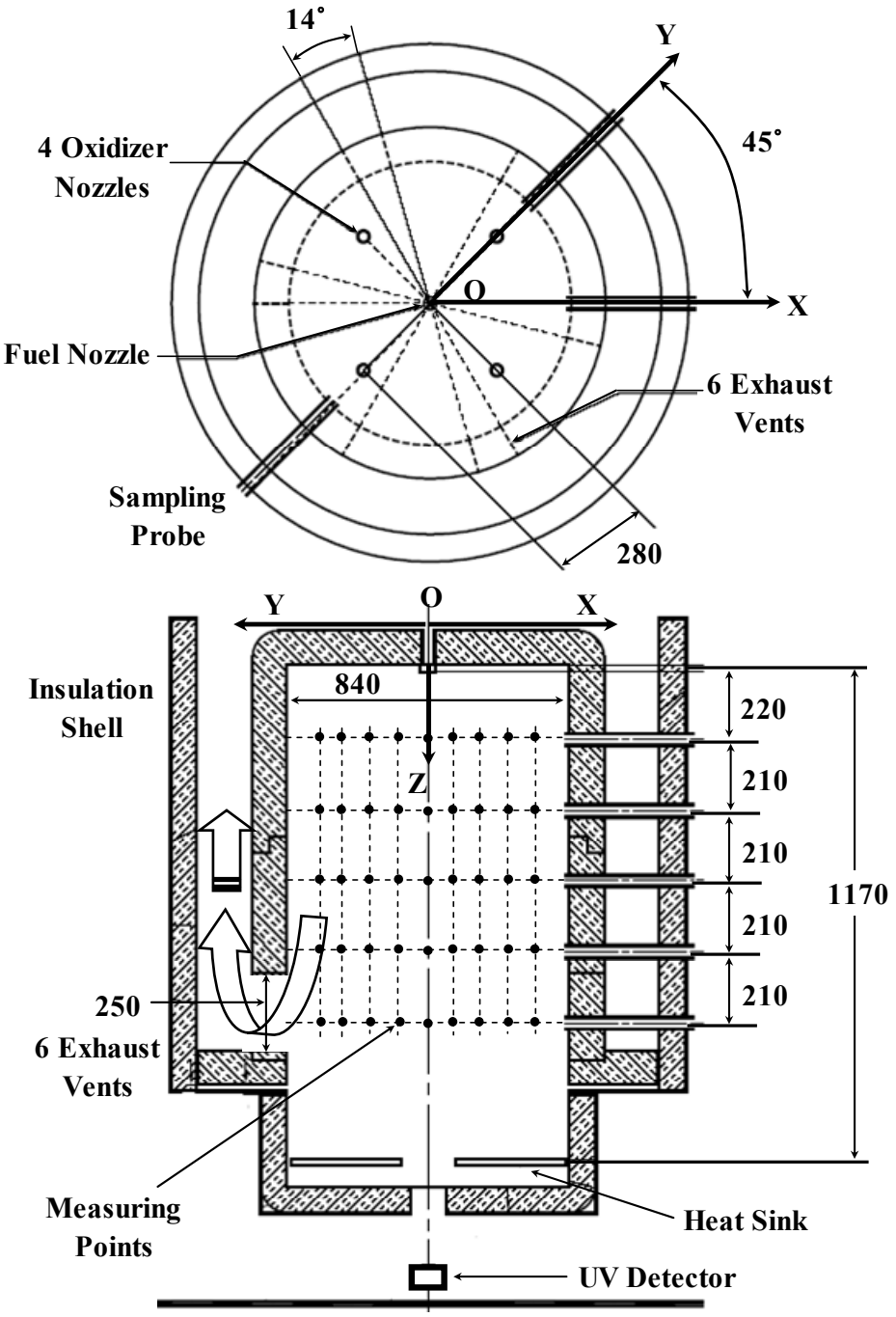
14˚
Y
45˚
4 Oxidizer
Nozzles
O
X
Fuel Nozzle
6 Exhaust
Vents
Sampling
Probe
280
Y
O
X
Insulation
Shell
840
220
210
210
210
210
Z
1170
250
6 Exhaust
Vents
Measuring
Points
Heat Sink
UV Detector

(a)

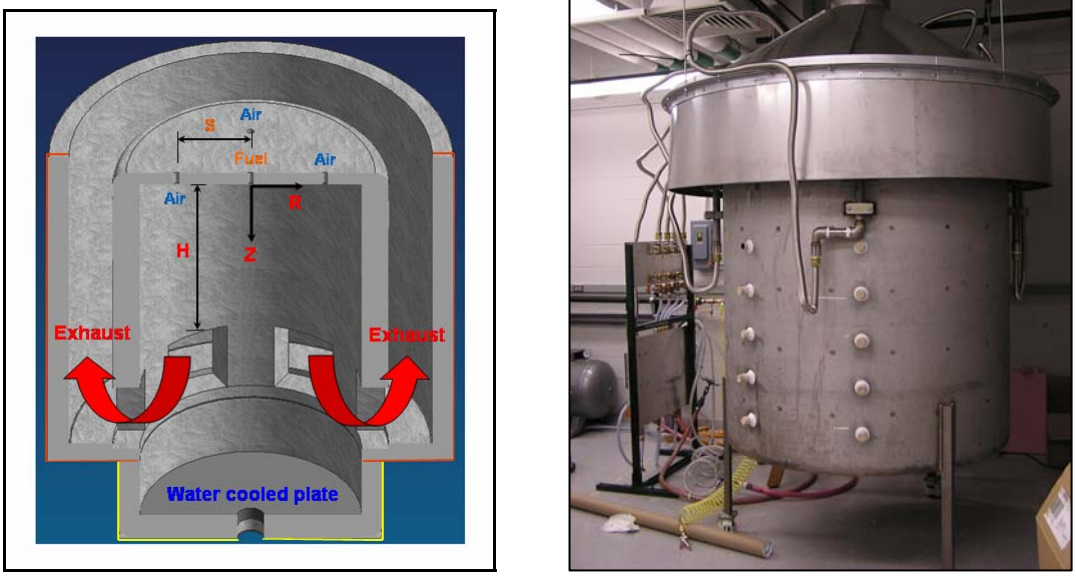

(b)

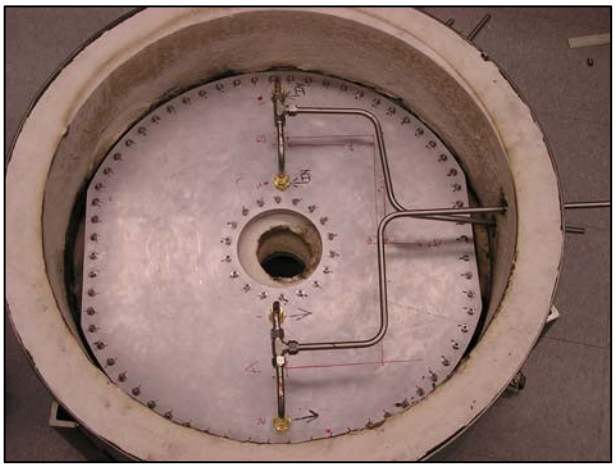

(c)

Figure 5.1: (a) The definition of coordinates and data measuring points and the structure of (b) furnace interior and exterior, and (c) heat sink

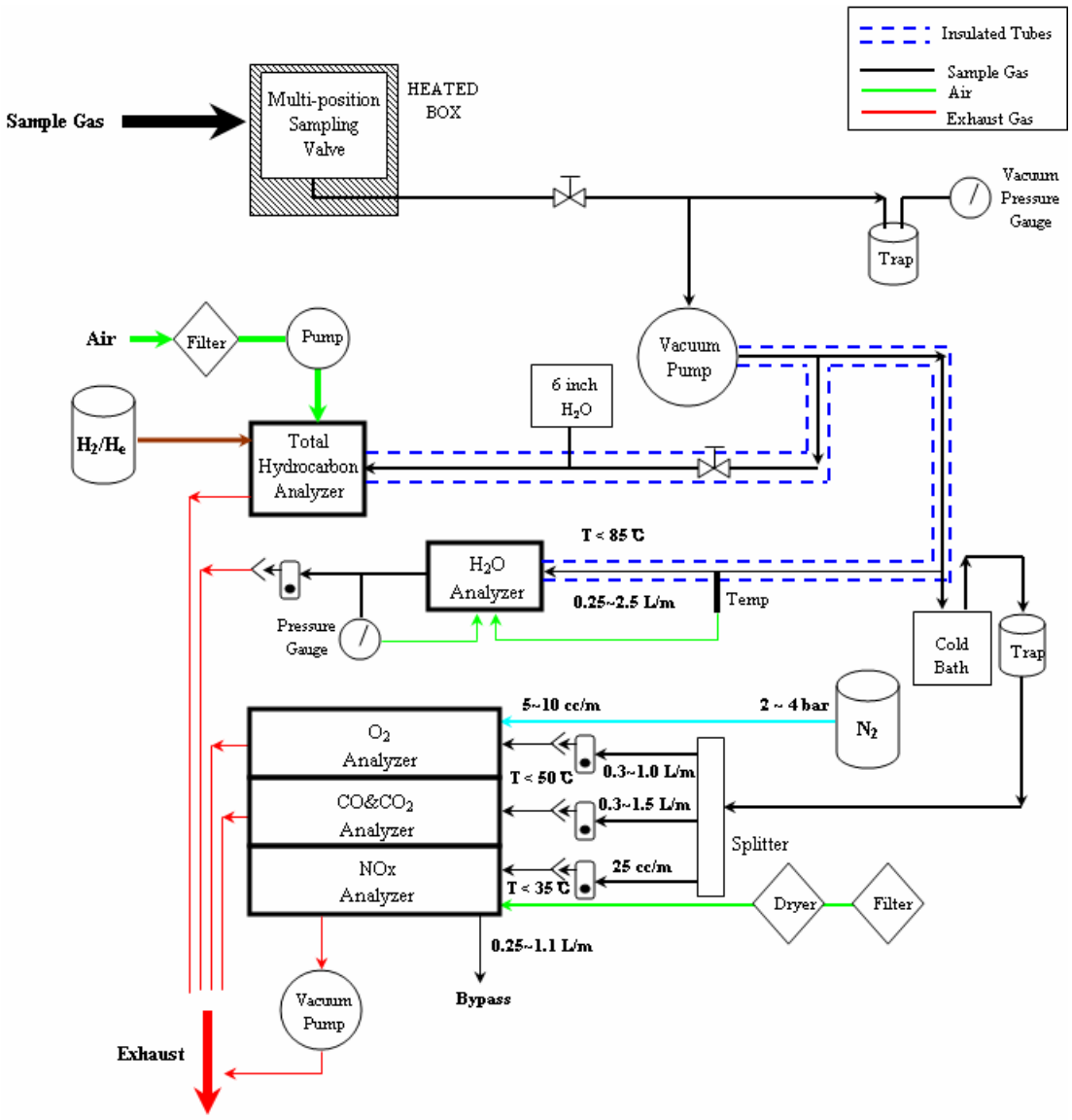

Figure 5.2: Schematic diagram of the gas analysis

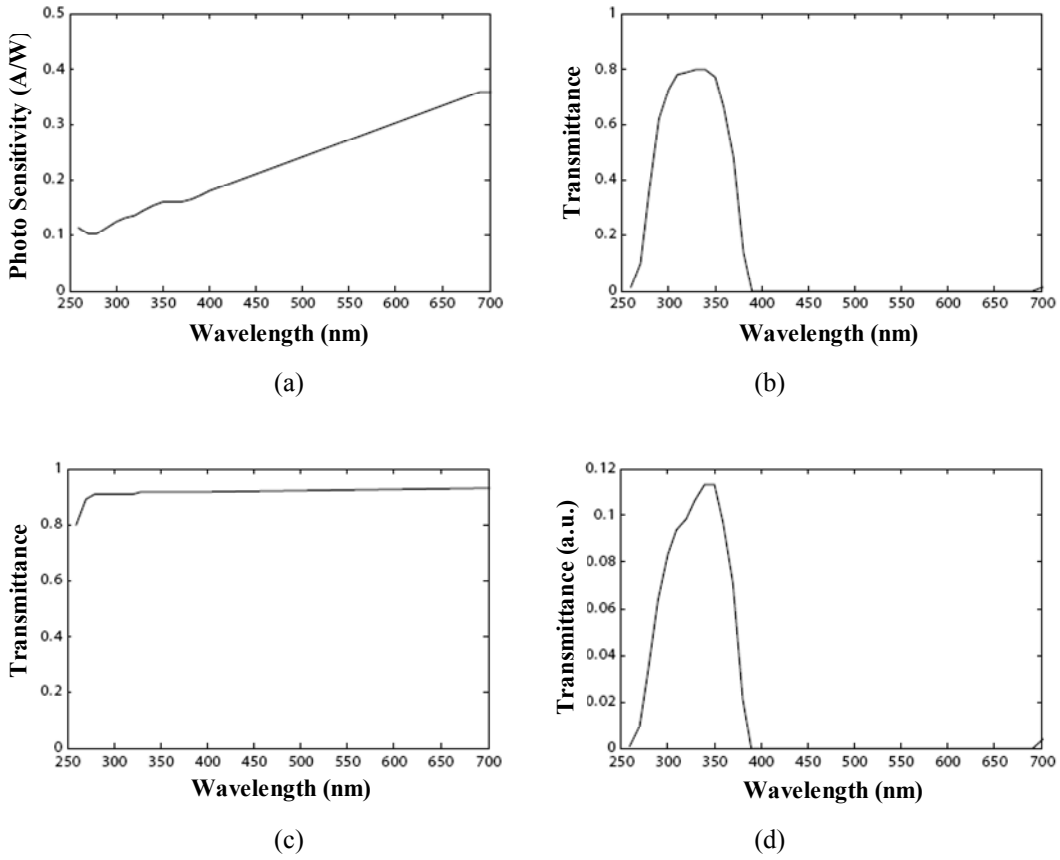

Figure 5.3: (a) Spectral sensitivity of the photodiode (Hamamatsu S1226-5BQ), (b) spectral transmittance of UV filter (HOYA U-340) (c) spectral transmittance of quartz plate (GE Type 124) and (d) total transmittance.

Case No.	d_{ox} (mm)	$X_{O2,ox}$	$\Phi_{overall}$	V_{ox} (m/s)	J_{ox} (N)	Measurement
D1O30E090	7.94	0.30	0.90	71.04	2.92E-01	T, U, P
D1O30E101	7.94	0.30	1.01	62.83	2.29 E-01	T, U, P
D1O30E100	7.94	0.30	1.00	63.31	2.32 E-01	T, G, U
D1O30E109	7.94	0.30	1.09	57.81	1.94 E-01	T, U, P
D1O31E110	7.94	0.31	1.10	56.28	1.84 E-01	T, G, U
D1O40E089	7.94	0.40	0.89	53.61	1.69 E-01	T, U, P
D1O41E102	7.94	0.41	1.02	45.93	1.24 E-01	T, U, P
D1O40E109	7.94	0.40	1.09	43.63	1.12 E-01	T, U, P
D2O21E081	15.9	0.21	0.81	28.14	1.81 E-01	T, U, P
D2O21E090	15.9	0.21	0.90	25.15	1.45 E-01	T, U, P
D2O21E100	15.9	0.21	1.00	22.78	1.19 E-01	T, U, P
D2O21E103	15.9	0.21	1.03	22.03	1.11 E-01	T, G, U
D2O21E111	15.9	0.21	1.11	20.48	9.60 E-02	T, U, P
D2O29E091	15.9	0.29	0.91	17.98	7.49 E-02	T, U, P
D2O30E091	15.9	0.30	0.91	17.58	7.16 E-02	T, G, U
D2O30E102	15.9	0.30	1.02	15.58	5.63 E-02	T, U, P
D2O30E101	15.9	0.30	1.01	15.67	5.69 E-02	T, G, U
D2O30E110	15.9	0.30	1.10	14.33	4.76 E-02	T, G, U
D2O31E110	15.9	0.31	1.10	14.11	4.62 E-02	T, U, P
D2O40E090	15.9	0.40	0.90	13.36	4.19 E-02	T, U, P
D2O41E103	15.9	0.41	1.03	11.45	3.08 E-02	T, U, P
D2O41E102	15.9	0.41	1.02	11.46	3.09 E-02	T, G, U
D2O40E111	15.9	0.40	1.11	10.76	2.72 E-02	T, U, P
D3O21E079	31.8	0.21	0.79	7.16	4.69 E-02	T, U, P
D3O21E090	31.8	0.21	0.90	6.29	3.62 E-02	T, U, P
D3O21E099	31.8	0.21	0.99	5.72	3.00 E-02	T, U, P
D3O21E111	31.8	0.21	1.11	5.12	2.40 E-02	T, U, P
D3O30E090	31.8	0.30	0.90	4.52	1.89 E-02	T, U, P
D3O29E099	31.8	0.29	0.99	4.09	1.55 E-02	T, G, U
D3O30E098	31.8	0.30	0.98	4.12	1.57 E-02	T, U, P
D3O31E110	31.8	0.31	1.10	3.50	1.13 E-02	T, G, U
D3O31E113	31.8	0.31	1.13	3.39	1.06 E-02	T, U, P
D3O39E090	31.8	0.39	0.90	3.39	1.08 E-02	T, U, P
D3O39E102	31.8	0.39	1.02	3.02	8.53 E-03	T, U, P
D3O41E111	31.8	0.41	1.11	2.65	6.63 E-03	T, U, P

Table 5.1: Experiment test conditions

CHAPTER 6

Experimental results and discussion of reacting flows

6.1. Overall characteristics of combustion

6.1.1. UV emissions and visual images

In general, it has been known that a bright flame with large fluctuation can be easily observed in the non-homogeneous combustion (conventional combustion) which emits a large amount of UV emission from OH radicals and others that are abundant in a flame front. On the other hand, the glowing reaction zone without visible flame and low UV emission with small fluctuation are characterized as homogeneous combustion. Therefore, the visible flame image and UV emission intensity can be important criterions to judge for homogeneous combustion condition.

Figure 6.1 shows the visible images of combustion and its corresponding UV emission intensities in the range of injection oxygen concentration, $X_{O2;ox}$ = 0.21 ~ 0.40 and overall equivalence ratio, $\Phi_{overall}$ = 0.9 ~ 1.1 for oxidizer jet diameter, d_{ox} =7.94, 15.9 and 31.8 mm. The homogeneous combustion modes are marked by the solid line, and transient modes between the homogeneous and non-homogeneous combustion conditions are indicated by dashed line in Figure 6.1. It is observed from Figure 6.1 that the homogeneous combustion mode shows quite smaller intensities of UV emission and fluctuations than those of the non-homogeneous combustion modes. The intensities of UV emission for homogeneous combustion modes are in the range of 0.016 ~ 0.054 (a.u.) with standard deviation 1.8 ~ 3.9 % of the mean intensity, while the intensities of UV emission for non-homogeneous combustion mode are in the range of 0.07 ~ 0.59 (a.u.) with standard deviation 17 ~ 36 % of the mean intensity.

Based on the visual images and UV emissions, the homogeneous combustion condition

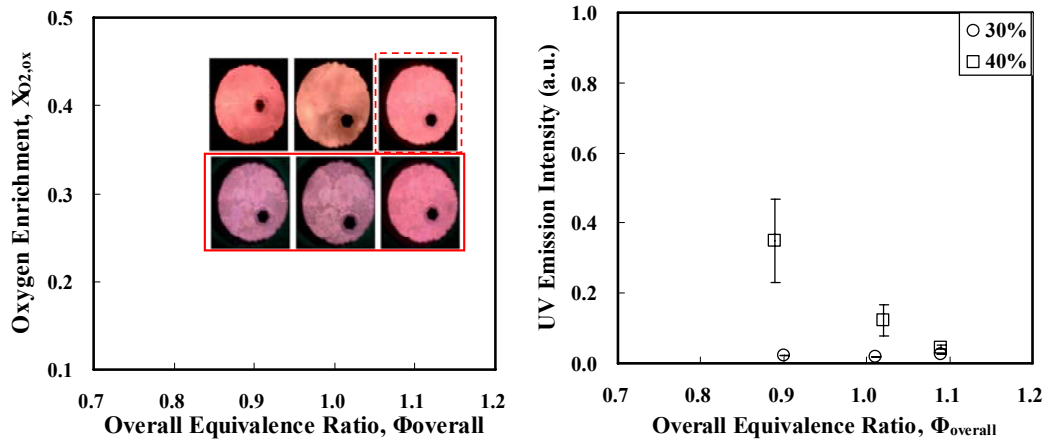

(a)

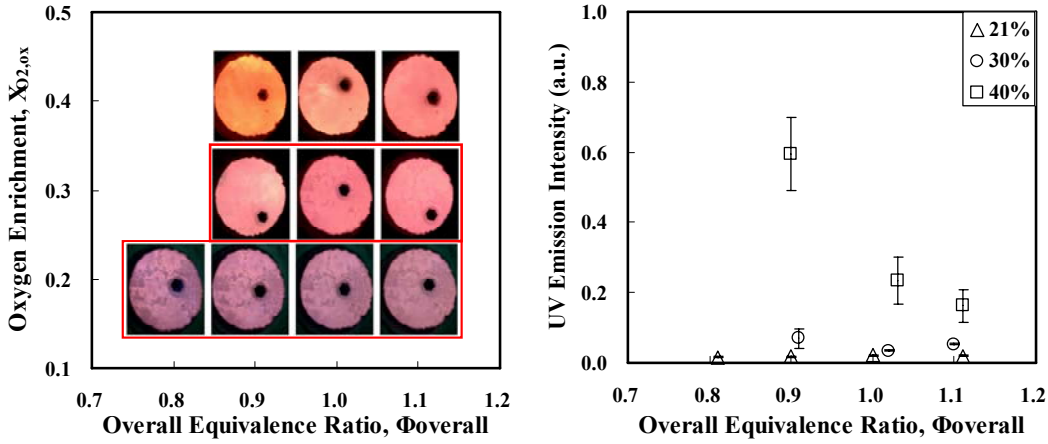

(b)

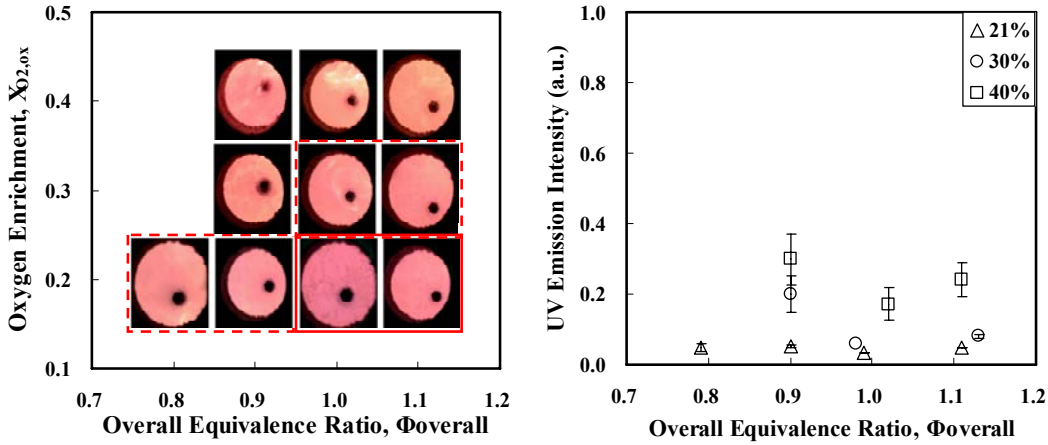

(c)

Figure 6.1: Visual images and UV emission intensities for (a) d_{ox} = 7.94 mm, (b) d_{ox} = 15.9 mm and (c)) d_{ox} = 31.8 mm

for normal air injection in the oxidizer jets, $X_{O2,ox}$ = 0.21, is obtained in the range of the overall equivalence ratio, $\Phi_{overall}$ = 0.8 ~ 1.1 with d_{ox} = 15.9 mm, and $\Phi_{overall}$ = 1.0 ~ 1.1 with d_{ox} = 31.8 mm. It is noted that a stable reaction is not achieved for d_{ox} = 7.94 mm with $X_{O2,ox}$ = 0.21 because the oxidizer jet momentum is so high that the flame easily blows out. It is believed that the furnace temperature falls lower than the auto-ignition temperature for these cases. For oxygen enrichment in the oxidizer jets, $X_{O2,ox}$ = 0.30, the homogeneous combustion condition is observed in the range of the overall equivalence ratio, $\Phi_{overall}$ = 0.9 ~ 1.1 with d_{ox} = 7.94 mm, and $\Phi_{overall}$ = 1.0 ~ 1.1 with d_{ox} = 15.9 mm. However, the stable homogeneous combustion condition for $X_{O2,ox}$ = 0.40, could not be achieved within the range of experimental conditions covered in this work. Only transient condition can be obtained for $X_{O2,ox}$ = 0.40, which might be thought that dilution by product gases in the oxidizer jets is not enough to get the homogeneous combustion condition due to lack of sufficient momentum of the oxidizer jets. Thus, It would be recommended that the oxidizer jet diameter should be smaller than 7.94 mm to achieve the stable homogeneous combustion for $X_{O2,ox}$ = 0.40.

It might be concluded that it is easier to obtain the homogeneous combustion condition for smaller diameter of the oxidizer jet, hence higher momentum of the oxidizer jet with same oxygen enrichment and the overall equivalence ratio. Thus, in case of oxygen enrichment combustion, the oxidizer jet with smaller diameter needs to be used to obtain the homogeneous combustion condition for enhancing dilution of the jets by recirculation of product gases.

6.1.2. Temperature profiles

The centerline temperatures of the fuel and oxidizer jets along with the axial distance for homogeneous combustion condition are shown in Figure 6.2. It is seen that the centerline temperature increases quickly at quite upstream region, Z/H=0.29, even without preheating, and shows flat profiles from middle range to bottom of the furnace. This supports that there is strong recirculation of product gases in the furnace with the aid of buoyancy effects and uniformity of combustion. The centerline temperatures of fuel jet are quite similar for all cases, while oxidizer jet centerline temperatures become flat faster with smaller oxidizer jet diameter. For smallest oxidizer jet diameter, d_{ox}=7.94 mm,

the centerline temperature of the oxidizer jet shows flat profile quickly from quite upstream region even at Z/H=0.15, whereas the increase of temperature is slower for d_{ox}=31.8 mm than other oxidizer jet diameters. This might be attributed the fact that the higher momentum of the oxidizer jet could enhance the jet entrainment and mixing intensity, and oxygen concentration in re-circulated flue gas also increases. Therefore, the reaction rates increase near the oxidizer jet exit region, as a result, the temperature increases [66].

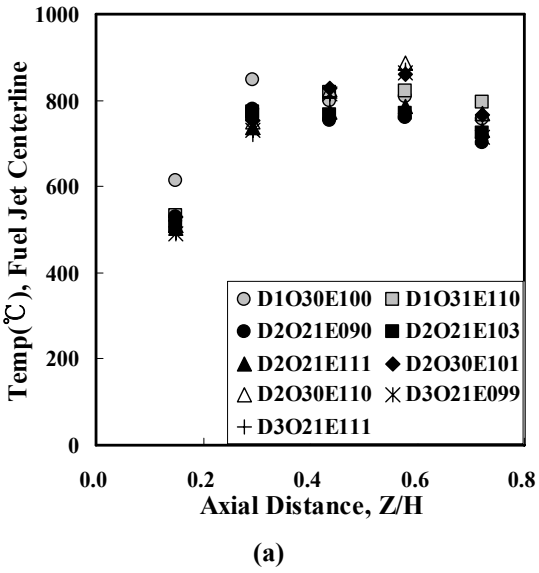

(a)

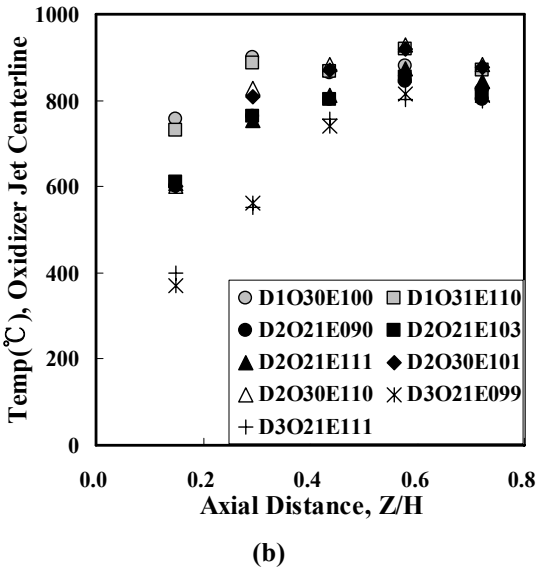

(b)

Figure 6.2: The centerline temperature of the (a) fuel and (b) oxidizer jet for homogeneous combustion condition.

Figure 6.3 shows the radial temperature profiles for homogeneous combustion condition. It can be seen from Figure 6.3 that the overall profiles of radial temperature are quite uniform and flat, which means that the reaction occurs widely and uniformly. It is also observed that the cases of d_{ox}=31.8 mm show less uniformity of temperature at upstream region of the furnace because of low momentum of the oxidizer jet and hence less mixing intensity. Another observation is that the temperature is high at upstream region near the jet exit, and then becomes lower along with the axial distance. It might be thought that the jets are less sufficiently diluted by product gases near the region of jet exit, thus the reaction occurs with high fuel and oxygen concentrations. However, the dilution of the jets increases to lower the reaction rate along with the axial distance, and hence the temperature decreases. It may be concluded that the sufficient dilution of the jets to lower the reaction rate is essential to obtain the homogeneous combustion mode, and uniformity of reaction can be enhanced by strong recirculation of product gases. As a result, the quite uniform and flat temperature profiles can be seen in homogeneous combustion mode without hot spots in temperature.

6.1.3. Gas composition profiles

Figure 6.4 shows the centerline THC and oxygen concentrations in the fuel and oxidizer jets, respectively. It is observed that the THC decreases very sharply along the axial distance due to dilution by product gases and combustion while the oxygen concentration in the oxidizer jet also decreases fast up to middle region of the furnace even with high oxygen injection cases. However, oxygen concentration in the oxidizer jet remains nearly constant at the lower region of the furnace. It is also observed that the radial oxygen concentration remains almost constant after Z/H=0.44 for some cases as shown in Figure 6.4. This can be attributed the fact that the oxidizer jet momentum is always higher than that of the fuel jet, thus the oxidizer jet can easily penetrate into the region of the fuel jet. In addition, the recirculation of the jet flow occurs strongly after some axial distance from the jet exit due to the confinement effect which makes the flow toward the fuel jet. As a result, the oxygen concentration can remain nearly constant in the lower part of the furnace. Another reason may be that the flow of the oxidizer jet bounces from the bottom of the furnace, and can reach up to middle range of the furnace due to high momentum of

the oxidizer jet for small oxidizer jet diameter or lean cases.

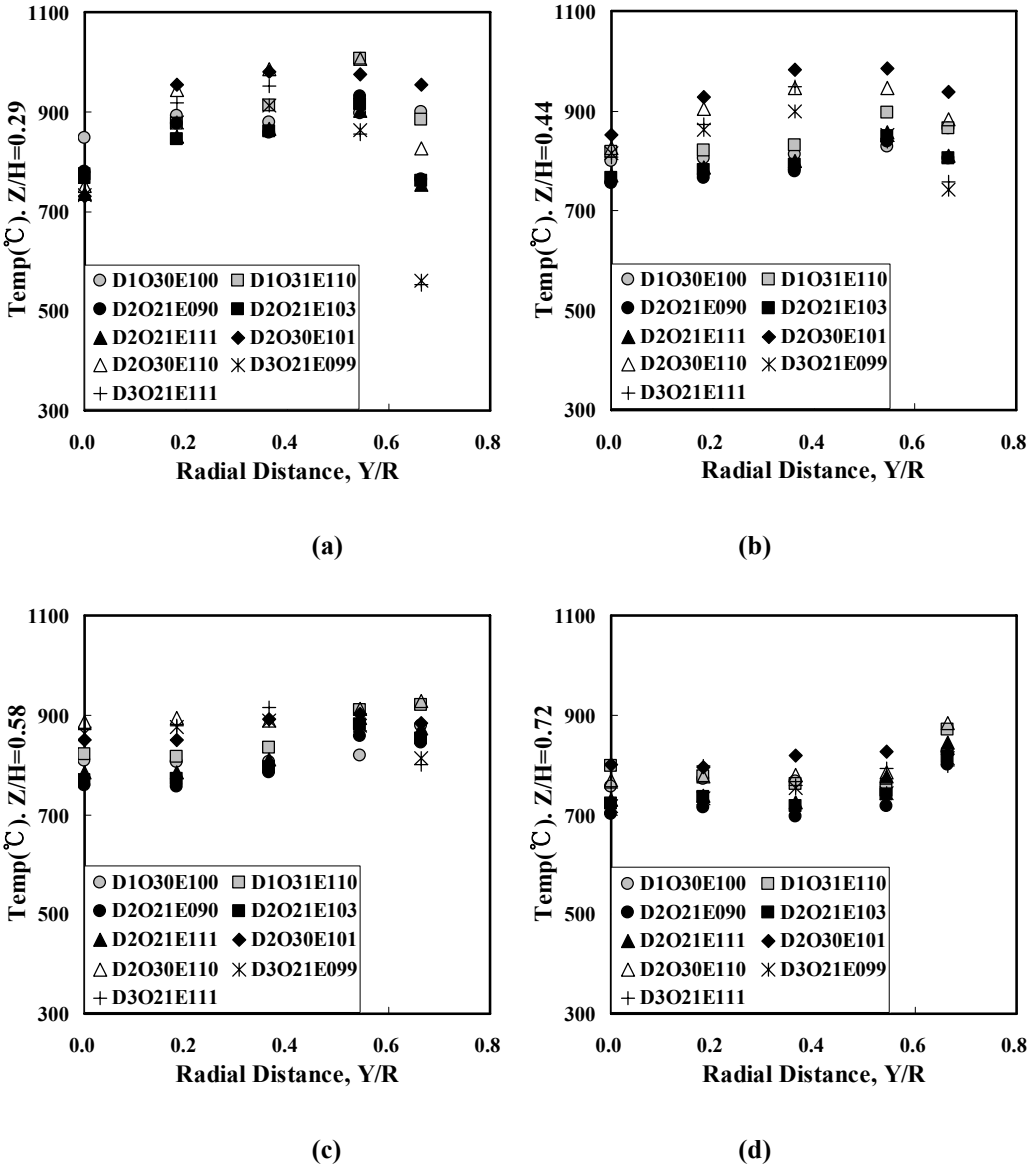

Figure 6.3: The radial temperature profiles for the homogeneous combustion condition at (a) *Z/H*=0.29 (b) *Z/H*=0.44 (c) *Z/H*=0.58 (d) *Z/H*=0.72

The radial THC and oxygen concentration at different axial distance are shown in Figure 6.6 and 7, respectively. It can be seen that the THC concentration decays slowly, and the oxygen concentration spreads less laterally with lower decay rate of oxygen concentration in the centerline of oxidizer jet decays for d_{ox}=31.8 mm with $X_{O2;ox}$=0.30. This might be thought that the oxidizer jet momentum decreases with increase of

diameter and injection oxygen concentration, thus the penetration of the oxidizer jet into the region of fuel jet flow becomes weak and hence less intensity of recirculation from the oxidizer jet. As a result, the THC concentration decays slowly and oxygen concentration spreads less in lateral direction. It is noted that the THC concentration is not detected at *Z/H*=0.72 for all cases as shown in Figure 6.6 (d).

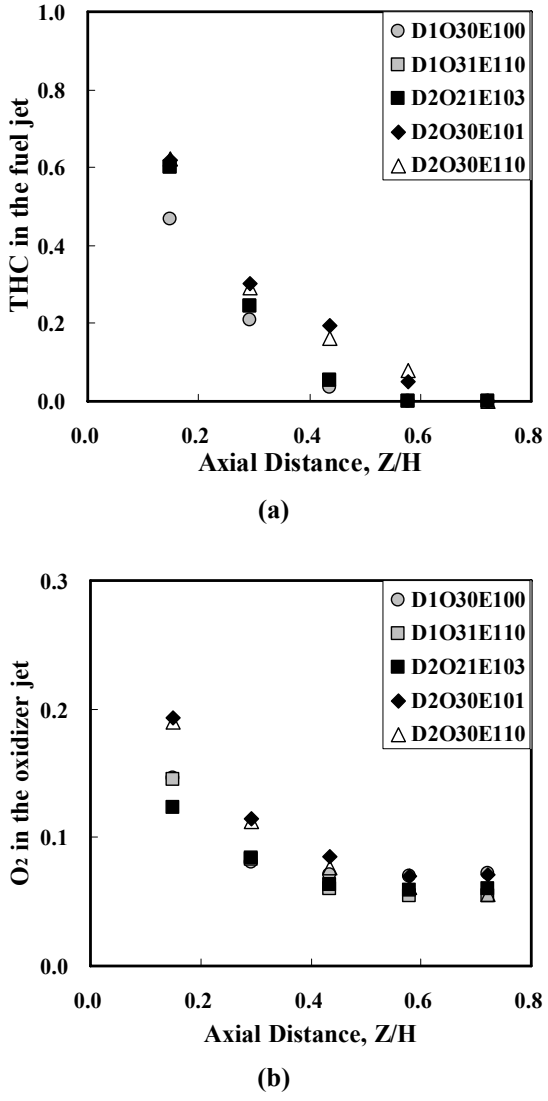

Figure 6.4: The centerline of (a) THC in the fuel jet and (b) oxygen concentration in the oxidizer jet for homogeneous combustion condition.

Figure 6.5 shows the carbon dioxide concentrations in the centerline of fuel and oxidizer jets for homogeneous combustion condition. It is observed that the carbon dioxide

concentration in the fuel and oxidizer jets increases with a certain slope along with the axial distance and then remains nearly constant. This means that recirculation of product gases occurs very well near upstream region, and quite uniform reaction is achieved in the latter region of the furnace. In addition, the radial profiles of carbon dioxide are really flat from the middle domain of the furnace as shown in Figure 6.8, which is the another evidence indicating the uniform and wide range of reaction in the furnace. It is noted that the cases of $X_{O2;ox}$=0.21 shows less carbon dioxide concentration because of low injection oxygen concentration in the oxidizer jet.

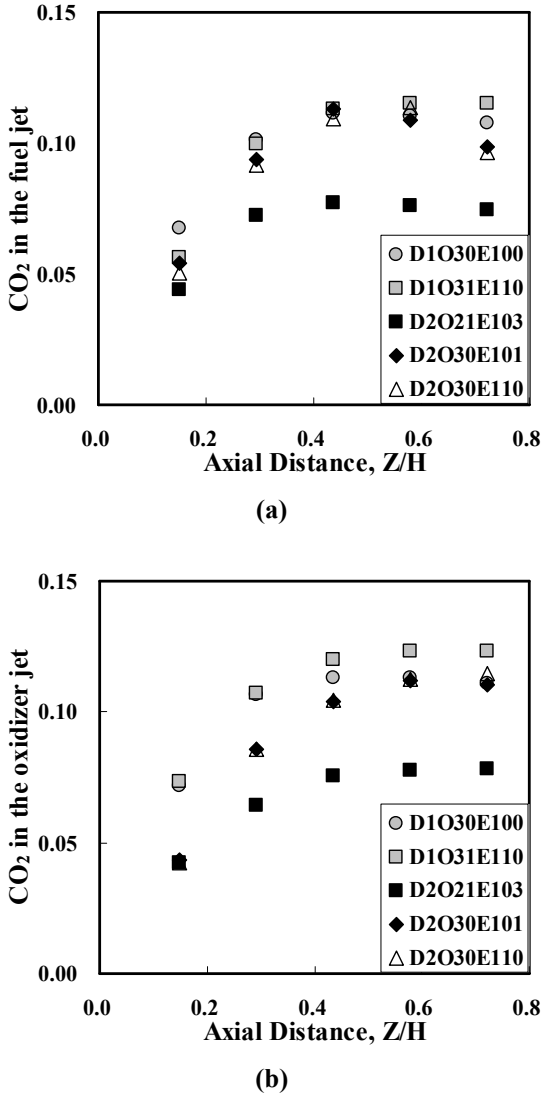

Figure 6.5: The centerline carbon dioxide concentration of the (a) fuel and (b) oxidizer jet for homogeneous combustion condition.

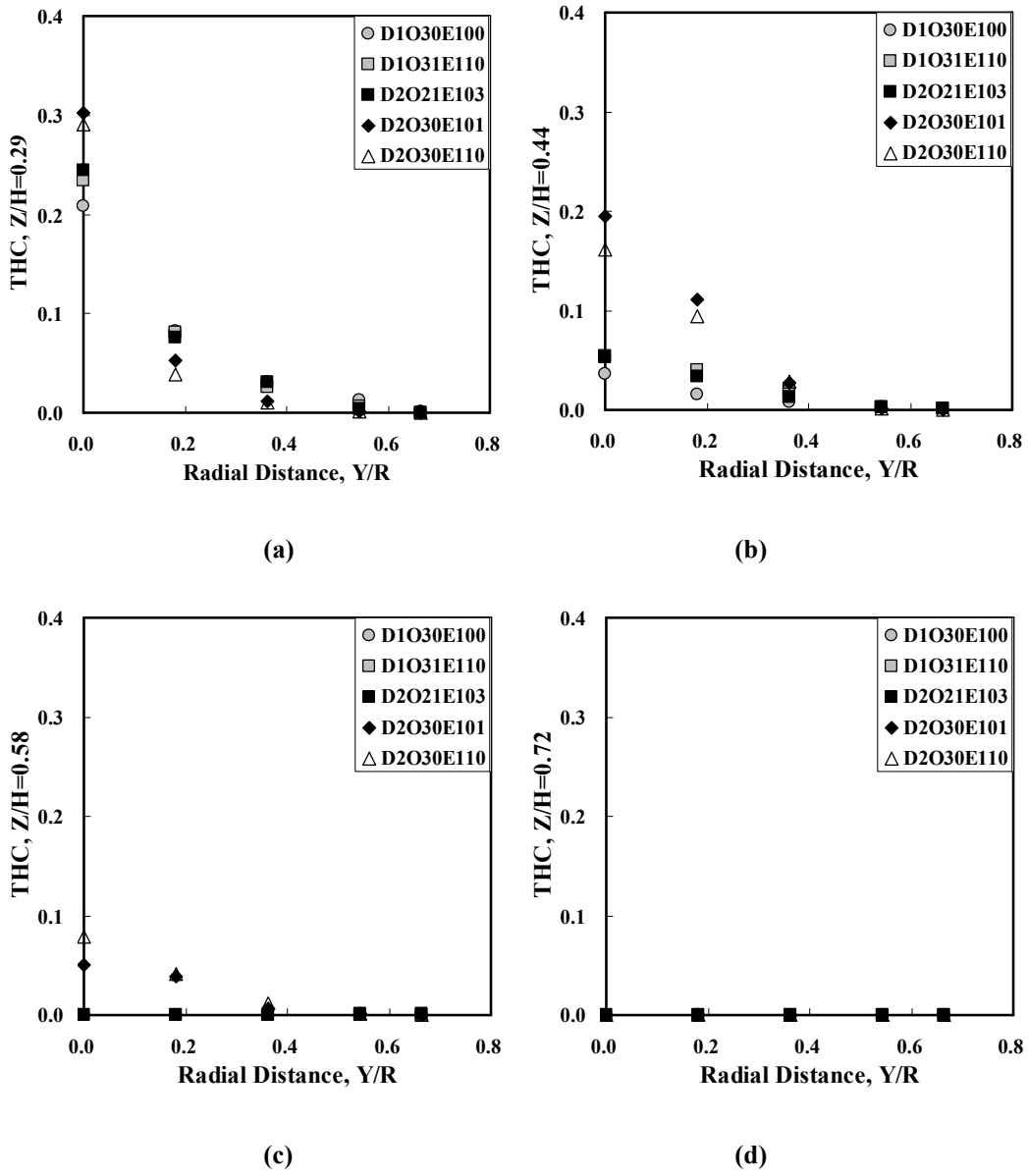

Figure 6.6: The radial THC concentration profiles for the homogeneous combustion condition at (a) *Z/H*=0.29 (b) *Z/H*=0.44 (c) *Z/H*=0.58 (d) *Z/H*=0.72

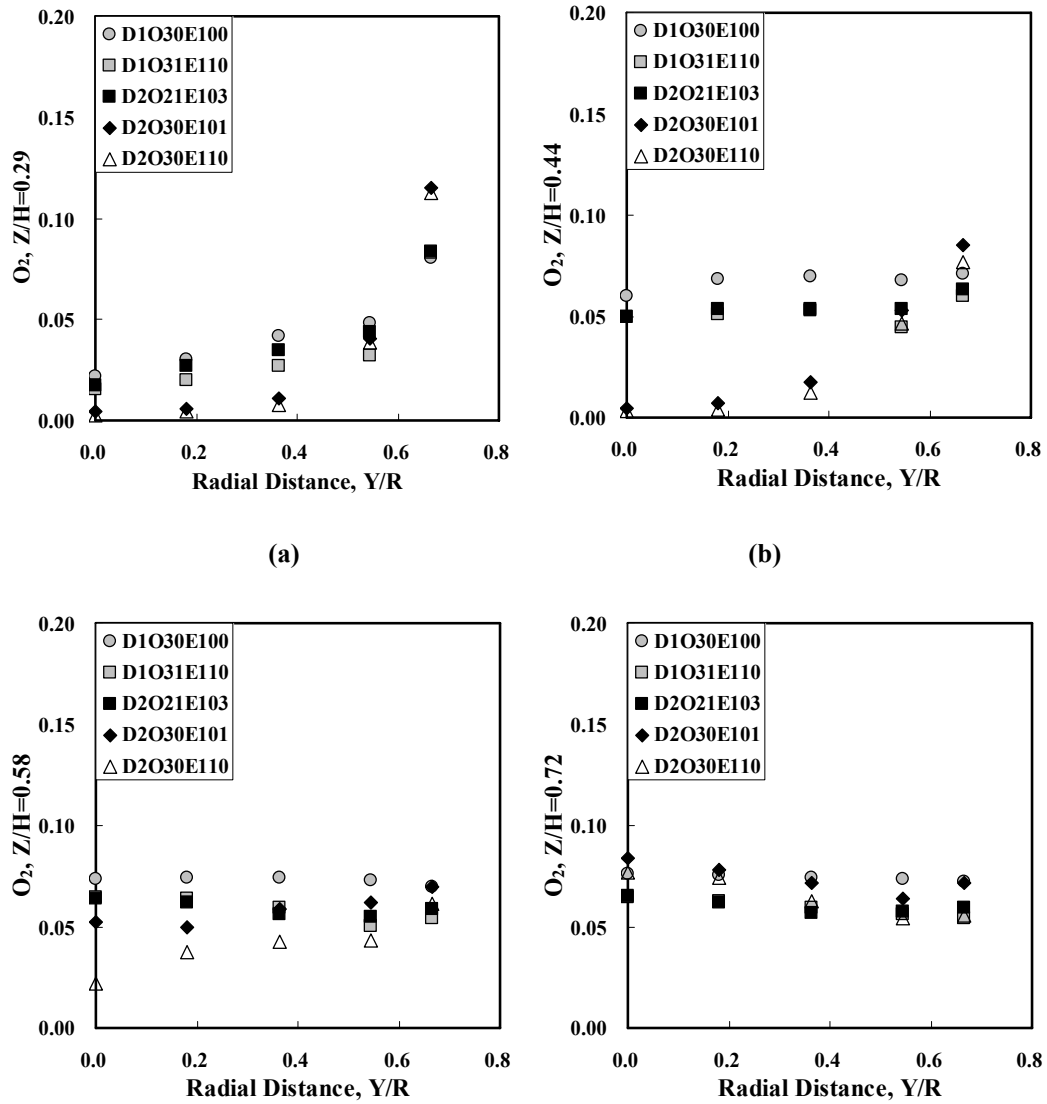

Figure 6.7: The radial oxygen concentration profiles for the homogeneous combustion condition at (a) *Z/H*=0.29 (b) *Z/H*=0.44 (c) *Z/H*=0.58 (d) *Z/H*=0.72

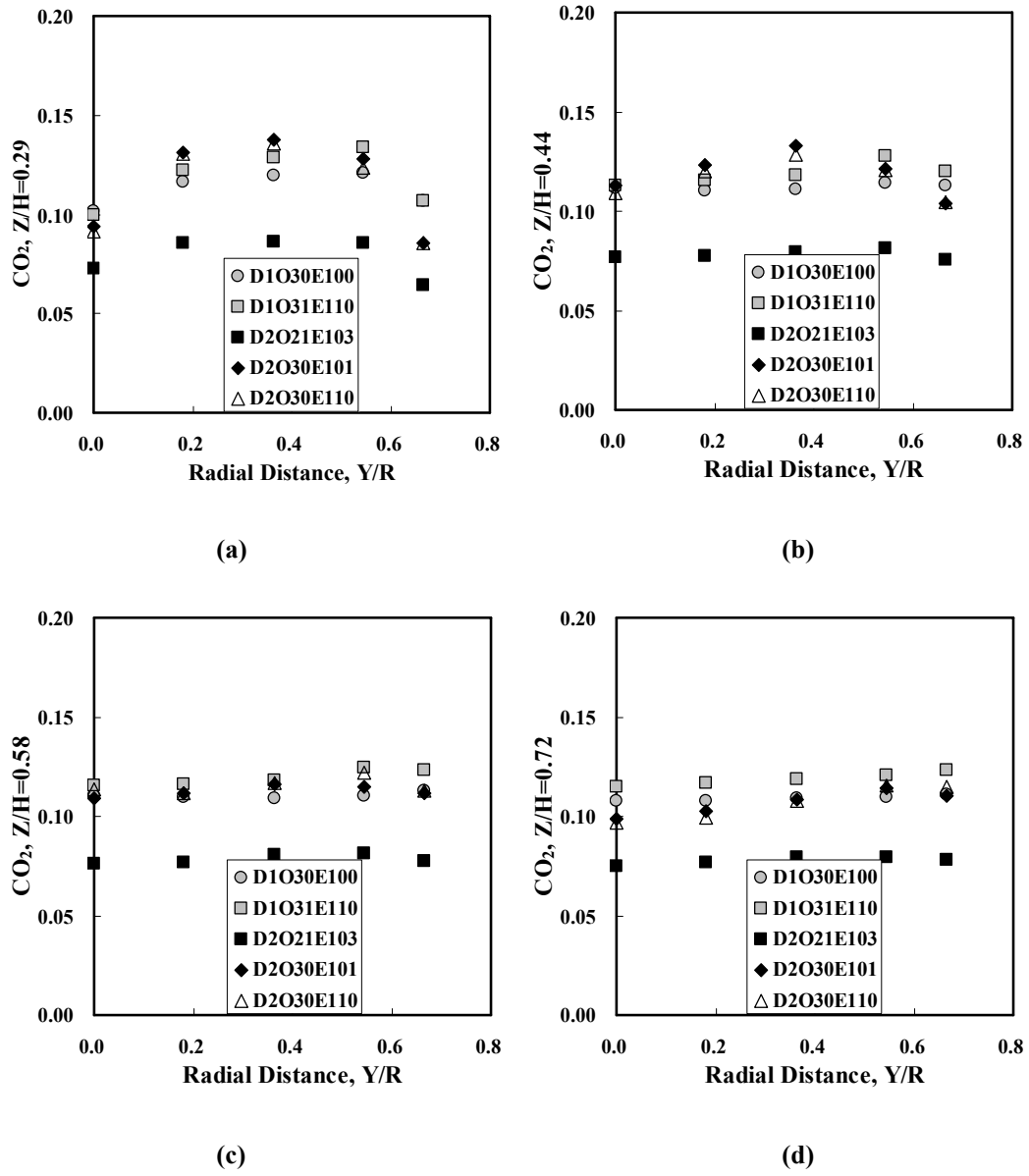

Figure 6.8: The radial carbon dioxide concentration profiles for the homogeneous combustion condition at (a) *Z/H*=0.29 (b) *Z/H*=0.44 (c) *Z/H*=0.58 (d) *Z/H*=0.72

6.1.4. Pollutant emissions

The efficient methods to reduce NOx emission are based on technologies to reduce either peak flame temperature or the residence time and oxygen concentration in high temperature zones [17, 18]. The homogeneous combustion can achieve a large reduction of NOx emissions by avoiding peaks of operating temperature and by reducing the concentration in oxygen through the high internal recirculation. The high internal recirculation leads to a significant dilution of the oxidizer by the combustion products before the reaction. In conventional burner and furnace systems, such pre-heating of the air leads to very high local temperatures in the flame, and therefore to high NOx emissions. The temperature profile induced by homogeneous combustion is relatively flat and uniform. The emissions of nitrogen oxides strongly influenced by the local temperature in the flame are thus very greatly reduced and the homogeneity of the temperature in the furnace is improved. As a result of the reduction of temperature peaks in the flame, the mean temperature level of the furnace zone can be increased, without leading to local hot spots in the vicinity of the burners [6, 8].

Figure 6.9 shows the radial NO emission profiles at Z/H=0.72, where is close to exhaust vents, for the homogeneous combustion condition. It is clearly seen from Figure 6.9 that quite low NO emission with one digit level is achieved for all homogeneous combustion conditions in this experimental work. The main reason for this excellent result stems from the well known circumstance, that *thermal NO* formation is extremely sensitive to flame temperature peaks and these are now cut away in homogeneous combustion mode. In addition, the other NO formation mechanisms are positively modified, as prompt NO depends on radicals that are abundant in a flame front, however, much reduced in homogeneous combustion mode [7].

For various performing conditions, the NO emissions in the exhaust gas are summarized in Figure 6.10. All of the NO concentration data are converted to 3 % oxygen on a dry basis. The NO emission data in the current experiments are compared with the previous researches of the homogeneous combustion burners in Figure 6.10. The data of the current work are located in low furnace temperature region due to the no air-preheat.

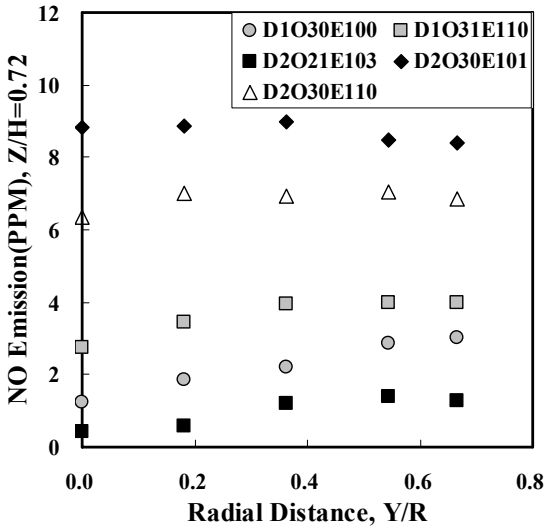

Figure 6.9: The radial NO emission profiles for the homogeneous combustion condition at *Z/H*=0.72

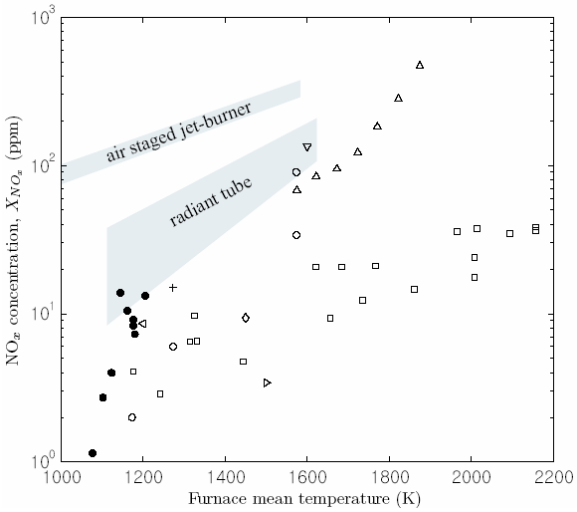

Figure 6.10: NO*x* emission data of the current work compared with previous results from literature. NO*x* is corrected to 3 % oxygen on a dry basis. NO data are used in the current work, and NO*x* data are used in the others. The current works ●, and the compared data with the fuel used: natural gas ([51] ○, [67] □, [68] △, [24] ▽), and methane ([69] ◁, [70] ▷, [31] ◊, [30] +). The representative working domains for the air staged jet-burner and the radiant tube were adopted from [51].

The radial carbon monoxide profiles at different axial distance for homogeneous combustion condition are shown in Figure 6.11. It is observed that the CO concentration is high at the region of the fuel jet and interface between the fuel and oxidizer jets. The high CO concentration at the region of the fuel jet is related to overly rich equivalence condition, as expected. On the other hand, less mixing with sufficient oxidizer or insufficient time for complete combustion due to high momentum of the jets is responsible for high CO concentration at the interface region between the fuel and oxidizer jets. It is also found that high CO concentration region moves with the high temperature region, and decreases after some axial distance. This might be thought that the reaction occurs under the condition that the jets are less sufficiently diluted by product gases at upstream region, whereas the dilution of the jets increases at further downstream region because of large scale of recirculation of the flow and hence the production of CO decreases.

The cases of d_{ox}=31.8 mm with $X_{O2;ox}$=0.30 show higher CO concentration than other cases, which is the same trend as the THC concentration profiles. It might be thought that the oxidizer jet momentum decreases with increase of diameter and injection oxygen concentration, thus the dilution of the jets becomes weak and reaction occurs with high fuel and oxygen concentration.

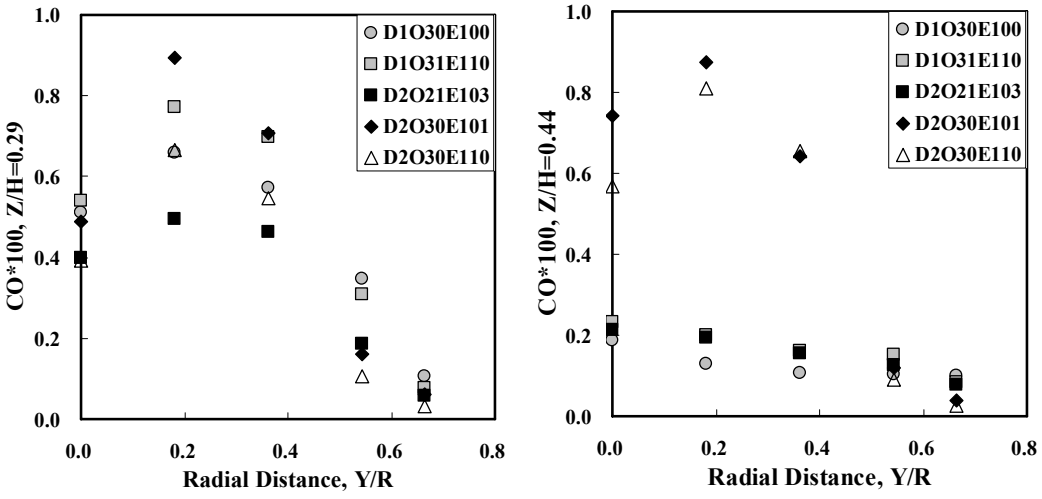

(a) (b)

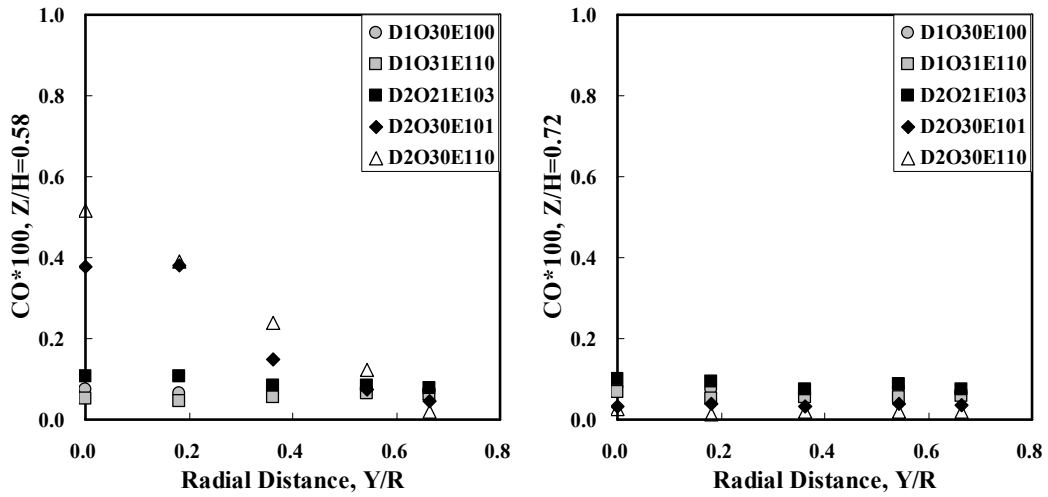

Figure 6.11: The radial carbon monoxide concentration profiles for the homogeneous combustion condition at (a) *Z/H*=0.29 (b) *Z/H*=0.44 (c) *Z/H*=0.58 (d) *Z/H*=0.72

6.2. The effects of Control parameters

In this section, the effects of the experimental control parameters for homogeneous combustion are presented. For more detailed analysis, extensive experimental studies on the effects of the oxidizer jet diameter, inlet oxygen concentration, and overall equivalence are performed in terms of temperature and gas compositions.

6.2.1. The effect of oxidizer jet diameter

The jet momentum plays a key role in achieving the homogeneous combustion condition as investigated in previous section. The most direct way to change the jet momentum is to change the size of the jet diameter. For this purpose, experimental studies are performed on three different sizes of the oxidizer jet diameter, d_{ox}=7.94, 15.9 and 31.8 mm, with same overall equivalence ratio, $\Phi_{overall}$ =1.0, and inlet oxygen concentration in the oxidizer jet, $X_{O2,ox}$ =0.30, whereas the diameter and flow rate of the fuel jet is kept same in this study to avoid the complexity. The properties of three cases are summarized in Table 6.1.

Case No.	d_{ox} (mm)	$X_{O2,ox}$	$\Phi_{overall}$	V_{ox} (m/s)	J_{ox} (N)	Mode.
D1O30E100	7.94	0.30	1.00	63.31	2.32 E-01	**H**
D2O30E101	15.9	0.30	1.01	15.67	5.69 E-02	**H**
D3O29E099	31.8	0.29	0.99	4.09	1.55 E-02	**T**

Table 6.1: The properties of three sizes of the oxidizer jet diameter.

6.2.1.1. Temperature

Jet Centerline Temperature

Figure 6.12 shows the centerline temperature of the fuel and oxidizer jets for different oxidizer jet diameters. It is observed that the centerline temperatures of the fuel and oxidizer jet increase faster with smaller oxidizer jet diameter. This trend is especially clearly shown in the oxidizer jet centerline. It might be attributed the fact that the momentum of oxidizer jet increases with smaller diameter, thus entrainment of product gases by the jets is enhanced. As a result, the rise of the centerline temperature is larger with smaller oxidizer jet diameter at the upstream region of the furnace.

Radial Temperature Profiles along with axial distance

The radial temperature profiles along with the various axial distances for different oxidizer jet diameters are shown in Figure 6.13.

It is observed that the temperature is high at upstream region near the jet exit, and then becomes lower along with the axial distance. This might be thought that the jets are less sufficiently diluted by product gases near the region of jet exit, thus the reaction rate is still high. However, the dilution of the jets increases to lower the reaction rate along with the axial distance, and hence the temperature decreases. It is observed that the temperature is lower for smallest oxidizer jet diameter than other cases. This might be attributed the fact that the recirculation of product gases occurs strongly with small oxidizer jet diameter because of increasing oxidizer jet momentum, and hence enhanced dilution of the jets. As a result, the reaction is delayed and temperature decreases due to enhanced dilution of the jets.

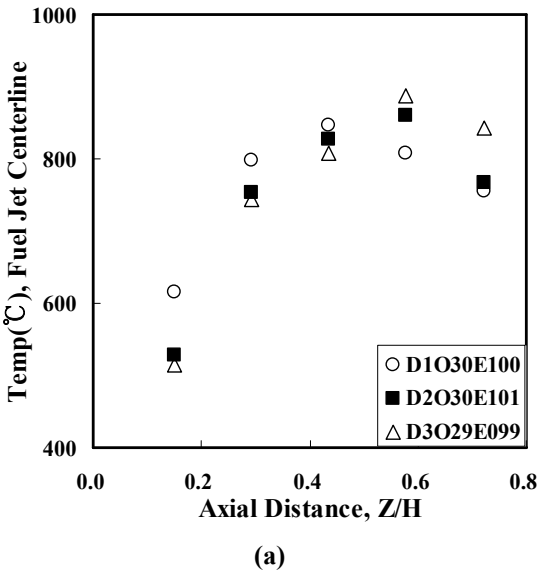

(a)

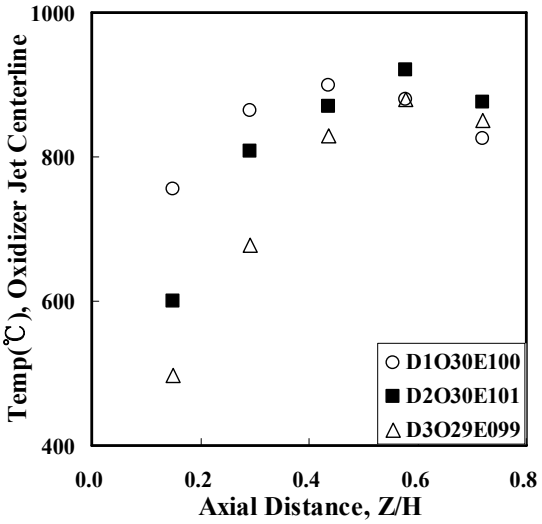

(b)

Figure 6.12: The centerline temperature of the (a) fuel and (b) oxidizer jet for different sizes of the oxidizer jet.

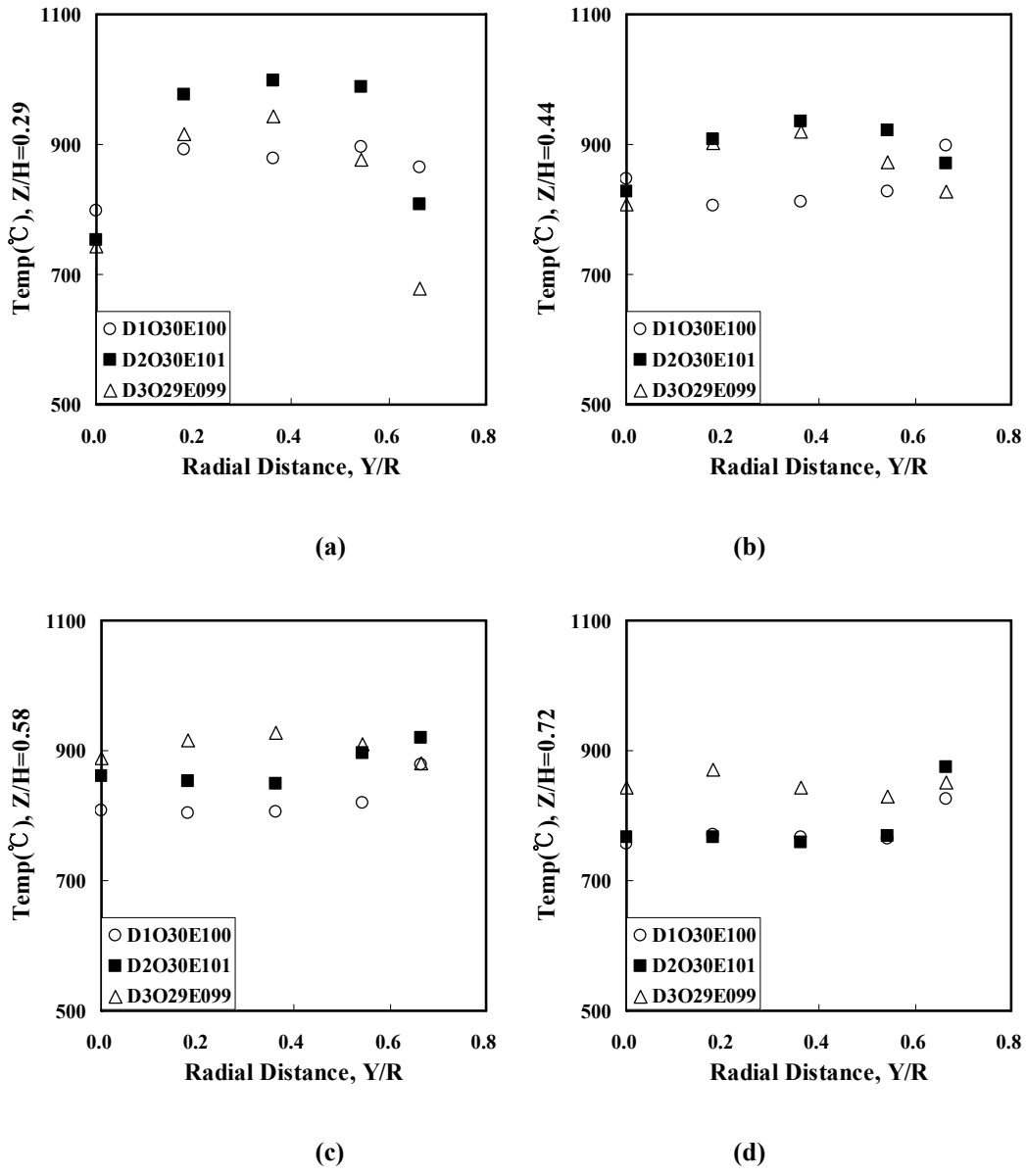

Figure 6.13: The radial temperature profiles at (a) *Z/H*=0.29 (b) *Z/H*=0.44 (c) *Z/H*=0.58 (d) *Z/H*=0.72 for different sizes of the oxidizer jet

6.2.1.2. Gas compositions

Jet Centerline gas composition

The THC (Total Hydrocarbons) concentration in the fuel jet centerline and oxygen concentration in the oxidizer jet centerline are shown in Figure 6.14. For the fuel jet centerline, the smallest oxidizer jet diameter shows the fast decay rate of the THC while other cases have similar values. However, the THC decays fast with decrease of the oxidizer jet diameter in the lower region of the furnace. The same trend is observed in

oxygen concentration in the oxidizer jet. Therefore, it can be concluded that both of the fuel and oxidizer jets decay faster as the oxidizer jet diameter decreases because of larger momentum of the oxidizer jet which promotes entrainment and dilution of the jets.

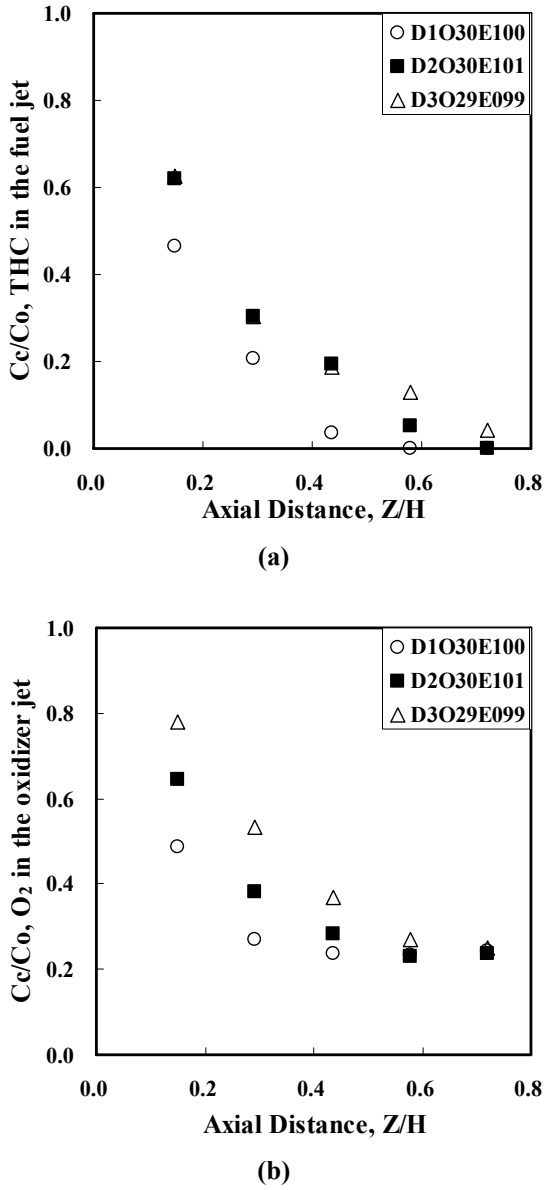

Figure 6.14: The centerline (a) THC in the fuel jet and (b) oxygen concentration in the oxidizer jet for different sizes of the oxidizer jet.

The scaled centerline THC in the fuel and oxygen concentration oxidizer jet for different oxidizer jet diameters are shown in Figure 6.15. In Figure 6.15, the centerline concentration is normalized by inlet concentration of each jet. The virtual origin is not

included in Figure 6.15 because the value of the virtual origin is generally small and negligible. It is clearly observed that the scaled THC in the fuel jet centerline decreases along with the axial distance, whereas the scaled oxygen concentration in the oxidizer jet increases. This indicates that the recirculation occurs from the oxidizer jet toward the fuel jet, thus the THC in the fuel jet can continue to decrease because the entrainment of product gases and inflow from oxidizer jet occur simultaneously. On the other hand, the oxygen concentration in the oxidizer jet initially decreases by entraining product gases like a free jet, and then decreases slowly or remains almost constant after the point where the recirculation of the jet flow occurs, which is the characteristic of the confined jet. Thus, the scaled values of the oxygen concentration in the oxidizer jet centerline increase along with the axial distance in the lower part of the furnace due to the confinement effect.

Another observation is that the scaled value of the THC and oxygen concentrations becomes lower with smaller oxidizer jet diameter. In addition, the onset point of confinement effect appears earlier with small oxidizer jet diameter, Z/H=0.30, 0.44 and 0.60 for d_{ox}=7.94, 15.9 and 31.8 mm, respectively. It might be attributed the fact that the recirculation of jet flow is enhanced and occurs early with increase of momentum under confined condition, and dilution of the jets is also promoted. Therefore, both of the fuel and oxidizer jets decay faster with decrease of the oxidizer jet diameter (increase of oxidizer jet momentum).

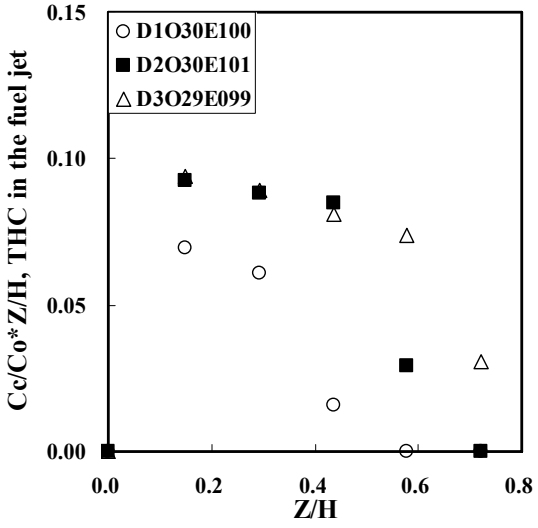

(a)

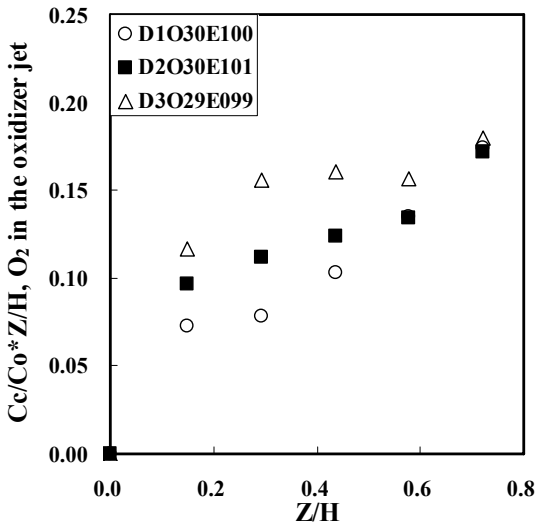

(b)

Figure 6.15: The scaled centerline (a) THC in the fuel jet and (b) oxygen concentration in the oxidizer jet for different sizes of the oxidizer jet.

Jet entrainment

For investigation of the jet entrainment, CO_2 concentrations in the fuel and oxidizer jet centerline are shown in Figure 6.16. CO_2 is one of the combustion products and a good gauge for jet entrainment. It is seen from Figure 6.16 that more CO_2 is found in the centerline of the fuel and oxidizer jets with smaller oxidizer jet diameter, whereas the difference between cases is relatively small in the fuel jet centerline. On the other hand, it is clearly observed that more CO_2 is found in the centerline of the fuel and oxidizer jets with smaller oxidizer jet diameter in order. This can be attributed the fact that the oxidizer jet momentum increases with decrease of the oxidizer jet diameter, and hence entrainment of product gases is promoted. Therefore, the CO_2 concentration in the oxidizer jet centerline increases with smaller diameter thanks to strong recirculation of product gases.

In terms of the fuel jet centerline, the flow rate and jet diameter are kept same for all cases and hence momentum is same. Thus, the amount of product gases entrained by the fuel jet can be assumed same for all cases in this study. However, the difference may occur between cases because of the effects of the oxidizer jet which has different diameters, inlet oxygen concentrations and momentums. In addition, the difference may also result from the effects of the combustion.

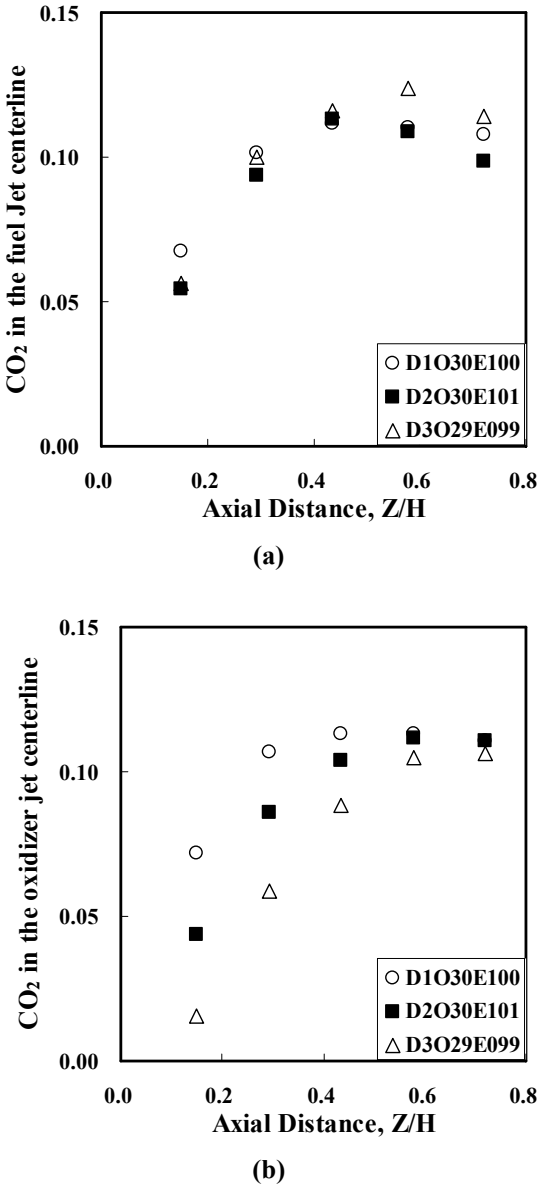

Figure 6.16: The centerline carbon dioxide concentration in the (a) fuel jet and (b) oxidizer jet for different sizes of the oxidizer jet.

According to the scaled THC concentration in the fuel jet centerline, the onset point of recirculation is earlier with smaller oxidizer jet diameter. Thus, it might be thought that the smallest oxidizer jet diameter shows higher CO_2 concentrations in the fuel jet centerline because of the strong recirculation of the jet flow and mixing from the oxidizer jet up to middle region of the furnace, whereas other cases show quite similar CO_2 concentrations because the recirculation of the jet flow begins later. In the more downstream region, the fuel jet can reach further downstream region of the furnace with

larger oxidizer jet diameter because of less momentum of the oxidizer jet. As a result, the reaction still occurs in further downstream region with larger oxidizer jet diameter, hence higher CO_2 concentration.

Radial gas composition profiles

The radial THC concentration profiles for different oxygen enrichments are shown in Figure 6.17. The profiles are almost identical for all cases at the upstream region of the furnace because the diameter and flow rate of the fuel jet are kept same for all cases. However, the fuel jet begins to be affected by oxidizer jets for the smallest diameter after *Z/H*=0.29, which is corresponding to the onset point of recirculation of the jet flow. Thus, other cases show quite similar pattern and value of the THC up to this region, and then the middle size of oxidizer jet diameter starts to show less THC than the largest diameter after *Z/H*=0.44, which is also corresponding to the onset point of recirculation of the jet flow for the middle size of diameter. In overall, the THC concentration decays faster with smaller oxidizer jet diameter. It might be thought that the oxidizer jet momentum increases with decrease of the oxidizer jet diameter, and hence the fuel jet is able to penetrate into the region of the oxidizer jet more easily and further downstream region of the furnace.

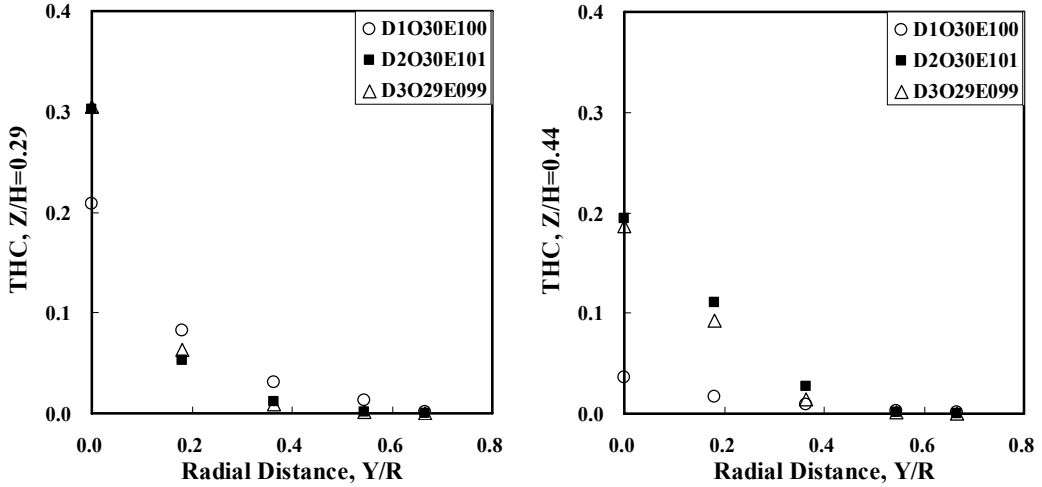

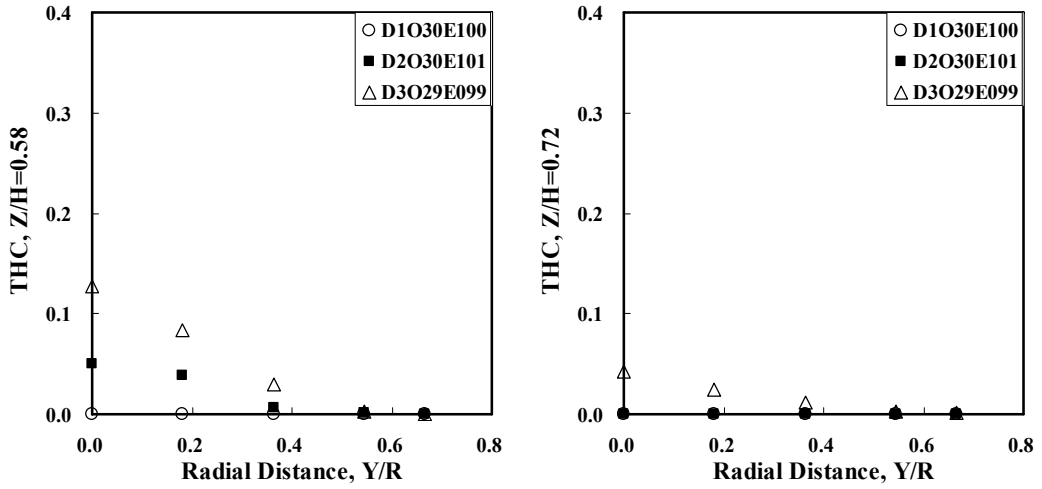

Figure 6.17: The radial THC concentration profiles at (a) *Z/H*=0.29 (b) *Z/H*=0.44 (c) *Z/H*=0.58 (d) *Z/H*=0.72 for different sizes of the oxidizer jet.

The radial oxygen concentration profiles for different oxygen inlet concentrations are shown in Figure 6.18. It is clearly seen that the oxygen concentration is lower with smaller oxidizer jet diameter in the oxidizer jet centerline, while higher at other regions. In addition, the oxygen concentration spreads more laterally with smaller oxidizer jet diameter. It can be attributed the fact that the oxidizer jet momentum increases with smaller oxidizer jet diameter, and hence the oxidizer jet is able to entrain more product gases. In addition, the oxidizer jet can penetrate into the region of the fuel jet more easily with increase of momentum, which is related to recirculation of the jet flow. As a result, the oxygen concentration decays faster in the oxidizer jet centerline and spreads more widely with smaller oxidizer jet diameter.

The radial carbon dioxide concentration profiles for different oxidizer jet diameters are shown in Figure 6.19. It is observed that the overall shape of the CO_2 concentration profile becomes flat across the radial direction along with the axial distance. However, the largest oxidizer jet diameter shows relatively less flat profiles of the CO_2 concentration, which means lack of uniformity in mixing and reaction. The CO_2 concentration is lower with the smallest oxidizer jet diameter than other cases except the fuel and oxidizer jet centerline, which is exactly opposite trend of the radial oxygen concentration profiles. In other words, the low carbon dioxide concentration at the region

between the jets results from the high oxygen concentration due to recirculation of the jet flow with high momentum.

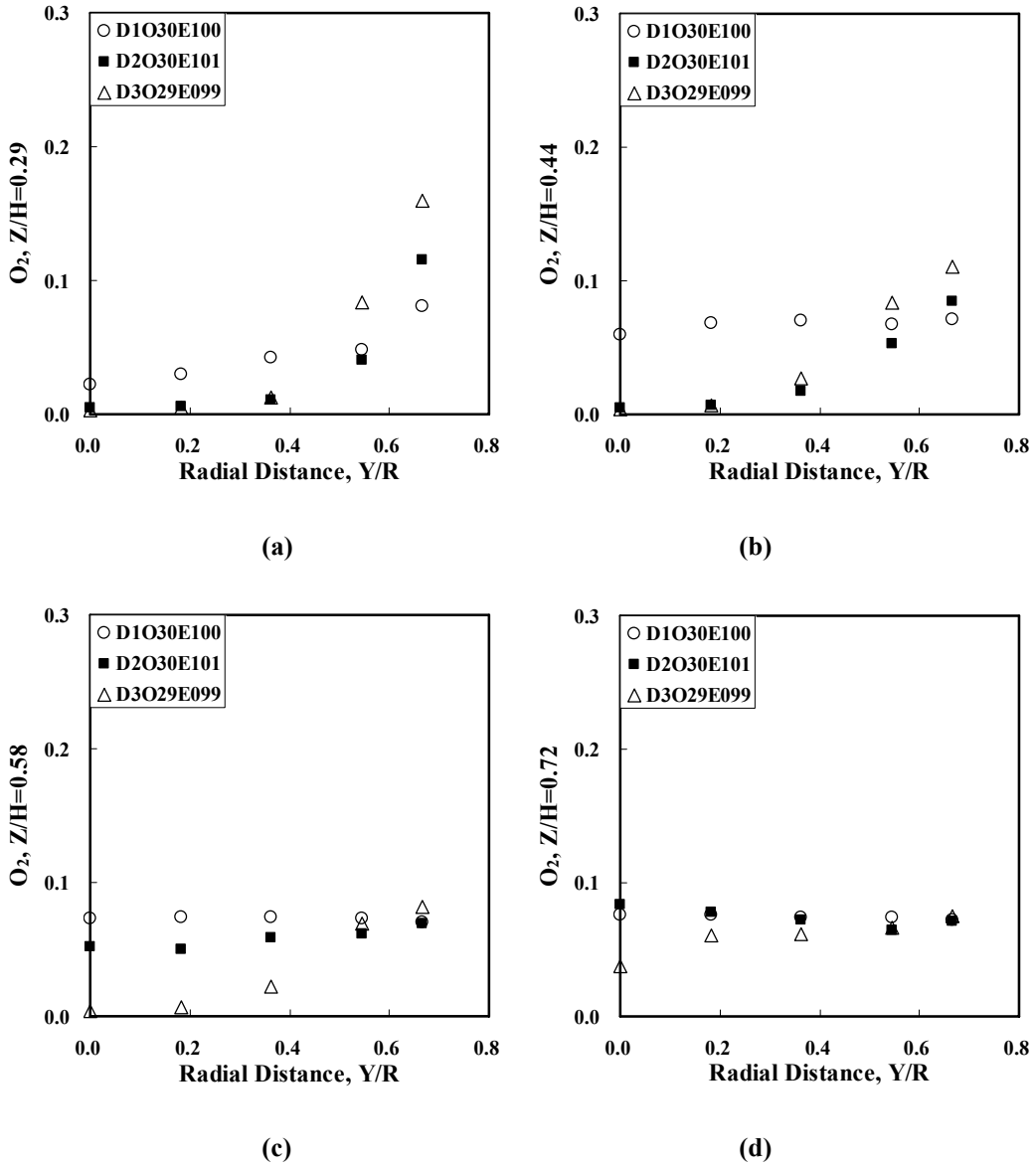

Figure 6.18: The radial oxygen concentration profiles at (a) *Z/H*=0.29 (b) *Z/H*=0.44 (c) *Z/H*=0.58 (d) *Z/H*=0.72 for different sizes of the oxidizer jet.

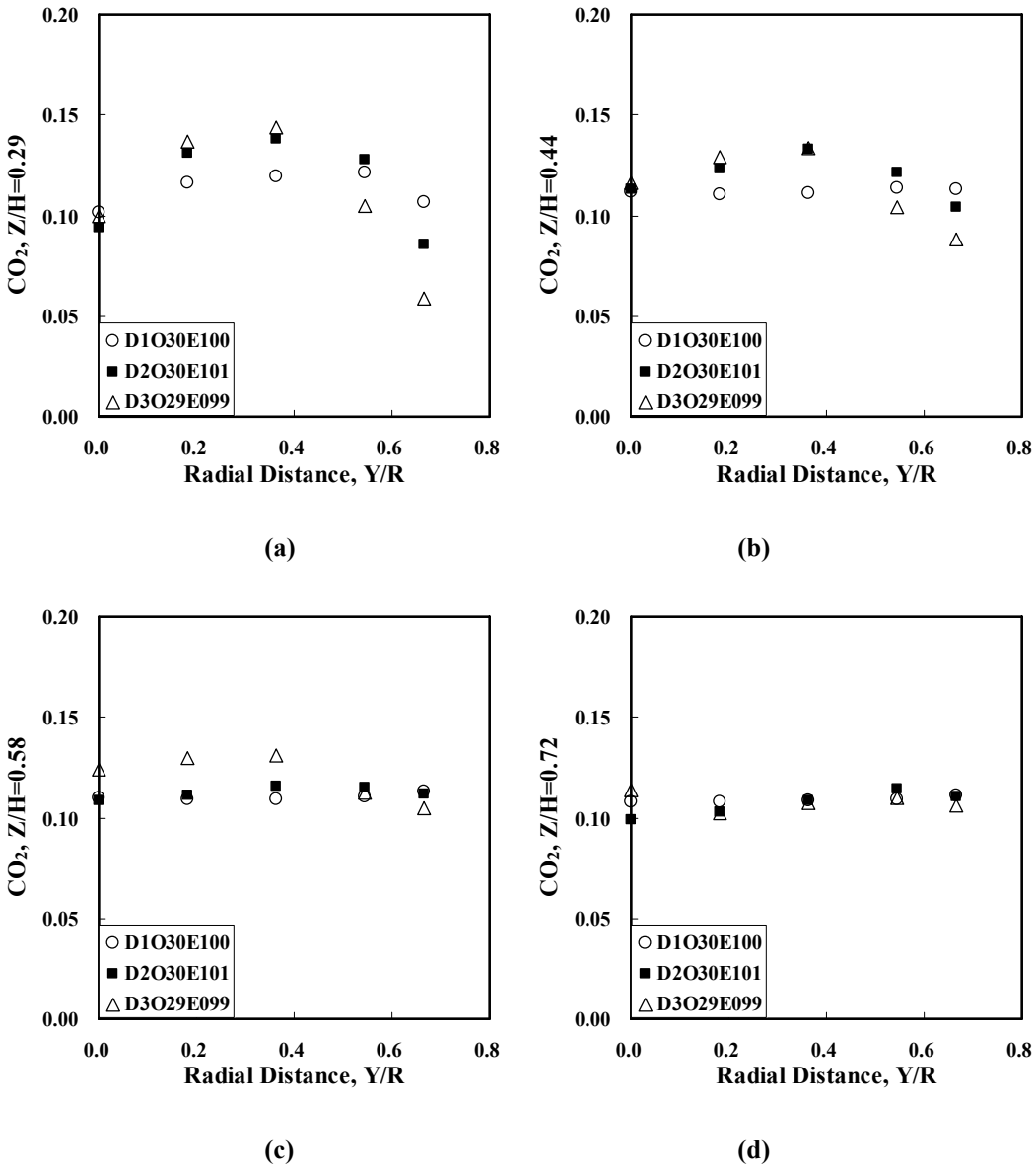

Figure 6.19: The radial carbon dioxide concentration profiles at (a) *Z/H*=0.29 (b) *Z/H*=0.44 (c) *Z/H*=0.58 (d) *Z/H*=0.72 for different sizes of the oxidizer jet.

Figure 6.20 shows the radial carbon monoxide profiles along with the axial distance with different oxidizer jet diameters. It is observed that the CO concentration is high at the region of the fuel jet and interface between the fuel and oxidizer jets. The high CO concentration at the region of the fuel jet is related to overly rich equivalence condition, as expected. On the other hand, less mixing with sufficient oxidizer or insufficient time for complete combustion due to high momentum of the jets is responsible for high CO concentration at the interface region between the fuel and oxidizer jets.

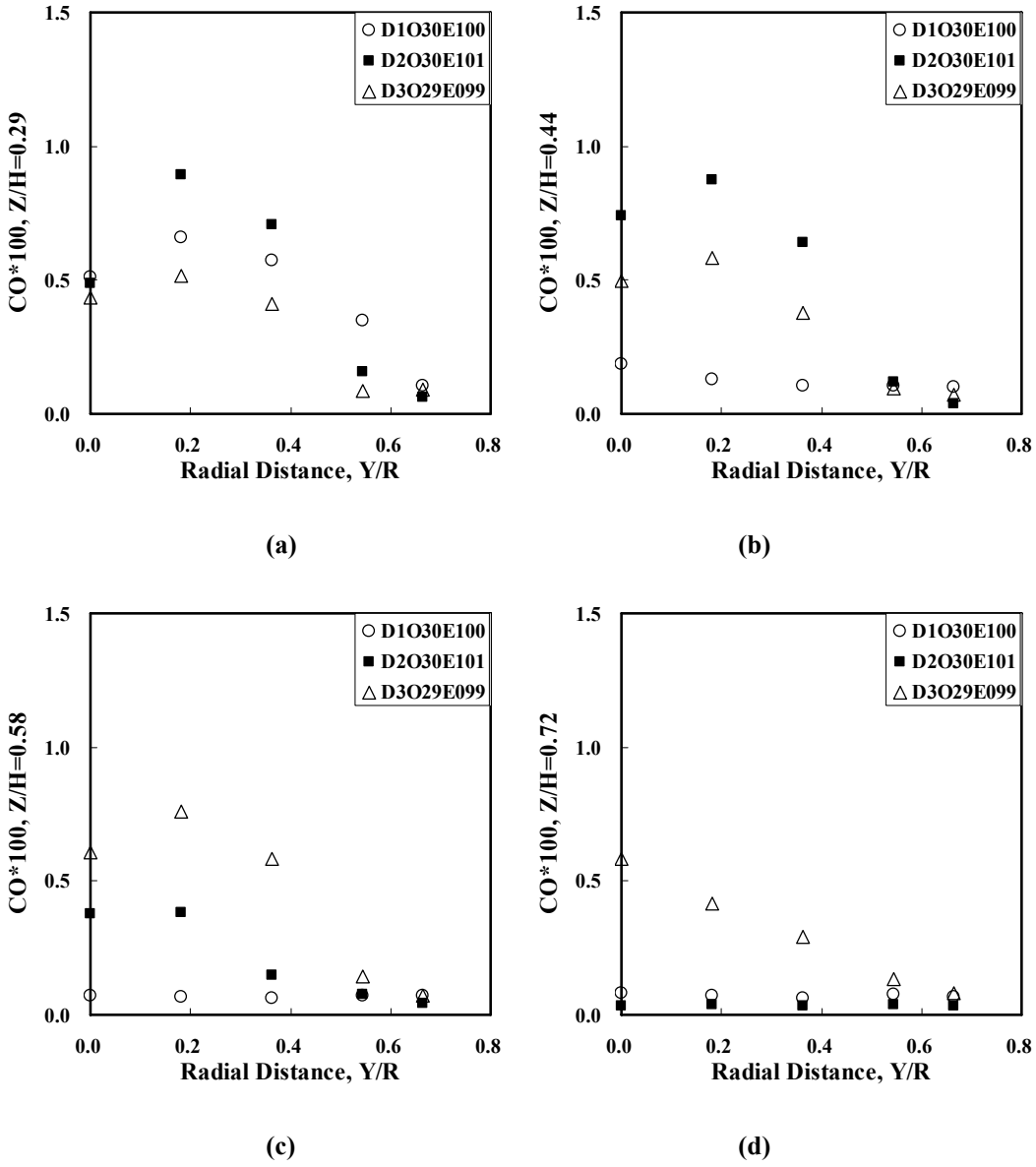

Figure 6.20: The radial carbon monoxide concentration profiles at (a) *Z/H*=0.29 (b) *Z/H*=0.44 (c) *Z/H*=0.58 (d) *Z/H*=0.72 for different sizes of the oxidizer jet.

It is found that high CO concentration region moves with the high temperature region, and decreases after the axial distance, *Z/H*=0.44, 0.58 for d_{ox}=7.94 and 15.9 mm, respectively. In other words, the CO concentration decreases in accordance with the onset point of recirculation of the flow. This might be thought that the reaction occurs under the condition that the jets are less sufficiently diluted by product gases at upstream region, whereas the dilution of the jets increases at further downstream region because of large scale of recirculation of the flow and hence the production of CO decreases.

The case of d_{ox}=31.8 mm shows the high CO concentration at quite downstream region, Z/H=0.72, which means that there is still incomplete combustion even near the bottom of the furnace. It can be attributed the fact that the jets are insufficiently diluted before the reaction occurs because of less oxidizer jet momentum, which induce the less uniformity of reaction and temperature. This is another main difference between the homogenous and non-homogenous combustion modes.

6.2.2. The effect of the inlet oxygen concentration

Atreya et al. (2004) proposed the novel solution in efficient energy saving method in industrial furnaces. The authors combined both concepts of internal recirculation of product gas to preheat the combustion air and oxygen-enriched combustion to reduce the volume of exhaust for enhancing the energy utilization efficiency. For this purpose, experimental studies are performed on three different inlet oxygen concentrations in the oxidizer jet, $X_{O2,ox}$ =0.21, 0.30 and 0.40, with same overall equivalence ratio, $\Phi_{overall}$ =1.0, and oxidizer jet diameter, d_{ox}=15.9 mm. The properties of three cases are summarized in Table 6.2.

Case No.	d_{ox} (mm)	$X_{O2,ox}$	$\Phi_{overall}$	V_{ox} (m/s)	J_{ox} (N)	Mode.
D2O21E103	15.9	0.21	1.03	22.03	1.11 E-01	**H**
D2O30E101	15.9	0.30	1.01	15.67	5.69 E-02	**H**
D2O41E102	15.9	0.41	1.02	11.46	3.09 E-02	**NH**

Table 6.2: The properties of three inlet oxygen concentrations in the oxidizer jet.

6.2.2.1. Temperature

Jet Centerline Temperature

Figure 6.21 shows the centerline temperature of the fuel and oxidizer jets for different inlet oxygen concentrations in the oxidizer jet. It is observed that the peak and gradient of the jet centerline temperature increases with increase of the inlet oxygen concentration. In addition, the profile of the jet centerline temperature shifts from flat to more parabolic with higher inlet oxygen concentration, which indicates lack of uniformity in temperature. This ununiformity of the temperature induces non-homogeneous combustion condition.

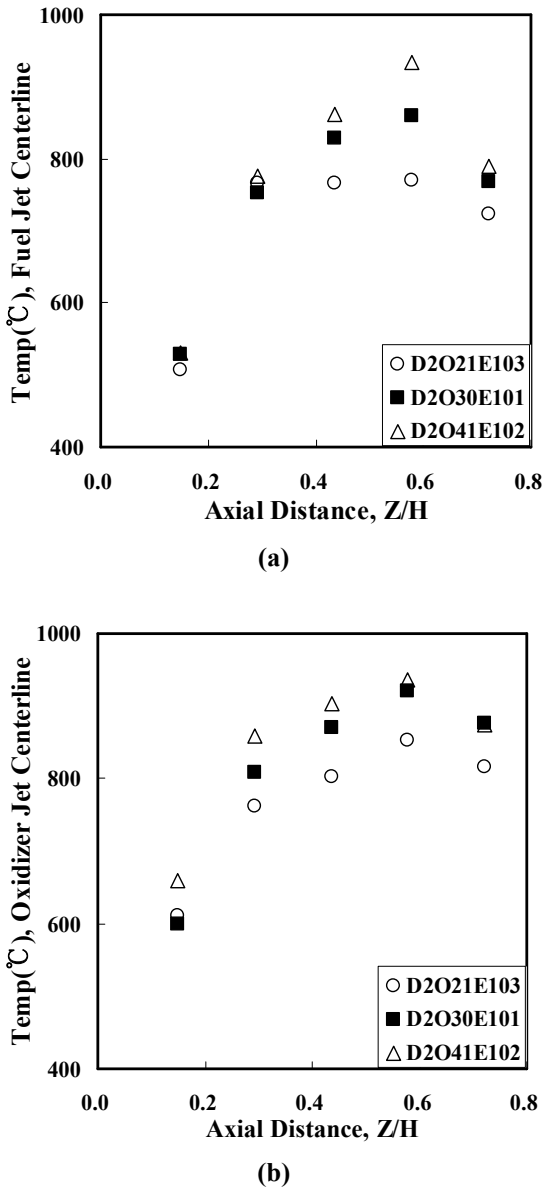

Figure 6.21: The centerline temperature of the (a) fuel and (b) oxidizer jet for different inlet oxygen concentrations in the oxidizer jet.

Radial Temperature Profiles along with axial distance

The radial temperature profiles along with the various axial distances for different inlet oxygen concentrations in the oxidizer jet are shown in Figure 6.22. It is observed that the temperature increases in order of inlet oxygen concentrations in the oxidizer jet because the reaction rate increases with high inlet oxygen concentration. This might be also attributed the fact that the recirculation of product gases occurs strongly with low inlet

oxygen concentration in the oxidizer jet because of increasing oxidizer jet momentum, and hence enhanced dilution of the jets. As a result, the reaction is delayed and temperature decreases due to enhanced dilution of the jets.

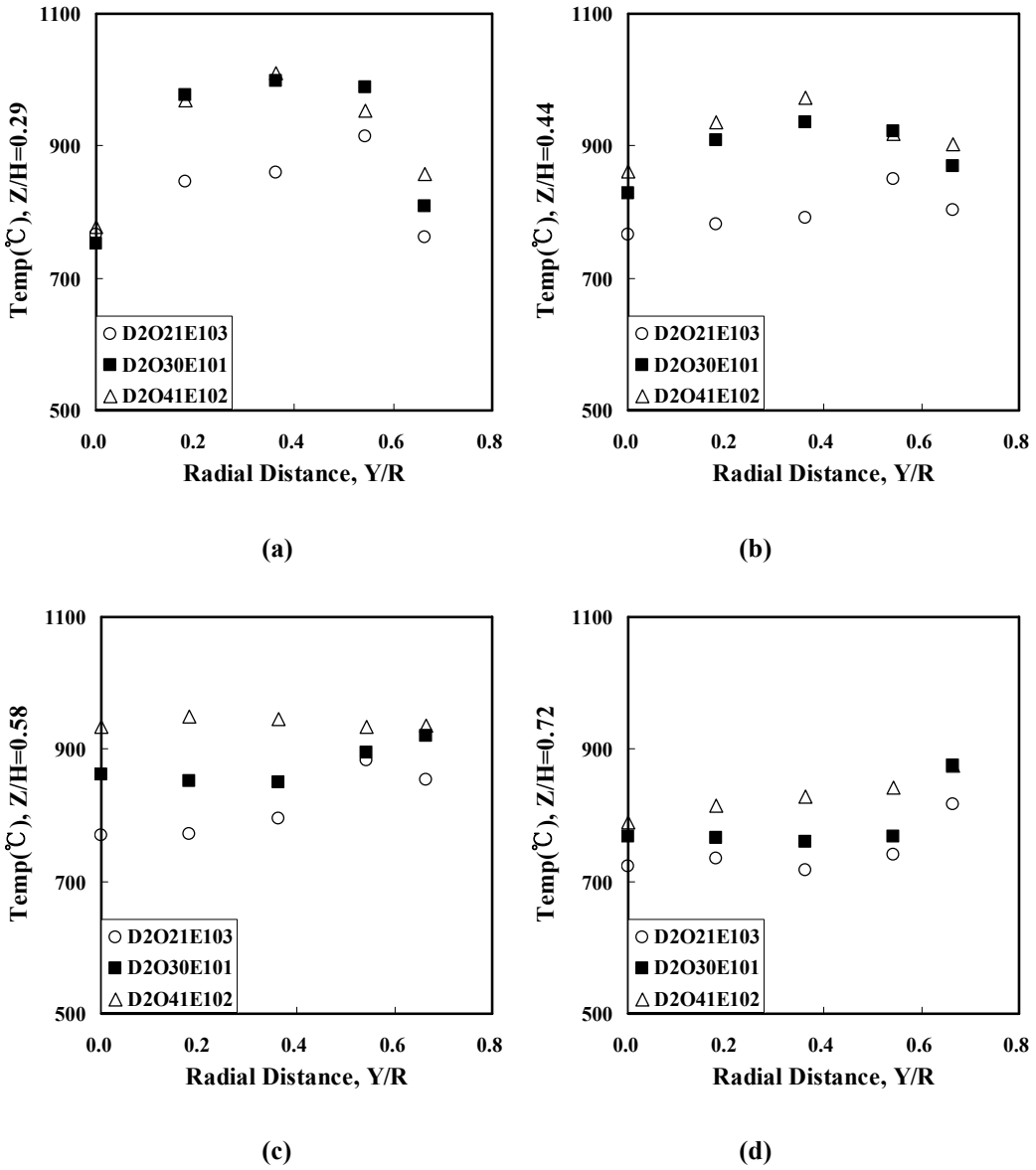

Figure 6.22: The radial temperature profiles at (a) *Z/H*=0.29 (b) *Z/H*=0.44 (c) *Z/H*=0.58 (d) *Z/H*=0.72 for different inlet oxygen concentrations in the oxidizer jet.

6.2.2.2. Gas compositions

Jet Centerline gas composition

The Total Hydrocarbons in the fuel jet centerline and oxygen concentration in the oxidizer jet centerline are shown in Figure 6.23. It is observed that the normal air inlet case, $X_{O2,ox}$=0.21, shows fast decay rate of the centerline THC in the fuel jet, while the decay patterns of the THC for $X_{O2,ox}$=0.30 and 0.40 are almost identical. On the other hand, the oxygen concentration decays slightly more with increase of the inlet oxygen concentration, however, the difference between cases is small as shown in Figure 6.23 (b).

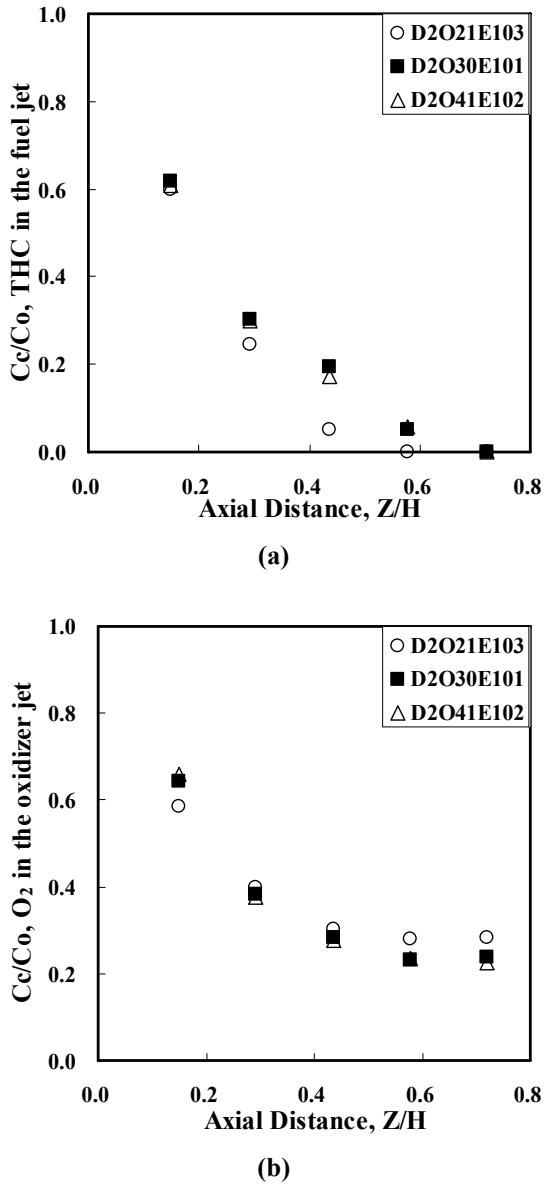

Figure 6.23: The centerline concentrations of (a) THC in the fuel jet and (b) oxygen in the oxidizer jet for different inlet oxygen concentrations in the oxidizer jet.

It is noted that the initial inlet concentrations of oxygen are different, while the oxidizer jet diameter is same for above cases. In Figure 6.23 (b), the centerline oxygen concentration, Cc_{O2}, is normalized by the inlet oxygen concentration, Co_{O2}. Thus, the real values of the centerline oxygen concentration, Cc_{O2}, are different between cases even though the decay rates of $(Cc/Co)_{O2}$ are nearly same for above cases. Considering the real values of the centerline oxygen concentration, the less inlet oxygen concentration shows the lower value of the centerline oxygen concentration as shown in Figure 6.24. This can be explained by the turbulent jet theory which states that the centerline concentration is proportional to initial inlet concentration and jet diameter. Thus, the higher oxygen concentration in the oxidizer jet centerline with increase of inlet oxygen concentration results from high initial oxygen concentration in oxidizer jet.

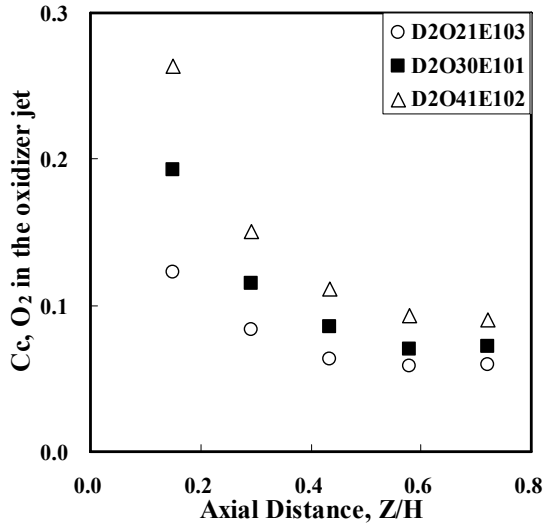

Figure 6.24: The centerline concentrations of (a) THC in the fuel jet and (b) oxygen in the oxidizer jet for different inlet oxygen concentrations in the oxidizer jet.

Another investigation is that the decay rate of the normalized centerline oxygen concentration in the oxidizer jet, $(Cc/Co)_{O2,}$, is nearly same even with high inlet oxygen concentration. However, the oxygen concentration should decrease more for high oxygen inlet case to obtain the homogeneous combustion mode. Therefore, the decay rate of the normalized centerline oxygen concentration, $(Cc/Co)_{O2}$, should be more less than normal air inlet within the range of the inlet oxygen concentration in this study. Based on the UV

emission and visual image, the case of $X_{O2,ox}$=0.21 and 0.30 are in the homogeneous combustion mode, whereas the highest oxygen inlet case, $X_{O2,ox}$=0.40, is in the non-homogeneous combustion mode. It might be thought that the dilution of the oxidizer jet is not sufficient to obtain the homogeneous combustion for $X_{O2,ox}$=0.40 because the decay rate of $(Cc/Co)_{O2}$ is almost same as $X_{O2,ox}$=0.30, which means that the real value of the oxygen concentration is higher than that of less inlet oxygen concentration cases. This higher oxygen concentration induces the non-homogenous combustion.

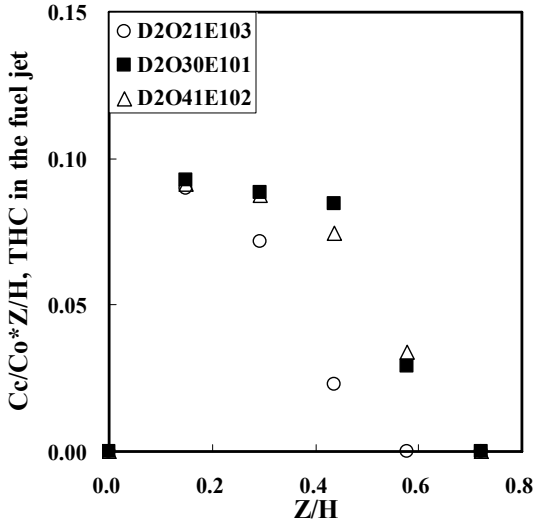

(a)

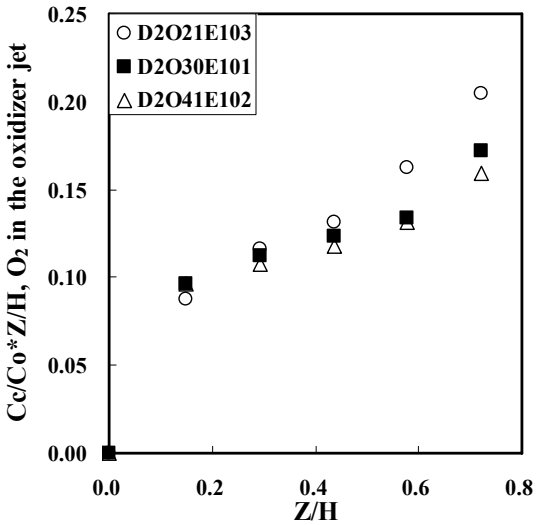

(b)

Figure 6.25: The scaled centerline concentrations of (a) THC in the fuel jet and (b) oxygen in the oxidizer jet for different inlet oxygen concentrations in the oxidizer jet.

Figure 6.25 shows the scaled centerline THC in the fuel jet and oxygen concentration in the oxidizer jet for different inlet oxygen concentrations. It is observed that the centerline THC in the fuel jet falls steeply, whereas the scaled centerline oxygen concentration in the oxidizer jet increases after showing flat shape along with the axial distance. This can be thought that the $(Cc/Co)_{THC}$ falls because of combustion, and the $(Cc/Co)_{O2}$ increases due to the recirculation of the oxidizer jet flow as explained in previous section. The each jet acts like a free single jet before the onset point of the recirculation the jet flow, as a result, the jets continue to be diluted. This can be shown as flat shape in Figure 6.25. However, the centerline oxygen concentration in the oxidizer jet drops slowly or remains nearly constant after occurring of the recirculation of the oxidizer jet flow. On the other hand, the scaled THC in the fuel jet decreases fast by mixing with oxidizer and combustion due to the recirculation the jet flow.

The scaled value of the centerline THC in the fuel jet fall fast for $X_{O2,ox}$=0.21, whereas other cases show nearly identical values of the THC concentration. On the other hand, the scaled centerline oxygen concentration in the oxidizer jet is slightly higher with less oxygen inlet. It might be attributed the fact that the oxidizer jet momentum increases with less oxygen inlet, and the recirculation of the jet flow occurs earlier. As a result, large scale of the mixing between the fuel and oxidizer jet occurs earlier and thus the centerline THC decreases fast. However, this trend is not found clearly between $X_{O2,ox}$=0.30 and 0.40. The onset point of the recirculation is almost same, and the centerline THC and oxygen concentration are quite identical. It might be thought that the dilution of the oxidizer jet is less achieved for considering the high oxygen inlet due to small momentum of the oxidizer jet, which induces the non-homogeneous combustion mode and makes the effect of the control parameter ambiguous for $X_{O2,ox}$=0.40.

Jet entrainment

For investigation of the jet entrainment, CO_2 concentrations in the fuel and oxidizer jet centerline are shown in Figure 6.26. It is noted that the injecting oxygen concentrations are different between cases because of various oxygen enrichments. Considering different initial inlet oxygen concentrations, the centerline concentrations of CO_2 are divided by inlet oxygen concentrations as shown in Figure 6.26 because the amount of CO_2 is

approximately proportional to inlet oxygen concentration. It is seen from Figure 6.26 that more CO_2 is found in the centerline both of the fuel and oxidizer jets for lower oxygen inlet concentration. This can be attributed the fact that the oxidizer jet momentum increases with lower oxygen inlet, and hence entrainment is promoted. On the other hand, the case of $X_{O2,ox}$=0.40 shows lower CO_2 concentration in the centerline for both of the jets than normal air inlet case even with high oxygen enrichment, which indicates the lower level of recirculation of product gases. However, more strong level of recirculation of product gases is needed to obtain the homogeneous combustion mode for high oxygen inlet case.

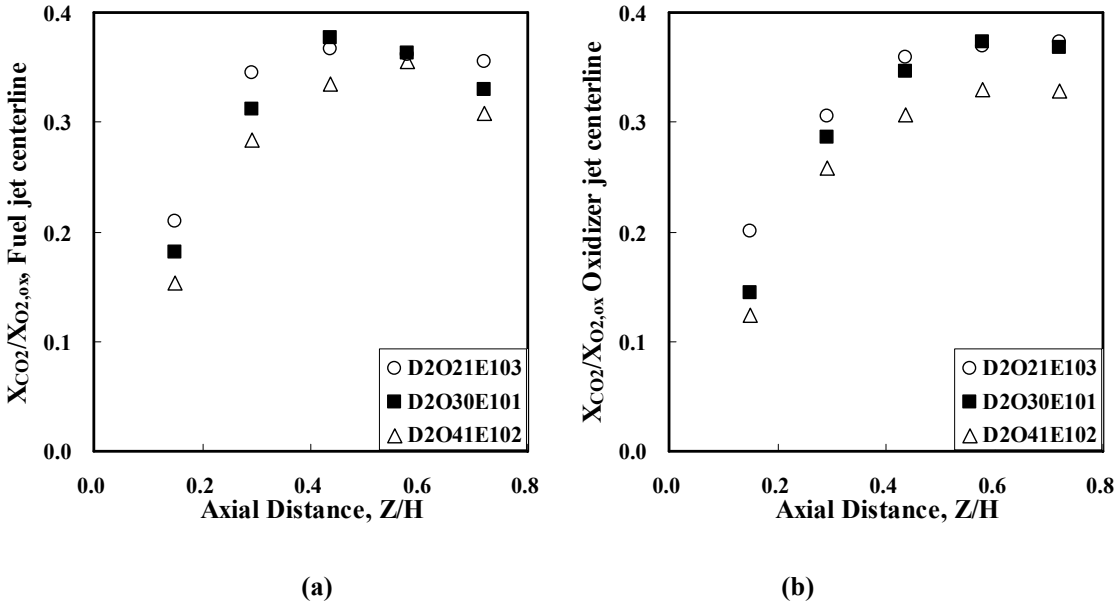

Figure 6.26: The normalized centerline carbon dioxide concentrations of in the (a) fuel jet and (b) oxidizer jet for different inlet oxygen concentrations in the oxidizer jet.

Radial gas composition profiles

Figure 6.27 shows the radial THC concentration profiles at various axial distances for different oxygen inlet in the oxidizer jet. The profiles are almost identical for all cases at the upstream region because the diameter and flow rate of the fuel jet are kept same for all cases. However, the THC concentration drops in centerline of the fuel jet for $X_{O2,ox}$=0.21 while other cases show identical values of the THC at Z/H=0.29, which is corresponding to the onset point of the recirculation of the jet flow for $X_{O2,ox}$=0.21. On

the other hand, the case of $X_{O2,ox}$=0.30 and 0.40 show very little difference within measuring error range. It might be thought that the case of $X_{O2,ox}$=0.40 is in the non-homogeneous combustion mode while $X_{O2,ox}$=0.30 is in the homogeneous combustion mode, thus it is hard to differentiate the effect of inlet oxygen concentration between cases because of lack of the uniformity in mixing and combustion.

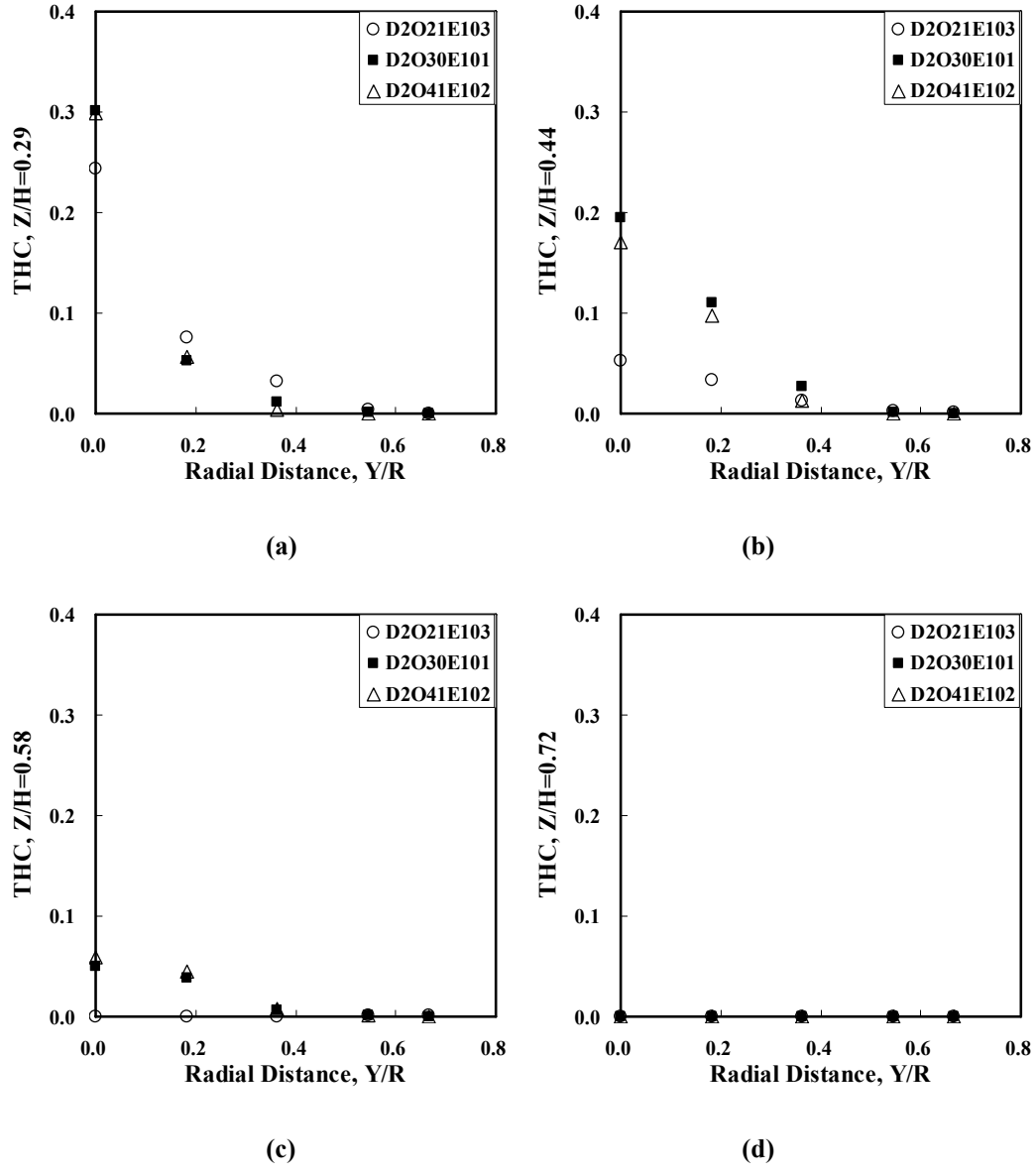

Figure 6.27: The radial THC concentration profiles at (a) *Z/H*=0.29 (b) *Z/H*=0.44 (c) *Z/H*=0.58 (d) *Z/H*=0.72 for different inlet oxygen concentrations in the oxidizer jet.

The radial oxygen concentration profiles for different oxygen inlet concentrations are shown in Figure 6.28. It is observed that the oxygen concentration is lower with less oxygen inlet in the oxidizer jet centerline, while higher at other regions. However, the oxygen concentration spreads more laterally with less oxygen inlet concentration. It can be attributed the fact that the oxidizer jet momentum increases with lower oxygen inlet concentration, and hence the oxidizer jet is able to penetrate into the region of the fuel jet more easily with increase of momentum. As a result, the oxygen concentration spreads more widely with lower oxygen inlet concentration.

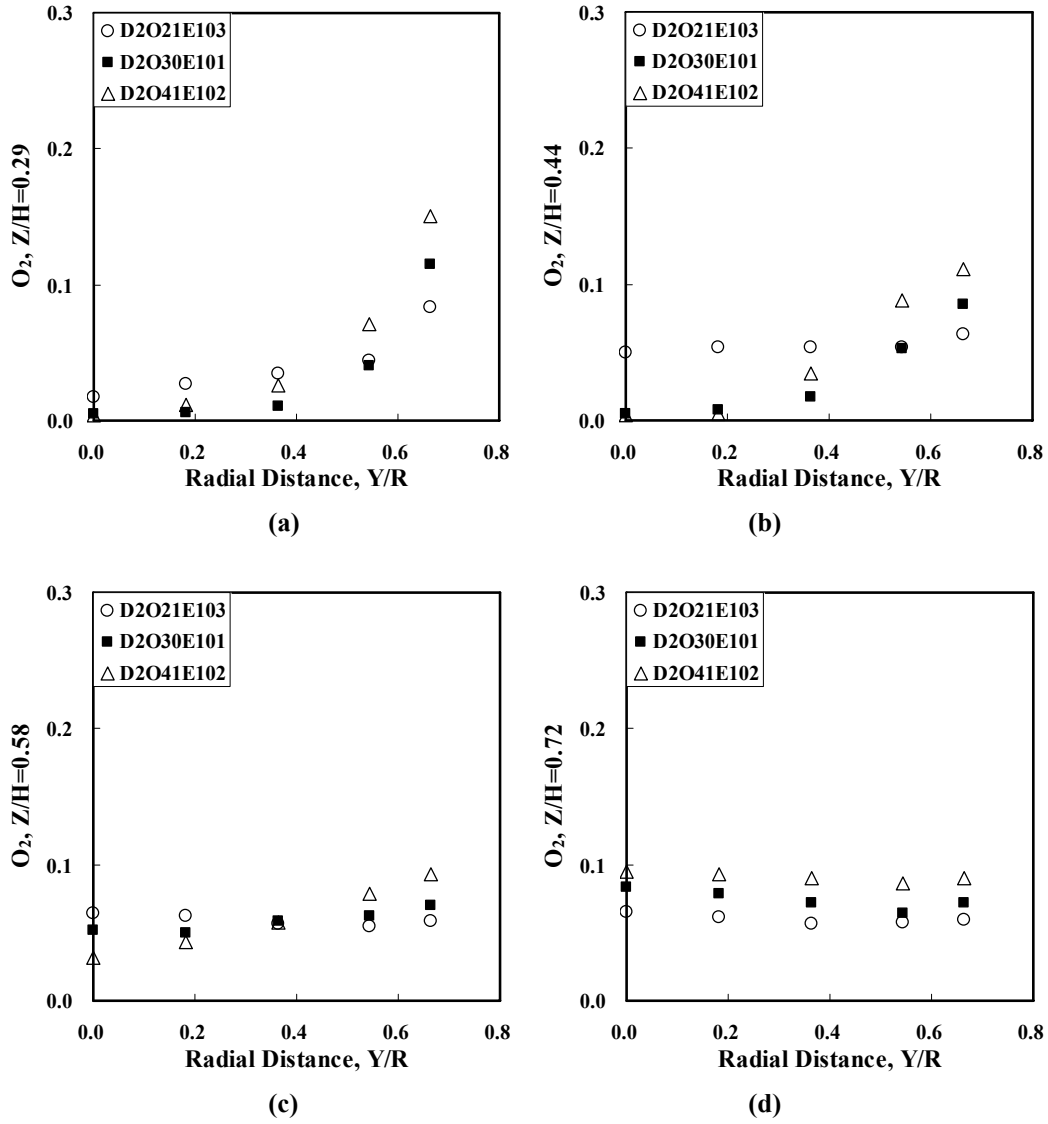

Figure 6.28: The radial oxygen concentration profiles at (a) *Z/H*=0.29 (b) *Z/H*=0.44 (c) *Z/H*=0.58 (d) *Z/H*=0.72 for different inlet oxygen concentrations in the oxidizer jet.

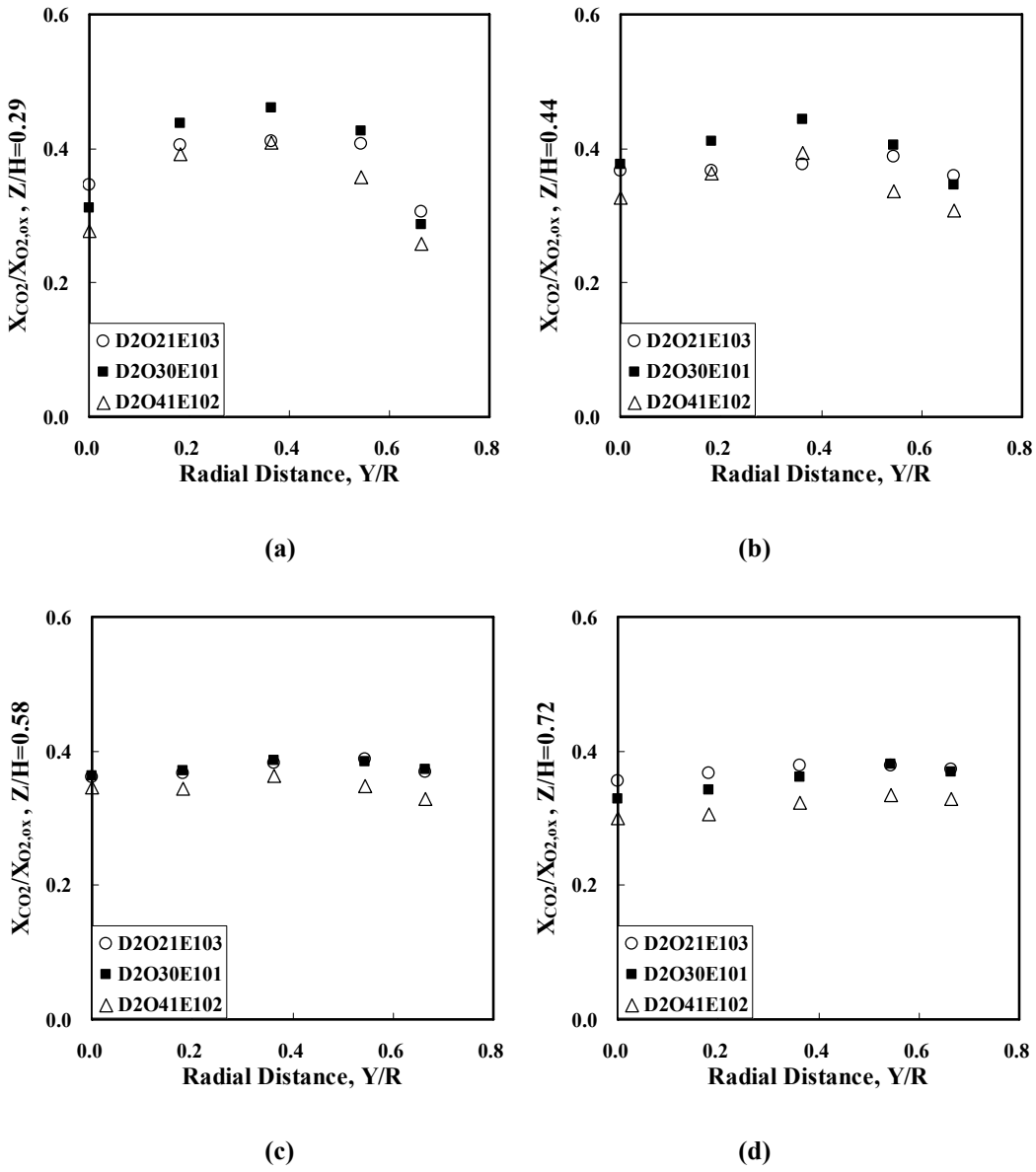

Figure 6.29: The radial carbon dioxide concentration profiles at (a) *Z/H*=0.29 (b) *Z/H*=0.44 (c) *Z/H*=0.58 (d) *Z/H*=0.72 for different inlet oxygen concentrations in the oxidizer jet.

The radial carbon dioxide concentration profiles for different oxygen inlet concentrations in the oxidizer jet are shown in Figure 6.29.

The CO_2 concentrations is definitely higher with high oxygen inlet in the oxidizer jet, thus it is hard to investigate the effect of different oxygen inlet on jet entrainment. For this purpose, the CO_2 concentrations are normalized by oxygen inlet concentrations as same way mentioned in the jet entrainment. It is observed from Figure 6.29 that the case of $X_{O2,ox}$=0.30 shows the higher CO_2 concentration, while $X_{O2,ox}$=0.40 have lower CO_2

concentration than normal air inlet case even with high oxygen enrichment. This indicates less production of CO_2 in the furnace for $X_{O2,ox}$=0.40. It might be thought that the production of CO_2 reduces because of the less uniform mixing and combustion.

Figure 6.30 shows the radial CO concentration profiles along with the axial distance with different oxygen inlet concentrations. It is observed that high CO regions correspond to rich regions, and CO concentration decreases after from the onset point of recirculation of the flow. The reason is quite same as discussed in the effect of the oxidizer jet diameter.

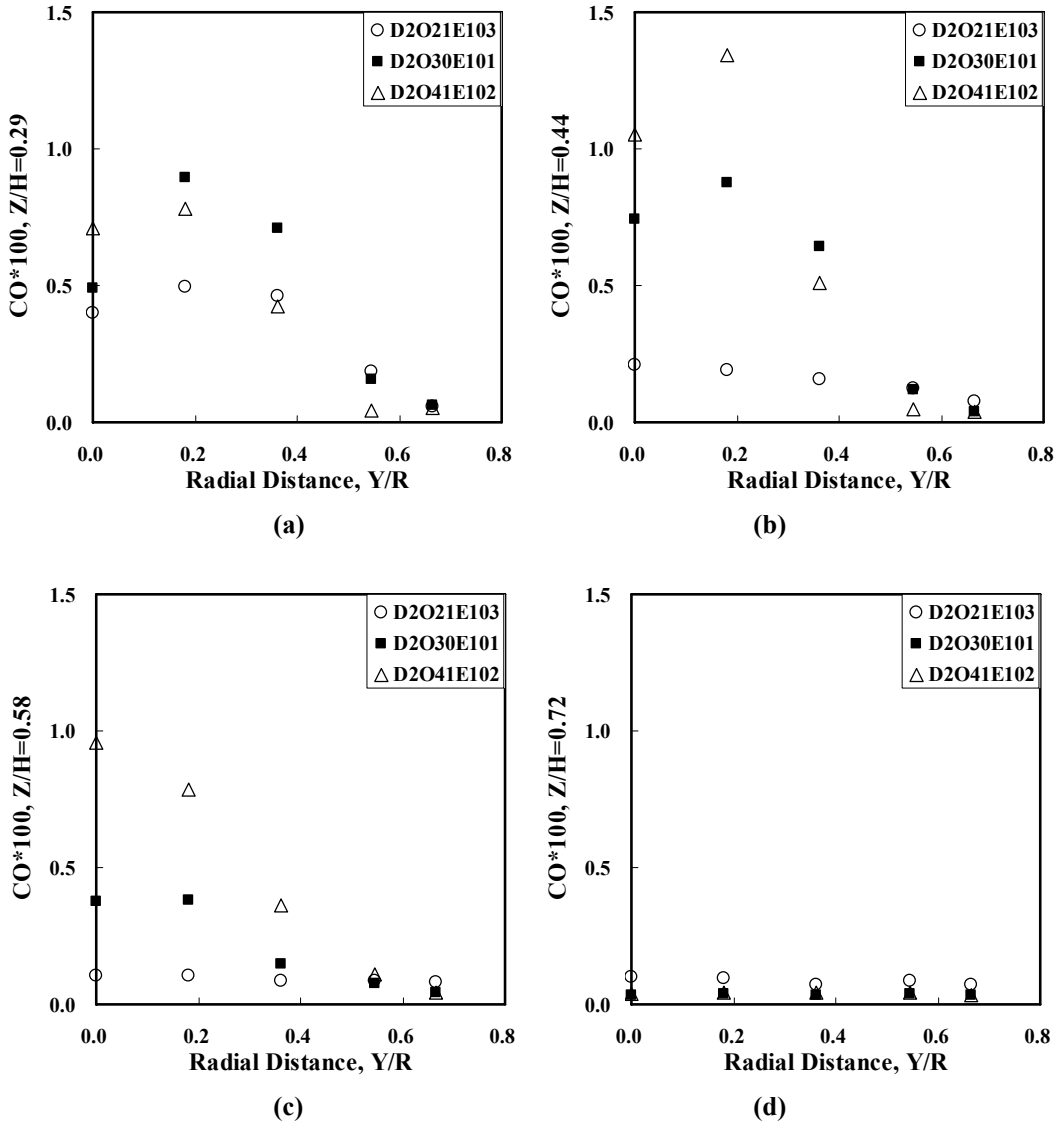

Figure 6.30: The radial carbon monoxide concentration profiles at (a) *Z/H*=0.29 (b) *Z/H*=0.44 (c) *Z/H*=0.58 (d) *Z/H*=0.72 for different inlet oxygen concentrations in the oxidizer jet.

6.2.3. The effect of overall equivalence ratio

In this section, the effect of the overall equivalence ratio are investigated on three different overall equivalence ratios, $\Phi_{overall}$ =0.9, 1.0, and 1.1 with same inlet oxygen concentration, $X_{O2,ox}$ =0.30 and oxidizer jet diameter, d_{ox}=15.9 mm. The properties of three cases are summarized in Table 6.3.

Case No.	d_{ox} (mm)	$X_{O2,ox}$	$\Phi_{overall}$	V_{ox} (m/s)	J_{ox} (N)	Mode
D2O30E091	15.9	0.30	0.91	17.58	7.16 E-02	**H**
D2O30E101	15.9	0.30	1.01	15.67	5.69 E-02	**H**
D2O30E110	15.9	0.30	1.10	14.33	4.76 E-02	**H**

Table 6.3: The properties of three overall equivalence ratios.

6.2.3.1. Temperature

Jet Centerline Temperature

The centerline temperatures of the fuel and oxidizer jets for different equivalence ratios are shown in Figure 6.31. It is observed that there is no clear difference between cases. All cases show quite similar trend in fuel jet centerline temperature, whereas the centerline temperature increases slightly with increase of the equivalence ratio for the oxidizer jet centerline, however, the increment is very small. This might result from the narrow range of the oxidizer jet momentum. The range of the oxidizer jet momentum ratio to reference momentum of $\Phi_{overall}$=1.0 is between 0.84 and 1.26 for $\Phi_{overall}$=1.1 and 0.9, respectively, which is relatively close to each other comparing with that of other parameters. Therefore, it is hard to see the differences due to the effect of equivalence ratio.

Radial Temperature Profiles along with axial distance

Figure 6.32 shows the radial temperature profiles along with the various axial distances for different equivalence ratios. As same with the centerline temperatures, all cases show quite similar profile and value of temperature because of narrow selection in oxidizer jet momentum. It is observed that the gradient of temperature becomes small, and radial

temperature profiles become quite flat from *Z/H*=0.44 where corresponds to middle region of the furnace, which indicates that uniform reaction occurs in the furnace.

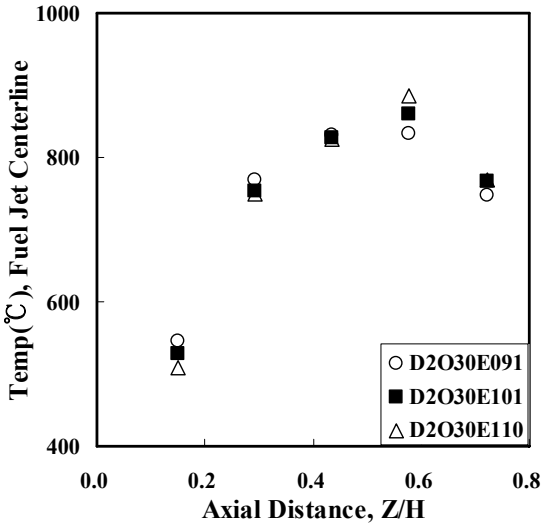

(a)

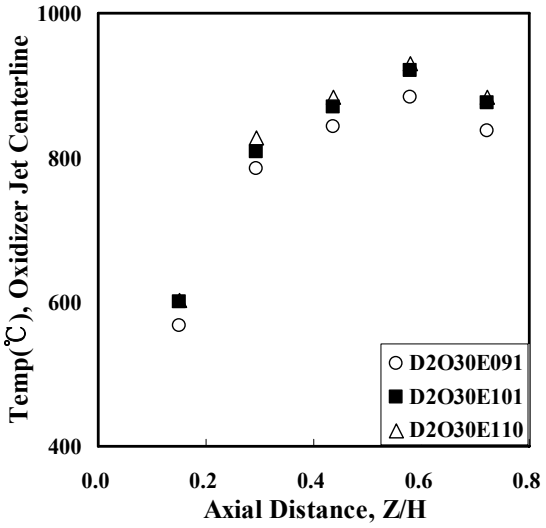

(b)

Figure 6.31: The centerline temperature of the (a) fuel and (b) oxidizer jet for different overall equivalence ratios.

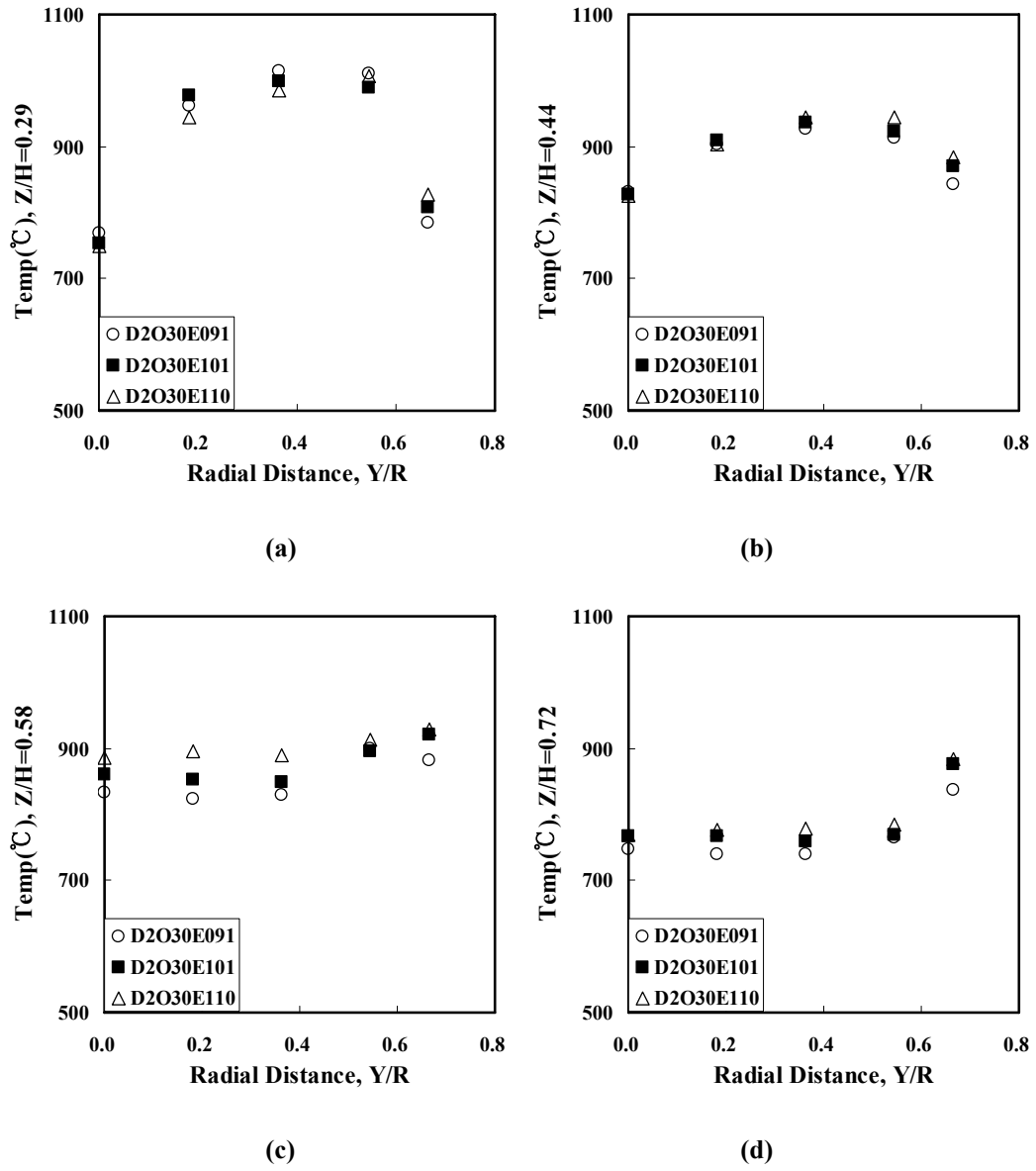

Figure 6.32: The radial temperature profiles at (a) *Z/H*=0.29 (b) *Z/H*=0.44 (c) *Z/H*=0.58 (d) *Z/H*=0.72 for different overall equivalence ratios.

6.2.3.2. Gas compositions

Jet Centerline gas composition

The THC concentration in the fuel jet centerline and oxygen concentration in the oxidizer jet centerline are shown in Figure 6.33. The decay patterns of the THC for different equivalence ratios are quite similar, which might be attributed the fact that the fuel jet momentum is kept same for all cases and little differences in the oxidizer jet momentum between cases. On the other hand, oxygen concentration in the oxidizer jet decays faster

with increase of equivalence ratio (decrease of oxidizer jet momentum). This is the different tendency from the jet mixing theory which the entrainment of the jet is enhanced with increase of momentum and hence dilution is promoted. However, the amount of available oxygen is less for high equivalence ratio. Thus, the oxygen concentration decays faster with higher equivalence ratio because of less amount of available oxygen for combustion while excess amount of oxygen remains for low equivalence ratio.

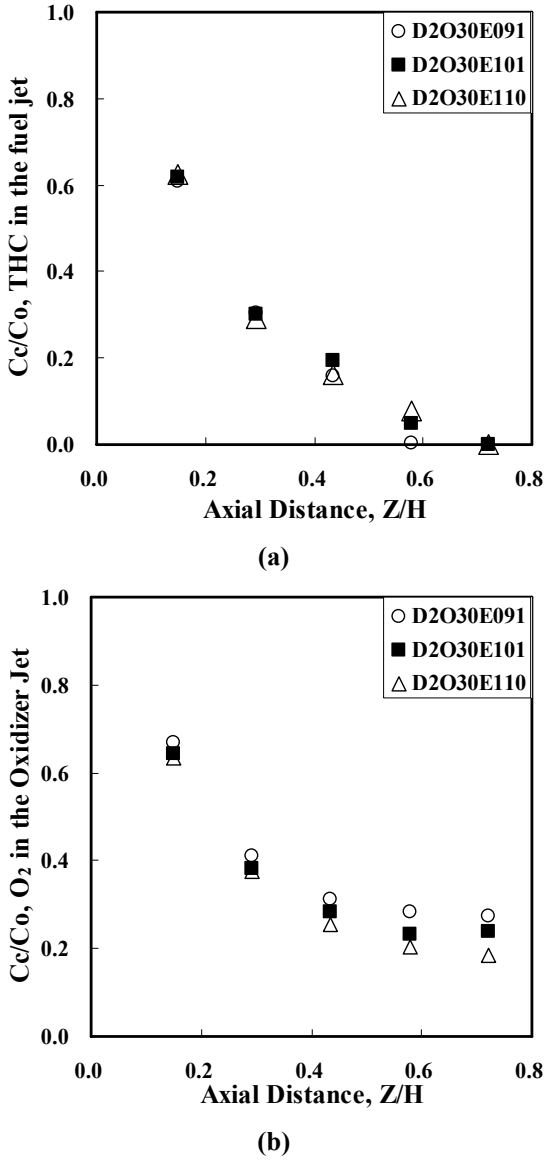

Figure 6.33: The centerline concentration of the (a) THC in the fuel jet and (b) oxygen in the oxidizer jet for different overall equivalence ratios.

Figure 6.34 shows the scaled values of the THC and oxygen concentration in the fuel and oxidizer jet centerline, respectively. It is observed that the THC falls down while oxygen concentration increases along with axial distance, which means that the recirculation of oxidizer flow occur toward the region of the fuel jet. The steeper slope of the oxygen concentration indicates more active recirculation of the oxidizer flow and slow decay of the oxygen concentration. The slope becomes steeper with decrease of the equivalence ratio because the oxidizer jet momentum increases with low equivalence ratio. As a result, the THC falls faster and the oxygen concentration shows higher value for $\Phi_{overall}$=0.9 due to strong recirculation of the oxidizer flow.

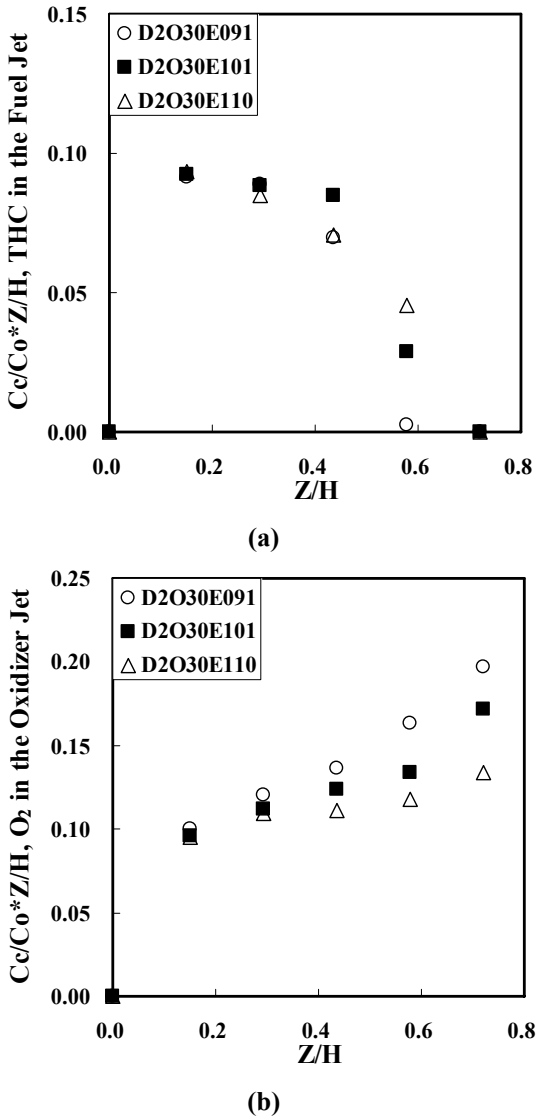

Figure 6.34: The scaled centerline concentrations of (a) THC in the fuel jet and (b) oxygen in the oxidizer jet for different overall equivalence ratios.

Jet entrainment

For investigation of the jet entrainment, CO_2 concentrations in the fuel and oxidizer jet centerline are shown in Figure 6.35. CO_2 is one of the combustion products and a good gauge for jet entrainment. The difference between cases is small as seen in Figure 6.35, however, less CO_2 is found in both of the fuel and oxidizer jet centerline for $\Phi_{overall}$=0.9. It might be thought that the excess oxygen remains and strong recirculation of the oxidizer flow occurs toward the fuel jet for low equivalence ratio, thus the other gas concentrations becomes less. However, the difference is very small, and lots of CO_2 are found in each jet centerline for all cases, which indicates the sufficient recirculation of product gases in the furnace chamber.

Radial gas composition profiles

The radial THC concentration profiles for different equivalence ratios are shown in Figure 6.36. It is observed that the profiles are initially almost identical for all cases, however, the difference occurs at the region of the fuel jet from Z/H=0.44. As the equivalence ratio decreases, the THC concentration decays faster. This might be thought that the oxidizer jet momentum increases with lower equivalence ratio, and hence the oxidizer jet is able to penetrate into the region of the fuel jet more easily with increase of momentum. As a result, the THC concentration in the fuel jet centerline falls faster with lower equivalence ratio. It is noted that the THC concentration is not detected at Z/H=0.72 for all cases as shown in Figure 6.36 (d).

The radial oxygen concentration profiles for different equivalence ratios are shown in Figure 6.37. The oxygen concentration is higher with decrease of the equivalence ratio, and spreads more laterally. It can be attributed the fact that the oxidizer jet momentum increases with lower equivalence ratio, and hence the oxidizer jet is bale to penetrate into the region of the fuel jet more easily with increase of momentum. As a result, the oxygen concentration spreads more widely with lower equivalence ratio. Another reason is that the available oxygen exists more with low equivalence ratio due to excess supply of oxidizer. Therefore, the oxygen concentration is higher with lower equivalence ratio.

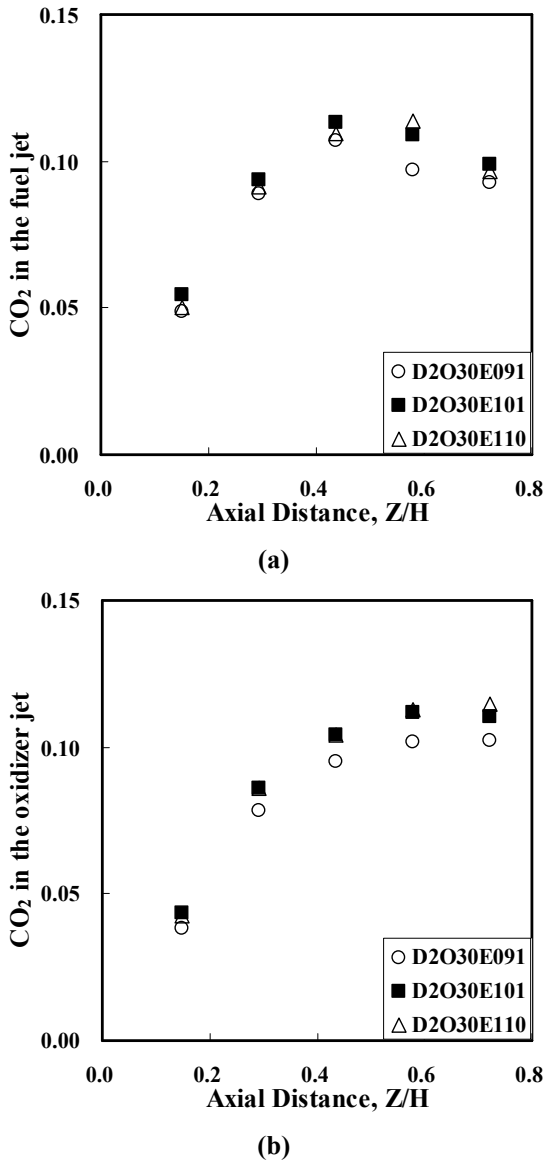

Figure 6.35: The centerline carbon dioxide concentration in the (a) fuel jet and (b) oxidizer jet for different overall equivalence ratios.

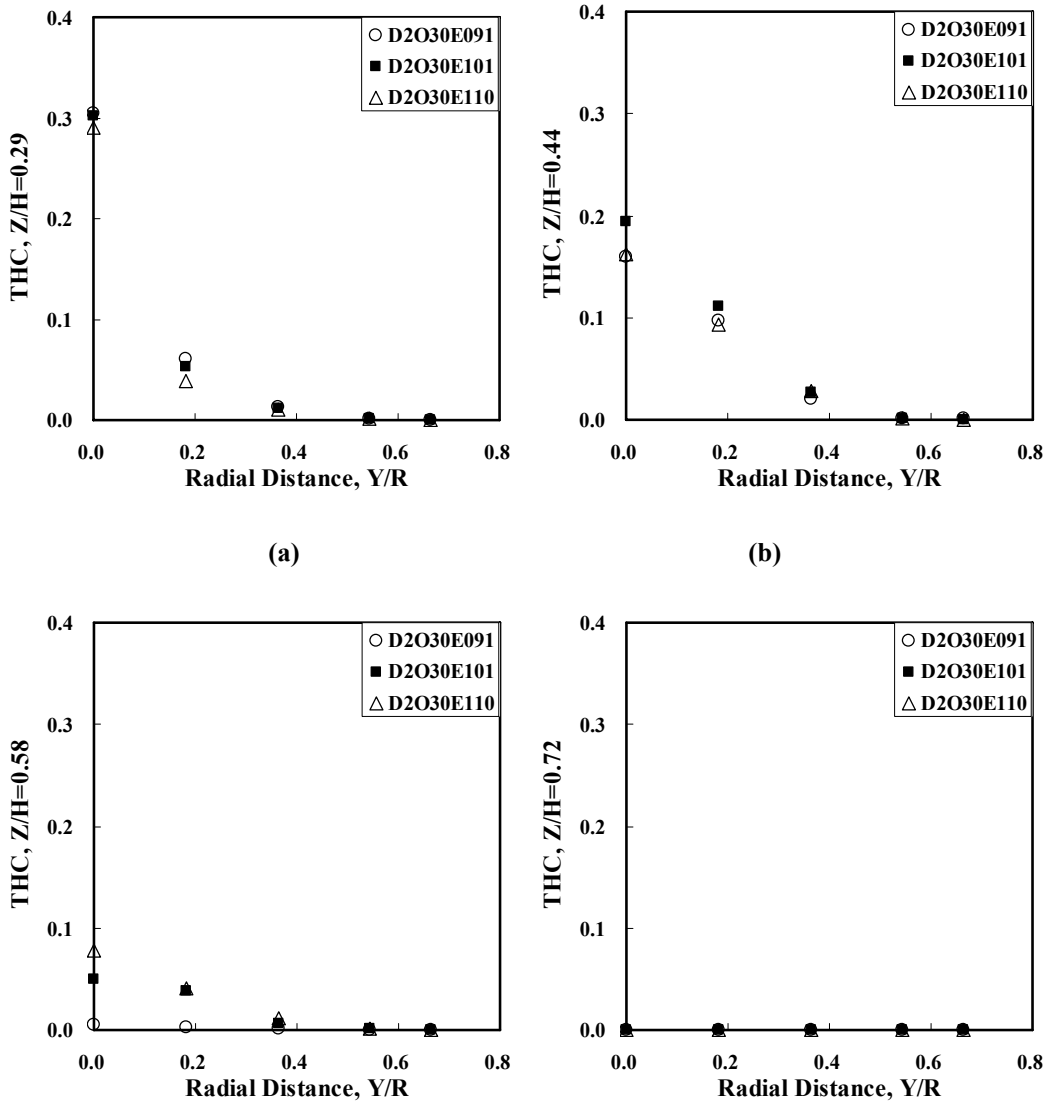

Figure 6.36: The radial THC concentration profiles at (a) *Z/H*=0.29 (b) *Z/H*=0.44 (c) *Z/H*=0.58 (d) *Z/H*=0.72 for different overall equivalence ratios.

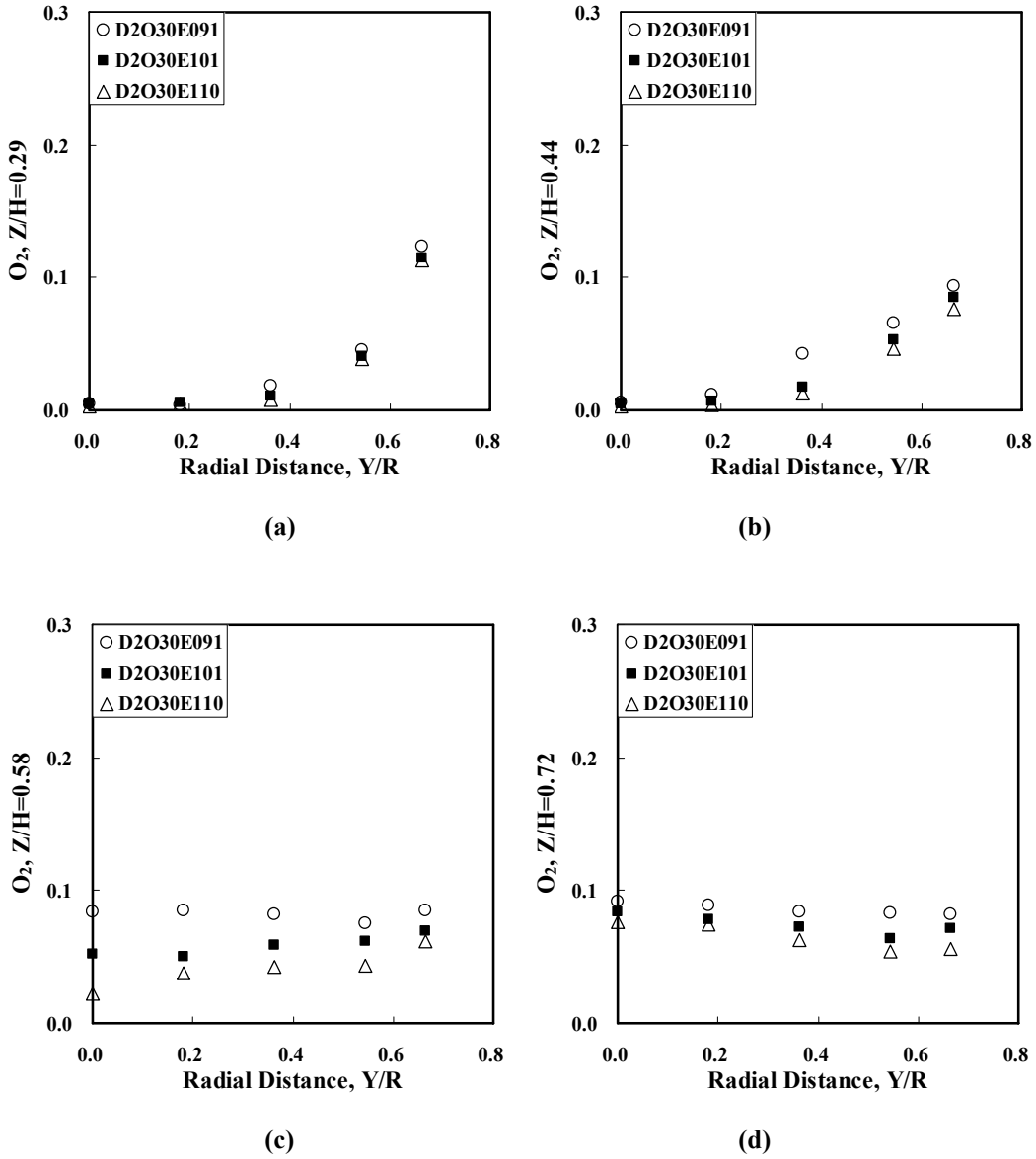

Figure 6.37: The radial oxygen concentration profiles at (a) *Z/H*=0.29 (b) *Z/H*=0.44 (c) *Z/H*=0.58 (d) *Z/H*=0.72 for different overall equivalence ratios.

The radial carbon dioxide concentration profiles for different equivalence ratios are shown in Figure 6.38. As shown in Figure 6.38, the CO_2 concentrations are quite flat for all equivalence ratios. This indicates the strong recirculation of product gases and uniform reaction in entire region of the furnace. It is observed that the difference between $\Phi_{overall}$=1.0 and 1.1 is quite small, whereas lowest equivalence ratio, $\Phi_{overall}$=0.9, shows less amount of CO_2 because of the excess supply of oxidizer.

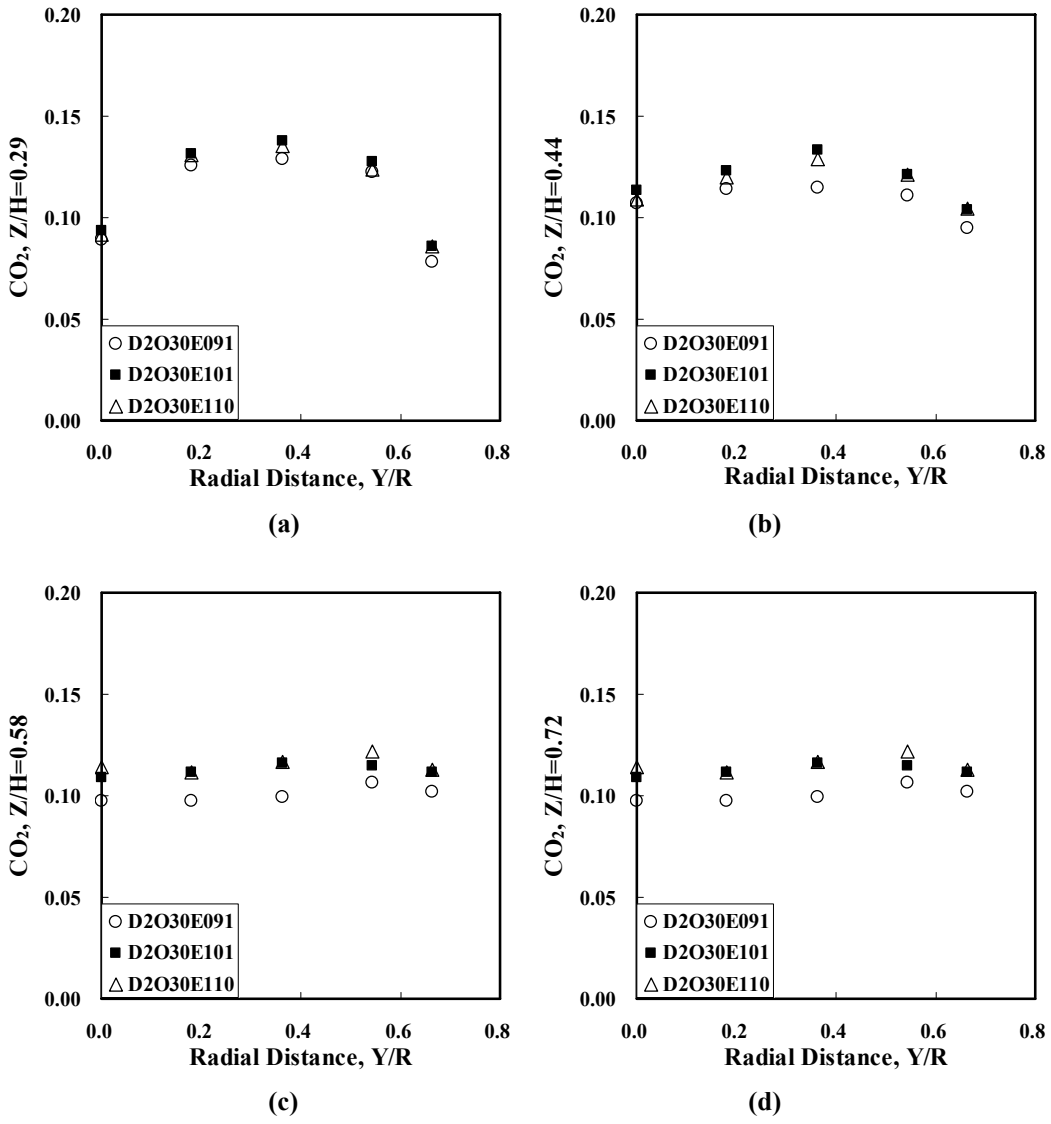

Figure 6.38: The radial carbon dioxide concentration profiles at (a) *Z/H*=0.29 (b) *Z/H*=0.44 (c) *Z/H*=0.58 (d) *Z/H*=0.72 for different overall equivalence ratios.

Figure 6.39 shows the radial CO profiles along with the axial distance with different equivalence ratios. It is observed that high CO concentration is shown near the fuel jet region which is overly rich for all cases. In temperature and gas compositions, the difference between cases is quite small. Thus, it can be expected similar radial CO concentration profiles, however, the case of $\Phi_{overall}$=0.91 shows higher CO than other cases up to *Z/H*=0.44 and lower CO after *Z/H*=0.58 while the case of $\Phi_{overall}$=1.01 and 1.10 show quite similar trend and value of CO concentration. This might be thought that high oxidizer jet momentum with low equivalence ratio could enhance the jet entrainment

and mixing intensity, however, the O_2 concentration in the re-circulating flow at upstream region also increase. Therefore, the presence of excess oxygen promotes the reaction at upstream region for the lean case [66], and hence the temperature and formation of CO increase. On the other hand, the dilution of the jets increases at further downstream region because of large scale of recirculation of the flow and hence the production of CO decreases.

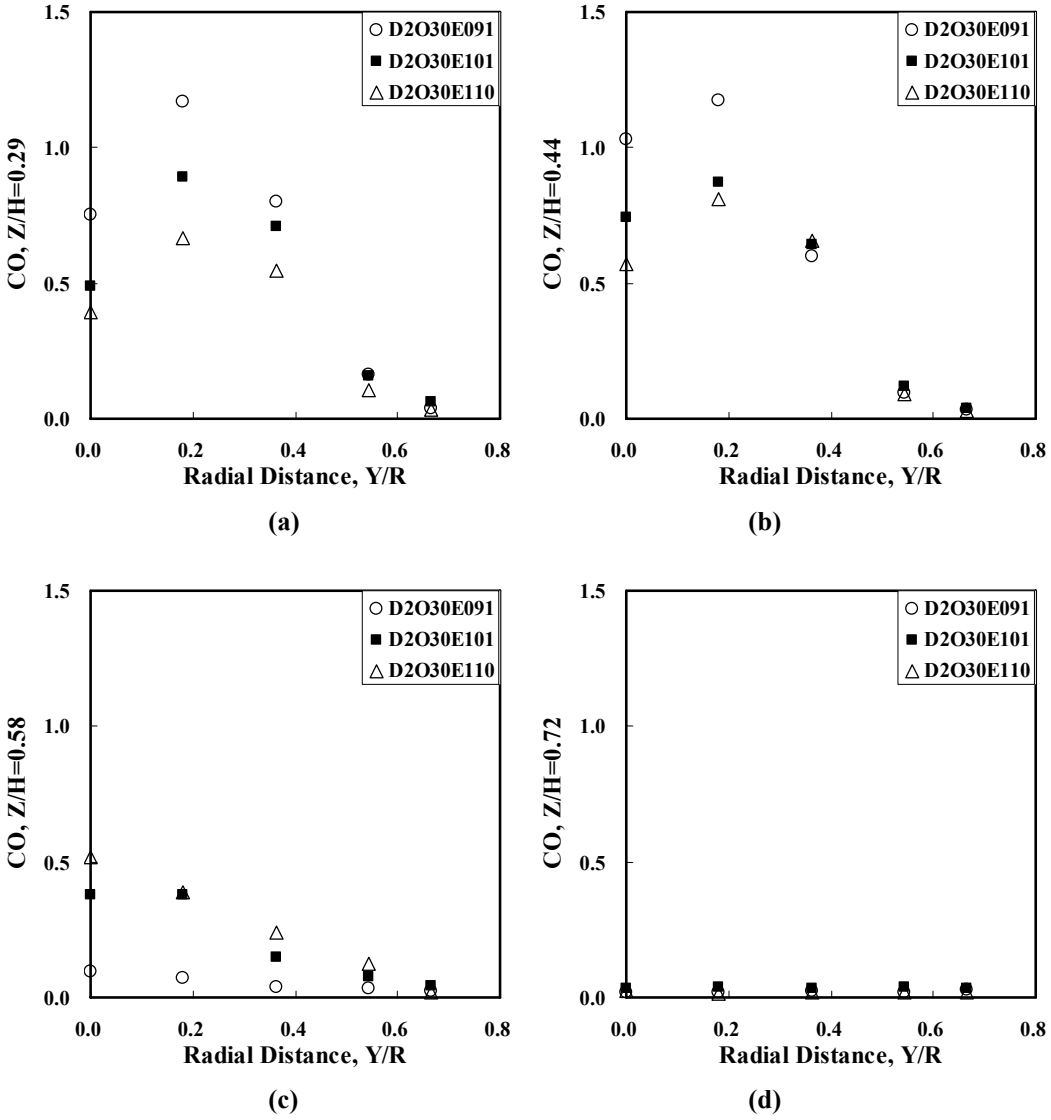

Figure 6.39: The radial carbon monoxide concentration profiles at (a) *Z/H*=0.29 (b) *Z/H*=0.44 (c) *Z/H*=0.58 (d) *Z/H*=0.72 for different overall equivalence ratios.

6.3. Elements & Heat balances for experiments on reacting flow

The current furnace configuration in this study does not provide a proper arrangement for measuring the exhaust gas compositions. However, the exhaust gas compositions might be estimated by substituting the mean gas concentrations of 4 probing points at *Z/H*=0.72 where are nearest to the exhaust vent of the chamber. Based on the temporal and spatial averaged temperature and product gas compositions near exhaust vent area, elements and heat balances are conducted as following,

Element Balance

Assuming measuring data of exhaust gas is correct, the reaction equation is,

$$\chi_{CH_4:In} + 2\chi_{CH_4:In}(O_2 + \frac{\chi_{N_2:ox}}{\chi_{O_2:ox}} N_2) + \alpha(O_2 + 3.76N_2) \rightarrow \chi'_{CH_4} CH_4 + \chi_{CO_2} CO_2 + \chi_{CO} CO + \chi_{O_2} O_2 + \chi_{H_2O} H_2O + \chi_{N_2} N_2 \quad (6\text{-}1)$$

Where, $\chi_{CH_4:In}$ is the input mole fraction of fuel, $\chi_{N_2:ox}$ is the injection mole fraction of nitrogen in the oxidizer jet, α is the air infiltration, and $\chi_{O_2:ox}$ is the injection mole fraction of oxygen in the oxidizer jet. In above equation, the methane mole fraction is measured on wet basis while mole fractions of CO_2, CO and O_2 are measured on dry basis, and the element mole fraction on wet and dry basis is expressed as χ and χ', respectively. In addition, the relational equations can be obtained from elements balance,

C balance, $\chi_{CH_4:In} = \chi'_{CH_4} + \chi_{CO_2} + \chi_{CO}$ (6-2)

O balance, $4\chi_{CH_4:In} + 2\alpha = 2\chi_{CO_2} + \chi_{CO} + 2\chi_{O_2} + \chi_{H_2O}$ (6-3)

H balance, $4\chi_{CH_4:In} = 4\chi'_{CH_4} + 2\chi_{H_2O}$ (6-4)

In addition, $\chi'_{CO_2} = \frac{\chi_{CO_2}}{1-\chi_{H_2O}}$, $\chi'_{CO} = \frac{\chi_{CO}}{1-\chi_{H_2O}}$, $\chi'_{O_2} = \frac{\chi_{O_2}}{1-\chi_{H_2O}}$ (6-5)

$\chi'_{CH_4} + \chi'_{CO_2} + \chi'_{CO} + \chi'_{O_2} + \chi'_{H_2O} + \chi'_{N_2} = 1.0$ (6-6)

Solving above equations, the amount of air infiltration in the furnace, α , can be calculated and the results are summarized in Table 6.4 and Figure 6.40. The amount of air infiltration is estimated in the range of 2.9 ~ 3.92 times the fuel input flow rate within 7 % discrepancy in amount of mole fraction of N_2, which indicates the error in calculations or measuring exhaust gas compositions. It might be thought that infiltrated air can not affect significantly the combustion in the main reaction zone because the infiltrated air would stay mainly in the bottom of the furnace due to lower temperature than that of the above main reaction zone.

Case No.	Air infiltration flow rate/Fuel flow rate
D1O30E100(H)	3.27
D1O31E110(H)	3.35
D2O21E103(H)	3.92
D2O30E091(NH)	3.23
D2O30E101(H)	3.23
D2O30E110(H)	3.47
D2O41E102(NH)	3.47
D3O29E099(T)	3.19
D3O31E110(T)	2.91

Table 6.4: Estimated air infiltration flow rate.

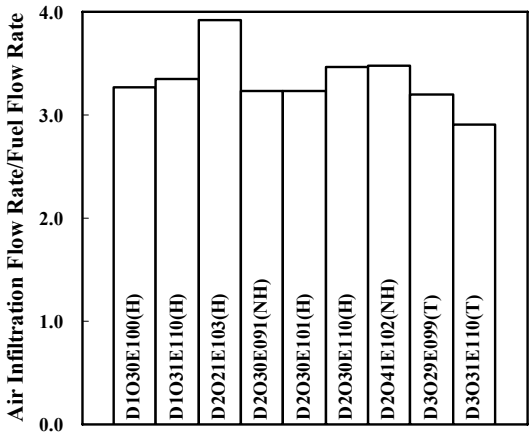

Figure 6.40: Estimated air infiltration flow rate.

Assuming all reacted oxygen appears in CO_2, CO and H_2O, the amount of non-reacted oxygen concentration is almost 0.0% of total remained oxygen mole fraction in exhaust gas for most cases except lean cases. Therefore, it might be concluded that the oxygen concentration in exhaust gas results from mainly air infiltration in the furnace. However,

low equivalence case (lean condition) shows that about 24% of oxygen concentration in exhaust gas is from non-reacting with fuel, which is the excess oxidizer, as expected. The estimated amount ratio of oxygen concentration due to non-reacting and air infiltration is summarized in Table 6.5.

Case No.	Non-reacting oxygen	Air infiltration oxygen
D1O30E100(H)	0.01	0.99
D1O31E110(H)	0.00	1.00
D2O21E103(H)	0.00	1.00
D2O30E091(NH)	0.24	0.76
D2O30E101(H)	0.00	1.00
D2O30E110(H)	0.00	1.00
D2O41E102(NH)	0.00	1.00
D3O29E099(T)	0.10	0.90
D3O31E110(T)	0.00	1.00

Table 6.5: The amount ratio of oxygen concentration in exhaust gas.

Heat Balance

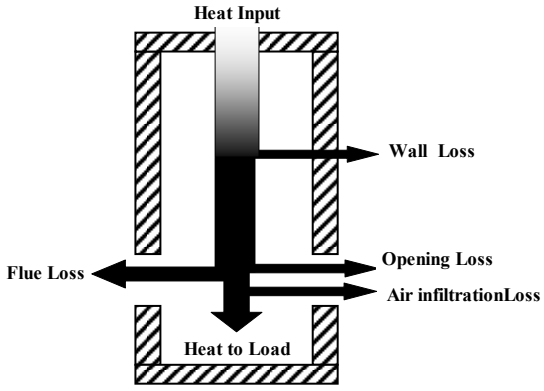

Figure 6.41: Heat losses in the furnace

The heat input is transferred to product, heat sink in this study, and heat losses in different areas and forms as shown in Figure 6.41. The heat losses include losses from wall, radiation losses from openings, heat carried by the cold air infiltration into the furnace. For estimating the amount of the heat losses in the furnace, heat balance of the furnace is analyzed as shown Fig based on the temporal and spatial averaged temperature and product gas compositions near exhaust vent area.

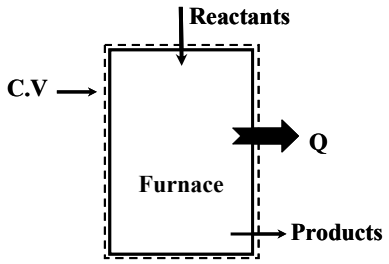

$$Q = \dot{n}_{Fuel}(H_R - H_P) = Q_{\text{Heatsink}} + Q_{\text{Losses}} \tag{7}$$

$$H_R = \sum n_R(\bar{h})_R,\ H_P = \sum n_P(\bar{h} + \Delta h)_P \tag{8}$$

$$Q_{Flue} = \dot{n}_{Fuel} \sum n_P(\Delta h)_P \tag{9}$$

where, the subscripts R and P refer to the reactants and products, respectively.

In calculating the heat losses from wall, the heat transfer coefficient can be obtained from thermal network. However, the heat transfer coefficient for convection is very small because of small Reynolds number of exhaust gas flow. Whatever the temperature of outgoing exhaust flow is, the heat losses of convection and conduction is very small comparing with other heat losses, less than 1.0 Kw which corresponds to 1.6% of heat input. The radiation heat losses from openings can be calculated from view factor between openings with emissivity for furnace inside, ε=1.0.

The results of heat balances for experiments are summarized in Table 6.6 and Figure 6.42. In this table and figure, all heat loss amounts are expressed as the ratio to heat input.

Heat loss ratio to Heat input

Case	Heat Sink	Heat Flue Gas	Heat Loss(Cond+Rad)	Error
D1O30E100(H)	0.53	0.36	0.06	0.05
D1O31E110(H)	0.56	0.35	0.06	0.03
D2O21E103(H)	0.47	0.46	0.06	0.01
D2O30E091(NH)	0.48	0.40	0.06	0.06
D2O30E101(H)	0.47	0.38	0.07	0.08
D2O30E110(H)	0.47	0.38	0.07	0.08
D2O41E102(NH)	0.48	0.35	0.07	0.10
D3O29E099(T)	0.45	0.42	0.07	0.05
D3O31E110(T)	0.43	0.42	0.08	0.07

Table 6.6: Heat balances for the furnace.

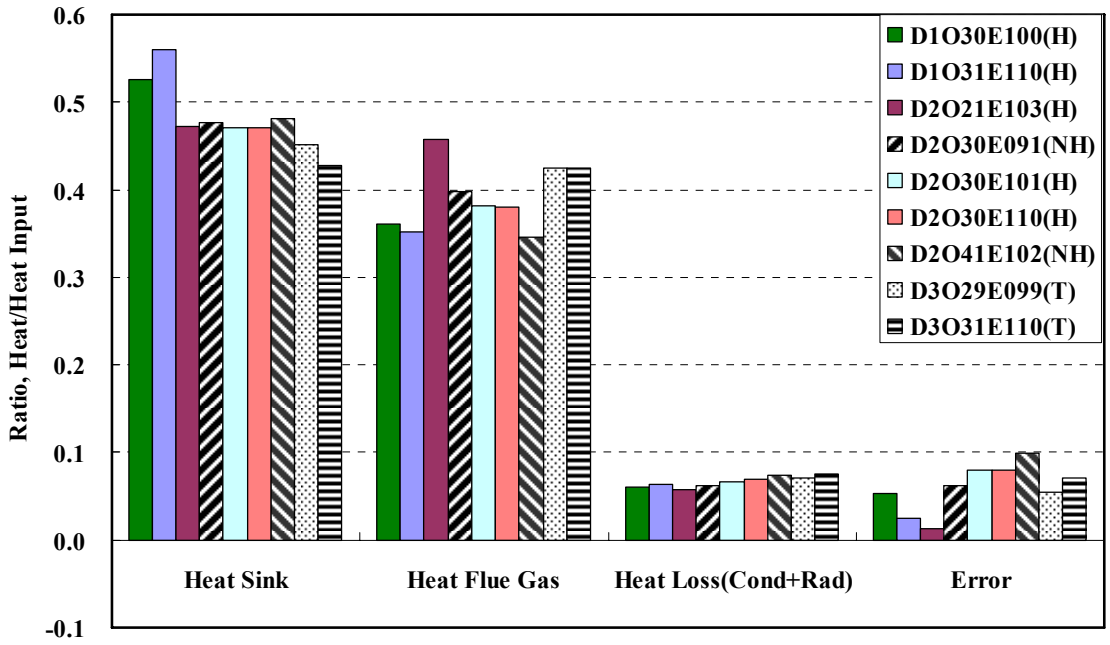

H: Homogeneous Mode, NH: Non-Homogeneous Mode, T: Transient

Figure 6.42: Heat balances for the furnace.

It is seen from Fig that approximately 48% of heat input is transferred to heat sink, 40% flows out of the furnace, and 7% is heat losses from the furnace to surroundings in the forms of conduction and radiation through the furnace walls and openings. The remains of heat input is the error in estimating heat balances that is less than 10%.

Heat Loss due to air infiltration

Another heat loss in the furnace results from the air infiltration. The cold air becomes heated to the furnace exhaust gas temperature and then exits through the flue system, wasting valuable fuel. The heat loss due to air infiltration is estimated about 10% of heat input for most cases as shown in Table 6.7 and Figure 6.43.

Case No.	Heat loss (Air infiltration) ratio to Heat input
D1O30E100(H)	0.10
D1O31E110(H)	0.10
D2O21E103(H)	0.11
D2O30E091(NH)	0.10
D2O30E101(H)	0.10
D2O30E110(H)	0.11
D2O41E102(NH)	0.11

D3O29E099(T)	0.10
D3O31E110(T)	0.10

Table 6.7: Heat loss due to air infiltration in the furnace.

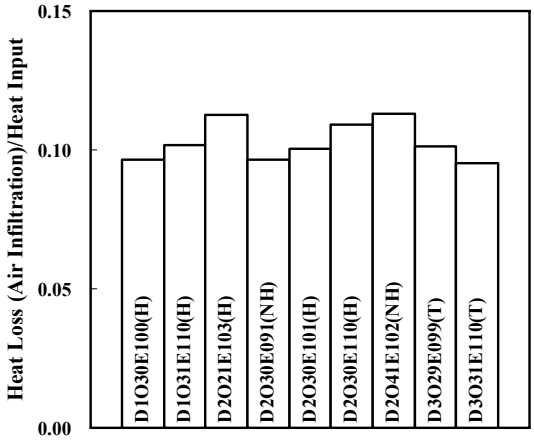

Figure 6.43: Heat loss due to air infiltration in the furnace.

CHAPTER 7

Numerical methods for reacting flows

7.1. Combustion Model

There are two kinds of combustion models implemented in FDS, which are the mixture fraction and finite rate reaction model. A conserved quantity, mixture fraction *Z*, is introduced in the first model. This quantity represents the mass fraction of gas mixture at a given point, and has the value of 1 for pure fuel and 0 for air by definition. The notable advantage of the mixture fraction model is that the mass fraction of all reactants and products can be simply tabulated from the empirical state relations, thus saving in simulation time. On the other hand, all gas species are defined by each reaction rate equation and tracked individually in the finite rate reaction model, as a result, more computation times and resources are inevitable. The combustion process can be evaluated by simplified global single step reaction or more detailed kinetics for different engineering applications in the finite rate reaction model.

Figure 7.1 and 7.2 shows the comparison of mixture fraction and finite reaction models for the case of d_{ox}=15.9 mm, $X_{O2;ox}$=0.21 and $\Phi_{overall}$ =1.0. It is observed that the mixture fraction model over-predicts the centerline temperature of the fuel jet, whereas the finite rate model shows a good agreement with the experimental data. An explanation for over-predicting the temperature in mixture fraction model is that the heat release rate per unit area (HRRPUA) should be prescribed at fuel side in mixture fraction model to sustain the reaction. Thus, the mixture fraction model is not suitable for simulating the current configuration where the fuel and oxidizer jet are injected separately with large separation distance between jets into the combustion chamber. On the other hand, the reaction occurs based on the feedback of temperature and gas species concentrations in finite rate

reaction model, thus it is more close to real combustion process.

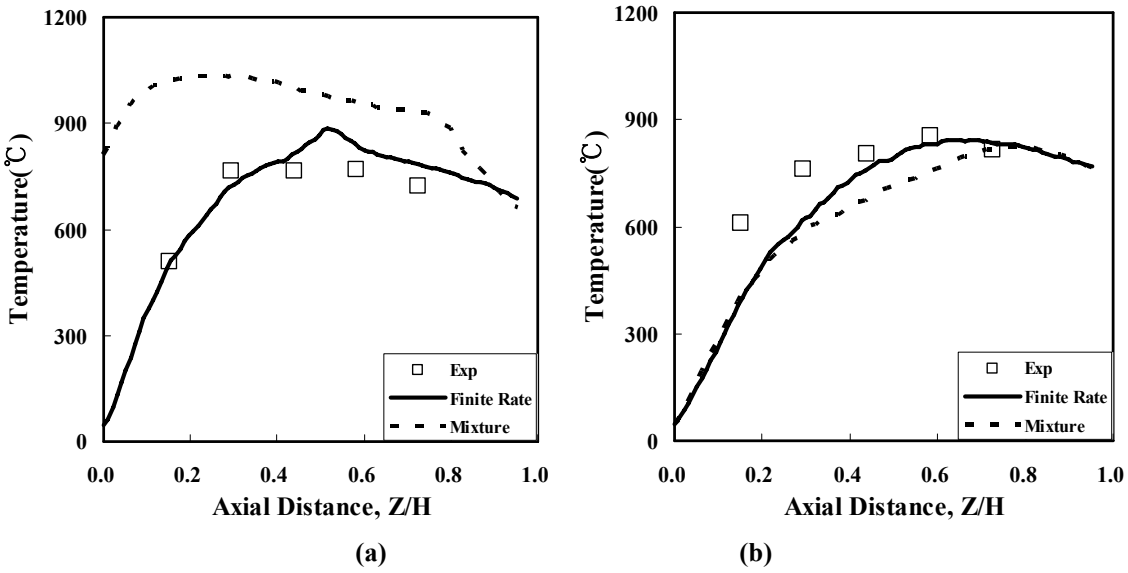

Figure 7.1: Comparison of the mixture fraction and finite rate reaction model for the centerline temperature of the (a) fuel jet and (b) oxidizer jet with d_{ox}=15.9 mm, $X_{O2;ox}$=0.21 and $\Phi_{overall}$ =1.0, and compared with experimental data.

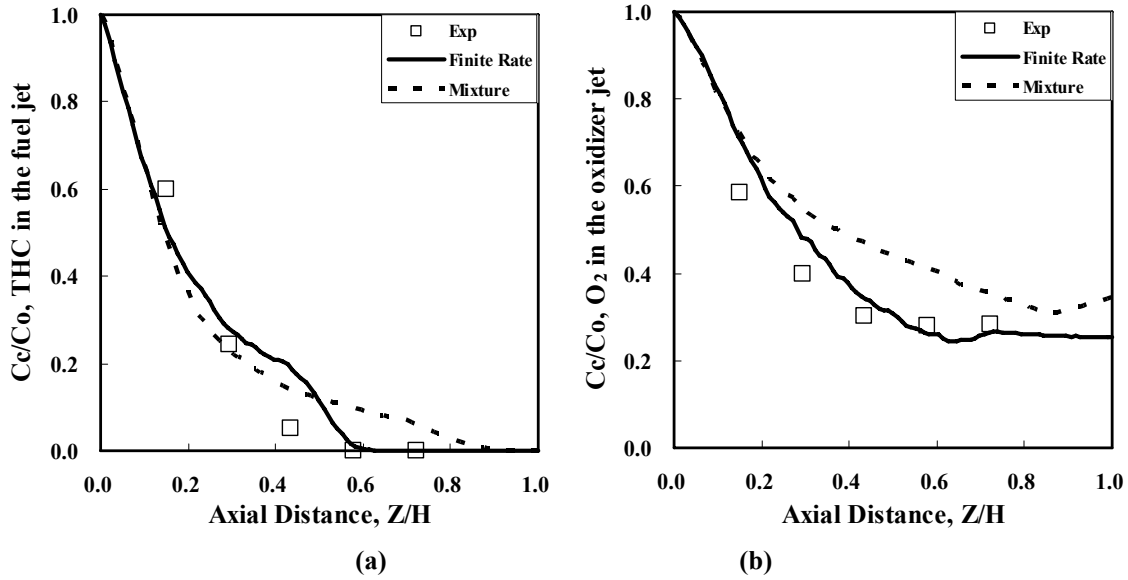

Figure 7.2: Comparison of the mixture fraction and finite rate reaction model for the decay patterns of the centerline (a) methane in the fuel jet and (b) oxygen concentration in the oxidizer jet with d_{ox}=15.9 mm, $X_{O2;ox}$=0.21 and $\Phi_{overall}$ =1.0, and compared with experimental data.

7.2. Finite-Rate Reaction model

Considering the reaction of methane and oxygen, the following single-step expression would be suggested for the global reaction,

$$\nu_{CH_4} CH_4 + \nu_{O_2} O_2 \rightarrow \nu_{CO_2} CO_2 + \nu_{H_2O} H_2O \tag{7-1}$$

$$\frac{d[CH_4]}{dt} = -A[CH_4]^a [O_2]^b e^{-E/RT} \tag{7-2}$$

Where, A is a constant termed the pre-exponential factor and E is the activation energy, and the values of exponents A, a, b and activation energy E are given in [71]. It would be possible to implement a multi-step set of reactions for more accurate prediction of the combustion behaviors in finite rate reaction model. For this purpose, carbon monoxide oxidation reaction is adopted in the finite reaction model as expressed in equation (7-3) and (7-4), and also compared with single-step reaction model for the case of d_{ox}=31.8 mm, $X_{O2;ox}$=0.30 and $\Phi_{overall}$ =1.0. as shown in Figure 7.3 to 7.6.

$$CH_4 + 1.5O_2 \rightarrow CO + 2H_2O, \quad \frac{d[CH_4]}{dt} = -A_1[CH_4]^{a_1} [O_2]^{b_1} e^{-E_1/RT} \tag{7-3}$$

$$CO + 0.5O_2 \rightarrow CO_2, \quad \frac{d[CO]}{dt} = -A_2[CO]^{a_2} [O_2]^{b_2} e^{-E_2/RT} \tag{7-4}$$

It is observed that the difference between two models is quite small and there is no advantage to add carbon monoxide oxidation in finite reaction model. This might be thought that the amount of carbon monoxide produced in the combustion chamber is relatively small comparing to other major combustion product gases, especially in large scale of fire such as the current configuration. Even though the global reaction model can not provide the details of combustion, it is still useful for approximate engineering evaluation. Compromising the accuracy in prediction and computation time, it can be conclude that one step reaction model is able to simulate the current configuration. According to technical documents of FDS, the computation time will increase about 5% for adding each additional reaction.

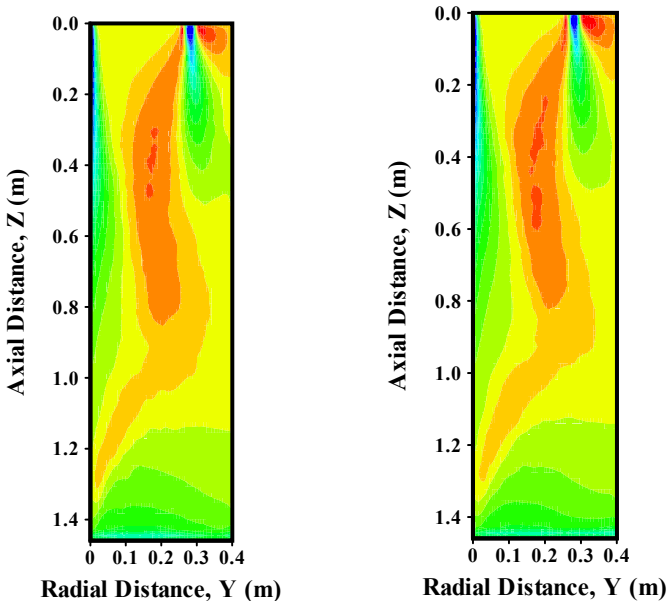

Figure 7.3: Comparison of the (a) single-step and (b) two-step model with carbon monoxide oxidation in finite rate reaction model for the temperature contour profile with d_{ox}=31.8 mm, $X_{O2;ox}$=0.30 and $\Phi_{overall}$ =1.0.

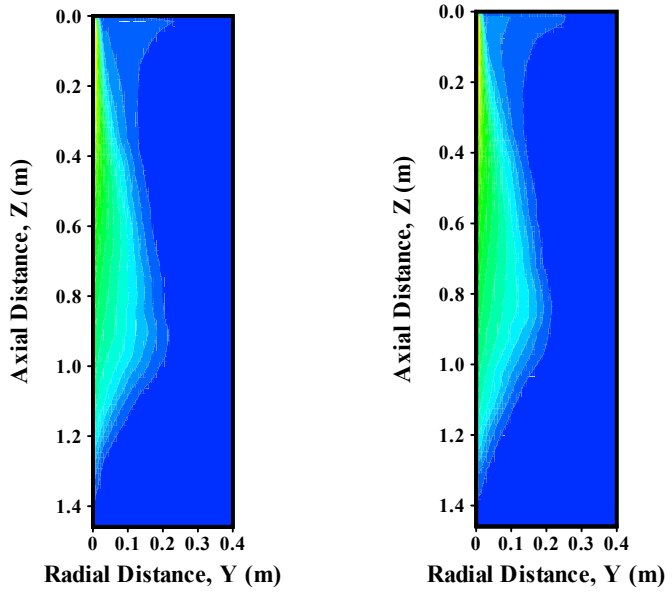

Figure 7.4: Comparison of the (a) single-step and (b) two-step model with carbon monoxide oxidation in finite rate reaction model for the methane concentration contour profile with d_{ox}=31.8 mm, $X_{O2;ox}$=0.30 and $\Phi_{overall}$ =1.0.

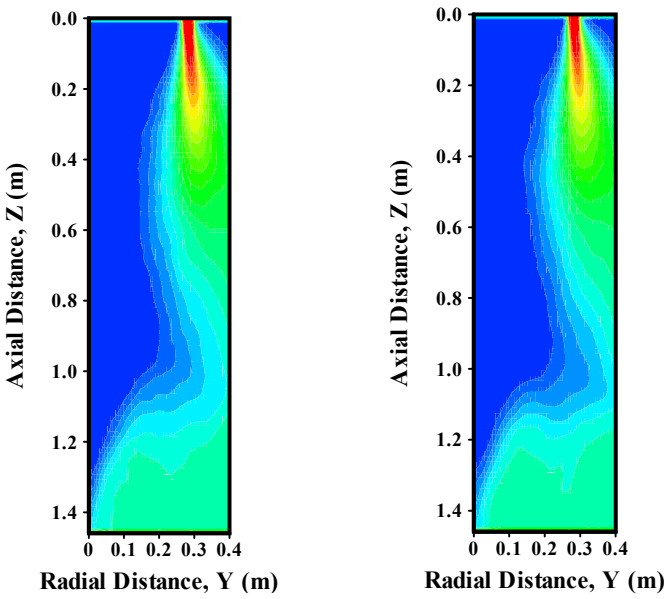

Figure 7.5: Comparison of the (a) single-step and (b) two-step model with carbon monoxide oxidation in finite rate reaction model for the oxygen concentration contour profile with d_{ox}=31.8 mm, $X_{O2;ox}$=0.30 and $\Phi_{overall}$ =1.0.

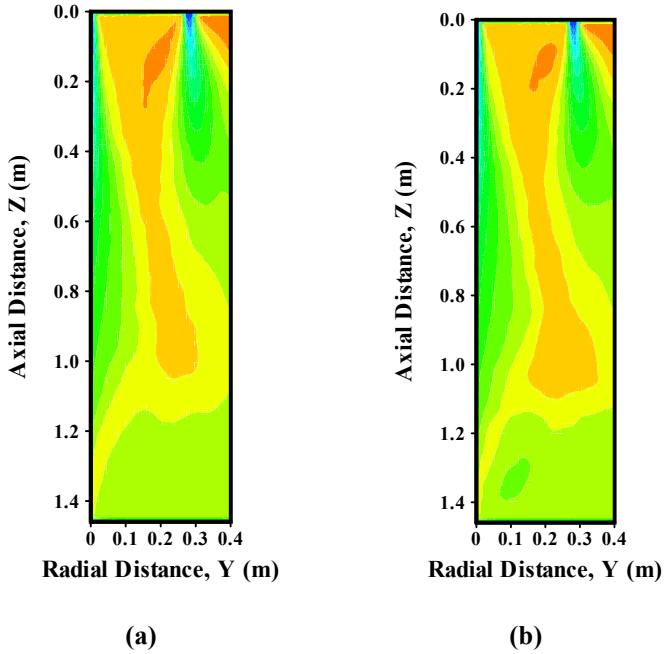

Figure 7.6: Comparison of the (a) single-step and (b) two-step model with carbon monoxide oxidation in finite rate reaction model for the carbon dioxide concentration contour profile with d_{ox}=31.8 mm, $X_{O2;ox}$=0.30 and $\Phi_{overall}$ =1.0.

7.3. Thermal Radiation

It is possible to assume the lightly sooting fuel such as methane as a gray medium that is independent of wavelength because soot has a continuous radiation spectrum and can be considered as a non-scattering material. Thus, the mean absorption coefficient can be reasonably used in the Radiation Transport Equation (RTE). The RTE for a non-scattering gray gas is expressed as,

$$\mathbf{S}\bullet\nabla I_{\lambda}(\mathbf{X},\mathbf{S}) = \kappa(\mathbf{X},\lambda)\left[I_b(\mathbf{X}) - I_{\lambda}(\mathbf{X},\mathbf{S})\right] \tag{7-5}$$

Where, $I_{\lambda}(\mathbf{X},\mathbf{S})$ is the radiation intensity at wavelength λ, $\mathbf{S}$ is the direction vector of the intensity, $\kappa(\mathbf{X},\lambda)$ is the local absorption coefficient and $I_b(\mathbf{X})$ is the source term given by the Planck function. The radiation spectrum can be divided into several discrete bands, and an individual RTE is derived as,

$$\mathbf{S}\bullet\nabla I_n(\mathbf{X},\mathbf{S}) = \kappa_n(\mathbf{X})\left[I_{b,n}(\mathbf{X}) - I_n(\mathbf{X},\mathbf{S})\right],\ n = 1..N \tag{7-6}$$

Where I_n is the intensity integrated over the band n, κ_n is the mean absorption coefficient for each band, and the source term can be expressed as a fraction of the black body radiation.

$$I_{b,n} = F_n(\lambda_{\min},\lambda_{\max})\sigma T^4/\pi \tag{7-7}$$

Where, σ is the Stefan-Boltzmann constant. The use of mean absorption coefficient κ_n results in reducing the amount of computation considerably since the values of κ_n is pre-calculated in FDS by employing RADCAL [72]. Thus, total intensity is calculated by summing all individual bands

$$I(\mathbf{X},\mathbf{S}) = \sum_{n=1}^{N} I_n(\mathbf{X},\mathbf{S}) \tag{7-8}$$

In this study, the six spectral bands are implemented with 100 solid angles for a gray gas as shown in Table 7.1.

ν (1/cm)	10000	3800	3400	2400	2174	1000	50
λ (μm)	1.00	2.63	2.94	4.17	4.70	10.0	200

6 Band	1	2	3	4	5	6
Major Species	Soot	CO_2 H_2O Soot	CH_4 Soot	CO_2 Soot	H_2O CH_4 Soot	Soot

Table 7.1: Limits of the spectral bands for 6 band model in FDS.

As described in Equation (7-7), the radiative source term depends on the temperature raised to the fourth power. Therefore, inaccurate computation of temperature results in large error in the radiation calculation, especially temperatures inside the flame zone are under-estimated if the spatial resolution is not sufficient to resolve the flame since the flame sheet occupies only a small fraction of the cell volume. To compensate for this limitation, FDS provides two options for the calculation of the source term inside the flame zone:

$$\kappa I_b = \begin{cases} \kappa\sigma T^4/\pi & \textit{Outside flame zone} \\ \max(\chi_r \dot{q}'''/4\pi,\ \kappa\sigma T^4/\pi) & \textit{Inside flame zone} \end{cases} \tag{7-9}$$

Where, $\dot{q}'''$ is the heat release rate per unit volume and χ_r is the radiative fraction decided by an empirical estimation.

In addition, the radiation intensity leaving a gray diffuse wall is given as

$$I_w(\mathbf{S}) = \frac{\varepsilon\sigma T_w^4}{\pi} + \frac{1-\varepsilon}{\pi}\int I_w(\mathbf{S}')\left|\mathbf{S}'\cdot\mathbf{n}_w\right| d\mathbf{S}' \tag{7-10}$$

Where, $I_w(\mathbf{S})$ is the intensity at the wall, ε is the emissivity, and T_w is the wall temperature. The value of 0.9 is used for the wall emissivity, which is chosen from the material properties used for insulation of the furnace.

CHAPTER 8

Numerical investigations on the effects of control parameters for reacting flows and comparison with experimental data

In this chapter, the numerical investigations on the effects of control parameters on reacting flows are performed by using the Fire Dynamics Simulator (FDS) and also compared with experimental data. It is noted that the diameter of the fuel jet, volumetric flow rate of fuel and separation distance between jets are kept same with d_F=15.2 mm, $\dot{V}_F$ =0.0019 m^3/s and S=280 mm, respectively in this study. The values of control parameters are adjusted by changing the diameter, flow rate and inlet oxygen concentration of oxidizer jets.

8.1. Effects of the overall equivalence ratio on reacting flows

8.1.1. Velocity field

The radial velocity profiles at different axial positions for various overall equivalence ratios $\Phi_{overall}$=0.9, 1.0 and 1.1 with d_{ox} =15.9 mm and $X_{O2;ox}$ =0.30 are shown in Figure 8.1.

It is clearly observed that there are two large scales of recirculation pattern for all cases. One is formed between jets with relatively small scale near the jet exit region; the other is at the center jet region in lower part of the furnace. In general, it has been known that re-circulating flow exists as a stable part of the flow under certain circumstances [59-61]. The recirculation at interface region between jets initially occupies widely and becomes smaller and weaker along with the axial distance. After some distance from the jet exit, the recirculation at the center jet region becomes more noticeable.

The overall trend of velocity field for all cases is quite similar. However, the difference

between cases exists in onset point and magnitude of recirculation at the center region. As the overall equivalence ratio decreases, the recirculation at the center region occurs earlier and stronger as shown in Figure 8.1. This trend is also clearly shown in Figure 8.2 showing the scaled centerline stream-wise velocity of the fuel jet. The region and magnitude of negative velocity increase with lower overall equivalence ratio.

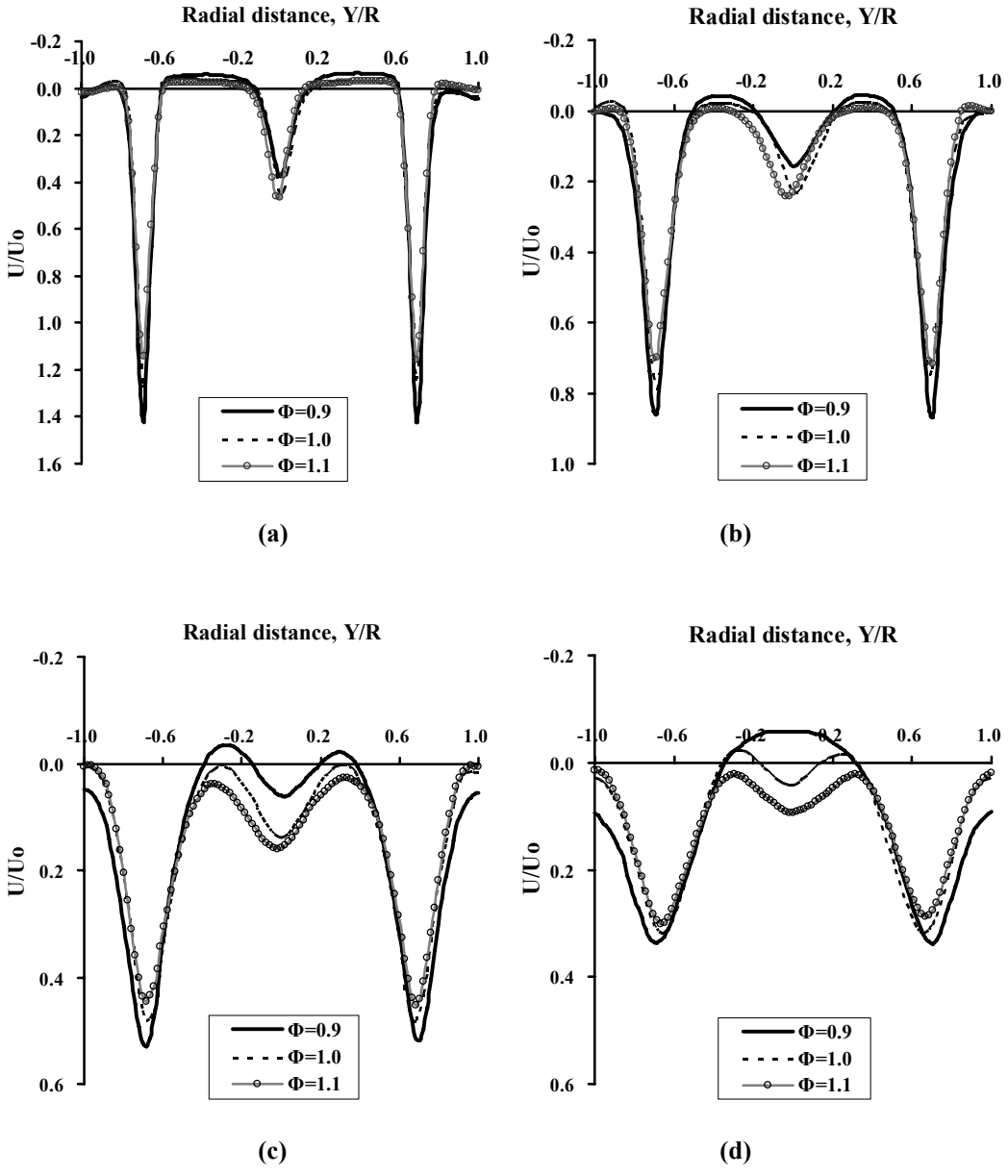

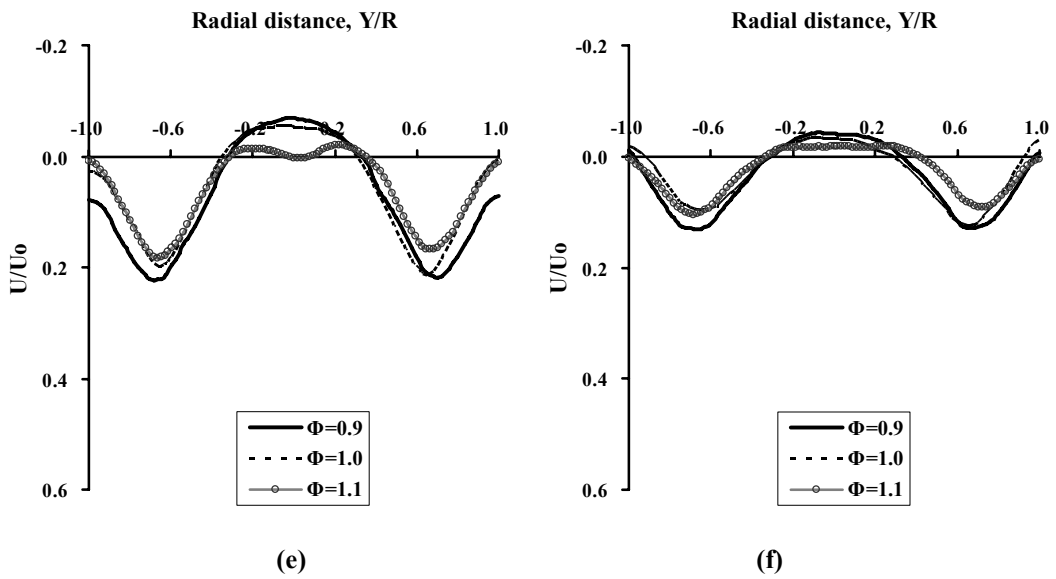

Figure 8.1: The radial stream-wise velocity profiles at different axial positions obtained from numerical calculations (a) *Z/H*=0.15, (b) *Z/H*=0.29, (c) *Z/H*=0.44, (d) *Z/H*=0.58, (e) *Z/H*=0.72 and (f) *Z/H*=0.86 for various overall equivalence ratios $\Phi_{overall}$= 0.9, 1.0 and 1.1 with d_{ox} =15.9 mm and $X_{O2;ox}$ =0.30.

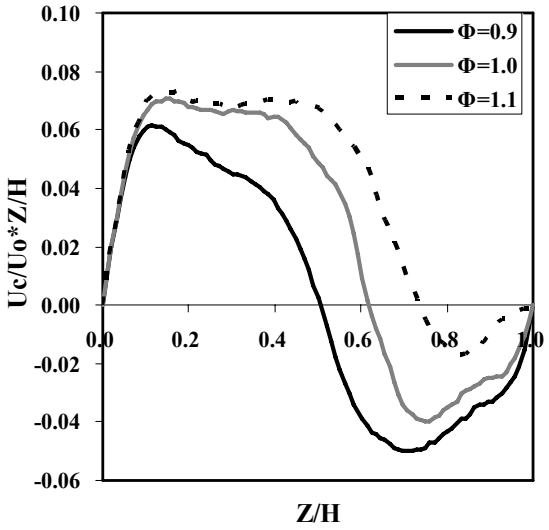

Figure 8.2: The scaled centerline stream-wise velocity of the fuel jet obtained from numerical calculations for various overall equivalence ratios $\Phi_{overall}$=0.9, 1.0 and 1.1 with d_{ox} =15.9 mm and $X_{O2;ox}$=0.30.

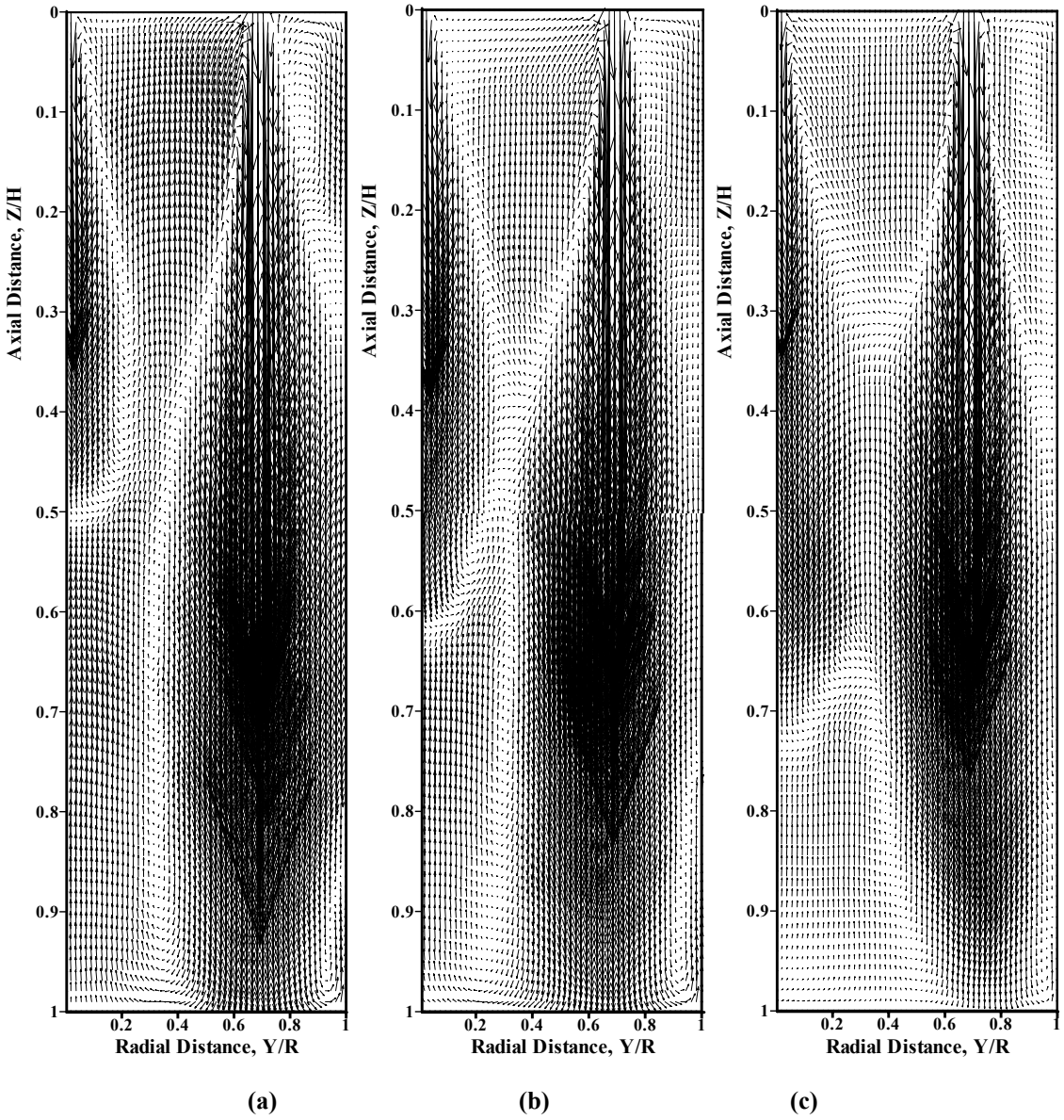

Figure 8.3: The velocity vector profiles of numerical calculations for various overall equivalence ratios (a) $\Phi_{overall}$ =0.9, (b) $\Phi_{overall}$ =1.0 and (c) $\Phi_{overall}$ =1.1 with d_{ox}=15.9 mm and $X_{O2;ox}$ =0.30.

Figure 8.3 shows the velocity vector profiles obtained from numerical calculations for various overall equivalence ratios $\Phi_{overall}$=0.9, 1.0 and 1.1 with d_{ox}=15.9 mm and $X_{O2;ox}$=0.30. It is observed that the fuel jet can expand more into the region of the oxidizer jet and farther downstream area of the furnace with higher equivalence ratio. The fuel jet reaches up to Z/H=0.48 for the case of $\Phi_{overall}$=0.9, while Z/H=0.6 and 0.72 for $\Phi_{overall}$=1.0 and1.1, respectively. This might be attributed the fact that the momentum of the oxidizer jet decreases with higher equivalence ratio due to less flow rate, thus the fuel

jet can penetrate more easily into the region of the oxidizer jet. In addition, the intensity of the velocity vectors in the recirculation zones increase with decrease of the overall equivalence ratio as shown in Figure 8.3. It might be thought that higher momentum of the oxidizer jet due to excess supply of oxidizers can enhance mixing intensity and entrainment, thus the large scale of recirculation pattern is formed earlier and its intensity also increases. This is well coincident with previous study on confined non-reacting multiple turbulent jets. The flow pattern from the side jets to the center jet is well established for small momentum ratio MR (ratio of center jet momentum to side jet momentum) because of high momentum of the side jets, thus the region of re-circulating flow is distributed widely at the center region.

8.1.2. Temperature

8.1.2.1. Jet Centerline Temperature

The centerline temperature of the jets obtained from experiments and numerical calculations for various overall equivalence ratios $\Phi_{overall}$ =0.9, 1.0 and 1.1 with d_{ox} =15.9 mm and $X_{O2;ox}$ =0.30 are shown in Figure 8.4.

The differences between the cases are not clearly shown in experimental data. However, the peak of the jet centerline temperature shifts slightly toward farther downstream with increase of the equivalence ratio in numerical calculations. In addition, the centerline temperature of the jet slightly increases with lower equivalence ratio up to Z/H=0.5, then opposite trend is shown at lower region of the furnace. This might be attributed the fact that the higher momentum of the oxidizer jet with low equivalence ratio could penetrate into the fuel jet region more easily at shorter distance from the jet exit, and enhance the mixing intensity and oxygen concentration in re-circulated flue gas. Therefore, the reaction rates increase near the jet exit region with the lower equivalence ratio [66].

On the other hand, the momentum of the oxidizer jets decreases with higher equivalence ratio, thus the fuel jet can reach more downstream region and penetrate more into the flow region of the oxidizer jets as shown in Figure 8.3. As a result, the reaction zone can be extended farther downstream region. However, the overall trend of the centerline temperature for all cases is quite similar in both experiments and numerical calculations. This might result from the selection of narrow range of the oxidizer jet momentum. The

range of the oxidizer jet momentum ratio to reference momentum of $\Phi_{overall}$ =1.0 is between 0.84 and 1.26 for $\Phi_{overall}$ =1.1 and 0.9, respectively, which is relatively close to each other comparing with those of other parameters.

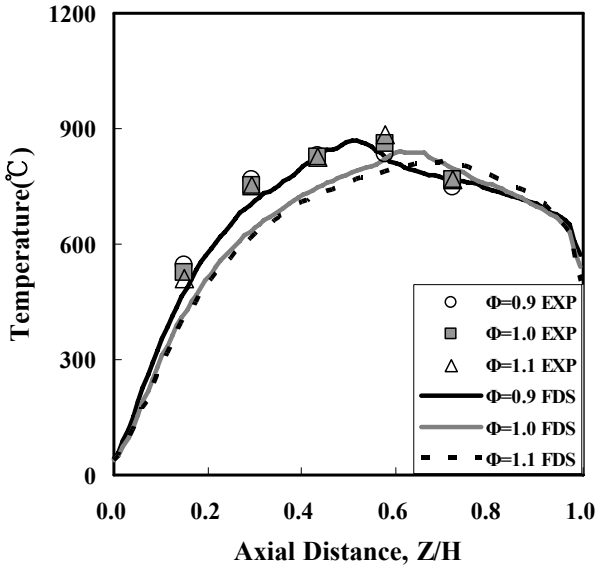

(a)

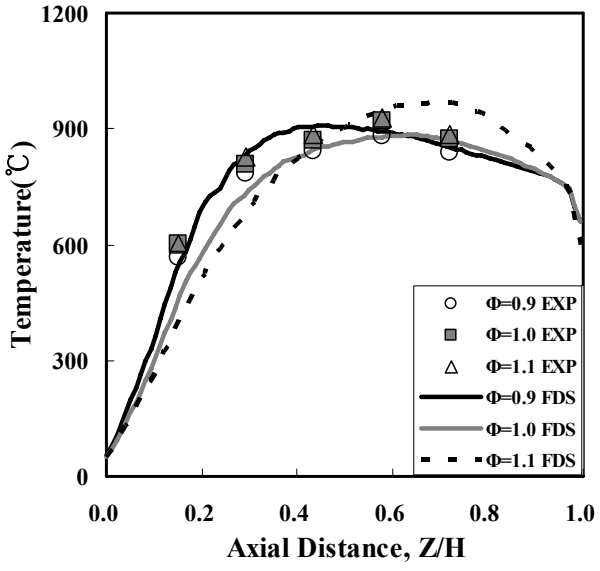

(b)

Figure 8.4: The centerline temperature of the (a) fuel jet and (b) oxidizer jet obtained from experiments and numerical calculations for various overall equivalence ratios $\Phi_{overall}$ =0.9, 1.0 and 1.1 with d_{ox}=15.9 mm and $X_{O2;ox}$ =0.30.

8.1.2.2. Radial Temperature Profiles along with axial distance

The contour temperature profiles for *Y-Z* plane and radial temperature profiles at different axial positions for various overall equivalence ratios $\Phi_{overall}$ =0.9, 1.0 and 1.1 with d_{ox}=15.9 mm and $X_{O2;ox}$ =0.30 are shown in Figure 8.5 and 6, respectively.

It is observed from Figure 8.5 that the region of high temperature shifts toward the oxidizer jet with increase of equivalence ratio, which is coincident with the expansion of the fuel jet due to decrease of oxidizer jet momentum. The radial temperature profiles initially show steep gradient near the jet exit *Z/H*=0.15, then becomes quite flat over the furnace domain as shown in Figure 8.6. The differences are not recognizable in experiments, while the temperature increases slightly with lower overall equivalence ratio up to middle range of the furnace in numerical calculations. It is quite same reason explained in the centerline temperature of the jets, increase of oxygen concentration in re-circulated flue gas due to high momentum of the oxidizer jet with low equivalence ratio.

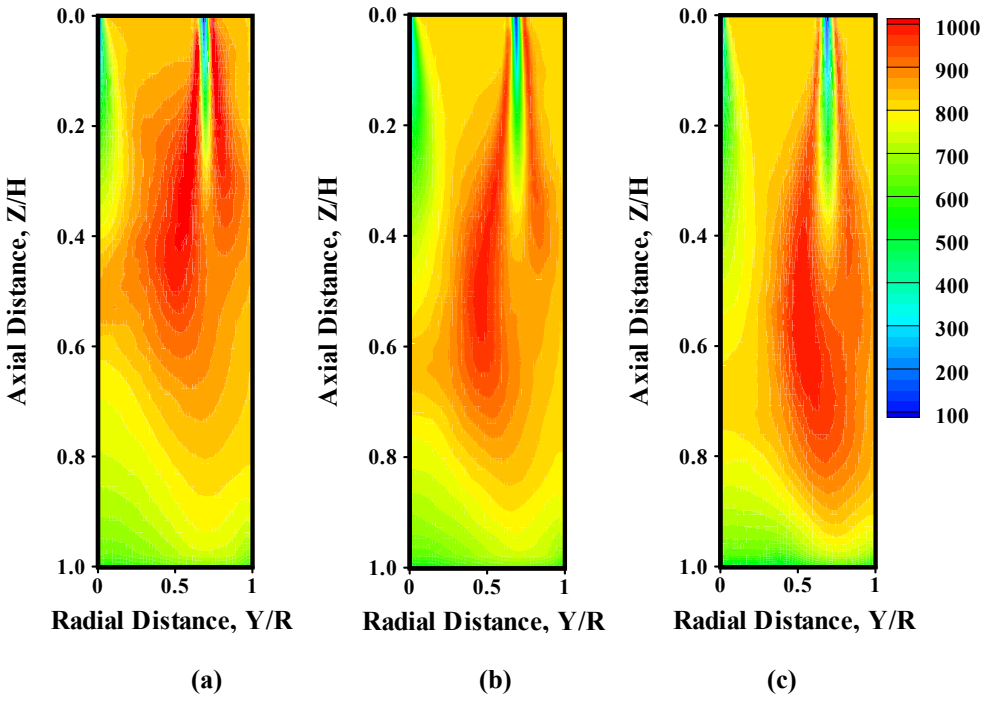

Figure 8.5: The contour profiles of temperature obtained from numerical calculations for various overall equivalence ratios (a) $\Phi_{overall}$ = 0.9, (b) $\Phi_{overall}$ = 1.0 and (c) $\Phi_{overall}$ = 1.1 with d_{ox}=15.9 mm and $X_{O2;ox}$ =0.30.

The discrepancies between experiments and numerical calculations occur at interface region between fuel and oxidizer jets while the peaks of temperature are well predicted at axial distance, Z/H=0.15 and 0.29 as shown in Figure 8.6. The temperature between jets at upstream region in experiments is higher than numerical predictions, which means that the more reactions occur between jets in experiments. This will be discussed later considering gas concentration profiles.

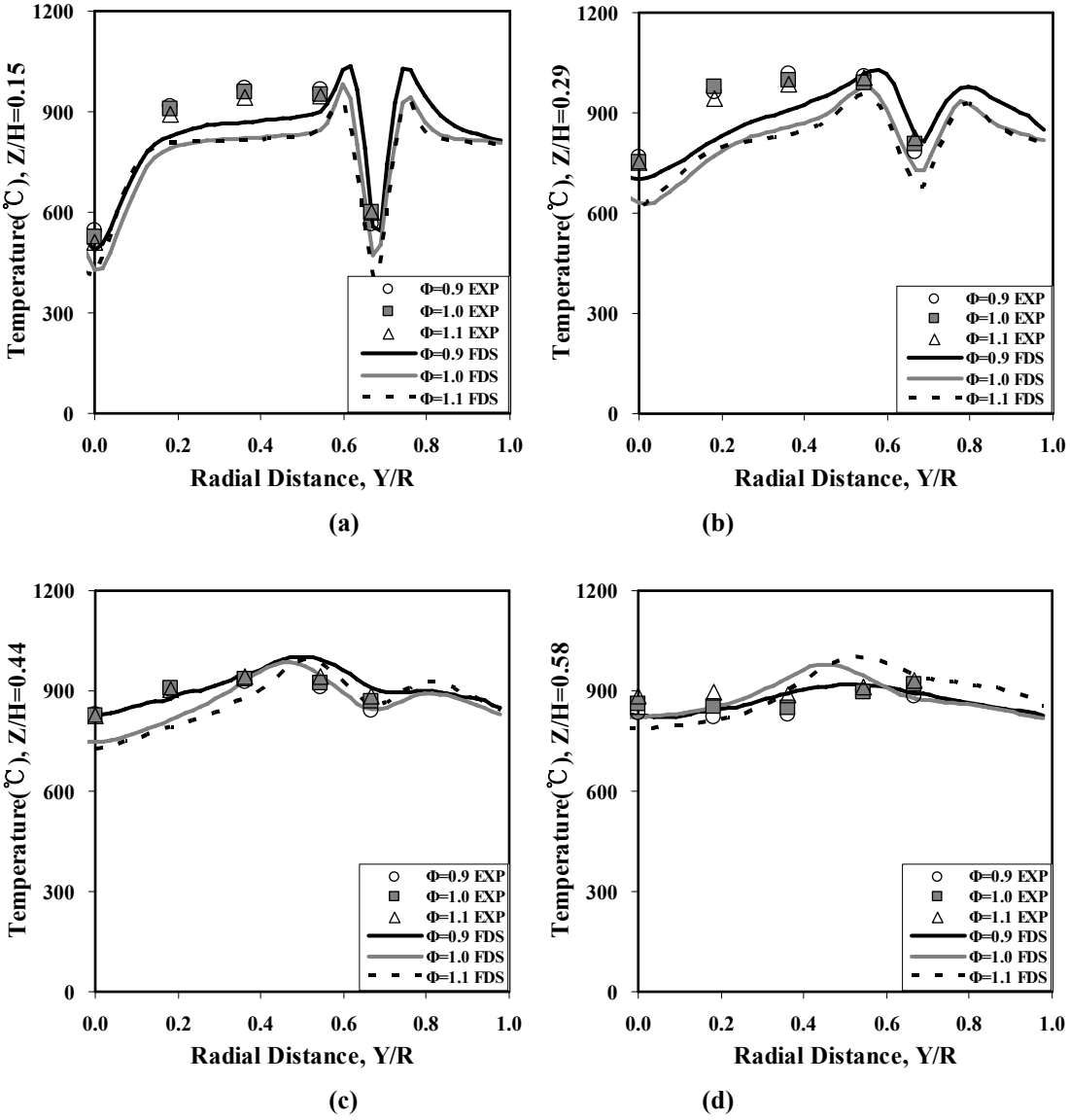

Figure 8.6: The radial temperature profiles at different axial positions obtained from experiments and numerical calculations (a) Z/H=0.15, (b) Z/H=0.29, (c) Z/H=0.44 and (d) Z/H=0.58 for various overall equivalence ratios $\Phi_{overall}$= 0.9, 1.0 and 1.1 with d_{ox} =15.9 mm and $X_{O2;ox}$ =0.30.

8.1.3. Gas compositions

8.1.3.1. Jet Centerline gas composition

Figure 8.7 shows the decay profiles of the centerline methane and oxygen concentrations in the fuel and oxidizer jet obtained from experiments and numerical calculations for various overall equivalence ratios $\Phi_{overall}$ =0.9, 1.0 and 1.1 with d_{ox}=15.9 mm and $X_{O2;ox}$ =0.30.

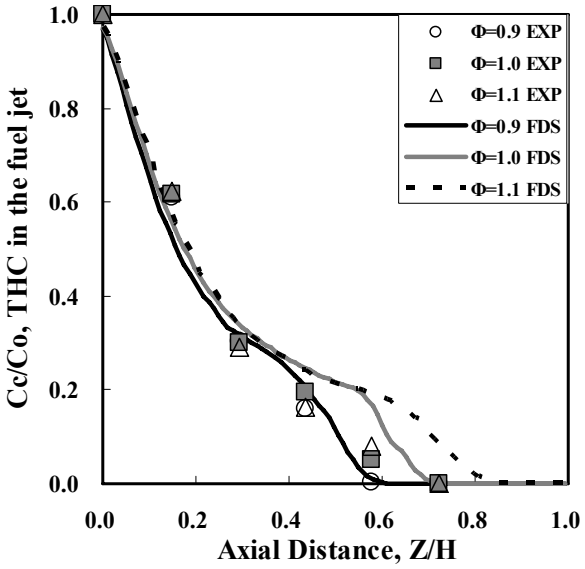

(a)

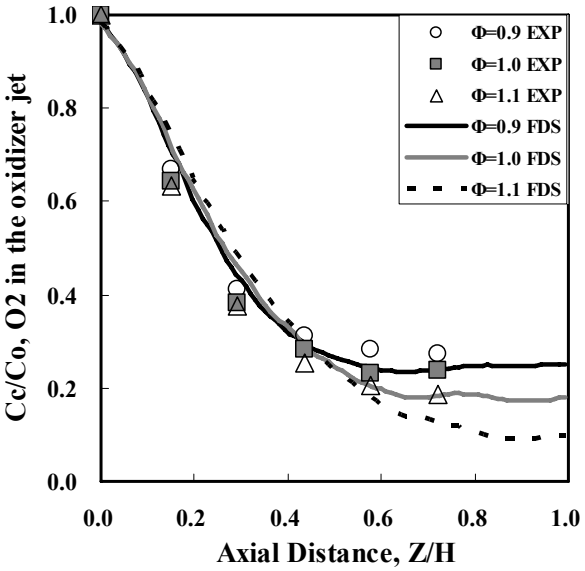

(b)

Figure 8.7: The decay profiles of the centerline concentration of the (a) CH_4 in the fuel jet and (b) O_2 in the oxidizer jet obtained from experiments and numerical calculations for various overall equivalence ratios $\Phi_{overall}$ =0.9, 1.0 and 1.1 with d_{ox}=15.9 mm and $X_{O2;ox}$ =0.30.

It is observed that the decay patterns of both jets are almost identical up to middle region of the furnace, Z/H=0.4, for all cases. Then the centerline methane concentration disappears faster, and the oxygen concentration increases with lower equivalence ratio in both experiments and numerical calculations. An explanation could be that the fuel jet can extend more axially and laterally because of less momentum of the oxidizer jets with higher equivalence ratio. Thus, the reaction zone can be extended farther downstream region, consequently higher methane and lower oxygen concentrations are observed at lower region of the furnace with high equivalence ratio. The higher oxygen concentration in the lower region of the furnace with low equivalence ratio results from the excess amount of oxidizer for low equivalence ratio. The difference between cases at lower region of the furnace is clearly shown in numerical predictions while less in experimental results. In addition, the oxygen concentration is higher in experiments while methane concentration is less than in numerical prediction. Therefore, it might be thought that the discrepancies between experiments and numerical calculations originate from the inaccuracy in controlling the flow rates of the jets, especially in oxidizer jet. According to the technical specification of flow meters and pressure gauges used in this study, about 6% and 2% of measuring error exists in experiments, respectively. Based on comparison results with numerical calculations, there is a possibility of supplying more oxidizer flow than target value in experiments. As a result, the oxidizer jet can have more momentum, and it is believed that this operating error obscure the effects of the equivalence ratio.

Figure 8.8 shows the scaled centerline methane concentration in the fuel jet and oxygen concentration in the oxidizer jet for different overall equivalence ratios $\Phi_{overall}$ =0.9, 1.0 and 1.1 with d_{ox}=15.9 mm and $X_{O2;ox}$ =0.30.

It is observed that the scaled centerline methane concentration in the fuel jet falls steeply at Z/H=0.4 for $\Phi_{overall}$=0.9 and Z/H=0.6, 0.7 for $\Phi_{overall}$=1.0 and 1.1, whereas the scaled centerline oxygen concentration in the oxidizer jet increases after showing flat shape along with the axial distance. This can be thought that each jet acts like a free single jet before the onset of the recirculation the jet flow, thus the jets continue to be diluted. This can be shown as flat shape in Figure 8.8. However, the centerline oxygen concentration in the oxidizer jet drops slowly or remains nearly constant after occurring of recirculation flow due to confinement effect, whereas the scaled centerline methane concentration in

the fuel jet decreases sharply by mixing with recirculation flow and combustion. In other words, the $(Cc/Co)_{CH4}$ falls sharply because of combustion, and the $(Cc/Co)_{O2}$ increases due to the recirculation of the oxidizer jet flow.

The scaled value of the centerline methane concentration in the fuel jet fall faster for the case of $\Phi_{overall}$=0.9 while other cases show nearly identical values in experiments, whereas the scaled centerline oxygen concentration in the oxidizer jet is higher with low overall equivalence ratio in both experiments and numerical calculations. However, the distinction between cases is more clearly shown in numerical calculations. The values of scaled centerline methane concentration decrease faster with low overall equivalence ratio. It might be attributed the fact that the oxidizer jet momentum increases with low overall equivalence ratio, and the recirculation flow occurs earlier. As a result, large scale of the mixing between the fuel and oxidizer jet occurs earlier and thus the centerline methane concentration decreases faster. The case of $X_{O2;ox}$=0.40 shows large decay rate of the scaled oxygen concentration between Z/H=0.4 and 0.9, which is related to combustion in the region of oxidizer jet.

8.1.3.2. Jet entrainment

For investigation of the jet entrainment, carbon dioxide concentrations in the fuel and oxidizer jet centerline are shown in Figure 8.8. The difference between cases in experiments is very small as seen in Figure 8.9, however, less carbon dioxide is found in both of the fuel and oxidizer jet centerline for $\Phi_{overall}$=0.9. It might be thought that the excess oxygen remains and strong recirculation of the oxidizer flow occurs toward the fuel jet for low equivalence ratio, thus the other gas concentrations becomes less. However, the difference is very small, and lots of carbon dioxide are found in each jet centerline for all cases, which indicates the sufficient recirculation of product gases in the furnace chamber.

In numerical calculations, the difference between cases is clearly captured. It is observed that the amount of carbon dioxide is almost identical for all equivalence ratios up to Z/H=0.45, then the case of high equivalence ratio shows higher amount of carbon dioxide in each jet centerline. This can be attributed the fact that the reaction zone is extended

farther downstream region because of momentum decrease of oxidizer jet with high equivalence ratio, thus reaction can still occur at lower region of the furnace.

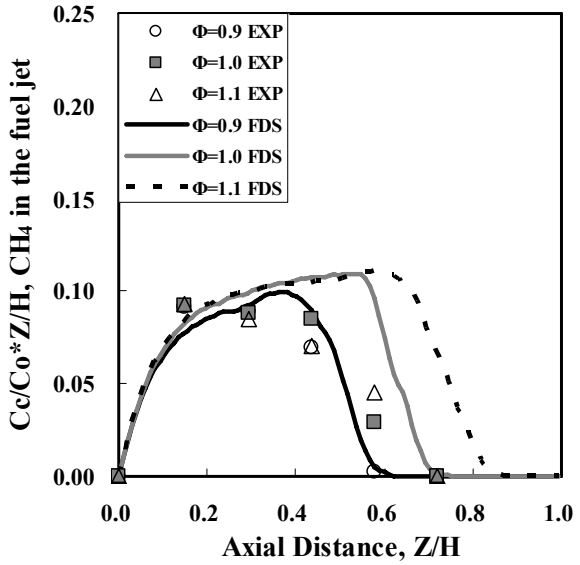

(a)

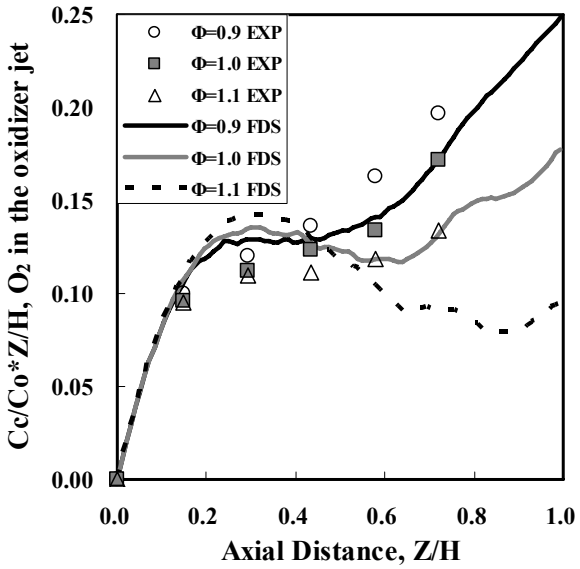

(b)

Figure 8.8: The decay profiles of the centerline concentration of the (a) CH_4 in the fuel jet and (b) O_2 in the oxidizer jet obtained from experiments and numerical calculations for various overall equivalence ratios $\Phi_{overall}$ =0.9, 1.0 and 1.1 with d_{ox}=15.9 mm and $X_{O2;ox}$ =0.30.

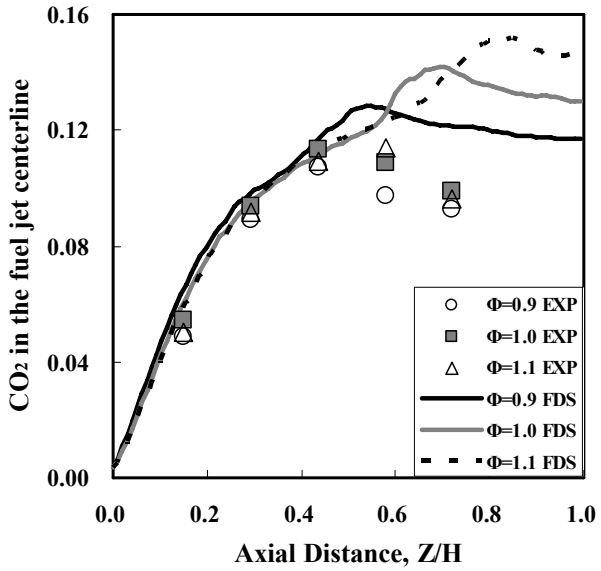

(a)

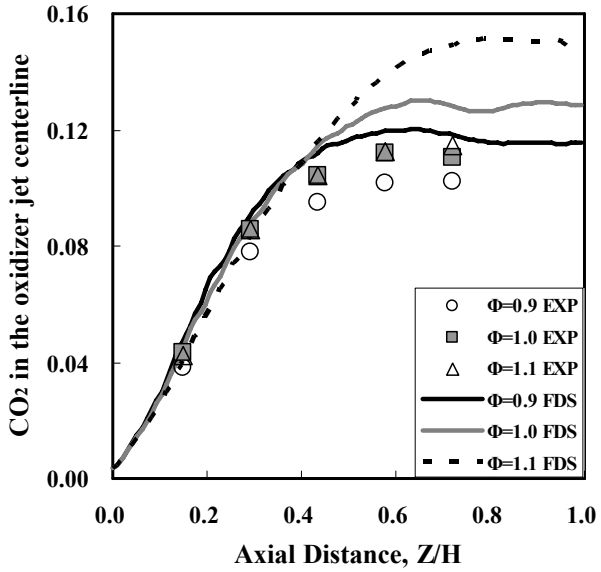

(b)

Figure 8.9: The centerline carbon dioxide concentrations of the (a) fuel jet and (b) oxidizer jet obtained from experiments and numerical calculations for various overall equivalence ratios $\Phi_{overall}$ =0.9, 1.0 and 1.1 with d_{ox}=15.9 mm and $X_{O2;ox}$ =0.30.

8.1.3.3. Radial gas composition profiles

The contour profiles for *Y-Z* plane and radial profiles of methane concentration at different axial distances obtained from experiments and numerical calculations for various overall equivalence ratios $\Phi_{overall}$ =0.9, 1.0 and 1.1 with d_{ox}=15.9 mm and $X_{O2;ox}$ =0.30 are shown in Figure 8.10 and 11.

It is clearly seen from Figure 8.10 that the methane concentration is distributed more widely and deeply with higher equivalence ratio due to decrease of oxidizer jet momentum. The difference between the cases is quite small up to *Z/H*=0.44 in both experiments and numerical calculations as shown in Figure 8.11. However, the methane concentration increases with higher overall equivalence ratio after *Z/H*=0.58. This trend is clearly shown in numerical calculations while relatively not clear in experimental data. It is noted that methane is not detected near the exhaust vent area *Y/R*=1.0 at *Z/H*=0.72 for all cases as shown in Figure 8.9 and 10.

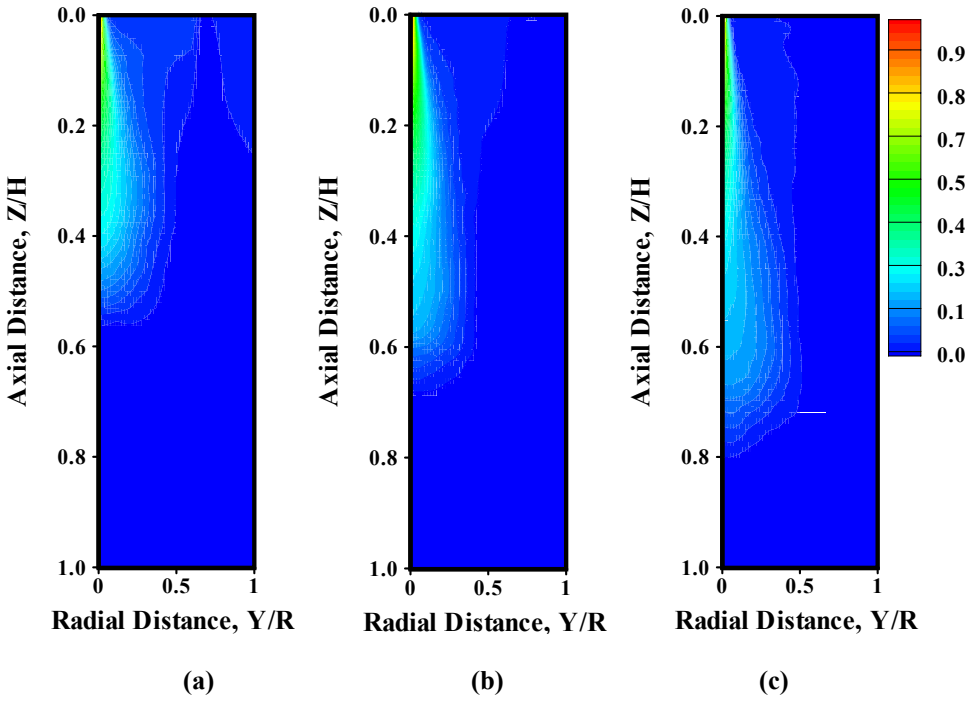

Figure 8.10: The contour profiles of methane concentration obtained from numerical calculations for various overall equivalence ratios (a) $\Phi_{overall}$ = 0.9, (b) $\Phi_{overall}$ = 1.0 and (c) $\Phi_{overall}$ = 1.1 with d_{ox}=15.9 mm and $X_{O2;ox}$ =0.30.

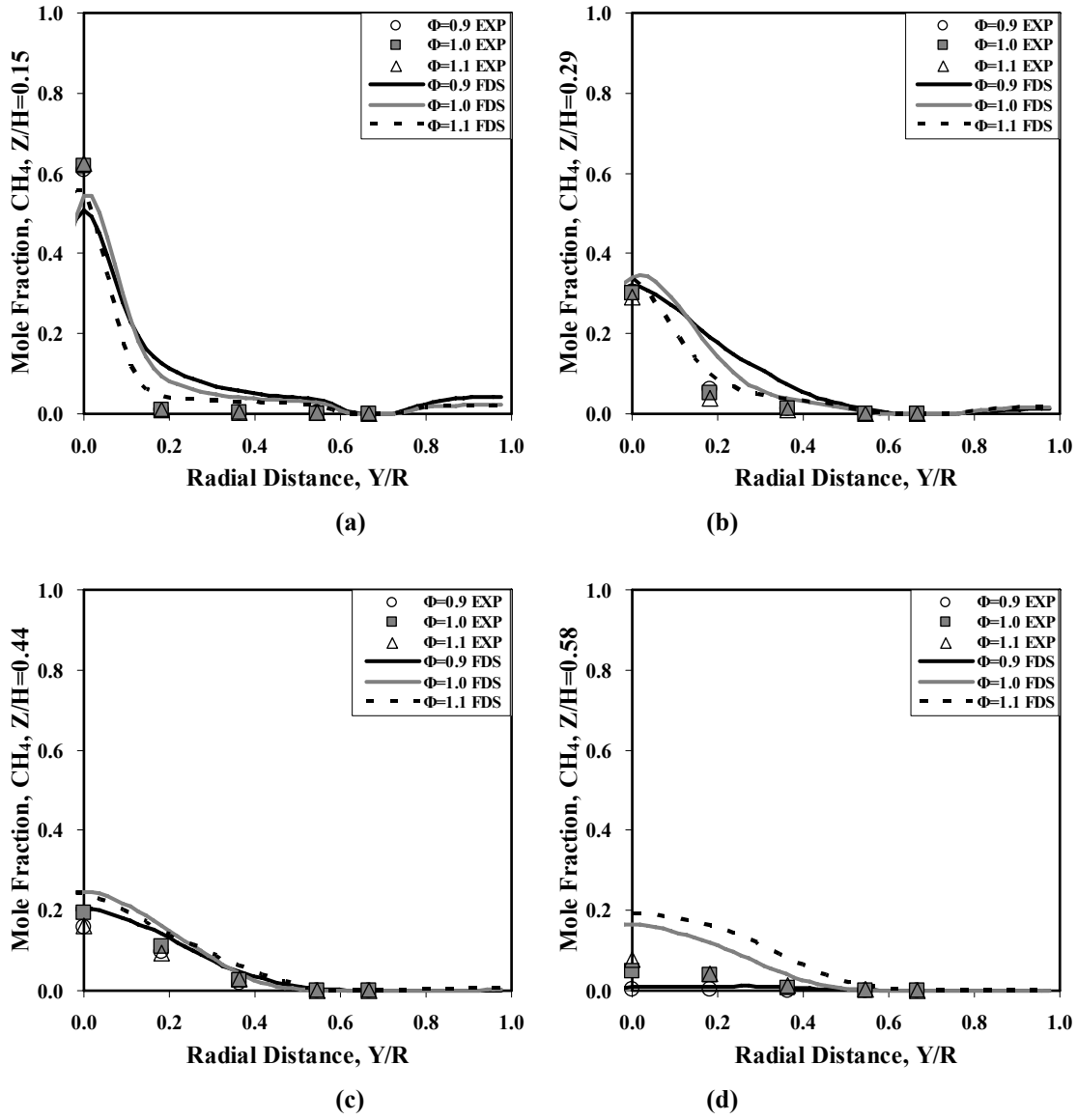

Figure 8.11: The radial profiles of methane concentration at different axial distances obtained from experiments and numerical calculations (a) *Z/H*=0.15, (b) *Z/H*=0.29, (c) *Z/H*=0.44 and (d) *Z/H*=0.58 for various overall equivalence ratios $\Phi_{overall}$= 0.9, 1.0 and 1.1 with d_{ox} =15.9 mm and $X_{O2;ox}$ =0.30.

Figure 8.12 and 13 show the contour and radial oxygen concentration profiles at different axial positions obtained from experiments and numerical calculations for various overall equivalence ratios $\Phi_{overall}$ =0.9, 1.0 and 1.1 with d_{ox}=15.9 mm and $X_{O2;ox}$ =0.30.

It is clearly observed that the oxygen concentration is higher with decrease of the equivalence ratio, and spreads more laterally in both experiments and numerical calculations. This can be attributed the fact that the oxidizer jet momentum increases with lower equivalence ratio, and hence the oxidizer jet is able to penetrate into the region of

the fuel jet more easily. As a result, the oxygen concentration spreads more widely with lower equivalence ratio as clearly shown in Figure 8.12. Another reason is that the more available oxygen exists with low equivalence ratio due to excess supply of oxidizer, thus the oxygen concentration is higher with lower equivalence ratio.

It is observed from Figure 8.13 that the numerical simulations predict the oxygen concentrations well comparing with the experimental data. The overall trend and peak values are in good agreement. However, the discrepancy between the experimental and numerical results appears from Z/H=0.44, and becomes large near the bottom of the furnace. This discrepancy might result from relatively inaccurate flow control in the experiments as explained in previous section. The higher momentum of the oxidizer jets in experiments could enhance the jet entrainment and mixing intensity, and oxygen concentration in re-circulated flue gas also increases. Thus, more oxygen concentration is found at interface region between jets in experimental data. In addition, the reaction rates increase near upstream regions [66], which is the reason for higher temperature at interface between jets at upstream regions in experiments.

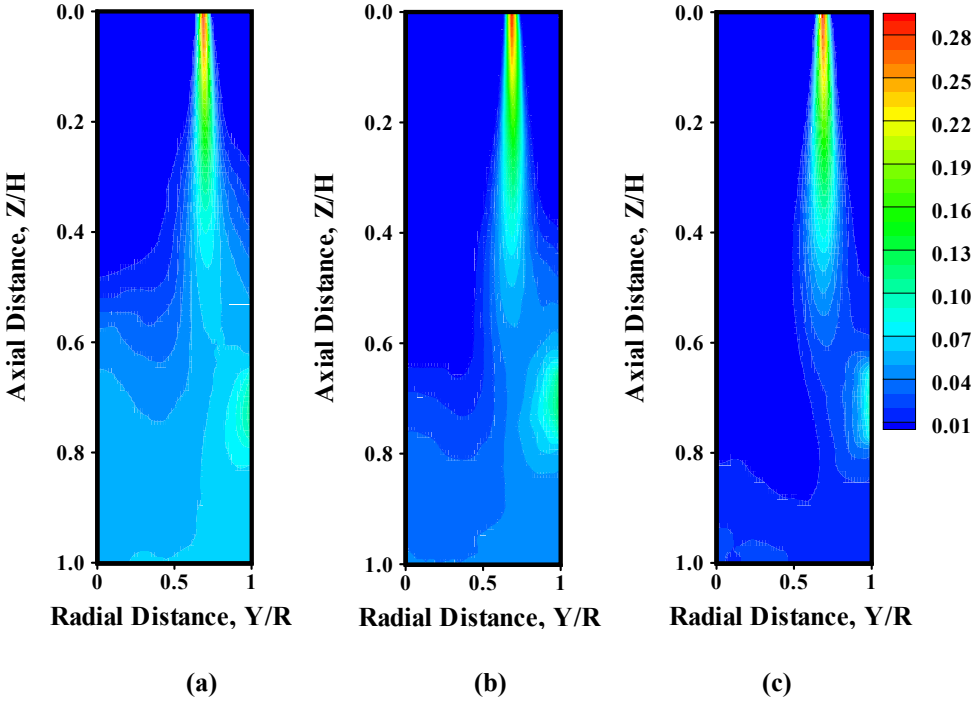

Figure 8.12: The contour profiles of oxygen concentration obtained from numerical calculations for various overall equivalence ratios (a) $\Phi_{overall}$ = 0.9, (b) $\Phi_{overall}$ = 1.0 and (c) $\Phi_{overall}$ = 1.1 with d_{ox}=15.9 mm and $X_{O2;ox}$ =0.30.

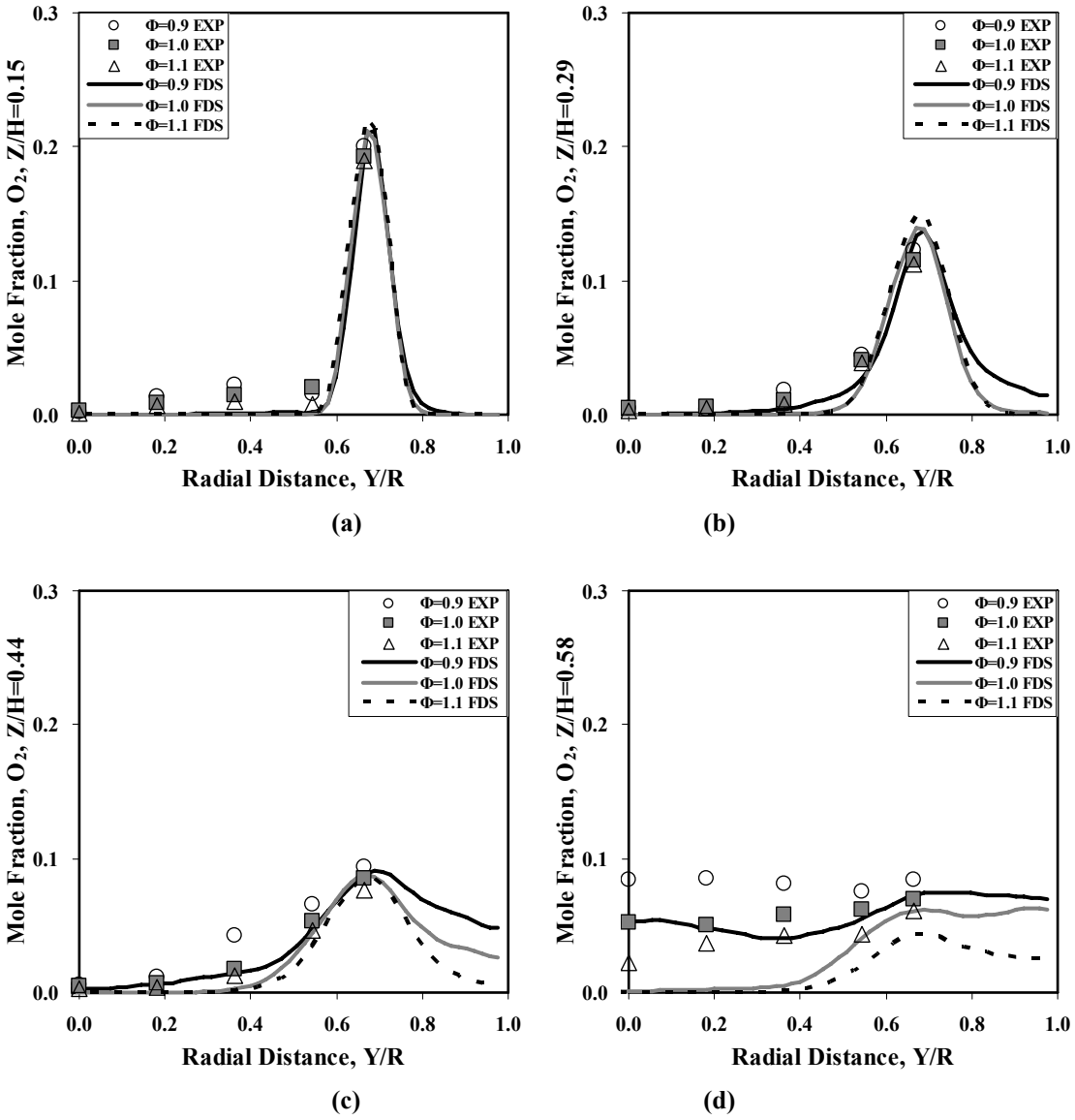

Figure 8.13: The radial profiles of oxygen concentration at different axial distances obtained from experiments and numerical calculations (a) *Z/H*=0.15, (b) *Z/H*=0.29, (c) *Z/H*=0.44 and (d) *Z/H*=0.58 for various overall equivalence ratios $\Phi_{overall}$= 0.9, 1.0 and 1.1 with d_{ox} =15.9 mm and $X_{O2;ox}$ =0.30.

The contour and radial carbon dioxide profiles at different axial positions obtained from experiments and numerical calculations for various overall equivalence ratios $\Phi_{overall}$ =0.9, 1.0 and 1.1 with d_{ox}=15.9 mm and $X_{O2;ox}$ =0.30 are shown in Figure 8.14 and 15, respectively.

As shown in Figure 8.14, the region of high carbon dioxide concentration extends farther downstream location with higher equivalence ratio, which is coincident with expansion of fuel jet. It is observed from Figure 8.15 that the radial profiles of carbon dioxide

concentration are quite flat for all equivalence ratios. This indicates the strong recirculation of product gases and uniform reaction in entire region of the furnace. The distributions of carbon dioxide are similar for all equivalence ratios, and the difference between cases is small in both experimental data and numerical calculations. The small amount of carbon dioxide concentration for the case of $\Phi_{overall}$ =0.9 is caused by high oxygen concentration due to excess supply of oxidizer. The discrepancy between experiments and numerical calculations can be found at Z/H=0.44 and 0.58. The amount of carbon dioxide in experiments is less than in numerical predictions. However, the consumption of methane is higher at the lower region of the furnace while oxygen consumption is less in experimental data. It might be thought that the reaction front is located at shorter distance from the jet exit than in numerical simulation, which results from more oxidizer flow in experiments.

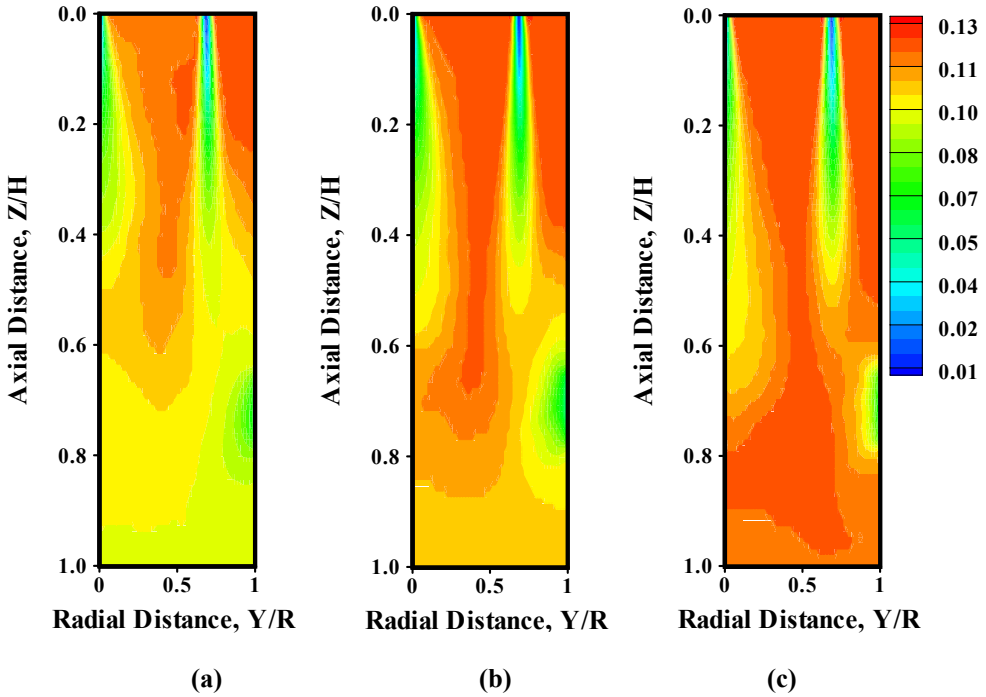

Figure 8.14: The contour profiles of carbon dioxide concentration obtained from numerical calculations for various overall equivalence ratios (a) $\Phi_{overall}$ = 0.9, (b) $\Phi_{overall}$ = 1.0 and (c) $\Phi_{overall}$ = 1.1 with d_{ox}=15.9 mm and $X_{O2;ox}$ =0.30.

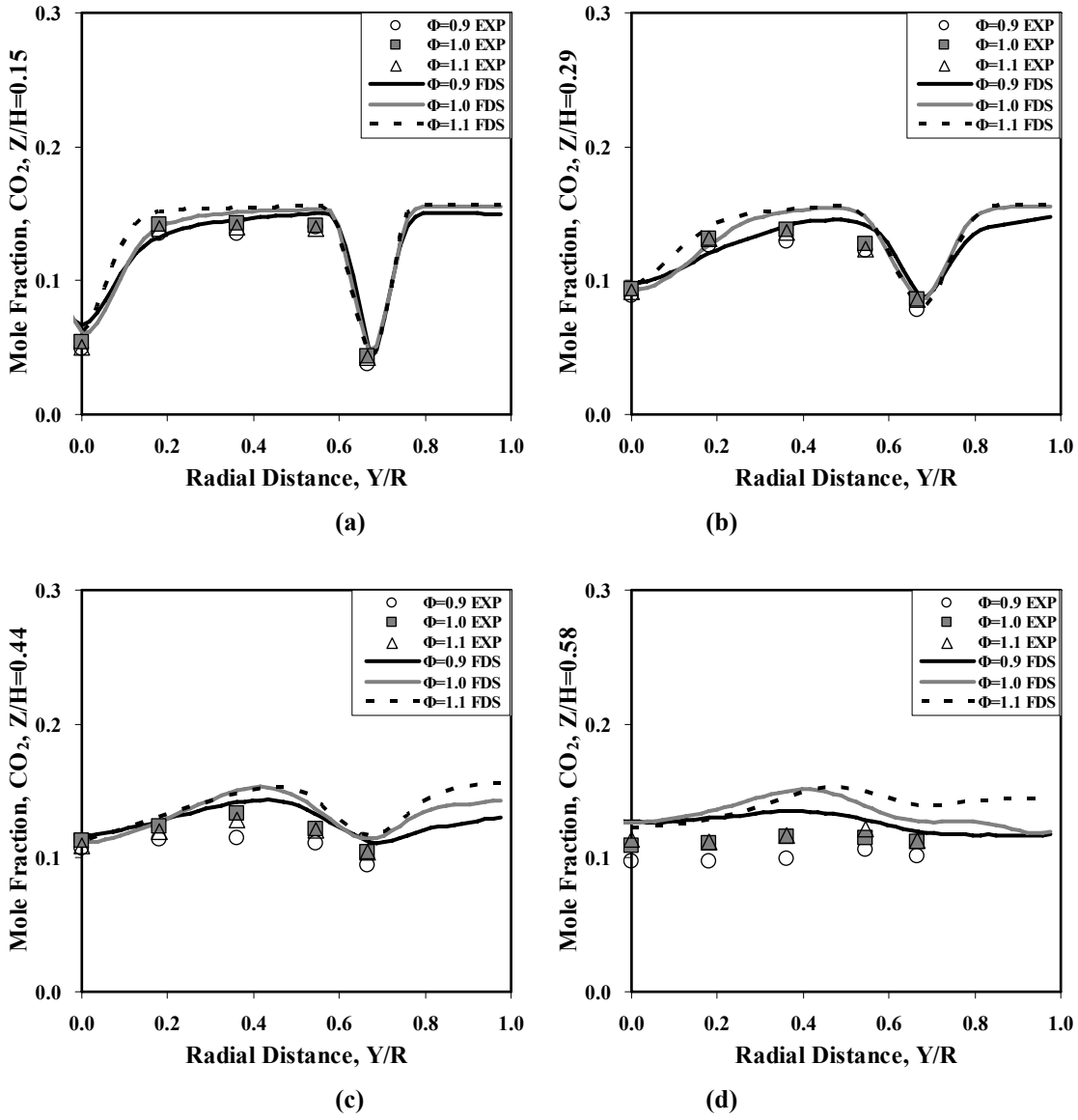

Figure 8.15: The radial profiles of carbon dioxide concentration at different axial distances obtained from experiments and numerical calculations (a) Z/H=0.15, (b) Z/H=0.29, (c) Z/H=0.44 and (d) Z/H=0.58 for various overall equivalence ratios $\Phi_{overall}$= 0.9, 1.0 and 1.1 with d_{ox} =15.9 mm and $X_{O2;ox}$ =0.30.

In summary, the distinction between cases is not clearly shown in experimental data, whereas it is noticeable in numerical calculations. As the overall equivalence ratio decreases, the recirculation flow can be formed earlier and its intensity also increases because of higher momentum of the oxidizer jet. Thus, the fuel concentration decays faster. Even though the difference between cases is not big in temperature and gas compositions, it might be helpful to increase the equivalence ratio slightly for obtaining

the homogeneous combustion condition because the reaction zone can extend farther downstream and wider under the configuration used in this study.

In overall, the numerical calculations predicts reasonably temperature and gas compositions comparing with experimental data for various overall equivalence ratio $\Phi_{overall}$ =0.9, 1.0 and 1.1. However, discrepancies between experiments and numerical calculations can be found at the bottom region of the furnace. It might be thought that these disagreements originate from the inaccuracy in controlling the flow rates of the jets in experiments, especially in oxidizer jet. Basically, the flow meters and pressure gauges used in this study contain about 6% and 2% of measuring error according to the technical specifications. Comparing with numerical calculations, there is possibility of excess supply of oxidizer in experiments; as a result, the oxidizer jet can have more momentum than target value. Therefore, it is believed that this operating error may obscure the effects of the equivalence ratio.

8.2. Effects of the inlet oxygen concentration on reacting flows

8.2.1 Velocity field

Figure 8.16 shows the radial velocity profiles at different axial positions for various inlet oxygen concentrations in the oxidizer jet $X_{O2;ox}$ =0.21, 0.30 and 0.40 with d_{ox}=15.9 mm and $\Phi_{overall}$ =1.0.

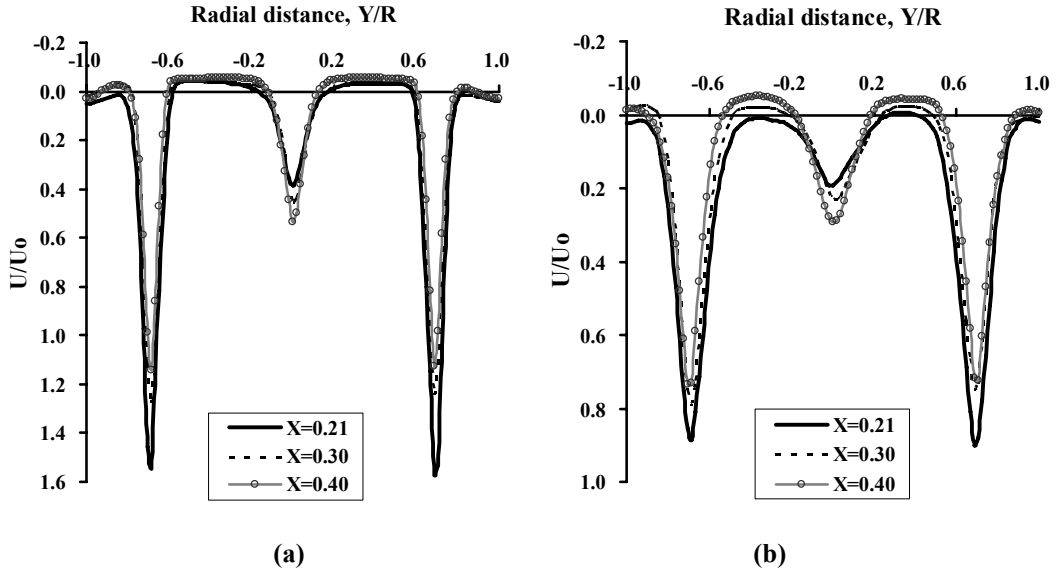

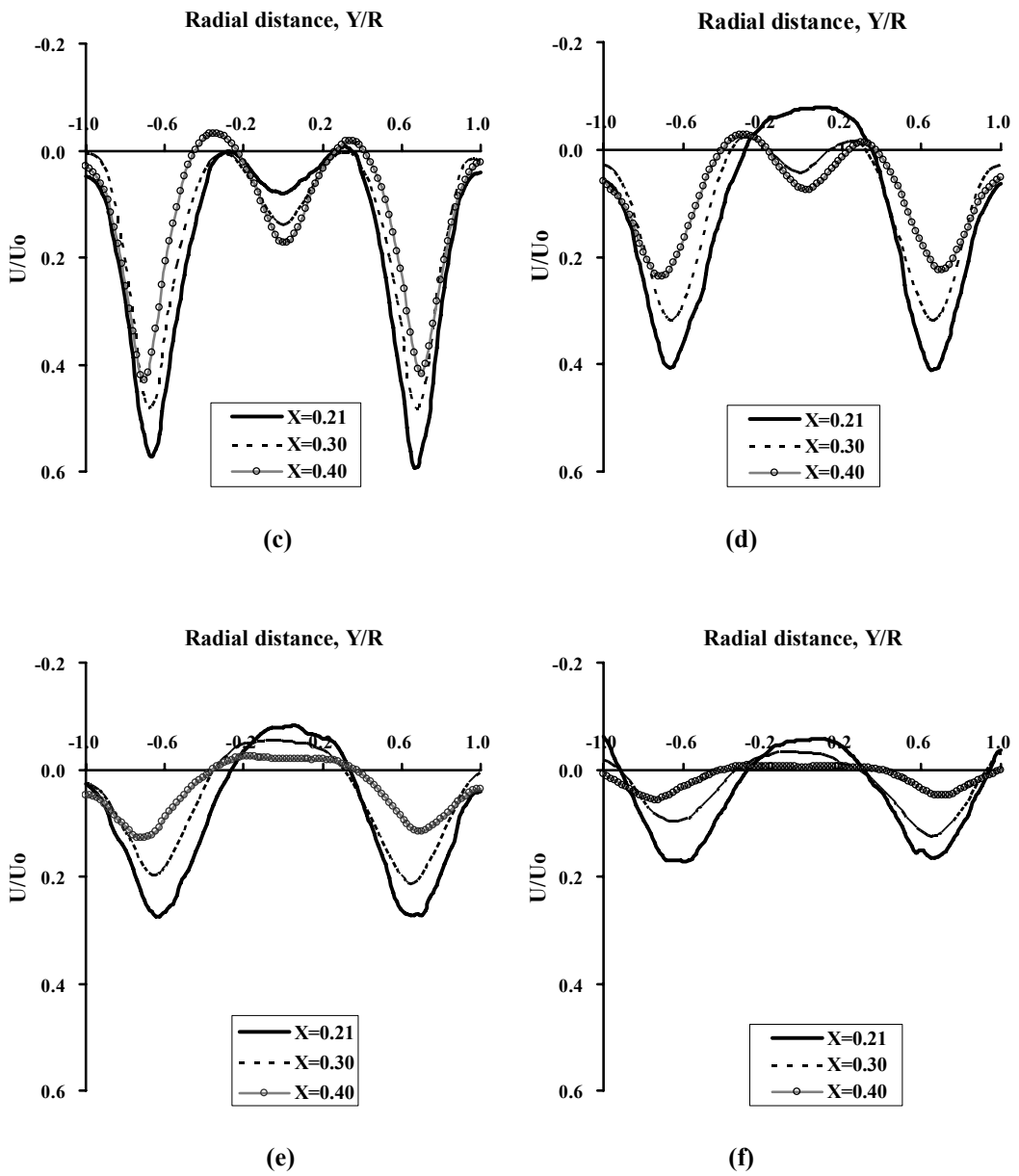

Figure 8.16: The radial stream-wise velocity profiles at different axial positions obtained from numerical calculations (a) Z/H=0.15, (b) Z/H=0.29, (c) Z/H=0.44, (d) Z/H=0.58, (e) Z/H=0.72 and (f) Z/H=0.86 for various inlet oxygen concentrations in the oxidizer jet $X_{O2;ox}$=0.21, 0.30 and 0.40 with $\Phi_{overall}$ =1.0 and d_{ox}=15.9 mm.

It is observed that the radial profiles for all cases are identical at jet exit region. However, the area of the recirculation at interface region between jets becomes smaller and weaker with less inlet oxygen concentration, whereas recirculation at the center jet region becomes more noticeable along with axial distance. In addition, for the case of high inlet oxygen concentration, the recirculation at interface regime still sustains up to bottom of

the furnace and finally merges into recirculation at the center jet region. This can be attributed the fact that the fuel jet can expand more wider with higher oxygen concentration due to decrease of momentum in the oxidizer jet, thus the recirculation of the fuel jet becomes dominant rather than that of the oxidizer jet. As a result, the recirculation at the center jet region occurs latter and weaker while recirculation between jets can sustain up to more downstream region of the furnace with higher oxygen concentration in the oxidizer jet. This trend is also clearly shown in Figure 8.17 showing the scaled centerline stream-wise velocity of the fuel jet. The region and magnitude of negative velocity decrease with higher inlet oxygen concentration, which means weak recirculation at the center regime.

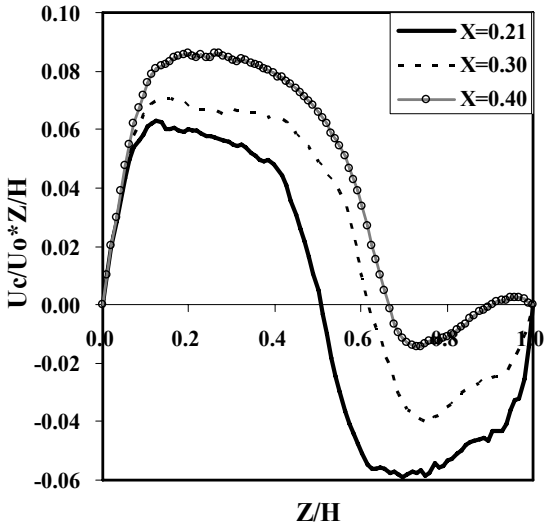

Figure 8.17: The scaled centerline stream-wise velocity of the fuel jet obtained from numerical calculations for various inlet oxygen concentrations in the oxidizer jet $X_{O2;ox}$=0.21, 0.30 and 0.40 with $\Phi_{overall}$ =1.0 and d_{ox}=15.9 mm.

Figure 8.18 shows the velocity vector profiles obtained from numerical calculations for various inlet oxygen concentrations in the oxidizer jet $X_{O2;ox}$ =0.21, 0.30 and 0.40 with d_{ox}=15.9 mm and $\Phi_{overall}$ =1.0. It is observed that the fuel jet can expand farther downstream region of the furnace with higher inlet oxygen concentration in the oxidizer jet. The fuel jet can reach up to Z/H=0.6 for the case of $X_{O2;ox}$ =0.21 while Z/H=0.72 and 0.8 for $X_{O2;ox}$ =0.30 and 0.40, respectively. This might be thought the fact that the momentum of the oxidizer jet decreases with higher inlet oxygen concentration, thus the

fuel jet can expand more easily in the furnace. The intensity of the velocity vectors in the recirculation region increase with decrease of the inlet oxygen concentration as shown in Figure 8.18. It might be thought that higher momentum of the oxidizer jet with lower inlet oxygen concentration in the oxidizer jet can enhance mixing intensity and entrainment, thus the large scale of recirculation pattern is formed earlier and its intensity also increases.

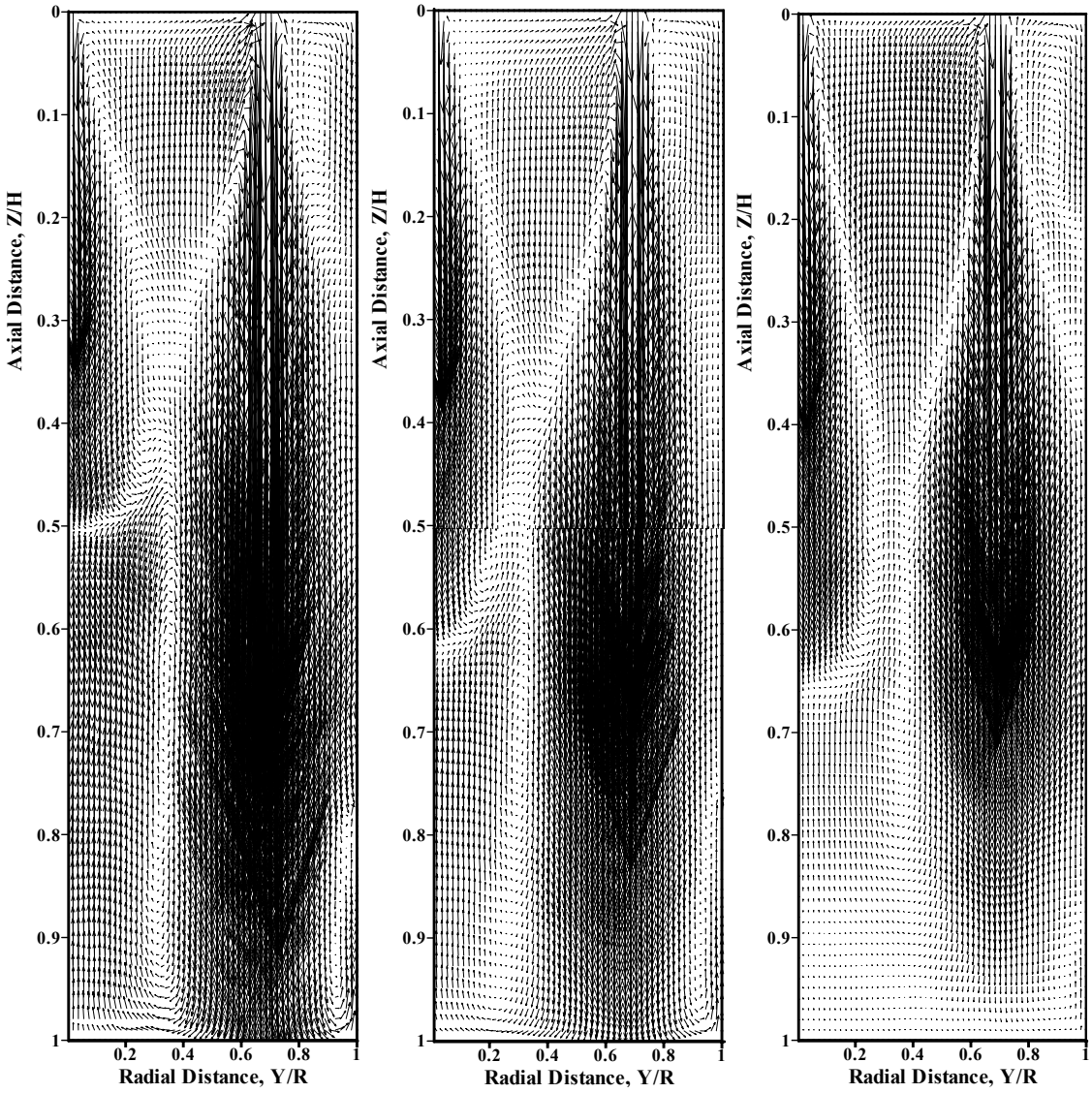

Figure 8.18: The velocity vector profiles of numerical calculations for various inlet oxygen concentrations in the oxidizer jet (a) $X_{O2;ox}$=0.21, (b) $X_{O2;ox}$=0.30 and (c) $X_{O2;ox}$=0.40 with $\Phi_{overall}$ =1.0 and d_{ox}=15.9 mm.

In terms of mixing and combustion, large scale of recirculation is preferable to achieve the homogeneous combustion because of enhanced mixing intensity and entrainment. However, the momentum of the fuel jet is too large, thus the recirculation of the fuel jet is dominant over the whole domain for the case of $X_{O2;ox}$ =0.40. As a result, small scale of recirculation at the interface region between jets prevails in the furnace.

8.2.2. Temperature

8.2.2.1. Jet Centerline Temperature

Figure 8.19 shows the centerline temperature of the fuel and oxidizer jets obtained from experiments and numerical calculations for various inlet oxygen concentrations in the oxidizer jet $X_{O2;ox}$ =0.21, 0.30 and 0.40 with d_{ox}=15.9 mm and $\Phi_{overall}$ =1.0.

The peak and gradient of the centerline temperature for both jets slightly increases with higher inlet oxygen concentration in experiments as shown in Figure 8.18. However, the centerline temperature of the fuel jet increases with lower inlet oxygen concentration in the oxidizer jet, whereas the oxidizer jet centerline temperature increases with higher inlet oxygen concentration in order in numerical calculations. This indicates that the reaction zone shifts toward the oxidizer jet with higher inlet oxygen concentration, which might be related to the expansion of the fuel jet with less momentum of the oxidizer jet as explained in velocity field.

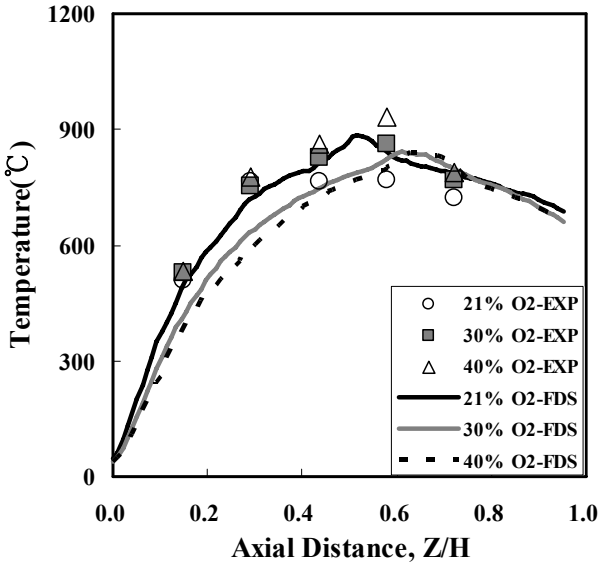

(a)

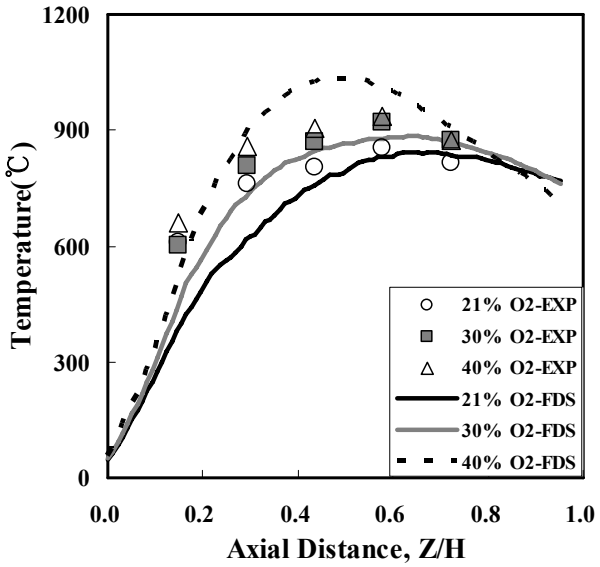

(b)

Figure 8.19: The centerline temperature of the (a) fuel jet and (b) oxidizer jet obtained from experiments and numerical calculations for various inlet oxygen concentrations in the oxidizer jet $X_{O2;ox}$=0.21, 0.30 and 0.40 with $\Phi_{overall}$ =1.0 and d_{ox}=15.9 mm.

It is clearly seen from Figure 8.19 (b) that the profile of the oxidizer jet centerline temperature becomes more parabolic with higher inlet oxygen concentration, which means lack of uniformity in temperature field. This non-uniformity of the temperature induces non-homogeneous combustion condition for the case of $X_{O2;ox}$ =0.40.

The difference between cases in experiments is not much noticeable as in numerical calculations. The numerical calculations predict the temperature reasonably comparing with experimental data for the case of $X_{O2;ox}$=0.21 and 0.30, whereas large discrepancy is shown for the case of $X_{O2;ox}$=0.40.

8.2.2.2. Radial Temperature Profiles along with axial distance

The contour profiles for *Y-Z* plane and radial temperature profiles at different axial positions for various inlet oxygen concentrations in the oxidizer jets $X_{O2;ox}$=0.21, 0.30 and 0.40 with d_{ox}=15.9 mm and $\Phi_{overall}$ =1.0 are shown in Figure 8.20 and 21, respectively.

It is clearly observed from Figure 8.20 that the high temperature region shifts and expand more toward the oxidizer jet with higher inlet oxygen concentration. The temperature between jets at upstream region is higher for the case of $X_{O2;ox}$=0.21, which might be thought that the intensity of recirculation at this region is enhanced due to higher

momentum of the oxidizer jet with decrease of inlet oxygen concentration as shown in Figure 8.18. Thus, the oxygen concentration in re-circulated flue gas increases and reaction rate is also enhanced at upstream region. The non-uniformity in temperature becomes notable with increase of inlet oxygen concentration. The case of $X_{O2;ox}$ =0.40 shows quite non-uniform temperature profiles, especially near the oxidizer jet region in numerical calculations as shown in Figure 8.21. According to the experimental observation of UV emissions and visual images, the case of $X_{O2;ox}$=0.21 and 0.30 are in the homogeneous combustion mode, whereas the highest inlet oxygen concentration $X_{O2;ox}$=0.40 is in the non-homogeneous combustion mode. The difference between homogeneous and non-homogeneous combustion conditions is clearly shown in numerical calculations, whereas it is hard to see the difference between cases in experimental data.

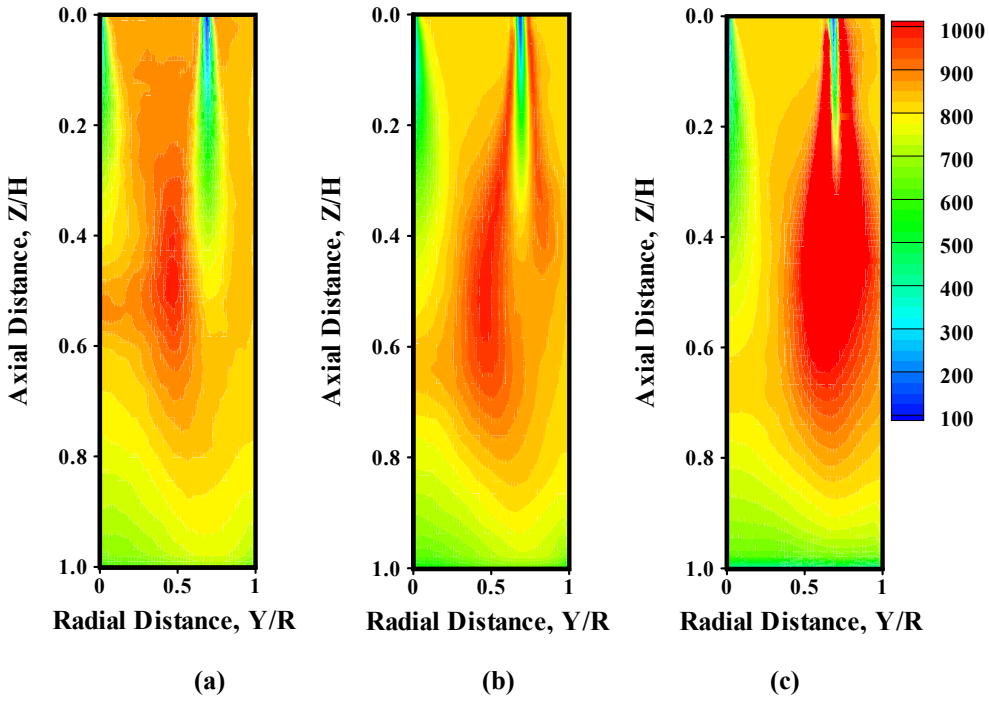

Figure 8.20: The contour profiles of temperature obtained from numerical calculations for various inlet oxygen concentrations in the oxidizer jet (a) $X_{O2;ox}$=0.21, (b) $X_{O2;ox}$=0.30 and (c) $X_{O2;ox}$=0.40 with $\Phi_{overall}$ =1.0 and d_{ox}=15.9 mm.

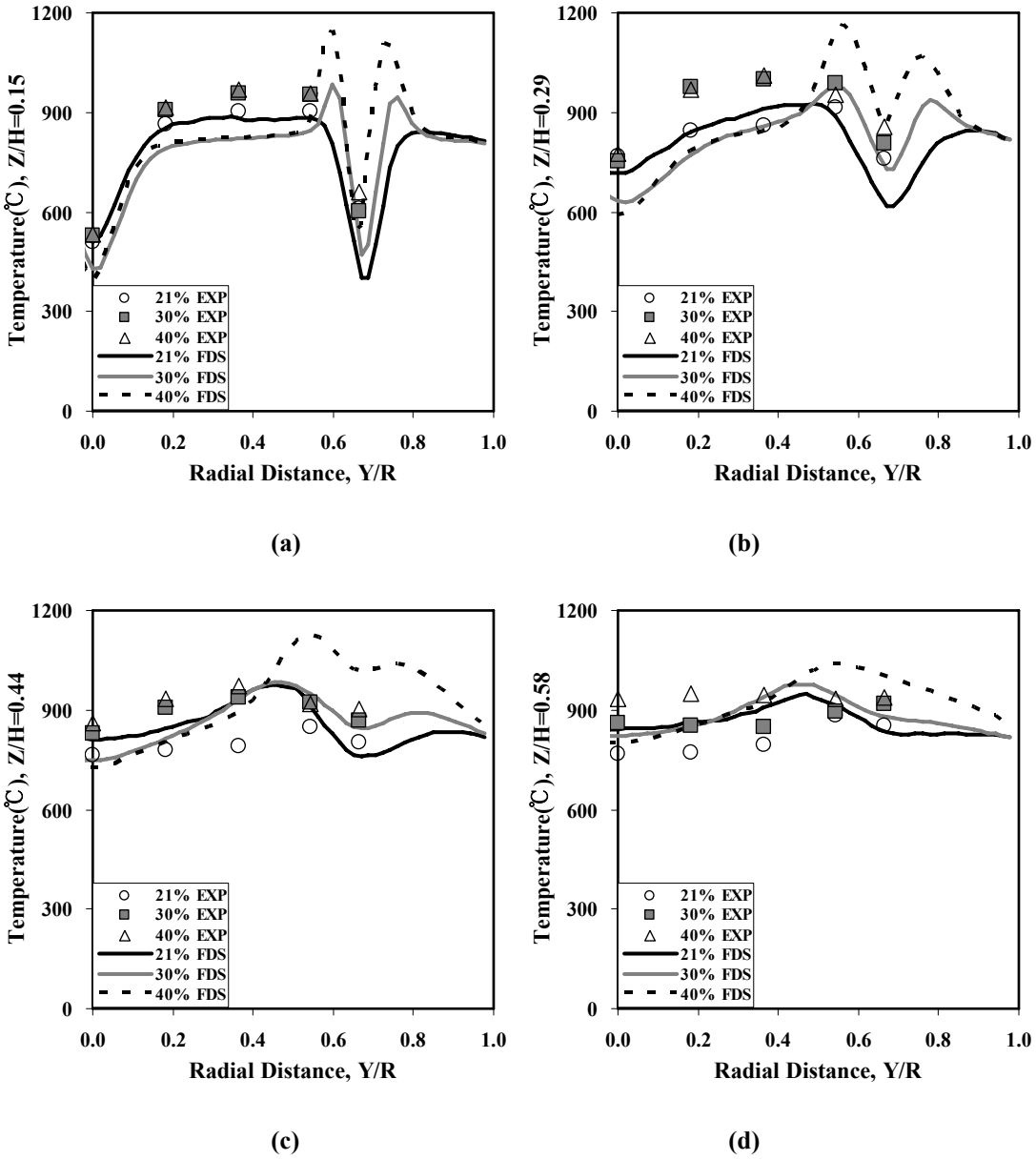

Figure 8.21: The radial profiles of temperature at different axial positions obtained from experiments and numerical calculations (a) Z/H=0.15, (b) Z/H=0.29, (c) Z/H=0.44 and (d) Z/H=0.58 for various inlet oxygen concentrations in the oxidizer jet $X_{O2;ox}$=0.21, 0.30 and 0.40 with $\Phi_{overall}$ =1.0 and d_{ox}=15.9 mm.

8.2.3. Gas compositions

8.2.3.1. Jet Centerline gas composition

The decay patterns of methane and oxygen concentration in the fuel and oxidizer jet centerline obtained from experiments and numerical calculations for different inlet

oxygen concentrations $X_{O2;ox}$ =0.21, 0.30 and 0.40 with d_{ox}=15.9 mm and $\Phi_{overall}$ =1.0 are shown in Figure 8.22.

It is observed that the case of $X_{O2;ox}$=0.21 shows large decay rate of methane concentration in the fuel jet centerline, whereas less decay rate of the oxygen concentration in the oxidizer jet centerline for both experiments and numerical calculations. In experiments, the decay patterns of methane and oxygen concentrations in the jet centerline for $X_{O2;ox}$=0.30 and 0.40 are almost identical. However, the distinction between cases is clearly shown in numerical calculations as shown in Figure 8.22. The numerical calculations show large decay rate of methane concentration and less decay rate of the oxygen concentration with lower inlet oxygen concentration in the oxidizer jet. An explanation is that the momentum of oxidizer jet increases with decrease of inlet oxygen concentration, thus the oxidizer jet can expand more easily into the region of the fuel jet. In addition, the recirculation flow pattern due to confinement is formed at shorter axial distance and the intensity of recirculation increases with high momentum as shown in Figure 8.18. As a result, the region of the fuel jet becomes smaller and the reaction front is located at shorter axial distance. Therefore, the fuel concentration decays faster with lower inlet oxygen concentration. On the other hand, the oxidizer jet can reach the bottom of the furnace without reaction with the fuel due to high momentum for the case of low inlet oxygen concentration while the most amount of oxidizer flow is consumed by reaction with the fuel for high inlet oxygen concentration as shown in Figure 8.20. Thus, the oxygen concentration is higher with low inlet oxygen concentration in the bottom region of the furnace. This explanation will be confirmed in later section of gas compositions.

It is noted that the initial inlet oxygen concentrations in the oxidizer jet are different, while the diameter of oxidizer jet is same for above cases. In Figure 8.22, the centerline oxygen concentration $(Cc)_{O2}$ is normalized by the inlet oxygen concentration $(Co)_{O2}$. Thus, the decay patterns of the centerline oxygen concentration $(Cc)_{O2}$ are different between cases. Considering the real values of the centerline oxygen concentration, the less inlet oxygen concentration shows the lower value of the centerline oxygen concentration as shown in Figure 8.23. This can be explained by the turbulent jet theory which states that the centerline concentration is proportional to initial inlet concentration

and jet diameter. Thus, the higher oxygen concentration in the oxidizer jet centerline results from high initial oxygen concentration in oxidizer jet because the oxidizer jet diameter is kept same for all case.

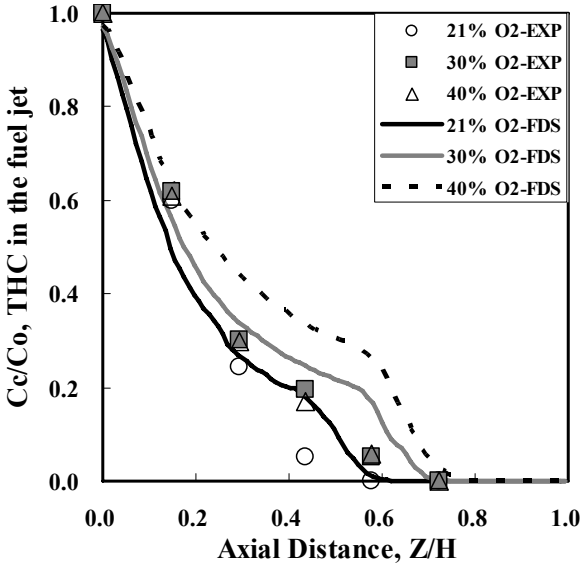

(a)

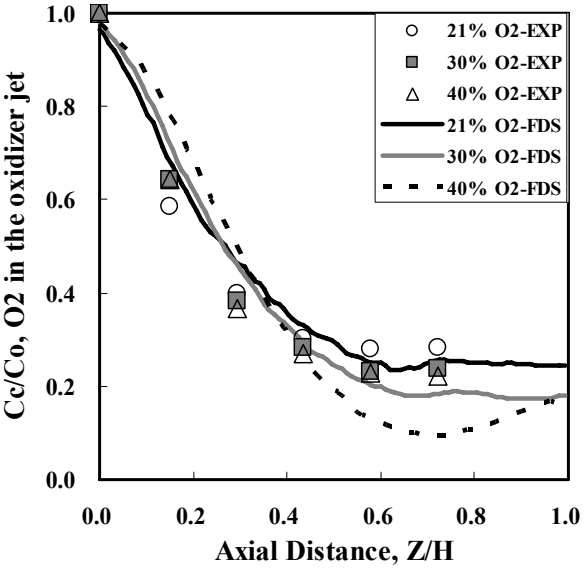

(b)

Figure 8.22: The decay patterns of normalized (a) methane concentration in the fuel jet centerline and (b) oxygen concentration in the oxidizer jet centerline obtained from experiments and numerical calculations for different inlet oxygen concentrations $X_{O2;ox}$=0.21, 0.30 and 0.40 with $\Phi_{overall}$ =1.0 and d_{ox}=15.9 mm.

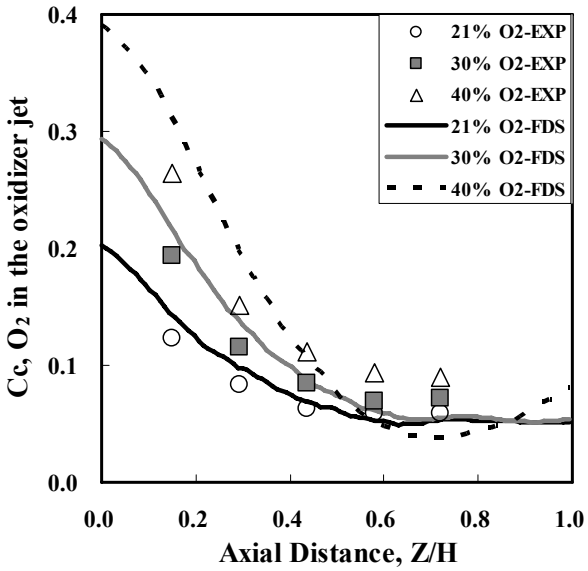

Figure 8.23: The decay patterns of oxygen concentration in the oxidizer jet centerline *Cc* obtained from experiments and numerical calculations for different inlet oxygen concentrations $X_{O2;ox}$=0.21, 0.30 and 0.40 with $\Phi_{overall}$ =1.0 and d_{ox}=15.9 mm.

Based on the UV emission and visual image in experiments, the case of $X_{O2;ox}$=0.21 and 0.30 are in the homogeneous combustion mode, whereas the highest inlet oxygen concentration $X_{O2;ox}$=0.40 is in the non-homogeneous combustion mode. It might be thought that the dilution of the oxidizer jet is not sufficient to obtain the homogeneous combustion for $X_{O2;ox}$=0.40 because of high value of oxygen concentration. This higher oxygen concentration induces the non-homogenous combustion. For achieving the homogeneous combustion condition with high inlet oxygen concentration, the oxidizer jet should be sufficiently diluted by product gases. Thus, it is strongly recommended that the size of the oxidizer jet should be smaller for the case of high inlet oxygen concentration.

Figure 8.24 shows the scaled centerline methane concentration in the fuel jet and oxygen concentration in the oxidizer jet for different inlet oxygen concentrations $X_{O2;ox}$=0.21, 0.30 and 0.40 with d_{ox}=15.9 mm and $\Phi_{overall}$=1.0.

It is observed that the scaled centerline methane concentration in the fuel jet falls steeply at Z/H=0.45 for $X_{O2;ox}$=0.21 and Z/H=0.6 for $X_{O2;ox}$=0.30 and 0.40 , whereas the scaled centerline oxygen concentration in the oxidizer jet increases after showing flat shape along with the axial distance. This can be thought that each jet acts like a free single jet before the onset of the recirculation the jet flow, thus the jets continue to be diluted. This

can be shown as flat shape in Figure 8.24. However, the centerline oxygen concentration in the oxidizer jet drops slowly or remains nearly constant after occurring of recirculation flow due to confinement effect, whereas the scaled centerline methane concentration in the fuel jet decreases sharply by mixing with recirculation flow and combustion. In other words, the $(Cc/Co)_{CH4}$ falls sharply because of combustion, and the $(Cc/Co)_{O2}$ increases due to the recirculation of the oxidizer jet flow.

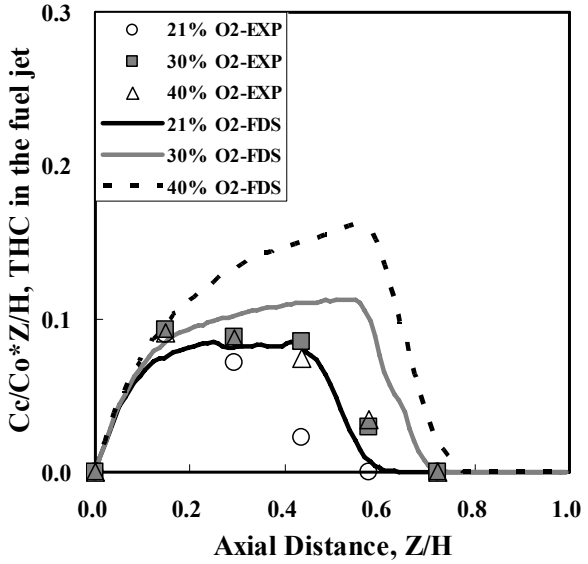

(a)

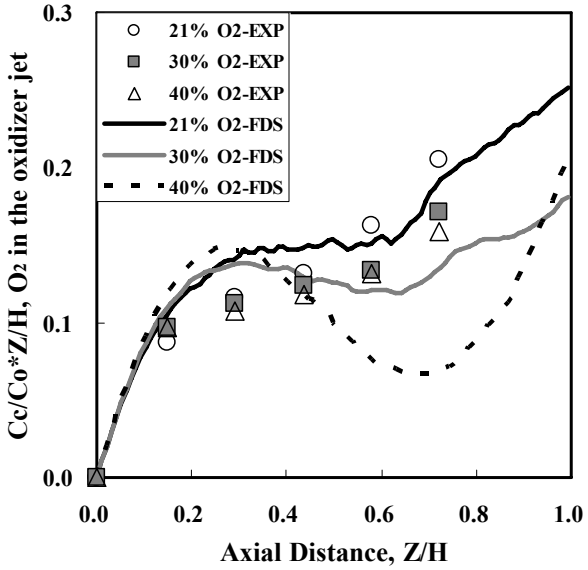

(b)

Figure 8.24: The scaled centerline (a) methane concentration in the fuel jet and (b) oxygen concentration in the oxidizer jet obtained from experiments and numerical calculations for different inlet oxygen concentrations $X_{O2;ox}$=0.21, 0.30 and 0.40 with $\Phi_{overall}$ =1.0 and d_{ox}=15.9 mm.

The scaled value of the centerline methane concentration in the fuel jet fall faster for the case of $X_{O2;ox}$=0.21 while other cases show nearly identical values, whereas the scaled centerline oxygen concentration in the oxidizer jet is slightly higher with low inlet oxygen concentration in experiments. However, the distinction between cases is quite clearly shown in numerical calculations. The values of scaled centerline methane concentration are lower and decrease faster with low inlet oxygen concentration. On the other hand, the values of scaled oxygen concentration are initially quite same for all cases and then become higher with low inlet oxygen concentration. It might be attributed the fact that the oxidizer jet momentum increases with low inlet oxygen concentration, and the recirculation flow occurs earlier. As a result, large scale of the mixing between the fuel and oxidizer jet occurs earlier and thus the centerline methane concentration decreases faster. The case of $X_{O2;ox}$=0.40 shows large decay rate of the scaled oxygen concentration between Z/H=0.3 and 0.7, which is related to combustion in the region of oxidizer jet.

8.2.3.2. Jet entrainment

The sufficient dilution of the jets by product gases is an essential condition for achieving the homogeneous combustion mode. Thus, it is very useful to investigate the amount of carbon dioxide in each jet centerline for evaluating the effects of inlet oxygen concentration. Figure 8.25 shows the mole fraction of carbon dioxide in the fuel and oxidizer jet centerline obtained from experiments and numerical calculations for various inlet oxygen concentrations in the oxidizer jet $X_{O2;ox}$=0.21, 0.30 and 0.40 with d_{ox}=15.9 mm and $\Phi_{overall}$ =1.0.

Considering different initial inlet oxygen concentrations, the centerline concentrations of carbon dioxide are divided by inlet oxygen concentrations as shown in Figure 8.25 because the amount of carbon dioxide is approximately proportional to inlet oxygen concentration. It is observed that less carbon dioxide is found in the fuel jet centerline with higher inlet oxygen concentration, which indicates the lower level of recirculation of product gases. On the other hand, nearly same amount of carbon dioxide is shown in the oxidizer jet centerline for the case of $X_{O2;ox}$=0.21 and 0.30 while the case of $X_{O2;ox}$=0.40 shows higher amount of carbon dioxide in the latter half region of the furnace. However,

high mole fraction of carbon dioxide for the case of $X_{O2;ox}$=0.40 is directly from the reaction, not from the entrainment of product gases because the reaction occurs mainly around the oxidizer jet as shown in contour profiles of temperature, Figure 8.20. For achieving the homogeneous combustion condition with high inlet oxygen concentration in the oxidizer jet, more strong level of recirculation of product gases in each jet should be implemented. However, the case of $X_{O2;ox}$=0.40 shows insufficient recirculation of product gases in each jet.

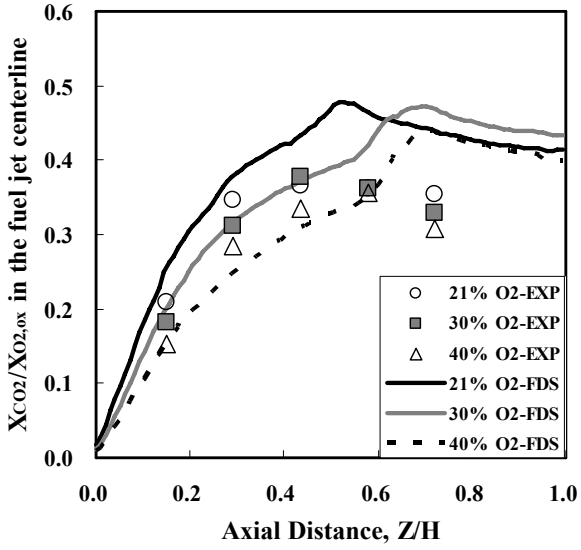

(a)

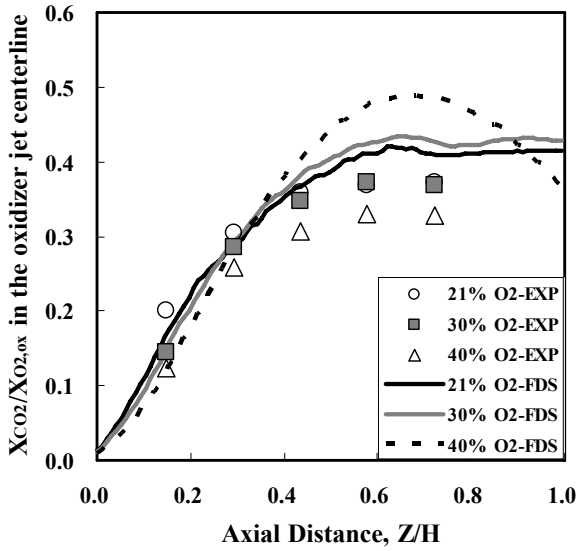

(b)

Figure 8.25: The normalized centerline carbon dioxide concentration in the (a) fuel jet and (b) oxidizer jet obtained from experiments and numerical calculations for different inlet oxygen concentrations $X_{O2;ox}$=0.21, 0.30 and 0.40 with $\Phi_{overall}$ =1.0 and d_{ox}=15.9 mm.

8.2.3.3. Radial gas composition profiles

The contour profiles of the methane concentration obtained from numerical calculations for different inlet oxygen concentrations $X_{O2;ox}$=0.21, 0.30 and 0.40 with d_{ox}=15.9 mm and $\Phi_{overall}$ =1.0 are shown in Figure 8.26. It is clearly seen that the region of the fuel jet expands more widely with increase of the inlet oxygen concentration. This can be attributed the fact that the momentum of the oxidizer jets becomes lower with oxygen enrichment, and hence the fuel jet can penetrate easily into the flow region of the oxidizer jets.

Figure 8.27 shows radial profiles of methane concentration at different axial positions obtained from experiments and numerical calculations for various inlet oxygen concentrations in the oxidizer jet $X_{O2;ox}$=0.21, 0.30 and 0.40 with fixed separation distance and $\Phi_{overall}$ =1.0.

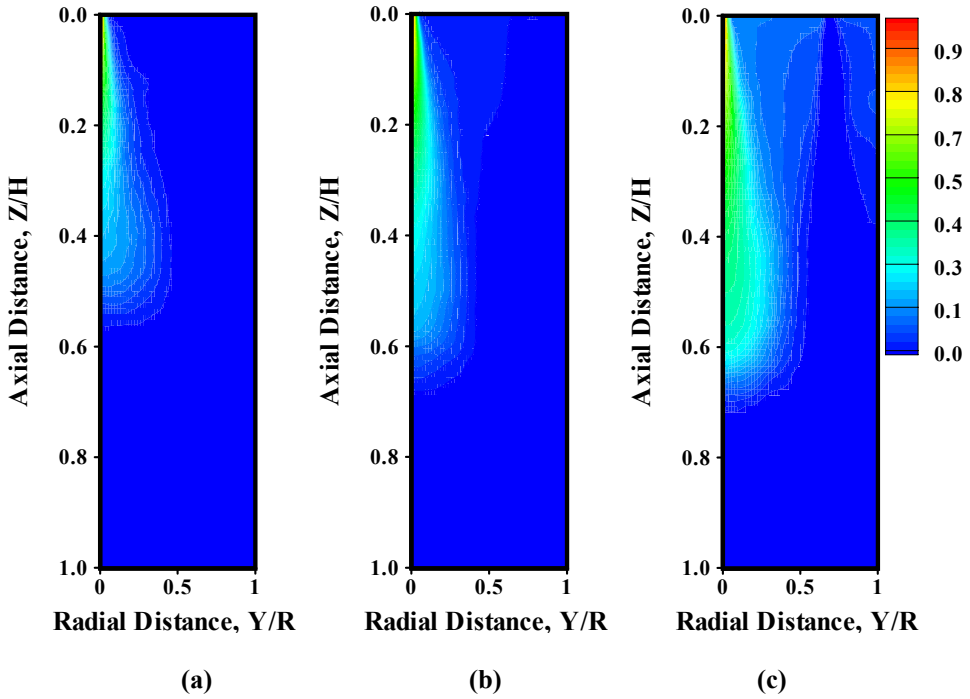

Figure 8.26: The contour profiles of methane concentration obtained from numerical calculations for various inlet oxygen concentrations in the oxidizer jet (a) $X_{O2,ox}$=0.21, (b) $X_{O2,ox}$=0.30 and (c) $X_{O2;ox}$=0.40 with $\Phi_{overall}$=1.0 and d_{ox}=15.9 mm.

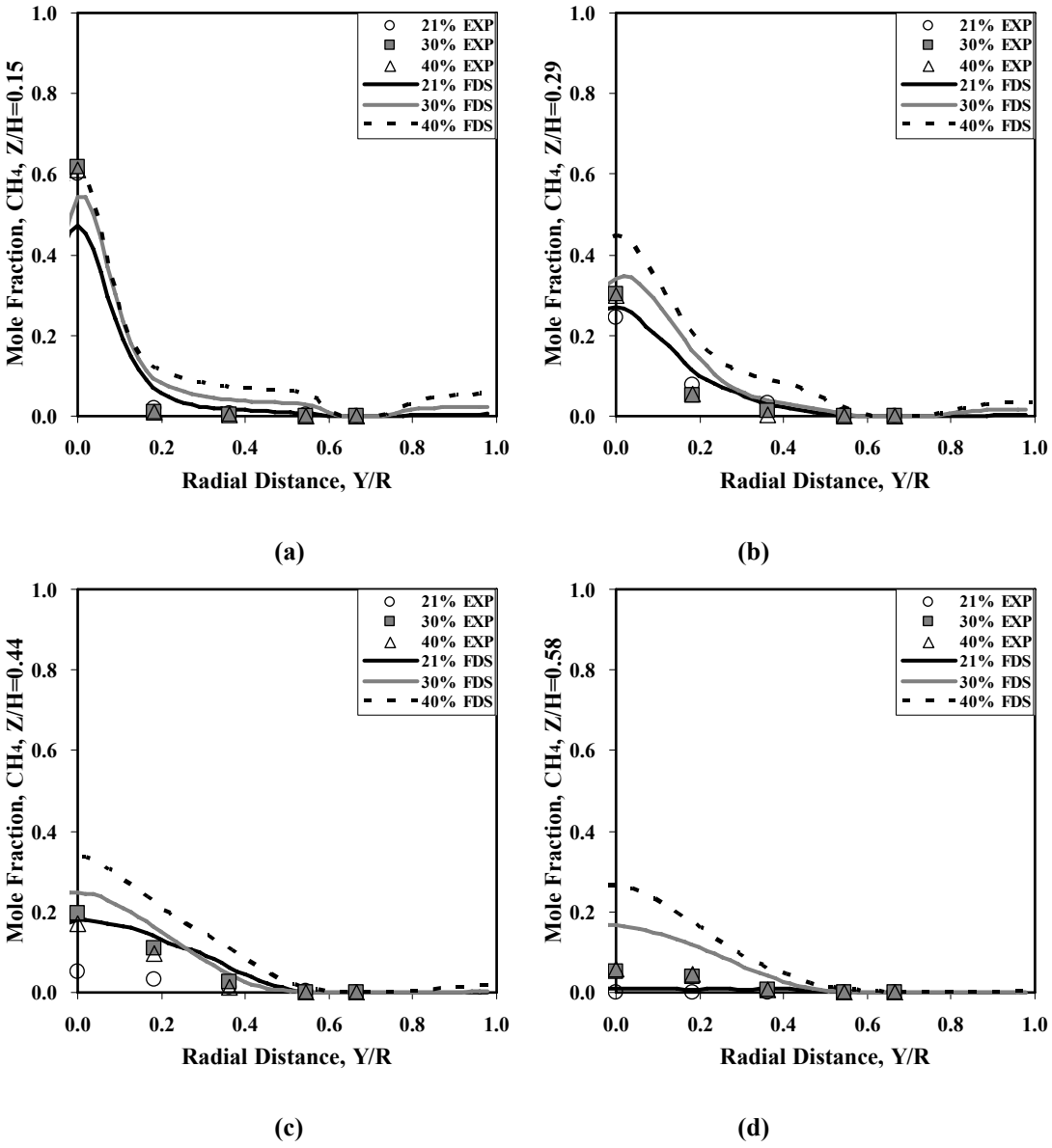

Figure 8.27: The radial profiles of methane concentration at different axial positions obtained from experiments and numerical calculations (a) Z/H=0.15, (b) Z/H=0.29, (c) Z/H=0.44 and (d) Z/H=0.58 for various inlet oxygen concentrations in the oxidizer jet $X_{O2;ox}$=0.21, 0.30 and 0.40 with $\Phi_{overall}$ =1.0 and d_{ox}=15.9 mm.

In overall, the methane concentration decays faster with lower inlet oxygen concentration. However, the difference between cases is very small and the profiles are almost similar for all cases in experiments while there is a clear distinction between cases in numerical calculations. It might be thought that the recirculation flow toward the fuel jet is formed earlier and the intensity of re-circulating flow becomes stronger with decrease of inlet oxygen concentration because of higher momentum of the oxidizer jet as shown in Figure

8.18. Therefore, the fuel jet begins to be affected by this recirculation flow at shorter axial distance and the methane concentration decays faster with lower inlet oxygen concentration in the oxidizer jet.

The contour profiles of oxygen concentration obtained from numerical calculations for various inlet oxygen concentrations $X_{O2;ox}$=0.21, 0.30 and 0.40 with d_{ox}=15.9 mm and $\Phi_{overall}$ =1.0 are shown in Figure 8.28. It is clearly seen that the distribution of oxygen concentration becomes wider with decrease of the inlet oxygen concentration, which is connected to the same reason for expansion of the fuel jet. In addition, the height that the flow of oxidizer jet can reach increases with less inlet oxygen concentration due to higher momentum. As a result, the reaction front is located at shorter distance and methane concentration decays faster with low inlet oxygen concentration in the oxidizer jet.

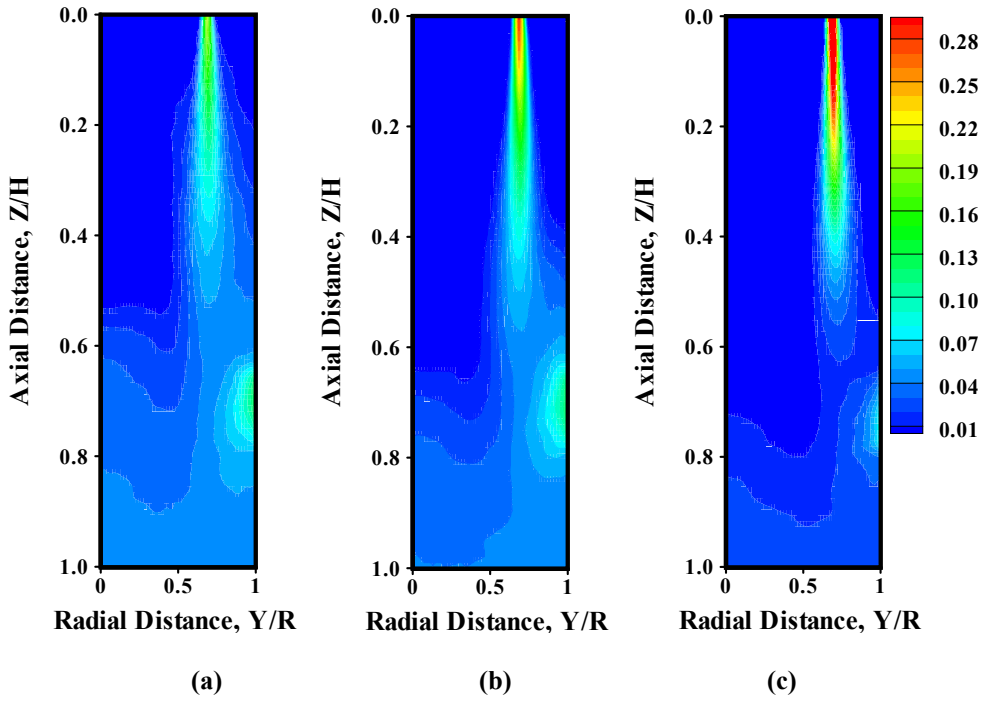

Figure 8.28: The contour profiles of oxygen concentration obtained from numerical calculations for various inlet oxygen concentrations in the oxidizer jet (a) $X_{O2,ox}$=0.21, (b) $X_{O2,ox}$=0.30 and (c) $X_{O2;ox}$=0.40 with $\Phi_{overall}$ =1.0 and d_{ox}=15.9 mm.

Figure 8.29 shows radial oxygen concentration profiles at different axial positions obtained from experiments and numerical calculations for various inlet oxygen

concentrations in the oxidizer jet $X_{O2;ox}$=0.21, 0.30 and 0.40 with d_{ox}=15.9 mm and $\Phi_{overall}$ =1.0.

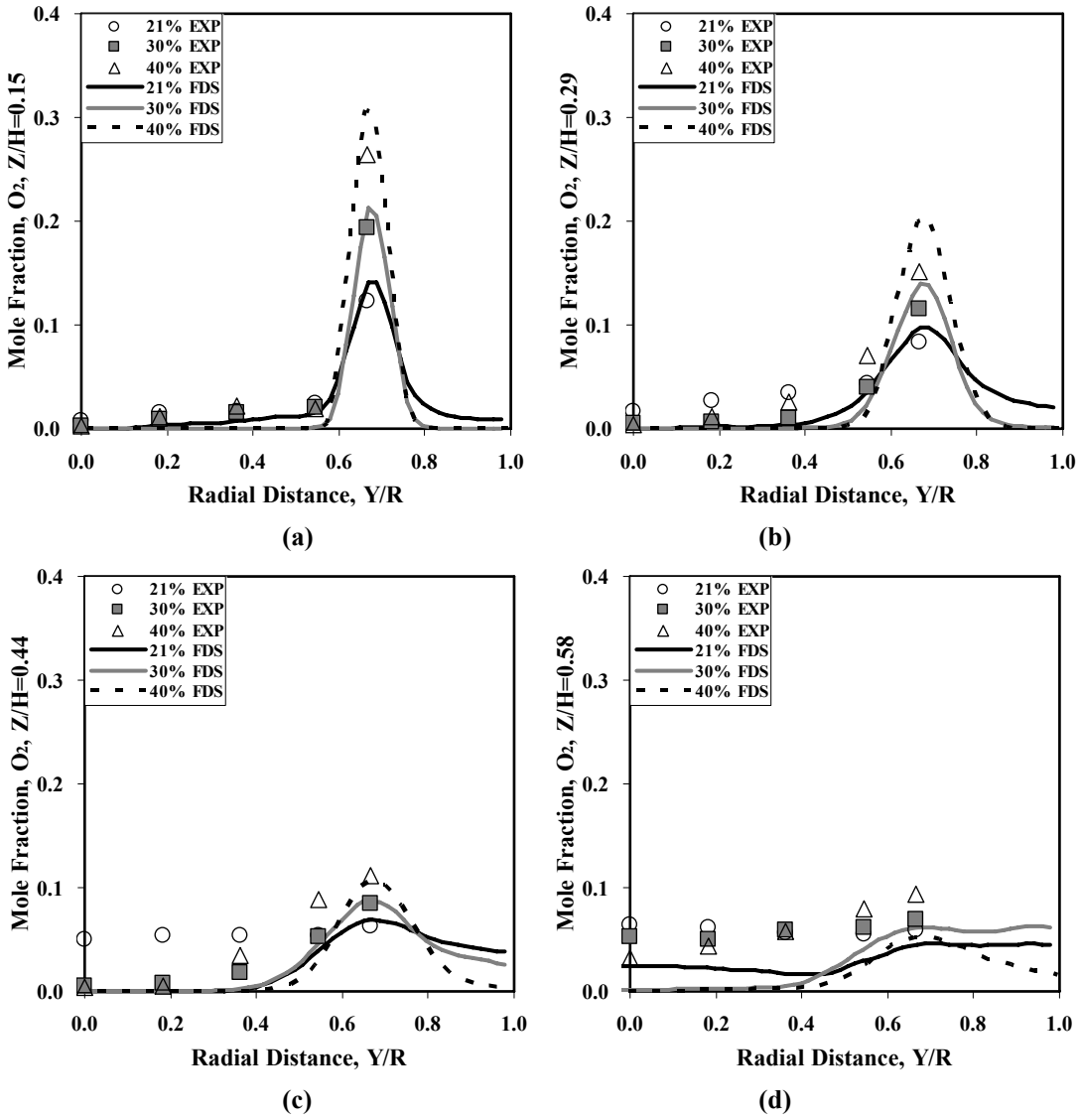

Figure 8.29: The radial oxygen concentration profiles at different axial positions obtained from experiments and numerical calculations (a) Z/H=0.15, (b) Z/H=0.29, (c) Z/H=0.44 and (d) Z/H=0.58 for various inlet oxygen concentrations in the oxidizer jet $X_{O2;ox}$=0.21, 0.30 and 0.40 with $\Phi_{overall}$ =1.0 and d_{ox}=15.9 mm.

The peaks of oxygen concentration in the oxidizer jet are well predicted in numerical calculations except for the case of $X_{O2;ox}$=0.40 as shown in Figure 8.29. It is observed that oxygen concentration at interface region between jets is higher for the case of $X_{O2;ox}$=0.21 than other cases. This can be attributed the fact that the lower inlet oxygen concentration case has higher momentum of the oxidizer jet, and non-reacting flow of the oxidizer jet

containing high oxygen concentration re-circulates to the region of middle of the furnace as shown in Figure 8.28.

The contour profiles of carbon dioxide concentration obtained from numerical calculations for various inlet oxygen concentrations $X_{O2;ox}$=0.21, 0.30 and 0.40 with d_{ox}=15.9 mm and $\Phi_{overall}$ =1.0 are shown in Figure 8.30. The distribution of carbon dioxide concentration is quite uniform for the case of $X_{O2;ox}$=0.21, and becomes less uniform with increase of inlet oxygen concentration.

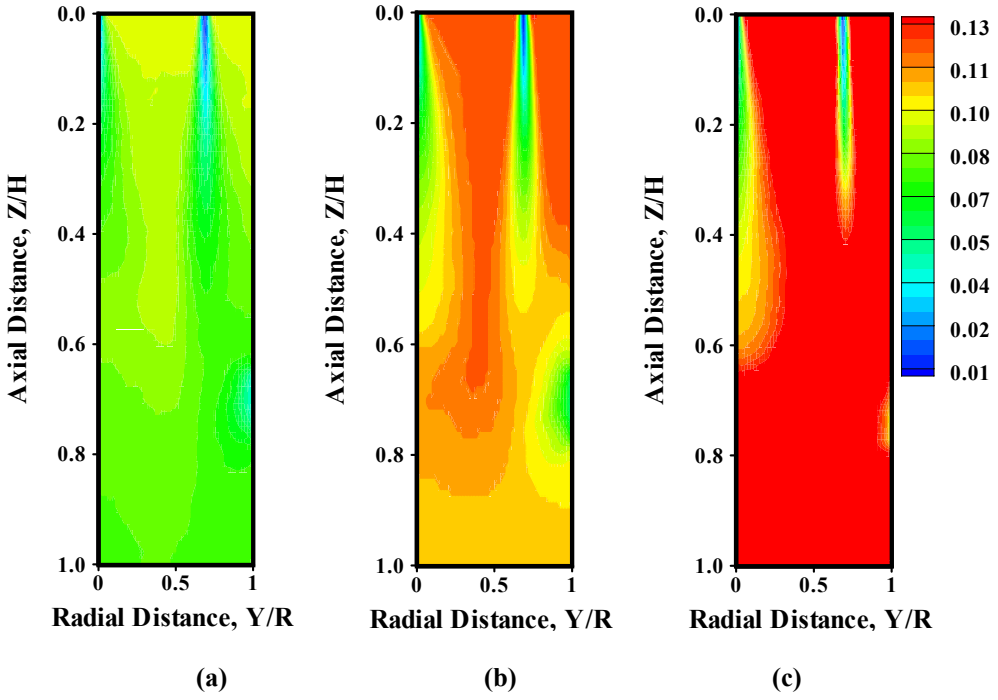

Figure 8.30: The contour profiles of carbon dioxide concentration obtained from numerical calculations for various inlet oxygen concentrations in the oxidizer jet (a) $X_{O2,ox}$=0.21, (b) $X_{O2,ox}$=0.30 and (c) $X_{O2;ox}$=0.40 with $\Phi_{overall}$ =1.0 and d_{ox}=15.9 mm.

Figure 8.31 shows radial carbon dioxide concentration profiles at different axial positions obtained from experiments and numerical calculations for various inlet oxygen concentrations in the oxidizer jet $X_{O2;ox}$=0.21, 0.30 and 0.40 with d_{ox}=15.9 mm and $\Phi_{overall}$ =1.0. It is observed from Figure 8.31 that the numerical predictions show quite good agreement with the experimental data for the case of $X_{O2;ox}$=0.21 and 0.30. However, the discrepancy between experiments and numerical predictions is large for the case of $X_{O2;ox}$ =0.40. The mole fraction of carbon dioxide obtained from experiments is quite less

than that of numerical calculations. It is believed that lower inlet oxygen concentration than target value flows into the furnace in experiments, which might result from inaccuracy of mixing air and oxygen for supplying target inlet oxygen concentration. The profiles of carbon dioxide becomes really flat from the middle of domain for the case of $X_{O2;ox}$ =0.21 and 0.30, which indicates the uniform reaction and strong recirculation of the product gases in the furnace. However, the profiles of carbon dioxide are found to be relatively less flat and consequently less uniformity in reaction for the case of $X_{O2;ox}$ =0.40.

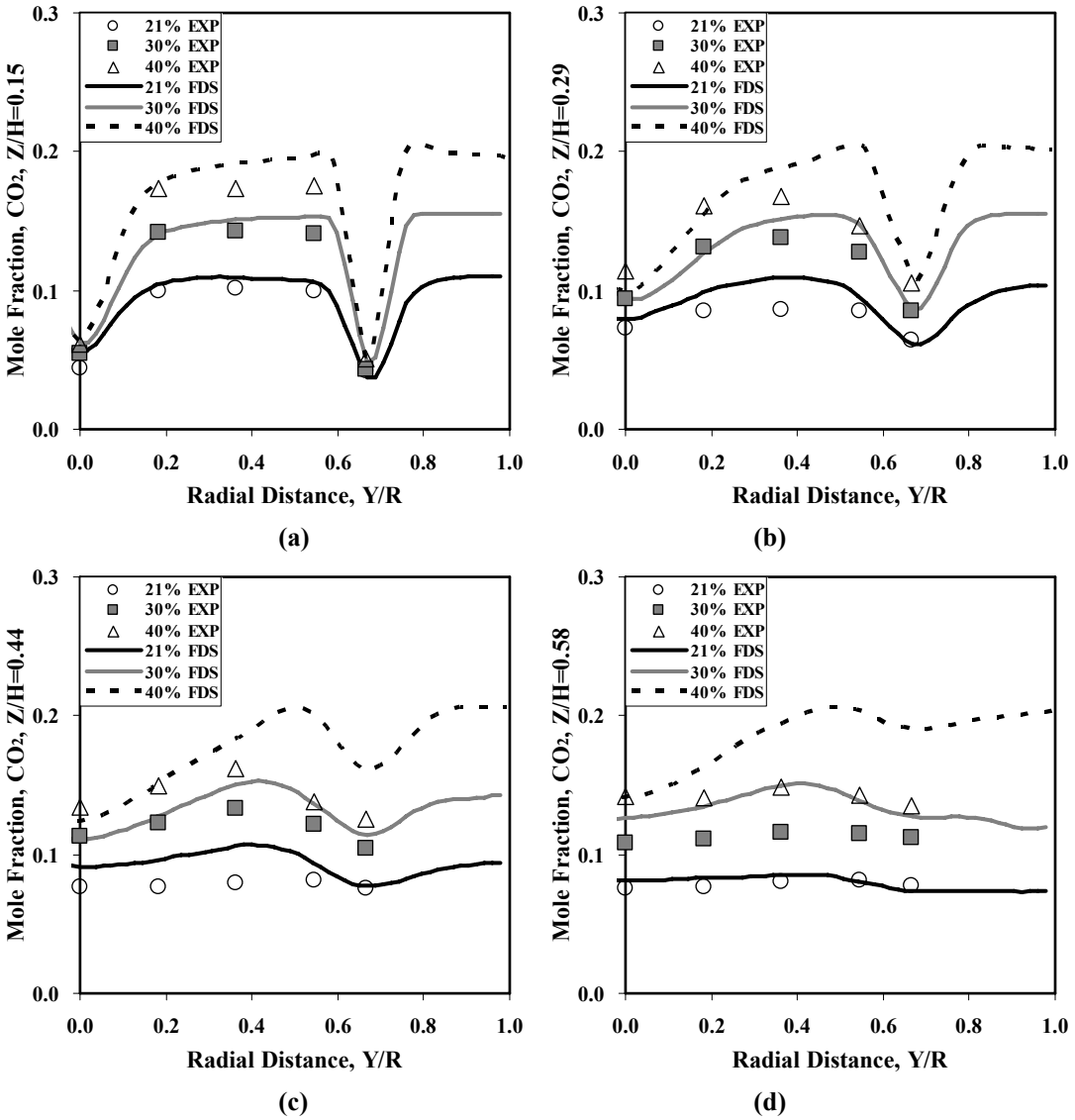

Figure 8.31: The radial carbon dioxide concentration profiles at different axial positions obtained from experiments and numerical calculations (a) *Z/H*=0.15, (b) *Z/H*=0.29, (c) *Z/H*=0.44 and (d) *Z/H*=0.58 for various inlet oxygen concentrations in the oxidizer jet $X_{O2;ox}$=0.21, 0.30 and 0.40 with $\Phi_{overall}$ =1.0 and d_{ox}=15.9 mm.

In summary, the numerical calculations are in good agreement with experimental data for the case of $X_{O2;ox}$=0.21 and 0.30, whereas large discrepancy is shown for the case of $X_{O2;ox}$=0.40. The inlet oxygen concentration is adjusted by mixing ambient air and oxygen in experiments, and the flow rates of the jets are calibrated by pressure correction. However, large fluctuation of supplying pressure has been experienced in mixing process, especially for the case of high inlet oxygen concentration because there is no device for accumulating the mixture of air and oxygen. Thus, the operating error in adjusting inlet oxygen concentration may exist in experimental data and this error becomes large for the case of high oxygen inlet concentration. It might be thought that lower inlet oxygen concentration than target value flows into the furnace in experiments comparing to numerical calculations.

8.3. Effects of the oxidizer jet diameter on reacting flows

8.3.1 Velocity field

Figure 8.32 shows the radial velocity profiles at different axial positions for various oxidizer jet diameters d_{ox}=7.94, 15.9 and 31.8 mm with $X_{O2;ox}$ =0.30 and $\Phi_{overall}$ =1.0.

The initial velocities in the oxidizer jet show a big gap between cases because of different size of the oxidizer jet diameter. It is observed that the region of the recirculation at interface region between jets becomes smaller and weaker, whereas recirculation at the center jet region becomes more noticeable along with axial distance for the case of d_{ox}=7.94 and 15.9 mm. On the other hand, for the case of the largest diameter d_{ox}= 31.8 mm, the recirculation at interface region is dominant over the whole furnace domain. This indicates that the recirculation of the fuel jet is quite strong rather than that of the oxidizer jet, consequently, the reaction front shifts toward the oxidizer jet and small scale of mixing is formed in the furnace. The scaled centerline stream-wise velocities of the fuel jet are shown in Figure 8.33. It is clearly observed that the region of negative velocity and its amplitude increases with smaller oxidizer jet diameter. The case of d_{ox}= 31.8 mm shows a quite small area of negative stream-wise velocity, which means low level of the recirculation at the center region.

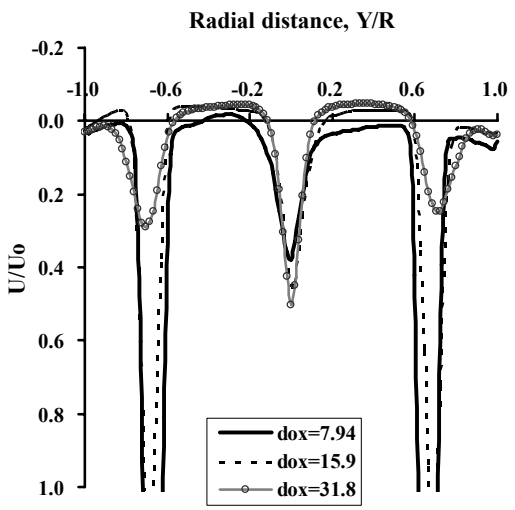
Radial distance, Y/R
-0.2
-1.0
-0.6
-0.2
0.2
0.6
1.0
0.0
0.2
0.4
0.6
0.8
1.0
U/Uo
dox=7.94
dox=15.9
dox=31.8

(a)

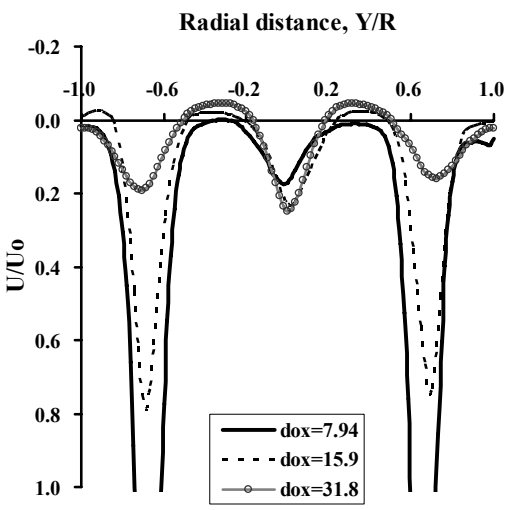
Radial distance, Y/R
-0.2
-1.0
-0.6
-0.2
0.2
0.6
1.0
0.0
0.2
0.4
0.6
0.8
1.0
U/Uo
dox=7.94
dox=15.9
dox=31.8

(b)

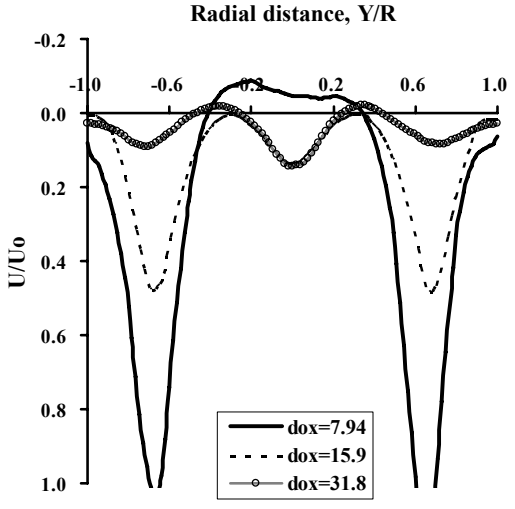
Radial distance, Y/R
-0.2
-1.0
-0.6
0.2
0.6
1.0
0.0
0.2
0.4
0.6
0.8
1.0
U/Uo
dox=7.94
dox=15.9
dox=31.8

(c)

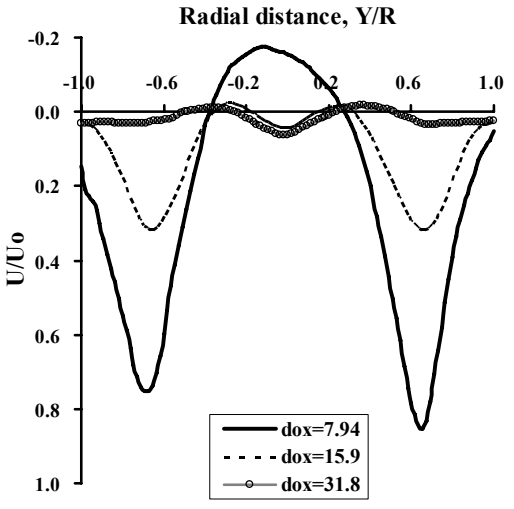
Radial distance, Y/R
-0.2
-1.0
-0.6
-0.2
0.2
0.6
1.0
0.0
0.2
0.4
0.6
0.8
1.0
U/Uo
dox=7.94
dox=15.9
dox=31.8

(d)

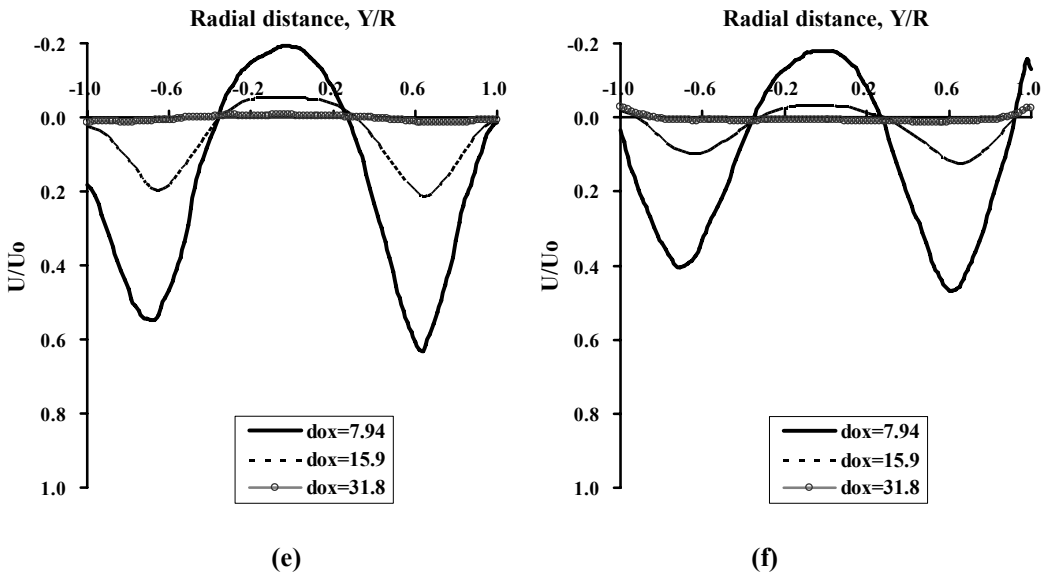

Figure 8.32: The radial stream-wise velocity profiles at different axial positions obtained from numerical calculations (a) *Z/H*=0.15, (b) *Z/H*=0.29, (c) *Z/H*=0.44, (d) *Z/H*=0.58, (e) *Z/H*=0.72 and (f) *Z/H*=0.86 for various oxidizer jet diameters and d_{ox}=7.94, 15.9 and 31.8 mm with $X_{O2;ox}$=0.30 and $\Phi_{overall}$ =1.0.

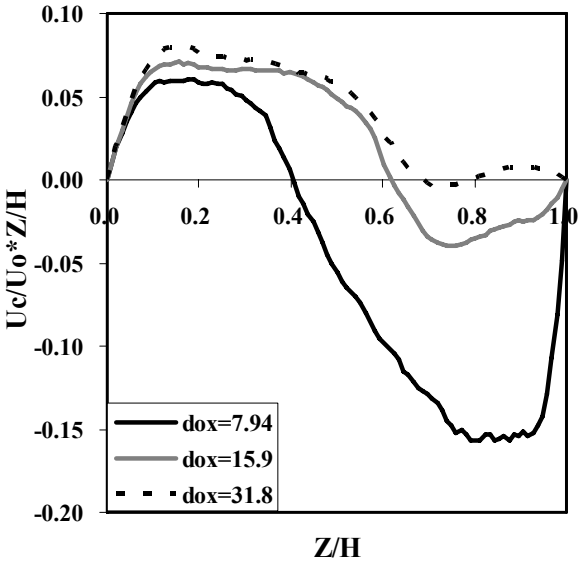

Figure 8.33: The scaled centerline stream-wise velocity of the fuel jet obtained from numerical calculations for various oxidizer jet diameters and d_{ox}=7.94, 15.9 and 31.8 mm *with* $X_{O2;ox}$=0.30 and $\Phi_{overall}$ =1.0.

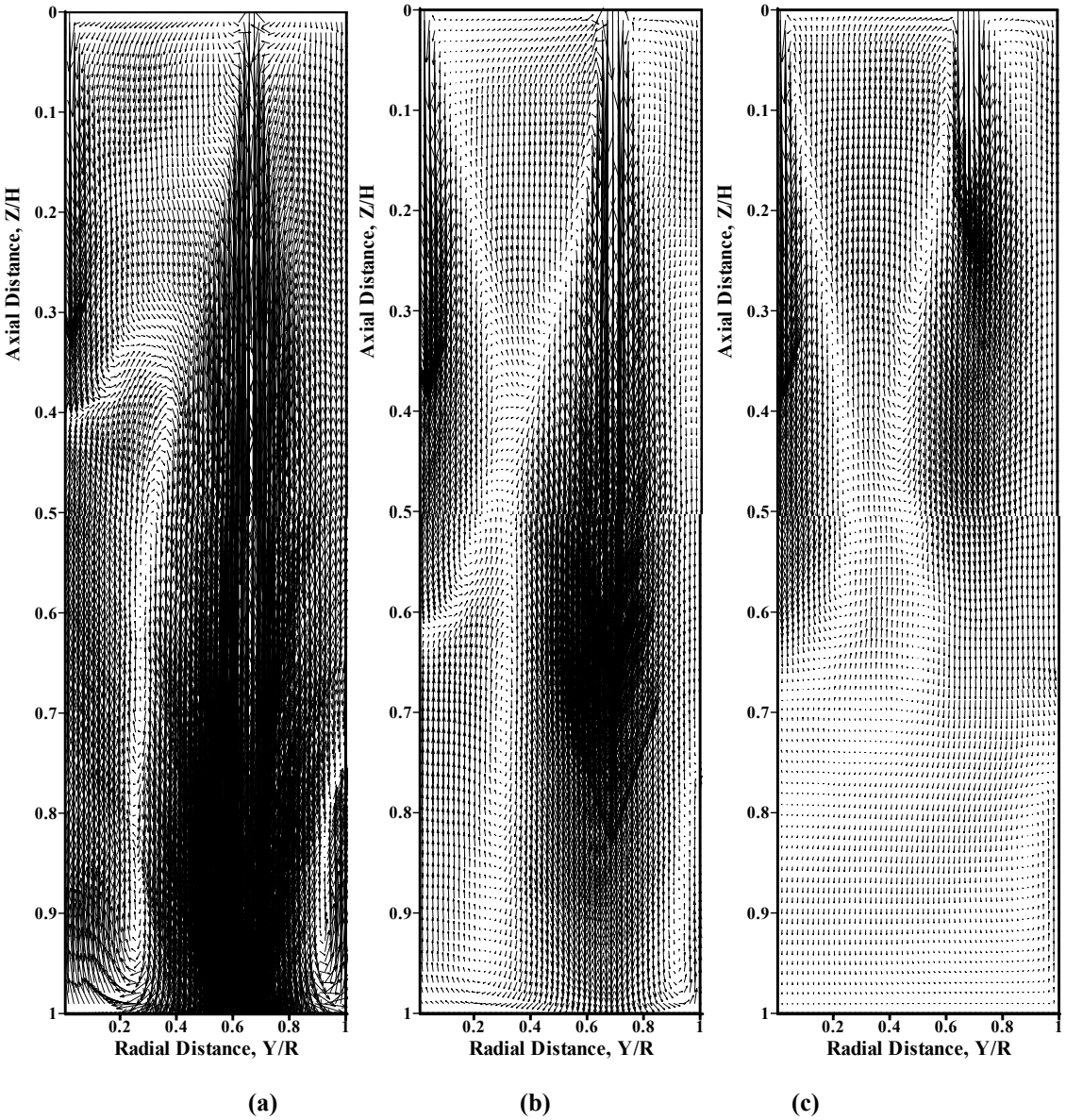

Figure 8.34: The velocity vector profiles of numerical calculations for various inlet oxygen concentrations in the oxidizer jet (a) d_{ox}=7.94, (b) d_{ox}=15.9 and (c) d_{ox}=31.8 mm with $X_{O2;ox}$ =0.30 and $\Phi_{overall}$ =1.0.

Figure 8.34 shows the velocity vector profiles obtained from numerical calculations for various oxidizer jet diameters d_{ox}=7.94, 15.9 and 31.8 mm with $X_{O2;ox}$ =0.30 and $\Phi_{overall}$ =1.0.

It is observed that the intensity of velocity vectors between jets is high for the case of d_{ox}=31.8 mm, however, this increase results from the recirculation of the fuel jet. With large separation distance between jets, it is preferable that the recirculation is formed at

the center region from the oxidizer jet toward the fuel jet for obtaining large scale of mixing in the furnace. However, large scale of recirculation from the oxidizer jet side is not formed sufficiently at the center region for the case of d_{ox}=31.8 mm because the momentum of the oxidizer jet is too weak and only small recirculation of the fuel jet is overwhelm over the furnace domain. This might be attributed the fact that less momentum of the oxidizer jet with larger diameter adversely affects mixing intensity and entrainment of product gases, thus unfavorable for achieving the homogeneous combustion condition.

8.3.2. Temperature

8.3.2.1. Jet Centerline Temperature

Figure 8.35 shows the centerline temperature of the fuel and oxidizer jets obtained from experiments and numerical calculations for various oxidizer jet diameters d_{ox}=7.94, 15.9 and 31.8 mm with $X_{O2;ox}$ =0.30 and $\Phi_{overall}$ =1.0. In this figure, the designation of *d1*, *d2* and *d3* mean oxidizer jet diameters d_{ox}=7.94, 15.9 and 31.8 mm, respectively in order of the diameter size.

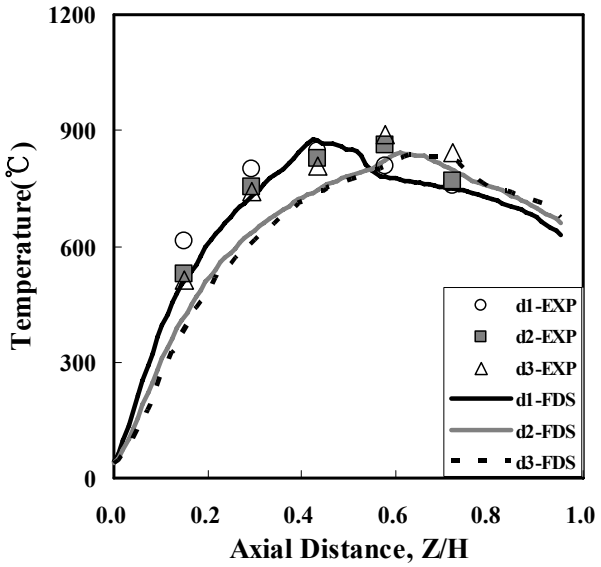

(a)

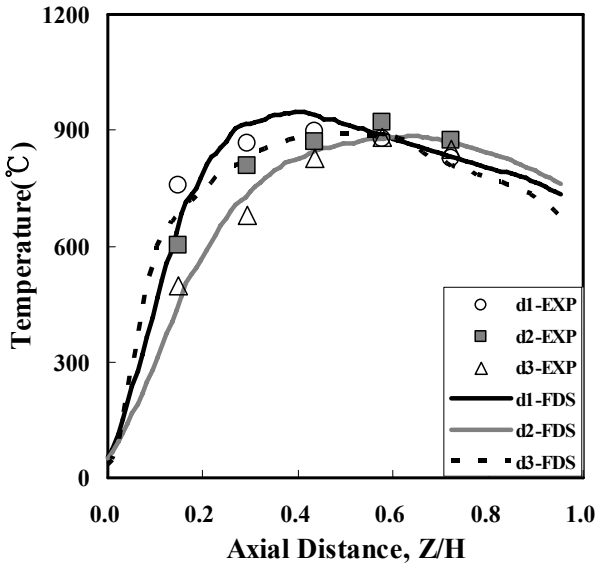

(b)

Figure 8.35: The centerline temperature of the (a) fuel jet and (b) oxidizer jet obtained from experiments and numerical calculations for various oxidizer jet diameters d_{ox}=7.94, 15.9 and 31.8 mm with $X_{O2;ox}$ =0.30 and $\Phi_{overall}$ =1.0.

The rising slope of the fuel jet centerline temperature is almost identical for the cases of $d_{ox=}$15.9 and 31.8 mm, whereas higher temperature is shown for the case of $d_{ox=}$7.94 mm. On the other hand, the slope of the oxidizer jet becomes steeper with decrease of the oxidizer jet diameter except for the case of d_{ox}=31.8 mm, which indicates that the reaction rate is enhanced at upstream region of the furnace. It might be thought that the recirculation is formed earlier and stronger with decrease of the oxidizer jet diameter because momentum of the oxidizer jet increases as shown in Figure 8.32 and 34. As a result, the oxygen concentration in re-circulated flue gas also increases and reaction rate is enhanced near the jet exit region.

8.3.2.2. Radial Temperature Profiles along with axial distance

The temperature contour profiles for *Y-Z* plane and radial temperature profiles at different axial positions for various oxidizer jet diameters d_{ox}=7.94, 15.9 and 31.8 mm with $X_{O2;ox}$ =0.30 and $\Phi_{overall}$ =1.0 are shown in Figure 8.36 and 37, respectively.

It is noted that the centerline of the oxidizer jet leans toward the furnace wall for the case of d_{ox}=31.8 mm in numerical calculation because momentum of the oxidizer jet is too

weak, thus the fuel jet flow can push the oxidizer flow laterally. However, this trend is not observed in experiments. As shown in Figure 8.36, the reaction occurs around the oxidizer jet with lager oxidizer jet diameter and the height of high temperature region decreases.

The case of d_{ox}=7.94 mm shows the lower temperature than other cases, and quite flat radial profiles quickly after Z/H=0.44 as shown in Figure 8.37. This might be attributed the fact that the recirculation flow occurs strongly with small oxidizer jet diameter because of increasing oxidizer jet momentum, hence enhanced dilution of the jets. As a result, the reaction is delayed and temperature decreases due to enhanced dilution of the jets and mixing is promoted by large scale of recirculation in the furnace.

However, it is hard to judge which case is in the homogeneous combustion condition or not by considering only temperature profiles because the overall trend is quite similar for all cases.

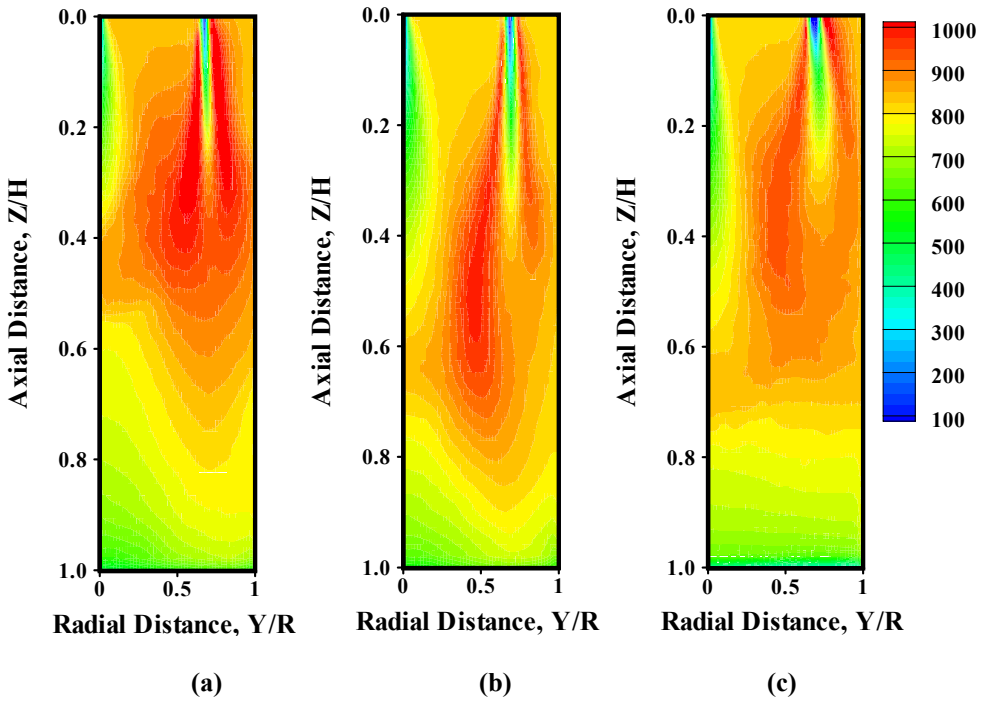

Figure 8.36: The contour profiles of temperature obtained from numerical calculations for various inlet oxygen concentrations in the oxidizer jet (a) d_{ox}=7.94, (b) d_{ox}=15.9 and (c) d_{ox}=31.8 mm with $X_{O2;ox}$ =0.30 and $\Phi_{overall}$ =1.0.

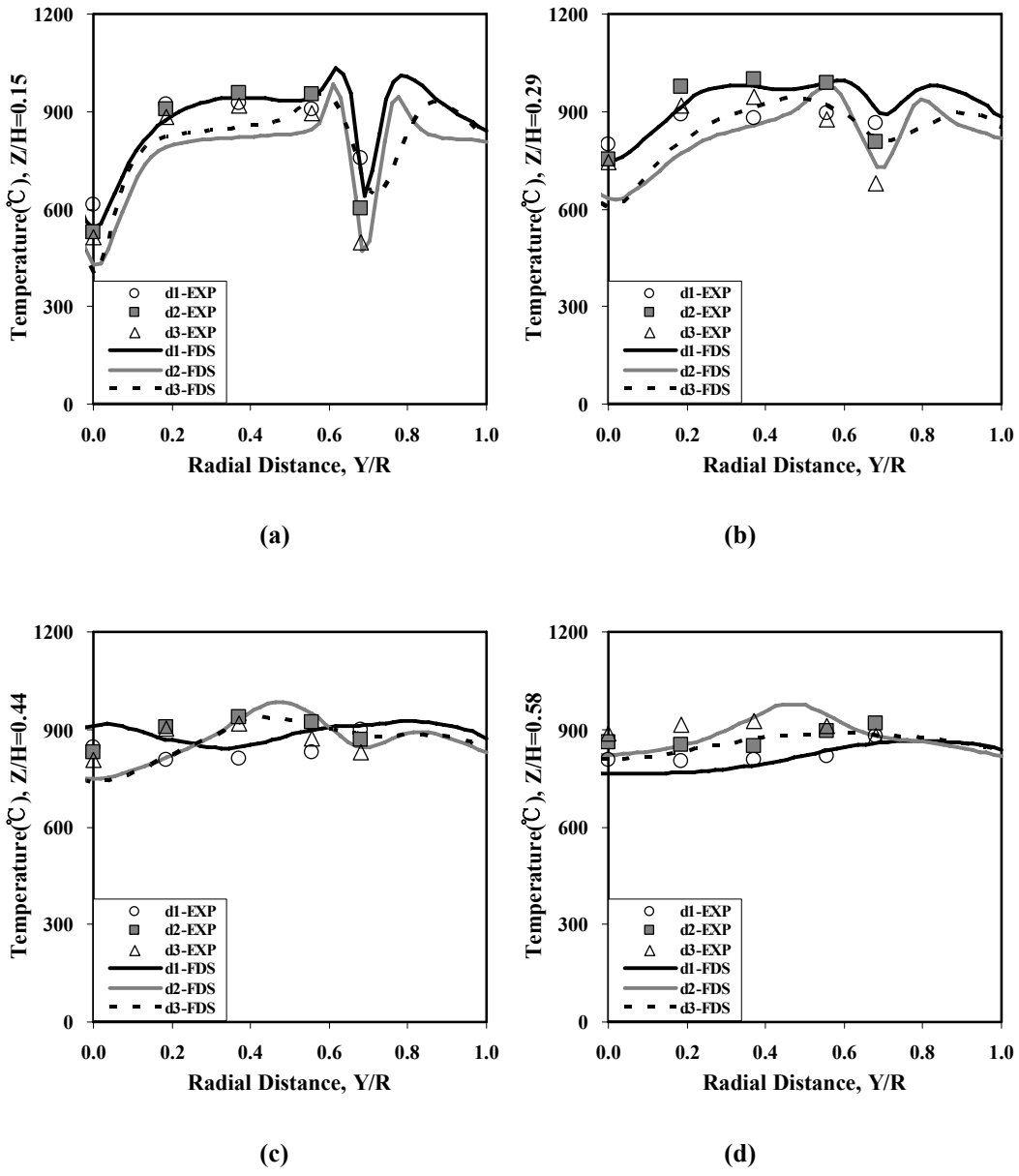

Figure 8.37: The radial profiles of temperature at different axial positions obtained from experiments and numerical calculations (a) Z/H=0.15, (b) Z/H=0.29, (c) Z/H=0.44 and (d) Z/H=0.58 for various oxidizer jet diameters and d_{ox}=7.94, 15.9 and 31.8 mm with $X_{O2;ox}$=0.30 and $\Phi_{overall}$ =1.0.

8.3.3. Gas compositions

8.3.3.1. Jet Centerline gas composition

The decay patterns of methane and oxygen concentration in the fuel and oxidizer jet centerline obtained from experiments and numerical calculations for various oxidizer jet diameters d_{ox}=7.94, 15.9 and 31.8 mm with $X_{O2;ox}$ =0.30 and $\Phi_{overall}$ =1.0 are shown in Figure 8.38.

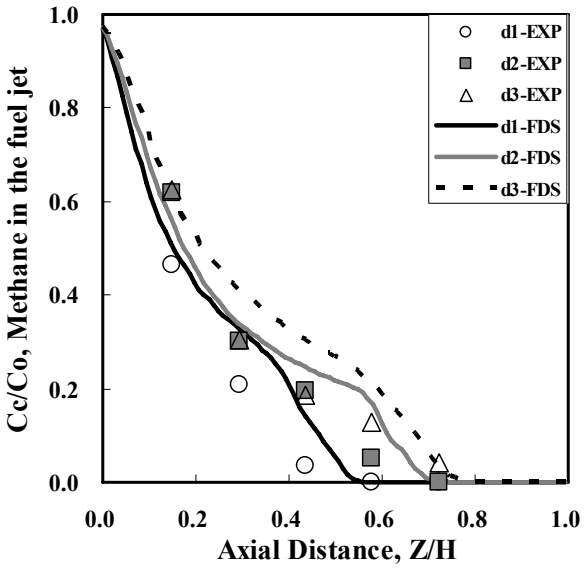

(a)

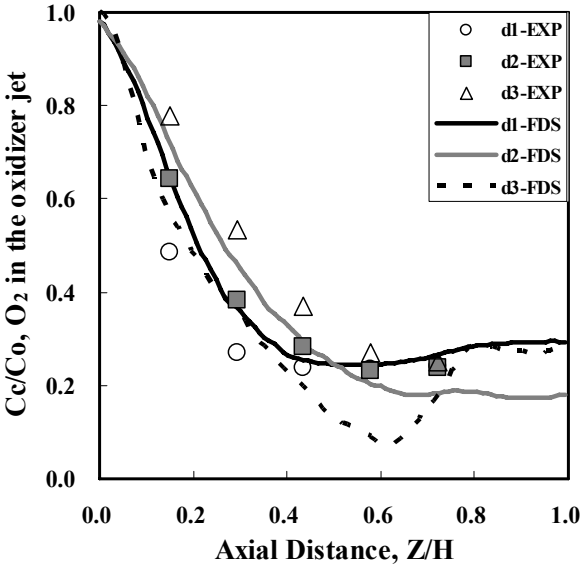

(b)

Figure 8.38: The decay patterns of normalized (a) methane concentration in the fuel jet centerline and (b) oxygen concentration in the oxidizer jet centerline obtained from experiments and numerical calculations for various oxidizer jet diameters d_{ox}=7.94, 15.9 and 31.8 mm with $X_{O2;ox}$ =0.30 and $\Phi_{overall}$ =1.0.

The decay rate of the centerline methane and oxygen concentrations becomes larger with smaller oxidizer jet diameter in both experiments and numerical calculations except for the case of d_{ox}=31.8 mm. This can be attributed the same reason explained in previous

section, which is related to the fuel jet expansion and momentum of the oxidizer jet. It is obvious that dilution of the jets is promoted due to larger momentum of the oxidizer jet with smaller diameter, and the recirculation pattern is also formed earlier and its intensity increases as shown in Figure 8.32 to 34.

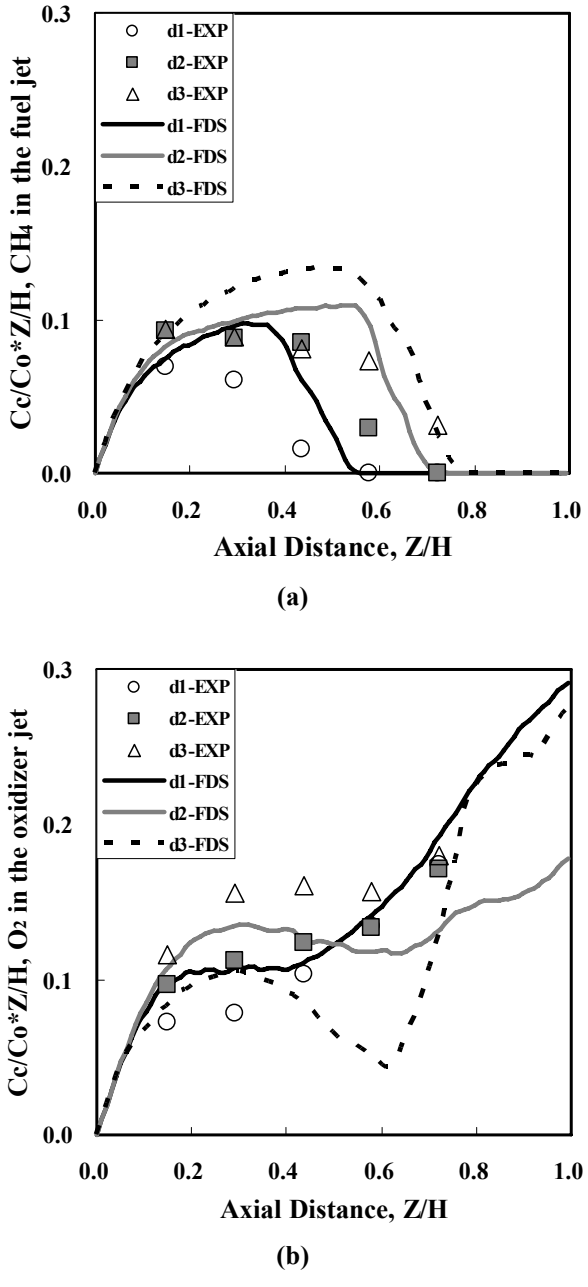

Figure 8.39: The scaled centerline (a) methane concentration in the fuel jet and (b) oxygen concentration in the oxidizer jet obtained from experiments and numerical calculations for various oxidizer jet diameters d_{ox}=7.94, 15.9 and 31.8 mm with $X_{O2;ox}$ =0.30 and $\Phi_{overall}$ =1.0.

The decay patterns of the centerline gas concentration can be expressed in other way as shown in Figure 8.39 showing the scaled centerline methane concentration in the fuel jet and oxygen concentration in the oxidizer jet. The scaled value of the centerline methane concentration in the fuel jet falls faster with small oxidizer jet diameter due to strong recirculation flow, and scaled value of the centerline oxygen concentration in the oxidizer jet is lower as the oxidizer jet diameter decreases except for the case of d_{ox}=31.8 mm. As mentioned before, the centerline of the oxidizer jet leans toward furnace wall for the case of d_{ox}=31.8 mm, thus reaction zone shifts to the oxidizer jet in numerical calculations. Consequently, the temperature and oxygen consumption becomes higher than measured data in experiments at the location of the oxidizer jet centerline.

Based on the UV emission and visual image in experiments, the case of d_{ox}=7.94 and 15.9 mm are in the homogeneous combustion mode, whereas the highest inlet oxygen concentration d_{ox}=31.8 mm is in the non-homogeneous combustion mode. It might be thought that the reaction occurs mainly around the oxidizer jet, and dilution of the oxidizer jet is achieved by combustion instead of entrainment of product gases. The jets should be sufficiently diluted by product gases before reaction occurs, however, for the case of d_{ox}=31.8 mm, the reaction precedes sufficient dilution of the oxidizer jet.

8.3.3.2. Jet entrainment

Figure 8.40 shows the mole fraction of carbon dioxide in the fuel and oxidizer jet centerline obtained from experiments and numerical calculations for various oxidizer jet diameters d_{ox}=7.94, 15.9 and 31.8 mm with $X_{O2;ox}$ =0.30 and $\Phi_{overall}$ =1.0.

It is clearly observed that the amount of carbon dioxide in the oxidizer jet increases with smaller oxidizer jet diameter in experiments, which is in accordance with jet theory stating that more dilution can be achieved with higher momentum. This dilution of the jets is quite essential to obtain the homogeneous combustion condition. On the other hand, numerical calculations shows a good agreement with experimental data for the cases of d_{ox}=7.94 and 15.9mm, whereas a poor result is shown for the case of d_{ox}=31.8 mm. The carbon dioxide concentration is larger than the case of d_{ox}=15.9 mm. However, the reaction zone shifts around the oxidizer jet as shown Figure 8.36, thus the amount of carbon dioxide increases entrained into the oxidizer jet and oxygen consumption

increases in numerical calculation. It is also observed that carbon dioxide concentration in the oxidizer jet drops sharply after Z/H=0.65 for the case of d_{ox} =31.8 mm in numerical calculation. This can be thought that infiltration from outside having higher oxygen concentration occurs through the exhaust vent, consequently carbon dioxide concentration falls quickly after Z/H=0.65.

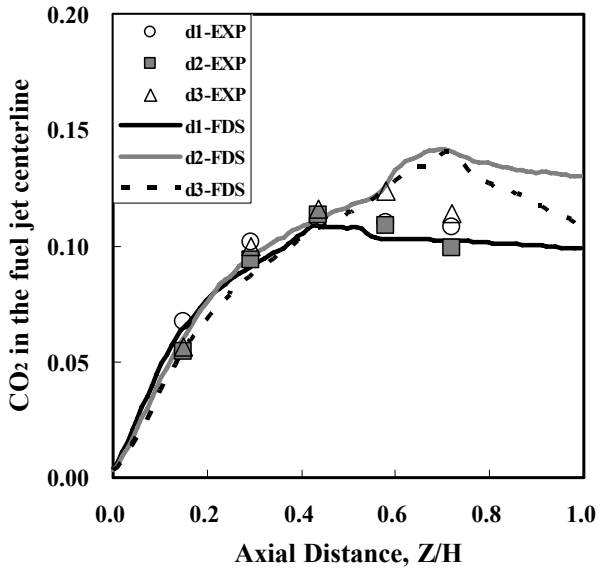

(a)

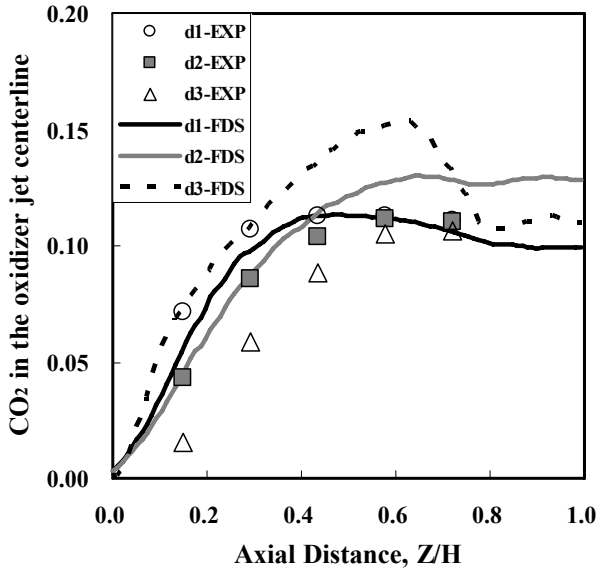

(b)

Figure 8.40: The normalized centerline carbon dioxide concentration in the (a) fuel jet and (b) oxidizer jet obtained from experiments and numerical calculations for various oxidizer jet diameters d_{ox}=7.94, 15.9 and 31.8 mm with $X_{O2;ox}$ =0.30 and $\Phi_{overall}$ =1.0.

8.3.3.3. Radial gas composition profiles

The contour profiles of the methane concentration obtained from numerical calculations for various oxidizer jet diameters d_{ox} =7.94, 15.9 and 31.8 mm with $X_{O2;ox}$=0.30 and $\Phi_{overall}$=1.0 are shown in Figure 8.41. It is clearly seen that the region of the fuel jet expands more laterally with increase of the oxidizer jet diameter because of weak momentum of the oxidizer jet. In addition, higher fuel concentration can be found near the oxidizer jet exit, which means that the recirculation of the fuel jet is enhanced with larger oxidizer jet diameter.

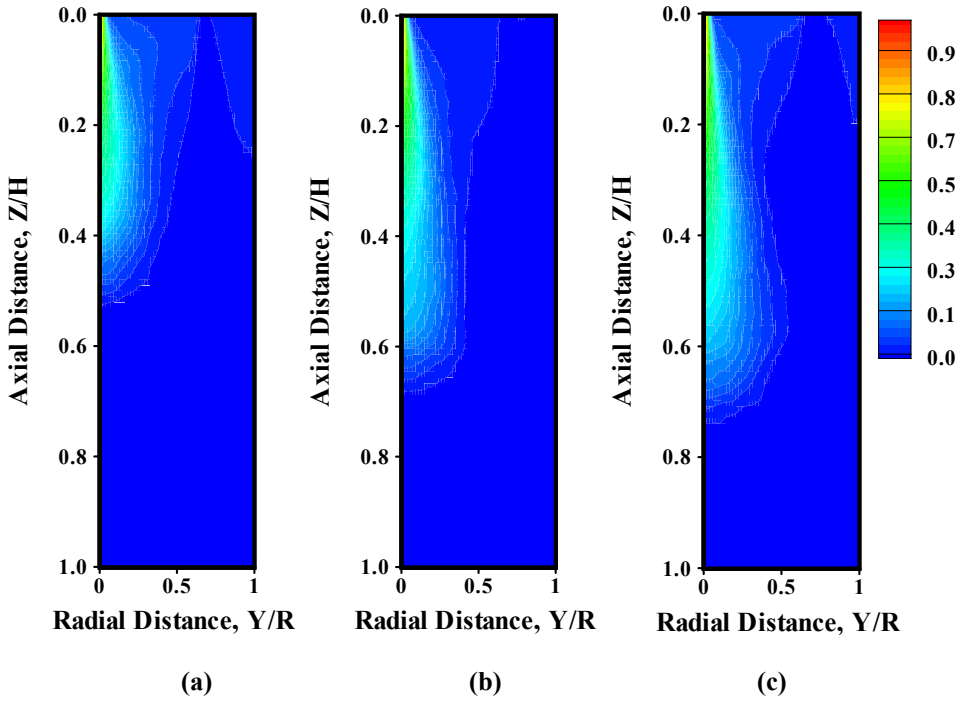

Figure 8.41: The contour profiles of methane concentration obtained from numerical calculations for various inlet oxygen concentrations in the oxidizer jet (a) d_{ox}=7.94, (b) d_{ox}=15.9 and (c) d_{ox}=31.8 mm with $X_{O2;ox}$ =0.30 and $\Phi_{overall}$ =1.0.

Figure 8.42 shows radial profiles of methane concentration at different axial positions obtained from experiments and numerical calculations for various oxidizer jet diameters d_{ox}=7.94, 15.9 and 31.8 mm with $X_{O2;ox}$ =0.30 and $\Phi_{overall}$ =1.0. Even though there is a discrepancy between experiments and numerical calculations, the overall trend of radial temperature profiles are well captured in numerical calculations. The methane concentration decays faster with smaller oxidizer jet diameter in both experiments and

numerical calculations. It might be thought that the fuel jet begins to be affected by recirculation flow at shorter axial distance and the methane concentration decays faster with smaller oxidizer jet diameter.

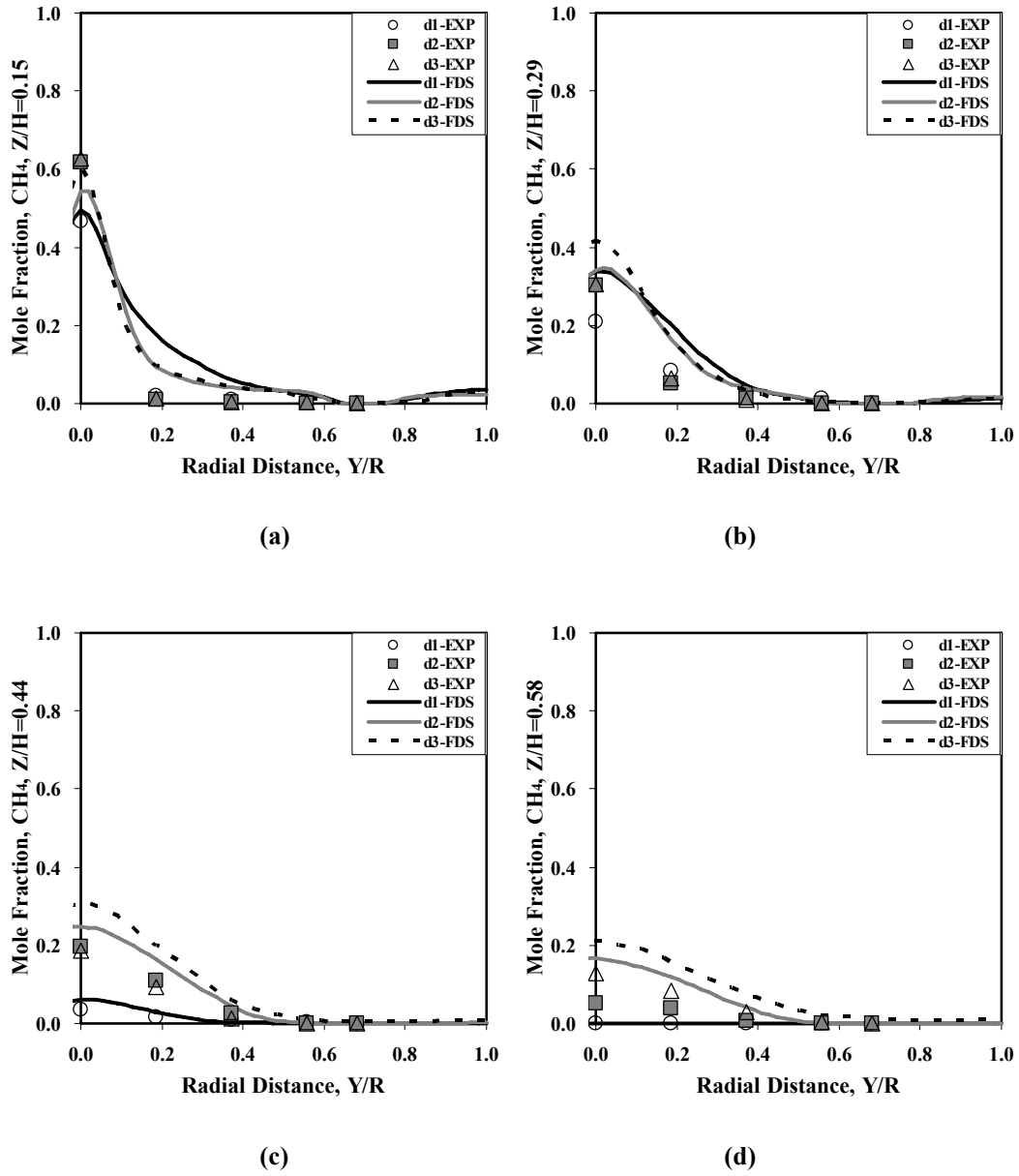

Figure 8.42: The radial profiles of methane concentration at different axial positions obtained from experiments and numerical calculations (a) *Z/H*=0.15, (b) *Z/H*=0.29, (c) *Z/H*=0.44 and (d) *Z/H*=0.58 for various oxidizer jet diameters and d_{ox}=7.94, 15.9 and 31.8 mm with $X_{O2;ox}$=0.30 and $\Phi_{overall}$ =1.0.

The contour profiles of oxygen concentration obtained from numerical calculations for various oxidizer jet diameters d_{ox}=7.94, 15.9 and 31.8 mm with $X_{O2;ox}$ =0.30 and $\Phi_{overall}$

=1.0 are shown in Figure 8.43. The consumption of oxygen is greater for the case of d_{ox}=31.8 mm, and oxygen disappears at about Z/H=0.6 because the reaction occurs mainly around the oxidizer jet. It is noted that air infiltration exists trough the exhaust vent corresponding Z/H=0.65~0.78, thus a little higher oxygen concentration can be found at the location of the exhaust vent.

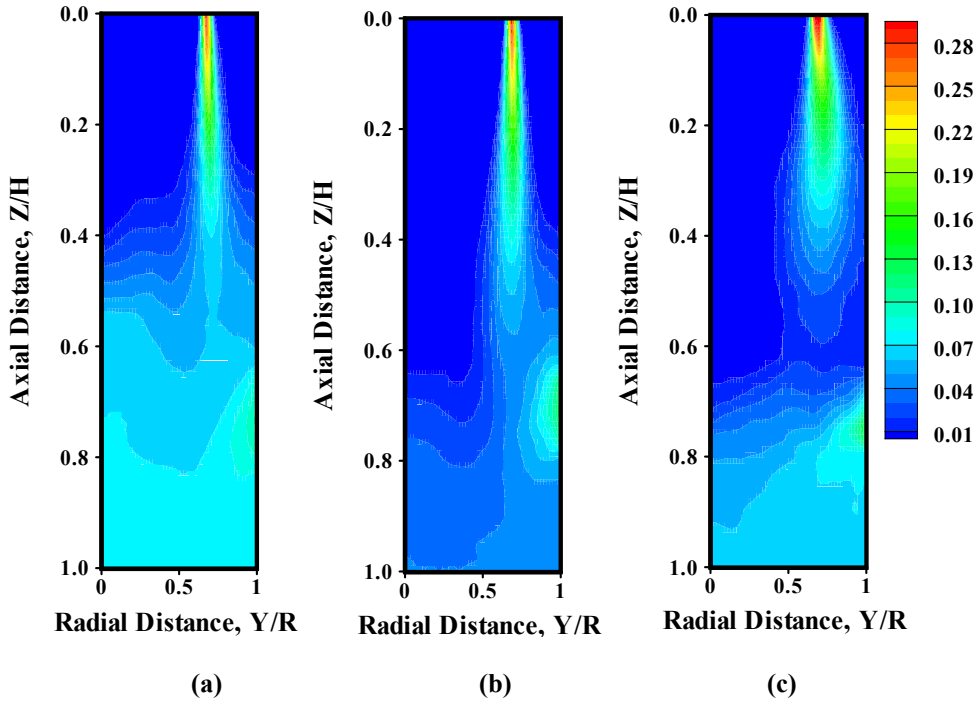

Figure 8.43: The contour profiles of oxygen concentration obtained from numerical calculations for various inlet oxygen concentrations in the oxidizer jet (a) d_{ox}=7.94, (b) d_{ox}=15.9 and (c) d_{ox}=31.8 mm with $X_{O2;ox}$ =0.30 and $\Phi_{overall}$ =1.0.

Figure 8.44 shows radial oxygen concentration profiles at different axial positions obtained from experiments and numerical calculations for various oxidizer jet diameters d_{ox}=7.94, 15.9 and 31.8 mm with $X_{O2;ox}$ =0.30 and $\Phi_{overall}$ =1.0.

It is observed that the lower oxygen concentration can be found in the oxidizer jet centerline with smaller oxidizer jet diameter, whereas higher concentration at interface region between jets. In addition, the oxygen concentration spreads more laterally with smaller oxidizer jet diameter. It can be attributed the fact that the oxidizer jet momentum increases with smaller oxidizer jet diameter, and hence entrainment of product gases is enhanced in the oxidizer jet. The recirculation flow also occurs intensively with smaller

oxidizer jet diameter. Therefore, the oxygen concentration decays faster in the oxidizer jet centerline and spreads more widely with smaller oxidizer jet diameter.

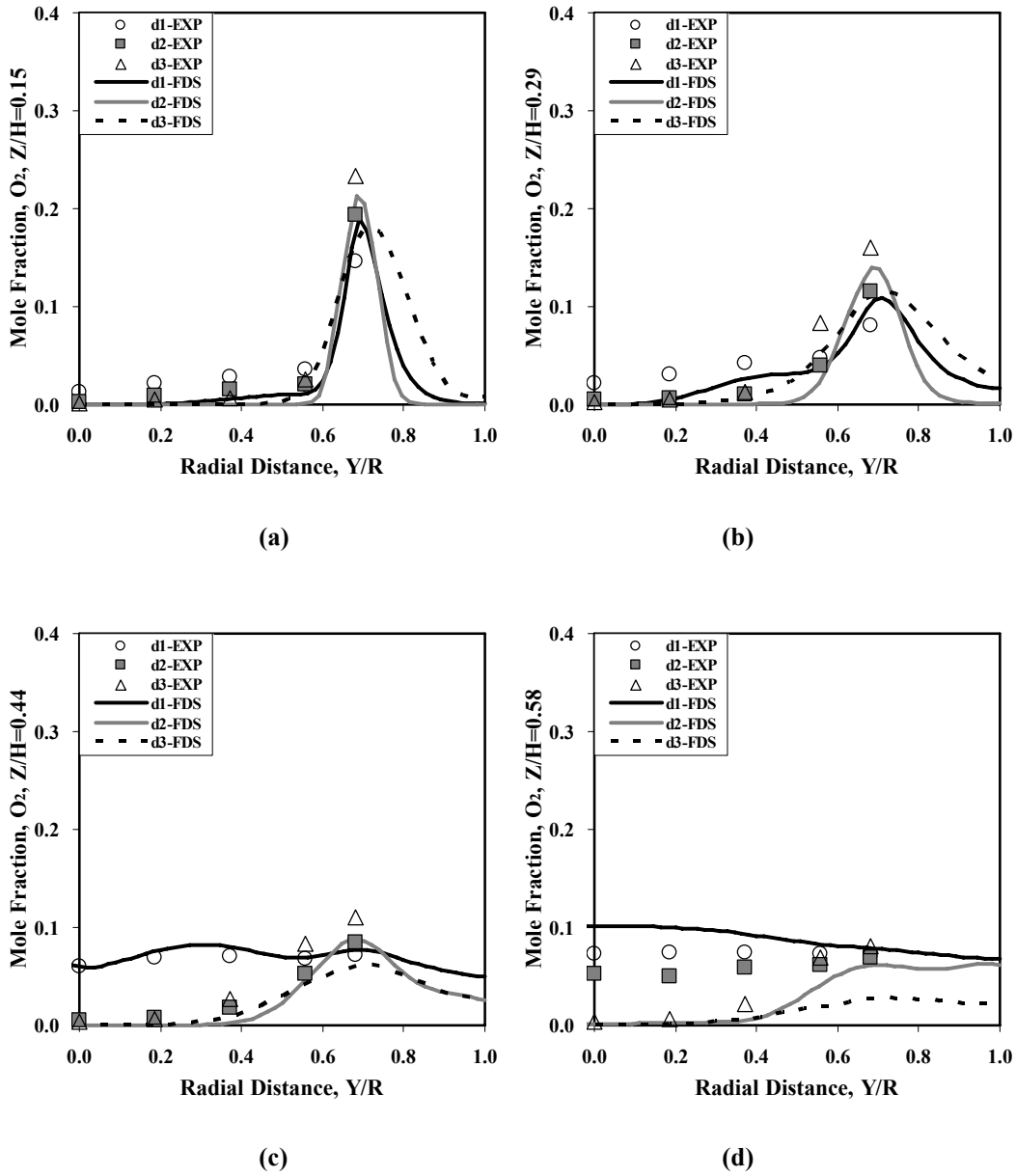

Figure 8.44: The radial oxygen concentration profiles at different axial positions obtained from experiments and numerical calculations (a) Z/H=0.15, (b) Z/H=0.29, (c) Z/H=0.44 and (d) Z/H=0.58 for various oxidizer jet diameters and d_{ox}=7.94, 15.9 and 31.8 mm with $X_{O2;ox}$=0.30 and $\Phi_{overall}$ =1.0.

The contour profiles of carbon dioxide concentration obtained from numerical calculations for various oxidizer jet diameters d_{ox}=7.94, 15.9 and 31.8 mm with $X_{O2;ox}$ =0.30 and $\Phi_{overall}$ =1.0 are shown in Figure 8.45.

The higher concentration of carbon dioxide is found at upstream region with larger oxidizer jet diameter, which indicates that the reaction rate increases at the region. It might be though that the recirculation of the fuel jet is quite remarkable for larger oxidizer jet diameter, thus the fuel concentration in re-circulated flow increases.

Figure 8.46 shows radial carbon dioxide concentration profiles at different axial positions obtained from experiments and numerical calculations for various oxidizer jet diameters d_{ox}=7.94, 15.9 and 31.8 mm with $X_{O2;ox}$ =0.30 and $\Phi_{overall}$ =1.0. It is seen from Figure 8.46 that the radial carbon dioxide profile becomes flat quickly across the radial direction with smaller oxidizer jet diameter, which indicates strong recirculation of product gases and uniform reaction in the furnace. The carbon dioxide concentration is lower with the smallest oxidizer jet diameter than those of other cases at interface region between jets. This results from the higher oxygen concentration due to strong recirculation of the jet flow with high momentum at this region.

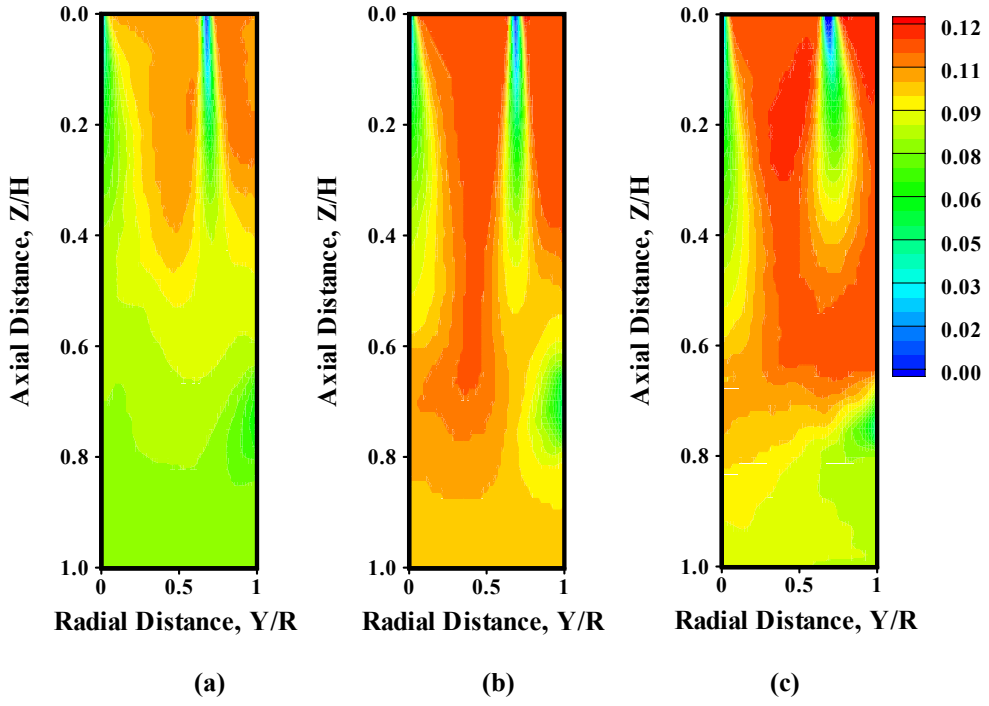

Figure 8.45: The contour profiles of carbon dioxide concentration obtained from numerical calculations for various inlet oxygen concentrations in the oxidizer jet (a) d_{ox} =7.94, (b) d_{ox} =15.9 and (c) d_{ox}=31.8 mm with $X_{O2;ox}$ =0.30 and $\Phi_{overall}$ =1.0.

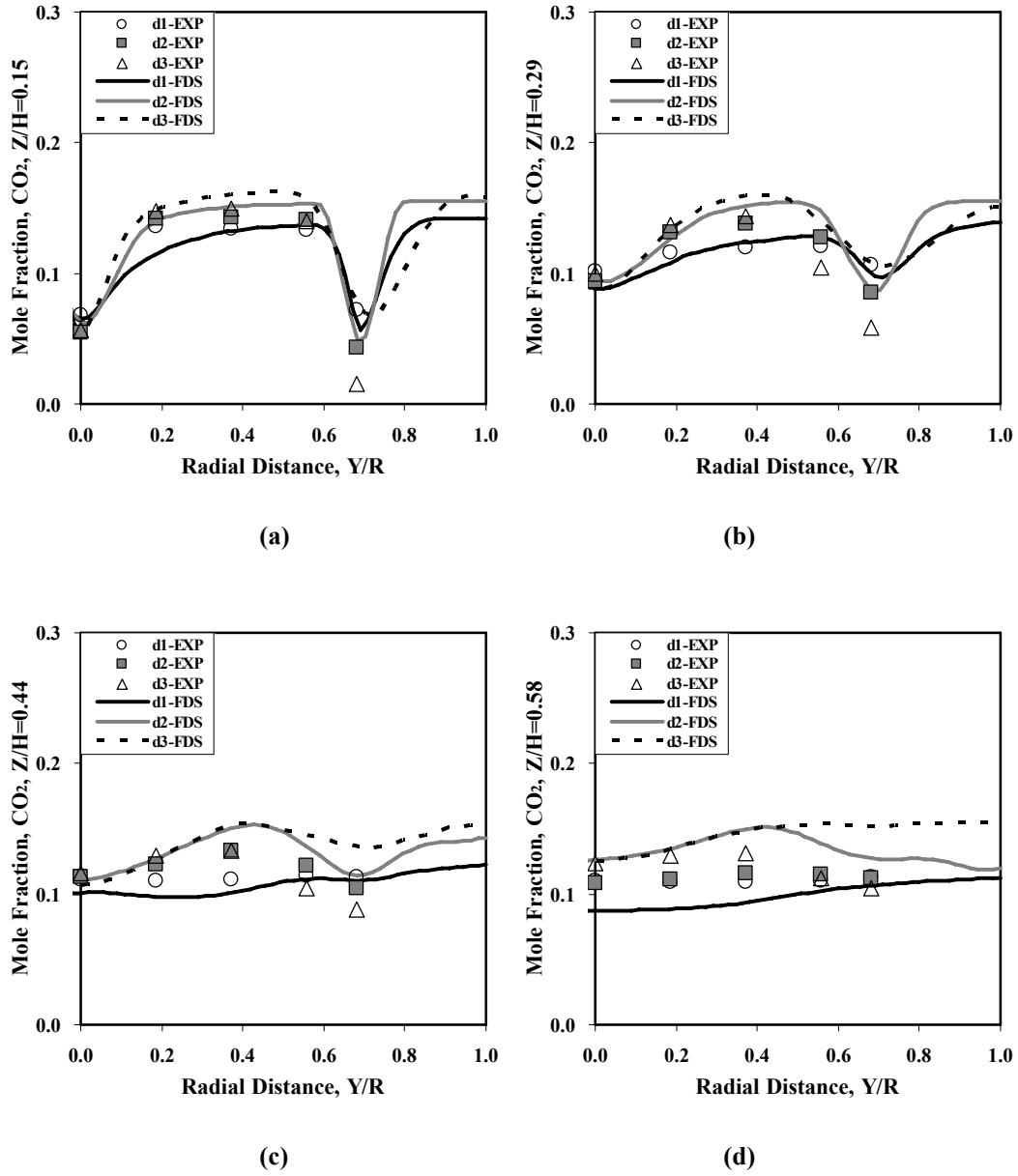

Figure 8.46: The radial carbon dioxide concentration profiles at different axial positions obtained from experiments and numerical calculations (a) Z/H=0.15, (b) Z/H=0.29, (c) Z/H=0.44 and (d) Z/H=0.58 for various oxidizer jet diameters and d_{ox}=7.94, 15.9 and 31.8 mm with $X_{O2;ox}$=0.30 and $\Phi_{overall}$ =1.0.

In summary, the numerical calculations are in good agreement with experimental data for the case of d_{ox}=7.94 and 15.9 mm. However, whereas poor prediction is shown for the case of d_{ox}=31.8 mm. The discrepancy originates from the location of reaction zone. The reaction still occurs mainly at interface region between jets even very low momentum of the oxidizer jet in experiments, whereas it shifts toward the oxidizer jet in numerical

calculations. As a result, the centerline temperature of the oxidizer jet is higher and oxygen concentration in the oxidizer jet centerline is lower than those of experiments.

The profiles of temperature and gas compositions becomes flat faster with decrease of oxidizer jet diameter, which means that well mixing and intense recirculation of product gases occurs in the furnace. Therefore, it can be concluded that smaller diameter of the jets (increase of momentum) is preferable to achieve the homogeneous combustion mode because of enhanced mixing, entrainment of product gases and strong recirculation of flow. It is recommended that small diameter of the jets should be selected among available sizes of the jet diameters in the case of using enriched oxygen combustion configuration.

8.4. Heat transfer in the furnace

The heat generated in the furnace is transferred to solid surface including the furnace walls and heat sink, and out of the furnace through the openings. Figure 8.47 shows the heat transfer ratio obtained from numerical calculations for various test conditions. In this figure, the ratio is defined as heat release rate to heat input.

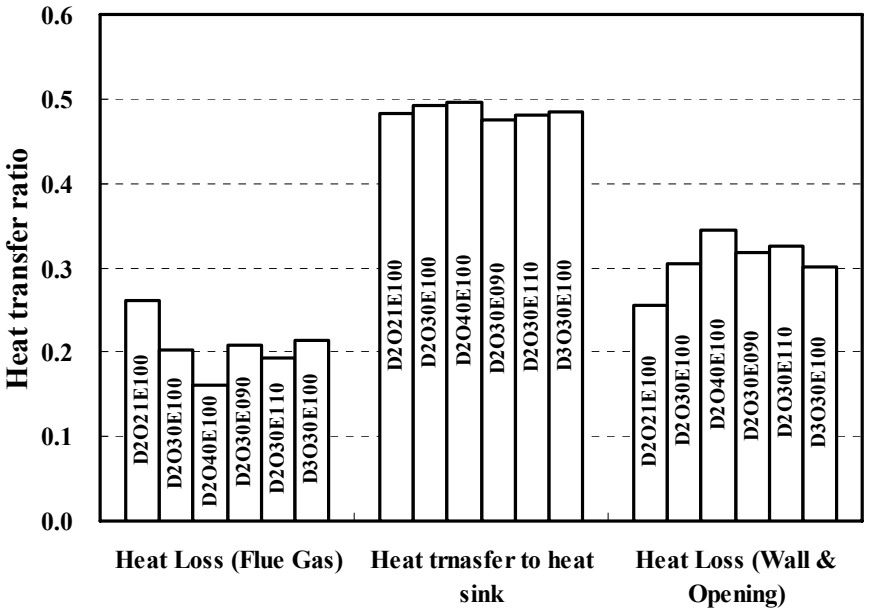

Figure 8.47: Heat transfer rate in the furnace obtained from numerical simulations for various test conditions.

The numerical simulations predict that approximately 50% of heat input is transferred to heat sink, 30% is going out of the furnace by conduction and radiation through walls and openings and 20% is going out of the furnace in the forms of convection by flue gases and radiation through openings.

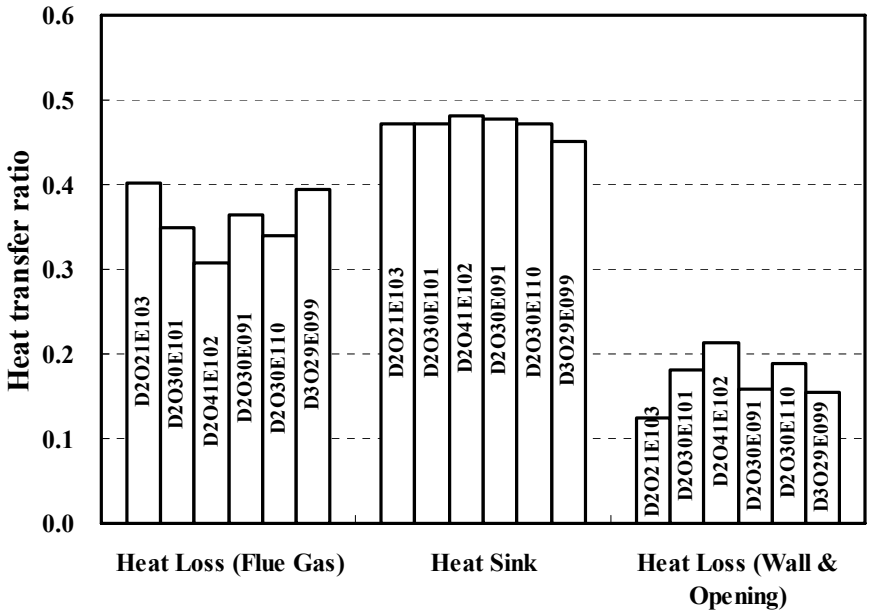

Figure 8.48: Heat transfer rate in the furnace obtained from experiments for various test conditions.

Comparing to numerical predictions, the results of experiment show quite large amount of flue losses because of adding the heat loss due to air infiltration. Figure 8.48 shows the heat transfer ratio obtained from experiments. In this figure, the heat losses due to air infiltration and radiation through openings are included. In experiments, around 47% of heat input is transferred to the heat sink and 17% goes to wall and opening losses while flue gases is carrying the remaining 36%. However, there is still discrepancy between experimental data and numerical predictions. The current furnace configuration in this study does not provide a proper arrangement for measuring the exhaust gas compositions. Thus, the exhaust gas compositions are estimated by substituting the mean gas concentrations of 4 probing points at Z/H=0.72 which are nearest to the exhaust vent of the chamber. It is thought that the discrepancy between experimental data and numerical predictions might result from this substitution for the exhaust exit which does not properly represent the actual exhaust gas conditions.

8.5. The effects of combustion on the velocity field

Figure 8.49 shows the radial velocity profiles of non-reacting and reacting flows obtained from numerical calculations for d_{ox}=15.9 mm, $X_{O2;ox}$ =0.30 and overall equivalence ratio $\Phi_{overall}$ =1.0.

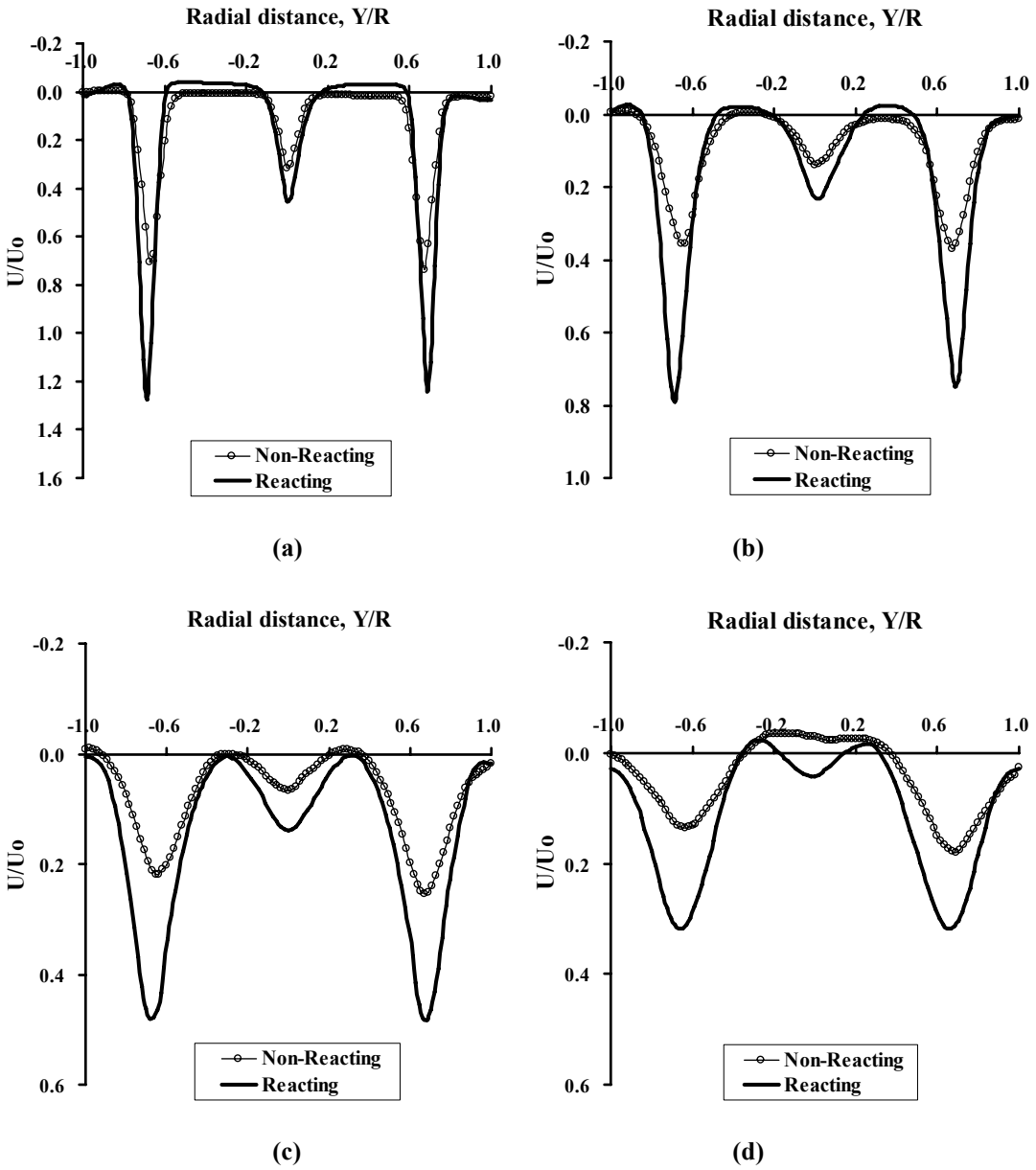

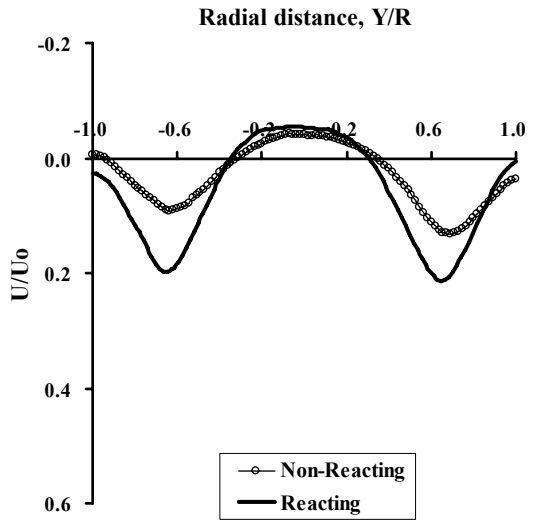

(e)

Figure 8.49: The radial stream-wise velocity profiles at different axial positions obtained from numerical calculations (a) *Z/H*=0.15, (b) *Z/H*=0.29, (c) *Z/H*=0.44, (d) *Z/H*=0.58, (e) *Z/H*=0.72 for non-reacting and reacting flows with overall equivalence ratios $\Phi_{overall}$= 1.0, $X_{O2;ox}$ =0.30 and d_{ox} =15.9 mm.

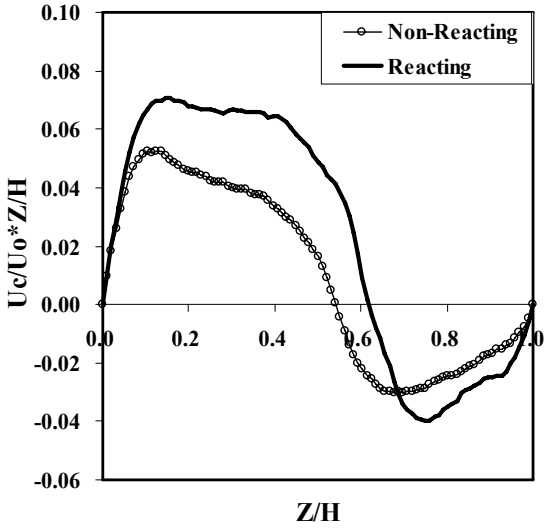

Figure 8.50: The scaled centerline stream-wise velocity of the fuel jet obtained from numerical calculations for non-reacting and reacting flows with overall equivalence ratios $\Phi_{overall}$= 1.0, $X_{O2;ox}$ =0.30 and d_{ox} =15.9 mm.

It is clearly observed that the spreading rate of the jet is lower in reacting flow. An explanation can be that the cold gases are injected into hot combustion products having low density due to combustion, thus the effect of thermal expansion becomes remarkable in reacting flow case. This thermal expansion lowers the velocity gradient between the jet and recirculation zone and hence jet spreading.

8.6. Buoyancy effects

The effect of buoyancy on reacting flow can be estimated by Richardson number, R_i, defined as the ratio of buoyant force F_B to inertial force F_I,

$$R_i = \frac{F_B}{F_I} = \frac{(\Delta\rho / \rho)gd}{U_o^2} \tag{8-1}$$

Where, ρ is the density of the jet flow, $\Delta\rho$ density difference of the jet flow and the environment gases, d jet diameter, and U_o jet exit velocity. In general, the criteria value of Richardson number to consider the buoyancy effect is about 0.05. If Ri is less than 0.05, the buoyancy may be assumed to be negligible. The estimated values of R_i in this study are in the ranges of 7×10^{-4} and 8×10^{-4}, thus the effect of buoyancy is quite small comparing to jet momentum. Therefore, the current configuration can be considered as momentum driven flow.

8.7. The effects of preheating the oxidizer jet

Figure 8.51 shows the centerline temperature of the fuel and oxidizer jet for different oxidizer preheating temperature $T_{preheat}$=30, 100 and 500℃ with d_{ox}=15.9 mm, $X_{O2;ox}$ =0.30 and $\Phi_{overall}$ =1.0. It is noted that only oxidizer jet is preheated, thus the fuel jet flow is supplied at ambient temperature.

The centerline temperature of the oxidizer jet increases with higher preheating temperature as expected, while the peak of the fuel jet temperature shifts farther downstream region. This trend is quite similar to the effects of momentum change of the oxidizer jet by varying the size of the oxidizer jet or inlet oxygen fraction.

With higher preheating temperature of the oxidizer jet, the fuel jet expansion increases while the oxidizer dissipates quickly because the reaction zone shifts toward the oxidizer jet due to less momentum as shown in Figure 8.52. It is clearly observed from Figure 8.53 that the location where the fuel disappears increases with higher preheating temperature, whereas the scaled value of oxygen concentration becomes lower. This can be thought that the fuel jet can expand more laterally for less momentum of the oxidizer jet due to high temperature and low density. As a result, the reaction zone moves toward the oxidizer jet, and the temperature of the oxidizer jet and consumption of oxygen increase. Consequently, the oxygen concentration decays so fast due to combustion.

It is recommended that preheating of oxidizer jet would be applicable for quite high momentum of the jet to avoid early reaction; otherwise the oxidizer jet momentum decreases and reaction will occur strongly near the oxidizer exit. This can induce the peak of temperature near the oxidizer jet and non-uniformity in reaction, consequently non-homogeneous combustion condition.

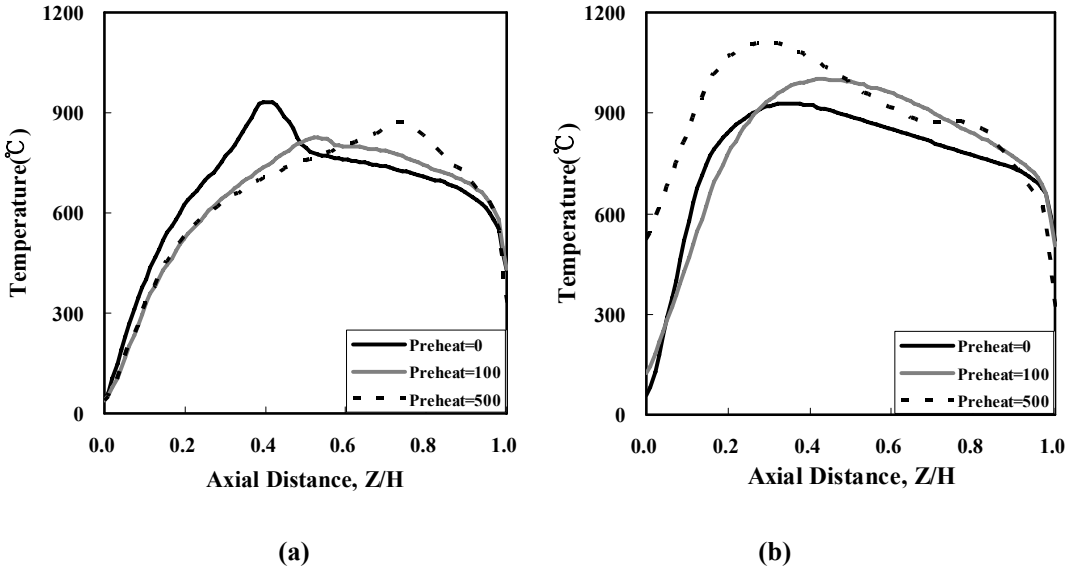

Figure 8.51: The centerline temperature of the (a) fuel jet and (b) oxidizer jet obtained from numerical calculations for various oxidizer jet preheating temperatures $T_{preheat}$= 30, 100 and 500℃ with overall equivalence ratios $\Phi_{overall}$= 1.0, $X_{O2;ox}$ =0.30 and d_{ox} =15.9 mm.

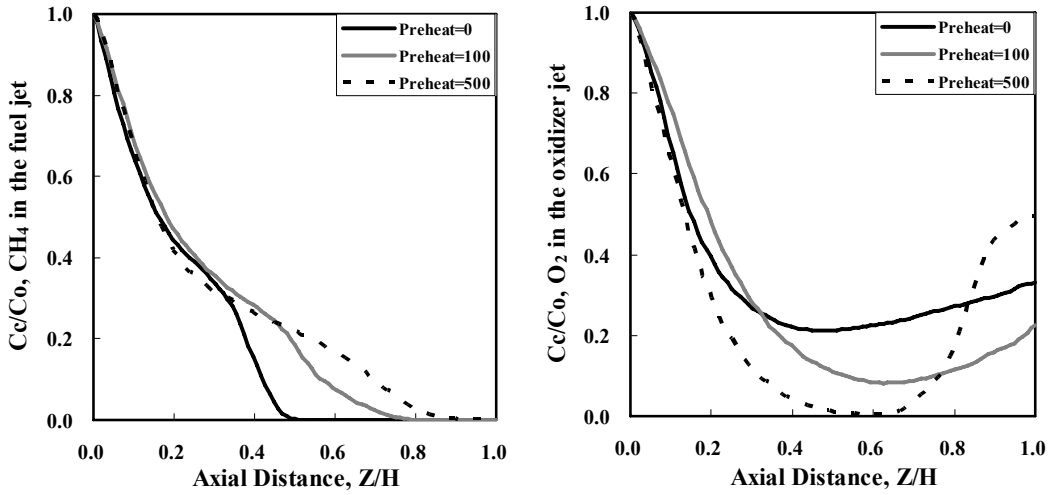

Figure 8.52: The decay profiles of the centerline concentration of the (a) CH_4 in the fuel jet and (b) O_2 in the oxidizer jet obtained from numerical calculations for various oxidizer jet preheating temperatures $T_{preheat}$= 30, 100 and 500℃ with overall equivalence ratios $\Phi_{overall}$ = 1.0, $X_{O2;ox}$ =0.30 and d_{ox}=15.9 mm.

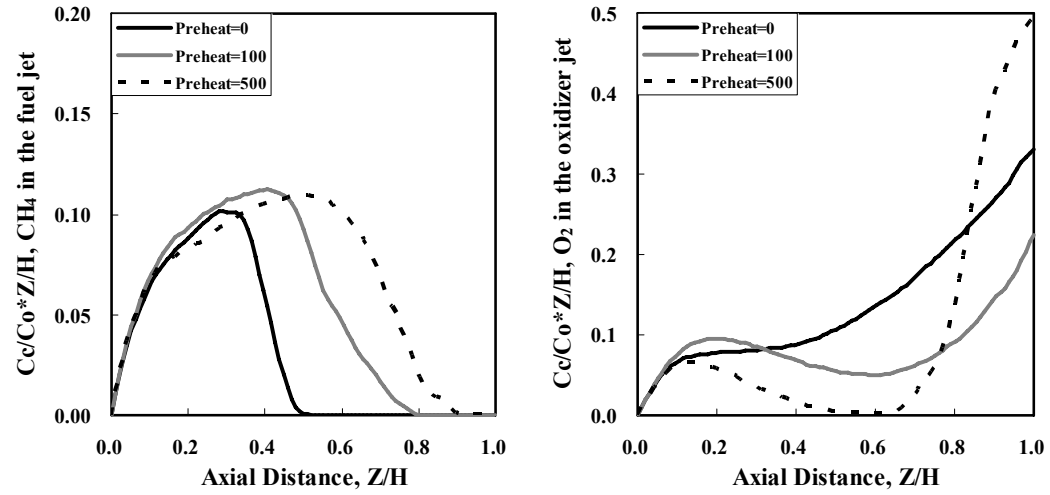

Figure 8.53: The scaled centerline concentration of the (a) CH4 in the fuel jet and (b) O2 in the oxidizer jet obtained from numerical calculations for various oxidizer jet preheating temperatures $T_{preheat}$= 30, 100 and 500℃ with overall equivalence ratios $\Phi_{overall}$ = 1.0, $X_{O2;ox}$ =0.30 and d_{ox}=15.9 mm.

CHAPTER 9

Summary, Conclusions and Future work

Non-reacting flow

Experimental [1] and numerical investigations were performed on the mixing characteristics and the resulting concentration fields in unconfined and non-reacting multiple turbulent jets. The control variables tested were separation distance and momentum ratio between jets. In addition, an extensive numerical study in a configuration representative of the furnace was conducted. This configuration consisted of confined but non-reacting five turbulent jets with a center fuel jet surrounded by four oxidizer jets. In this work, water jet experiments (done by Lee, [1]) were used to validate the FDS model for furnace design. The following conclusions were obtained.

- For unconfined non-reacting jets, the numerical results were found to agree well with the experimental data [1] giving confidence in modeling.
- Numerical calculations that agree well with experimental measurement [1] show that the centerline concentration decays faster in multiple jet configurations than in a single jet because of the strong interactions between jets and enhanced entrainment of the surrounding fluid. In multiple turbulent jets, the greater dilution of the mean centerline concentration of the center (fuel) jet occurred at lower separation distance due to enhanced interaction and thus mixing between jets. For large separation distance, the entrainment of the surrounding is promoted and mixing between jets is delayed to further downstream.
- Decreasing the momentum ratio, defined as the ratio of center jet momentum to side jet momentum, showed more dilution as a result of increased entrainment of

the surrounding fluid while high momentum ratio showed enhanced mixing between jets. However, it is possible that reaction may occur near the jet exit region due to strong mixing between jets for large momentum ratios and small separation distances.

- The main difference between unconfined and confined jets is the availability of surrounding fluid. In unconfined configuration, the entrainment from surrounding fluid which is unlimited in amount occurs, whereas the quantity of surrounding fluid is limited in confined configuration. Hence, the recirculation flow is established as a stable part of the flow, and the pattern of mixing and entrainment is quite different in confined jets because of recirculation flow entrained by the jets.
- The numerical results of this study showed that the centerline stream-wise velocity decays faster in the confined jet configuration than in the unconfined jet configuration because of recirculation flow due to the presence of wall limiting the jet expansion.
- In confined multiple turbulent jets, jet mixing is achieved simultaneously by two ways; the one is interaction between jets as same in unconfined jets, the other is entrainment of recirculation flow. Better mixing occurred at moderate separation distance due to ideal combination of enhanced interaction between jets and recirculation flow of their mixture. Decreasing the momentum ratio showed better mixing as a result of widely distributed recirculation flow region and increased entrainment of the recirculation flow.
- In terms of achieving homogeneous combustion, the jets should be sufficiently diluted by the surrounding fluid before mixing together. The mixing between jets should be delayed for some distance from the jet exit to enable sufficient dilution by the surrounding fluid. Therefore, to achieve homogeneous combustion, the separation distance should be kept sufficiently large and lower momentum ratio between jets is preferable to promote dilution by the surrounding fluid to avoid early reaction. In addition, the combination of high momentum ratio and small separation distance should be avoided because of early reaction due to strong interaction between jets to obtain homogeneous combustion.

Reacting flow

For investigating the structure of homogeneous combustion operating in the furnace, experimental study was performed in a laboratory-scale furnace with downward evolving separate fuel and oxidizer jets. The local distributions of temperature and gas composition of total hydrocarbon, oxygen, nitric oxide, carbon monoxide and carbon dioxide were measured and analyzed for different parameters (oxidizer nozzle diameter – which controls the oxidizer jet momentum, oxygen enrichment and the overall equivalence ratio) for the same fuel flow rate and fuel nozzle diameter. The UV emission intensities from the flame zone were recorded for various conditions and their trend was compared with the visual images. The experimental results were compared with predictions using modified Fire Dynamics Simulator (FDS) developed by National Institute of Standards and Technology (NIST). Numerical calculations that agree well with experimental measurement show that:

- The oxidizer jet momentum plays a very important role in achieving the homogeneous combustion condition. By increasing the oxidizer jet momentum (obtained by decreasing the oxidizer jet diameter or decreasing inlet oxygen concentration while maintaining the same equivalence ratio), homogeneous combustion can be easily obtained.
- Recirculation flow at different location occurs depending on the oxidizer jet momentum. The large scale recirculation is well formed for higher momentum oxidizer jets.
- With the aids of large scale of recirculation flows in the center region stabilized by buoyancy, homogeneous combustion is easily obtained.

Experimental results show that (done with Lee, [1]):

- The temperature profiles are quite uniform and flat with little fluctuations for the homogeneous combustion condition. It is also observed that a strong and efficient recirculation of product gases was obtained by combining sufficiently large separation distance between jets (which promotes the entrainment by the jet

based on the results of non-reacting flow) and downward evolving jets (with the help of buoyancy) as explained in section 5.1.

- In the homogeneous combustion condition, the flame is invisible without temporal and spatial fluctuations, and UV emission is uniform and low.
- NOx emission is very low because of low peak temperatures and also reduced prompt NOx due to reduction of OH concentration.

Future works

1. The separation distance between jets is another important control parameter affecting the mixing and reaction patterns in furnace. According to different separation distance, the furnace configuration may be changed to obtain the homogeneous combustion because the recirculation flow is formed at different locations. As shown in this study, the recirculation flow patterns play a key role in achieving the homogeneous combustion condition. Thus, it would be worthwhile to investigate the effects of different separation distance on reacting flow.

2. It has been long recognized that the significant energy saving method in industrial furnaces can be accomplished either by recycling heat or reducing the flue gas volume (removing/reducing the nitrogen ballast by oxygen enrichment) or combining both of them. In the recycling heat method, combustion air is preheated by recovering heat from the exhaust gas and transported back to the furnace using recuperators or regenerators. In addition, the flame stability limits increase significantly at high air preheats and even with low oxygen concentration air. In this study, the proper devices for capturing the exhaust gas enthalpy are not installed in experiments. As a result, flame becomes unstable and finally is blown out for the case of $X_{O2;o}$ =0.21 with the smallest oxidizer jet diameter, d_{ox}=7.94 mm because of low temperature in furnace. However, it is expected that the viable operating range of obtaining the homogeneous combustion can be extended with high

air preheat using recuperators or regenerators. Therefore, it is recommended performing the experimental study on the effects of air preheating.

3. Atreya et al. [73-76] proposed the novel solution in efficient energy saving method in industrial furnaces. The authors combined both concepts of recapturing wasted flue gas enthalpy to preheat the combustion air and reducing the total amount of exhaust by using oxygen-enriched air. Clearly, reducing or eliminating the exhaust of hot N_2 by using oxygen-enriched air will significantly increase the energy utilization efficiency. However, it will also create significant temperature non-uniformities (or hot spots) and increase NO production if N_2 is present without uniform burning in reaction zones and energy transfer via radiation.

4. This concept is diametrically opposite to the flameless oxidation concept. In the flameless oxidation concept, high regenerative preheating (above the auto ignition temperature) of combustion air along with excessive dilution by exhaust gas recirculation is utilized to enable burning in a very low oxygen concentration atmosphere. However, both these concepts can be profitably combined to yield additional advantages under the conditions that uniform burning is accomplished via distributed reaction zones and flame temperatures are reduced by intense flame radiation, thus energy is transferred at a very high rate from these reaction zones via radiation. Since radiation is the primary mode of heat transfer in the furnace, intensely and spatially uniformly radiating flames is a desirable attribute. The principal object of this concept is that nearly homogeneous burning occurs in distributed reaction zones under slightly rich conditions that enable increasing the flame radiation. Experiments conducted on turbulent non-premixed flames (Atreya et al. [73-76]) showed that the presence of even small amounts of soot in the high temperature reaction zone significantly increased the flame emissivity. Thus, oxygen enriched conditions can be beneficial as long as they are accompanied by high flame radiation. However,

there is no soot model implemented in FDS and only soot production rate from the fuel mass can be assigned in fire simulation based on empirical correlation for the mixture fraction model. The addition of a proper soot model in FDS will be needed to evaluate the effects of soot production.

BIBLIOGRAPHY

1. H.S.Lee, Experimental Studies on Mixing of Multiple Turbulent Jets in Non-Reacting and Reacting Flows. Doctoral Dissertation, 2007(University of Michigan).

2. Tanaka, R., New progress of energy saving technology towards the 21st century, Frontier of combustion and heat transfer technology. Proceedings of the 11th Members Conference of the International Flame Research Foundation, 1995.

3. Flamme, M., Low NOx combustion technologies for high temperature applications Energy Conversion and Management, 2001. 42(15-17): p. 1919-1935.

4. Milani, A., NOx emission from gas fired reheating furnaces for steelmaking plants. 19th World Gas Conference, 1994.

5. Mastorako, E., A.M. Taylor, and J.H. Whitelaw, Turbulent counterflow flames with reactants diluted by hot products. Joint Meeting of the British and German sections, 1993.

6. Katsuki, M. and T. Hasegawa, The science and technology of combustion in highly preheated air. Symposium (International) on Combustion, 1998. 27(2): p. 3135-3146.

7. Plessing, T., N. Peters, and J.G. Wünning, Laseroptical investigation of highly preheated combustion with strong exhaust gas recirculation. Symposium (International) on Combustion, 1998. 2: p. 3197-3204.

8. Wünning, J.A. and J.G. Wünning, Flameless oxidation to reduce thermal no-formation. Progress in Energy and Combustion Science, 1997. 23(1): p. 81-94.

9. Ahadi-Osuki, T., Heat Flux From Highly Preheated Air Combustion and Swirl Combustion. MS thesis, 2000(University of Maryland).

10. Tsuji, H., et al., High Temperature Air Combustion: From Energy Conservation to Pollution Reduction. Energy Conservation to Pollution Reduction, 2003: p. 401.

11. Hasegawa, T., S. Mochida, and A.K. Gupta, Development of advanced industrial furnace using highly preheated combustion air. Journal of Propulsion and Power, 2002. 18(2): p. 233-239.

12. Gupta, A.K., Thermal characteristics of gaseous fuel flames using high temperature air. Transactions of the ASME. Journal of Engineering for Gas Turbines and Power, 2004. 126(1): p. 9-19.

13. Lille, S., W. Blasiak, and M. Jewartowski, Experimental study of the fuel jet combustion in high temperature and low oxygen content exhaust gases. Energy, 2005. 30(2-4): p. 373-84.

14. Kishimoto, K., et al., Observational study of chemiluminescence from flames with preheated and low oxygen air. The First Asia-Pacific Conference on Combustion, 1997: p. 468–71.

15. Bolz, S. and A.K. Gupta, Effect of air preheat temperature and oxygen concentration on flame structure and emission. ASME, 1998. 1: p. 193–205.

16. Fujimori, T., D. Riechelmann, and J. Sato, Effect of lift-off on NOx emission of turbulent jet flame in high temperature co flowing air. 27th International Symposium on Combustion, 1998.

17. Garg, A., Specify better low-NOx burners for furnaces. Chem Eng Prog, 1994: p. 46~49.

18. Wood, S.C., Slect the right NOx control technology. 1994.

19. Orsino, S., R. Weber, and U. Bollettini, Numerical simulation of combustion of natural gas with hightemperature air. Combustion Science and Technology, 2001.

20. Eddings, E. and A. Sarofim, Advances in the use of computer simulations for evaluating combustion alternatives. 3rd CREST Int. Symp, 2000.

21. Dally, B.B., E. Riesmeier, and N. Peters, Effect of fuel mixture on moderate and intense low oxygen dilution combustion. Combustion and Flame, 2004. 137(4): p. 418-431.

22. Lallemant, N., A. Sayre, and R. Weber, Evaluation of emissivity correlations for H2O-CO2-N2/air mixtures and coupling with solution methods of the radiative transfer equation. Progress in Energy and Combustion Science, 1996. 22(6): p. 543-574.

23. Awosope, I.O. and F.C. Lockwood, Prediction of Combustion and NOx Emission Characteristics of Flameless Oxidation Combustion. IFRF Combustion Journal, 2005.

24. Krothapalli, A., D. Gaganoff, and K. Karamcheti, Development and structure of a rectangular jet in a multiple jet configuration. AIAA Journal, 1980. 18(8): p. 945-50.

25. Raghunathan, S. and I.M. Reid, A study of multiple jets. AIAA Journal, 1981. 19(1): p. 124-7.

26. Mostafa, A.A., M.M. Khalifa, and E.A. Shabana, Experimental and numerical investigation of multiple rectangular jets. Experimental Thermal and Fluid Science, 2000. 21(1): p. 171-178.

27. Chuang, S.-H., Z.-C. Hong, and J.-H. Wang, Multiple-plane-jet turbulent mixing analysis via a kinetic theory approach. International Journal for Numerical Methods in Fluids, 1991. 13(1): p. 83-107.

28. Wang, J., G.H. Priestman, and W. Dongdi, An analytical solution for incompressible flow through parallel multiple jets. Transactions of the ASME. Journal of Fluids Engineering, 2001. 123(2): p. 407-10.

29. Becker, H.A. and B.D. Booth, Mixing in the interaction zone of two free jets. AIChE Journal, 1975. 21(5): p. 949-58.

30. Moustafa, G.H., Experimental investigation of high-speed twin jets. AIAA Journal, 1994. 32(11): p. 2320-2322.

31. Okamoto, T., et al., Interaction of twin turbulent circular jet. Bulletin of the Japan Society of Mechanical Engineers, 1985. 28(238): p. 617-22.

32. Grandmaison, E.W. and N.L. Zettler, Turbulent mixing in coflowing plane jets. Canadian Journal of Chemical Engineering, 1989. 67(6): p. 889-97.

33. Wlezien, R.W., Nozzle geometry effects on supersonic jet interaction. AIAA Journal, 1989. 27(10): p. 1361-7.

34. Manohar, C.H.I., et al., A numerical and experimental investigation of the interactions between a non-uniform planar array of incompressible free jets. International Journal for Numerical Methods in Fluids, 2004. 44(4): p. 431-446.

35. Yimer, I., H.A. Becker, and E.W. Grandmaison, The Strong-jet/Weak-jet Problem: New Experiments and CFD. Combustion and Flame, 2001. 124(3): p. 481-502.

36. McGrattan, K.B., et al., Fire Dynamics Simulator—Technical References Guide. 20005, National Institute of Standards and Technology

37. Shin, S.J., H.S. Lee, and A. Atreya, A Study of Dilution and Mixing of Unconfined Multiple Turbulent Jets for Industrial Furnaces. 5th U. S. Combustion Meeting, 2007.

38. Horiuti, K., A proper velocity scale for modeling subgrid-scale eddy viscosities in large eddy simulation. Physics of Fluids A (Fluid Dynamics), 1993. 5(1): p. 146-57.

39. Deardorff, J.W., A numerical study of three-dimensional turbulent channel flow at large Reynolds numbers. Journal of Fluid Mechanics, 1970. 41: p. 435-52.

40. Moin, P., et al. Large eddy simulation of turbulent shear flows. 1979. Tbilisi, USSR: Springer-Verlag.

41. Murakami, S., Overview of turbulence models applied in CWE-1997. Journal of Wind Engineering and Industrial Aerodynamics, 1998. 74-76: p. 1-24.

42. Mizutani, K., et al., Study on influence of change of Smagorinsky constant. Proceedings of the Architectural Institute of Japan Annual Meeting 1991.

43. Clark, R.A., J.H. Ferziger, and W.C. Reynolds, Evaluation of subgrid-scale models using an accurately simulated turbulent flow. Journal of Fluid Mechanics, 1979. 91: p. 1-16.

44. Geurts, B.J. and J. Frohlich, A framework for predicting accuracy limitations in large-eddy simulation. Physics of Fluids, 2002. 14(6): p. 41-4.

45. Hussein, H.J., S.P. Capp, and W.K. George, Velocity measurements in a high-Reynolds-number, momentum conserving, axisymmetric, turbulent jet. . Fluid Mech, 1994. 258: p. 31-75.

46. Webster, D.R., P.J.W. Roberts, and L. Ra'ad, Simultaneous DPTV/PLIF measurements of a turbulent jet. Experiments in Fluids, 2001. 30(1): p. 65-72.

47. Fukushima, A., L. Aanen, and J. Westerweel, Simultaneous velocity and concentration measurements of an axisymmetric turbulent jet using a combined PIV/LIF. 5th JSME-KSME Fluids Engineering Conference, 2002: p. 17-21.

48. Panchapakesan, N.R. and J.L. Lumley, Turbulent measurement in axisymmetric jets of air and helium. Part 1. Air jet. J. Fluid Dyn, 1993. 246: p. 197–223.

49. Becker, H.A., H.C. Hottel, and G.C. Williams, The nozzle-fluid concentration field of the round, turbulent, free jet. Journal of Fluid Mechanics, 1967. 30: p. 285-304.

50. Birch, A.D., et al., The turbulent concentration field of a methane jet. Journal of Fluid Mechanics, 1978. 88: p. 431-49.

51. Dahm, W.J.A. and P.E. Dimotakis. MEASUREMENTS OF ENTRAINMENT AND MIXING IN TURBULENT JETS. 1985. Reno, NV, USA: AIAA, New York, NY, USA.

52. Dowling, D.R. and P.E. Dimotakis, Similarity of the concentration field of gas-phase turbulent jets. Journal of Fluid Mechanics, 1990. 218: p. 109-41.

53. Lockwood, F.C. and H.A. Moneib, FLUCTUATING TEMPERATURE MEASUREMENTS IN A HEATED ROUND FREE JET. Combustion Science and Technology, 1980. 22(1-2): p. 63-81.

54. Wilson, R.A.M. and P.V. Danckwerts, Studies in turbulent mixing--II : A hot-air jet. Chemical Engineering Science, 1964. 19(11): p. 885-895.

55. Dimotakis, P.E., The mixing transition in turbulent flows. Journal of Fluid Mechanics, 2000. 409: p. 69-98.

56. Lubbers, C.L., G. Brethouwer, and B.J. Boersma, Simulation of the mixing of a passive scalar in a round turbulent jet. Fluid Dynamics Research, 2001. 28(3): p. 189-208.

57. LePera, S. and U. Vandsburger, Coupled multiple jet excitation. Aerospace Sciences Meeting & Exhibit, 35th, 1997.

58. Gokarn, A., et al., Simulations of mixing for a confined co-flowing planar jet. Computers & Fluids, 2006. 35(10): p. 1228-1238.

59. So, R.M.C., S.A. Ahmed, and M.H. Yu, The near field behavior of turbulent gas jets in a long confinement. Experiments in Fluids, 1987. 5: p. 2-10.

60. Sunavala, P.D., C. Hulse, and M.W. Thring, Mixing and combustion in free and enclosed turbulent jet diffusion flames. Combustion and Flame, 1957. 1(2): p. 179-193.

61. Dealy, J.M., Momentum Exchange in a Confined Circular Jet with Turbulent Source. Ph. D. Thesis, University of Michigan, 1964.

62. Kandakure, M.T., V.C. Patkar, and A.W. Patwardhan, Characteristics of turbulent confined jets. Chemical Engineering and Processing. In Press, Corrected Proof.

63. Heitor, M.V. and A.L.N. Moreira, Thermocouples and sample probes for combustion studies. Progress in Energy and Combustion Science, 1993. 19(3): p. 259-278.

64. Beyler, C.L., Development and Burning of a Layer of Products of Incomplete Combustion Generated by a Buoyant Diffusion Flame. Doctor of Philosophy Thesis, 1983.

65. Fleck, B.A., A. Sobiesiak, and H.A. Becker, Experimental and numerical investigation of the novel low NOx CGRI burner. Combustion Science and Technology, 2000. 161(1-6): p. 89-112.

66. Murer, S., B. Pesenti, and P. Lybaert, Simulation of flameless combustion of natural gas in a laboratory scale furnace. Turkish Journal of Engineering and Environmental Sciences, 2006. 30(3): p. 135-43.

67. Cavaliere, A. and M. de Joannon, Mild Combustion. Progress in Energy and Combustion Science, 2004. 30(4): p. 329-366.

68. Knystautas., R., The turbulent jet from a series of holes in line. The Aeronautical Quarterly, 1964. 15.

69. Papanicolaou, P.N. and E.J. List, Statistical and spectral properties of tracer concentration in round buoyant jets. International Journal of Heat and Mass Transfer, 1987. 30(10): p. 2059-71.

70. Yuu, S., F. Shimoda, and T. Jotaki, Hot wire measurement in the interacting two-plane parallel jets. AIChE Journal, 1979. 25(4): p. 676-85.

71. Westbrook, C.K. and F.L. Dryer, Simplified Reaction Mechanisms for the Oxidation of Hydrocarbon Fuels in Flames. Combustion Science and Technology, 1981. 27: p. 31–43.

72. Grosshandler, W., A Narrow Band Model for Radiation Calculations in a Combustion Environment. NIST Technical Note TN 1402, 1993.

73. Atreya, A., et al. Effect of changes in the flame structure on the formation and destruction of soot and NOx in radiating diffusion flames. 1996. Napoli, Italy: Combustion Inst, Pittsburg, PA, USA.

74. Mungekar, H.P. and A. Atreya. Control of soot luminosity and soot emission in counter-flow flames by partial premixing. 2001. Ananheim, CA, United States: American Society of Mechanical Engineers, New York, NY 10016-5990, United States.

75. Mungekar, H.P. and A. Atreya, Flame radiation and soot emission from partially premixed methane counterflow flames. Journal of Heat Transfer, 2006. 128(4): p. 361-367.

76. Mungekar, H.P. and A. Atreya, Effect of partial premixing on the sooting structure of methane flames. Combustion and Flame, 2006. 144(1-2): p. 336-348.